



2014-10-01

Application of Variation of Parameters to Solve Nonlinear Multimode Heat Transfer Problems

Travis J. Moore

Brigham Young University - Provo

Follow this and additional works at: <https://scholarsarchive.byu.edu/etd>



Part of the [Mechanical Engineering Commons](#)

BYU ScholarsArchive Citation

Moore, Travis J., "Application of Variation of Parameters to Solve Nonlinear Multimode Heat Transfer Problems" (2014). *All Theses and Dissertations*. 4254.

<https://scholarsarchive.byu.edu/etd/4254>

This Dissertation is brought to you for free and open access by BYU ScholarsArchive. It has been accepted for inclusion in All Theses and Dissertations by an authorized administrator of BYU ScholarsArchive. For more information, please contact scholarsarchive@byu.edu, ellen_amatangelo@byu.edu.

Application of Variation of Parameters to Solve Nonlinear
Multimode Heat Transfer Problems

Travis J. Moore

A dissertation submitted to the faculty of
Brigham Young University
in partial fulfillment of the requirements for the degree of

Doctor of Philosophy

Matthew R. Jones, Chair
Brian D. Iverson
Vladimir P. Soloviev
Dale R. Tree
Brent W. Webb

Department of Mechanical Engineering

Brigham Young University

October 2014

Copyright © 2014 Travis J. Moore

All Rights Reserved

ABSTRACT

Application of Variation of Parameters to Solve Nonlinear Multimode Heat Transfer Problems

Travis J. Moore
Department of Mechanical Engineering, BYU
Doctor of Philosophy

The objective of this work is to apply the method of variation of parameters to various direct and inverse nonlinear, multimode heat transfer problems. An overview of the general method of variation of parameters is presented and applied to a simple example problem. The method is then used to obtain solutions to three specific extended surface heat transfer problems: 1. a radiating annular fin, 2. convective and radiative exchange between the surface of a continuously moving strip and its surroundings, and 3. convection from a fin with temperature-dependent thermal conductivity and variable cross-sectional area. The results for each of these examples are compared to those obtained using other analytical and numerical methods.

The method of variation of parameters is also applied to the more complex problem of combined conduction-radiation in a one-dimensional, planar, absorbing, emitting, non-gray medium with non-gray opaque boundaries. Unlike previous solutions to this problem, the solution presented here is exact. The model is verified by comparing the temperature profiles calculated from this work to those found using numerical methods for both gray and non-gray cases.

The combined conduction-radiation model is then applied to determine the temperature profile in a ceramic thermal barrier coating designed to protect super alloy turbine blades from large and extended heat loads. Inverse methods are implemented in the development of a non-contact method of measuring the properties and temperatures within the thermal barrier coating. Numerical experiments are performed to assess the effectiveness of this measurement technique.

The combined conduction-radiation model is also applied to determine the temperature profile along the fiber of an optical fiber thermometer. An optical fiber thermometer consists of an optical fiber whose sensing tip is coated with an opaque material which emits radiative energy along the fiber to a detector. Inverse methods are used to infer the tip temperature from spectral measurements made by the detector. Numerical experiments are conducted to assess the effectiveness of these methods. Experimental processes are presented in which a coating is applied to the end of an optical fiber and connected to an FTIR spectrometer. The system is calibrated and the inverse analysis is used to infer the tip temperature in various heat sources.

Keywords: variation of parameters, multimode heat transfer, inverse heat transfer, conduction-radiation, thermal barrier coating, optical fiber thermometer

ACKNOWLEDGEMENTS

The author wishes to acknowledge Professor Matthew R. Jones for his guidance and expertise and Professors Dale R. Tree and David D. Allred for their input. He wishes to thank Kevin Reece and Josh Schmidt for their help with the experiments. He would also like to thank the members of his committee. This work would not be possible without the support of the author's family. The author also admits to receiving Divine assistance.

TABLE OF CONTENTS

LIST OF TABLES	ix
LIST OF FIGURES	x
NOMENCLATURE.....	xiv
1 Introduction.....	1
1.1 Multimode Heat Transfer.....	1
1.2 Nonlinear Heat Transfer Problems	2
1.3 Variation of Parameters	2
1.4 Radiatively Participating Media	3
1.5 Inverse Radiative Heat Transfer Problems	4
1.5.1 Thermal Barrier Coatings	5
1.5.2 Optical Fiber Thermometers	5
1.6 Overview.....	6
2 Prior Work	9
2.1 Nonlinear Multimode Heat Transfer Problems	9
2.2 Variation of Parameters for Nonlinear Problems	10
2.3 Inverse Heat Transfer Problems	11
2.4 Thermal Barrier Coatings	11
2.5 Optical Fiber Thermometers.....	12
3 The Method of Variation of Parameters.....	15
3.1 Method Overview	15
3.2 Verification of the Method of Variation of Parameters with a Simple Problem	18
4 Solving Nonlinear Extended Surface Heat Transfer Problems using Variation of Parameters.....	23
4.1 Radiating Annular Fin	24

4.2	Continuously Moving Convective-Radiating Pin Fin	29
4.3	Exponential Convective Fin with Temperature-Dependent Thermal Conductivity	31
4.4	Conclusion	35
5	Radiatively Participating Media.....	37
5.1	Semitransparent Media	37
5.2	Radiative Properties	38
5.3	Radiative Transfer Equation (RTE).....	38
5.4	Overall Energy Conservation.....	39
5.5	Total Radiative Heat Flux.....	40
6	Temperature Profile in a Non-Gray Medium Surrounded by Non-Gray Boundaries	41
6.1	Introduction.....	41
6.2	Problem Formulation	43
6.3	Analytical Solution	45
6.4	Evaluation	56
6.5	Results and Discussion	58
6.6	Conclusion	64
7	Inverse Radiative Heat Transfer Analyses	65
7.1	Genetic Algorithm	66
7.2	Generalized Reduced Gradient Algorithm	67
7.3	Ill-Posed Problems	67
8	A Non-Contact Method of Measuring The Properties Of Thermal Barrier Coatings	69
8.1	Introduction.....	69
8.2	Problem Overview	71
8.3	Temperature Profile	72

8.3.1	Interfacial Reflectance at a Diffuse Boundary	74
8.3.2	Verification of Temperature Profile Model	76
8.3.3	Temperature Profile of an Actual TBC	77
8.4	Forward Problem	77
8.5	Unknown Parameters	81
8.6	Measurement Band Selection	81
8.7	Inverse Problem	84
8.8	Results of Numerical Experiments	86
8.9	Future Work	89
8.10	Conclusion	90
9	Optical Fiber Thermometer: Theoretical Analysis.....	91
9.1	Introduction.....	91
9.2	Forward Problem	93
9.3	Temperature Profile along the Fiber.....	97
9.4	Heat Source Temperature	104
9.5	Simplifications to the Forward Problem.....	106
9.5.1	Constant Thermal Conductivity	107
9.5.2	Neglect Internal Radiation	109
9.5.3	Linearized Solution.....	112
9.6	Summary of the Forward Problem.....	115
9.7	Measurement Band Selection	116
9.8	Inverse Problem	119
9.9	Numerical Experiments	119
9.10	Determining the Heat Source Temperature	123
9.11	Heated Fiber.....	125

9.11.1 Forward Problem	126
9.11.2 Inverse Problem	129
9.11.3 Numerical Experiments	130
9.12 Conclusion	131
10 Optical Fiber Thermometer: Experimental Methods	133
10.1 Introduction.....	133
10.2 Optical Fiber	134
10.3 Cavity.....	135
10.4 Coating Material	135
10.5 Coating Process.....	136
10.6 Detection System	136
10.6.1 FTIR Spectrometer.....	137
10.6.2 Experimental Characterization of the Detector Response	139
10.7 Verification of Cavity Formation	145
10.8 OFT Calibration.....	147
10.8.1 Spectral Absorption Coefficient of the Fiber	148
10.8.2 Instrument Response Function for the OFT.....	153
10.8.3 Measuring Temperature using the OFT	155
10.9 Experiments	155
10.10 Conclusion and Future Work.....	161
11 Summary and Contributions	163
REFERENCES.....	165
Appendix A. Source Code	177
A.1 Variation of Parameters Example Problem, Section 3.2.....	177
A.2 Flux Gauge Problem, Section 4.1	178

A.3	Continuously Moving Fin, Section 4.2	180
A.4	Exponential Fin with Variable Thermal Conductivity, Section 4.3.....	181
A.5	Non-gray Medium Surrounded by Non-Gray Boundaries, Section 6.4.....	182
A.6	Non-gray Thermal Barrier Coating, Section 8.3.2.....	191
A.7	Genetic Algorithm for TBC, Section 8.8.....	197
A.8	Instrument Response Function for OFT, Section 10.9	204

LIST OF TABLES

Table 6-1: Spectral properties for two non-gray cases.	62
Table 8-1: Properties used in three cases to verify the model	76
Table 8-2: Example of setting used in the genetic algorithm	87
Table 8-3: Example of optimum parameter values found from the genetic algorithm.....	88
Table 8-4: Example of optimum parameter values found from the genetic algorithm with 10% measurement error	88
Table 8-5: Example of optimum parameter values found from the genetic algorithm with 20% measurement error	89
Table 9-1: System parameters for hypothetical OFT system.....	107
Table 9-2: Example of known parameters used in the GRG algorithm.....	120
Table 9-3: Example of optimum unknown parameter values found from the GRG algorithm	121
Table 9-4: Example of optimum unknown parameter values found from the GRG algorithm with 10% measurement error	121
Table 9-5: Example of optimum unknown parameter values found from the GRG algorithm with 20% measurement error	122
Table 9-6: Comparison of optimums found with differing fiber lengths.....	122
Table 9-7: Average error between optimum values and actual values with and without measurement error	123
Table 9-8: Parameters used in example temperature distribution in two-zone system.....	128
Table 9-9: Comparison of optimums found with differing lengths of the heated portion of the fiber.....	131

LIST OF FIGURES

Figure 3-1: Comparison of traditional method and variation of parameters over $x = 2$ to $x = 6$	21
Figure 3-2: Comparison of traditional method and variation of parameters over $x = 7$ to $x = 12$	21
Figure 4-1: Schematic diagram of a typical circular foil heat flux gauge.	24
Figure 4-2: Comparison of the dimensionless temperature profiles found from variation of parameters to those found from a Green’s function approach and numerical methods for various values of the parameters A and B	28
Figure 4-3: Comparison of dimensionless temperature profiles found from variation of parameters to those found from HAM and numerical methods for $N_c = 4$, $N_r = 4$, $Pe = 3$, and $L^* = 1$	32
Figure 4-4: Comparison of the dimensionless temperature profiles found from variation of parameters to those found from DTM and numerical methods for $a = 1$ and $N = 1$ for various values of β	36
Figure 6-1: Absorbing-emitting medium between two diffuse boundaries. Coordinates used in the theoretical analysis are shown	44
Figure 6-2: Comparison of present method to numerical methods for case of gray medium ($\kappa = 1$) with black boundaries for various conduction-to-radiation parameters.....	59
Figure 6-3: Comparison of present method to finite strip method for case of gray medium ($\kappa = 1$) with $\varepsilon_0 = \varepsilon_L = 1$ and $\varepsilon_0 = \varepsilon_L = 0.1$ for $N = 0.001$	60
Figure 6-4: Comparison of present method to CFD solutions for case of gray medium ($\kappa = 0.1$) with $\varepsilon_0 = 0.75$ and $\varepsilon_L = 0.1$ for various conduction-to-radiation parameters.....	61
Figure 6-5: Comparison of present method to CFD solutions for case of gray medium ($\kappa = 1$) with $\varepsilon_0 = 0.2$ and $\varepsilon_L = 0.9$ for various conduction-to-radiation parameters.....	61
Figure 6-6: Comparison of present method to CFD solutions for various thermal conductivities with non-gray properties corresponding to Case 1 in Table 6-1	62
Figure 6-7: Comparison of present method to CFD solutions for various thermal conductivities with non-gray properties corresponding to Case 2 in Table 6-1	63
Figure 7-1: Basic flowchart of a genetic algorithm	66

Figure 8-1: Schematic of the proposed experimental setup.....	72
Figure 8-2: Reflection and transmission of radiation at the interface of two semi-transparent media.....	75
Figure 8-3: Comparison of present method to CFD solutions for properties shown in Table 8-1.....	77
Figure 8-4: Coordinates used in the theoretical analysis of a TBC.....	78
Figure 8-5: Measured spectral absorption coefficients of YSZ, 8YSZ, zirconia, and the spectral emittance of a NiCrAlY bond coat.....	82
Figure 8-6: Sensitivity of spectral irradiation on detector to changes in the substrate temperature.....	83
Figure 8-7: Sensitivity of spectral irradiation on detector to changes in the TBC surface temperature.....	84
Figure 9-1: Coordinates used in the theoretical analysis of the optical fiber thermometer.....	93
Figure 9-2: Illustration of total internal reflection.....	94
Figure 9-3: Differential volume of optical fiber with energy interactions.....	98
Figure 9-4: Energy interactions with the OFT sensing tip.....	105
Figure 9-5: Temperature profiles in a fiber of diameter 0.01m at two different values of k for the parameters shown in Table 9-1.....	108
Figure 9-6: Temperature profiles in a fiber of diameter 0.0001m at two different values of k for the parameters shown in Table 9-1.....	108
Figure 9-7: Temperature profiles in a fiber of diameter 0.01m with and without internal radiation.....	111
Figure 9-8: Temperature profiles in a fiber of diameter 0.0001m with and without internal radiation.....	112
Figure 9-9: Temperature profiles in a fiber of diameter 0.01m with linearized and non-linearized models.....	114
Figure 9-10: Temperature profiles in a fiber of diameter 0.0001m with linearized and non-linearized models.....	115
Figure 9-11: Sensitivity of spectral irradiation on detector to changes in the cavity temperature.....	117

Figure 9-12: Sensitivity of spectral irradiation on the detector to changes in the convection coefficient in the heated section of the fiber	118
Figure 9-13: Sensitivity of the heat source temperature to changes in the convection coefficient and the surface emittance of the cavity at $k = 10$ W/mK.....	124
Figure 9-14: Sensitivity of the heat source temperature to changes in the convection coefficient and the surface emittance of the cavity at $k = 50$ W/mK.....	124
Figure 9-15: Schematic of two-zone OFT system	126
Figure 9-16: Example of a two-zone temperature distribution with parameters shown in Table 9-8	129
Figure 10-1: Schematic of the layers of an optical fiber.....	134
Figure 10-2: Optical path used to direct radiant energy from fiber to detection system	137
Figure 10-3: Basic components in an FTIR spectrometer	137
Figure 10-4: Experimental setup used to characterize the response of the FTIR detectors.....	139
Figure 10-5: Spectral blackbody emissive power at various temperatures as a function of the FTIR signal from the DTGS detector for five different frequencies	141
Figure 10-6: Comparison of the blackbody spectral intensity at 969°C calculated from the instrument response function of the DTGS detector to that calculated from the Planck function	143
Figure 10-7: Spectral blackbody emissive power at various temperatures as a function of the FTIR signal from the MCT detector for four different frequencies	143
Figure 10-8: Comparison of the blackbody spectral intensity at 353°C calculated from the instrument response function of the MCT detector to that calculated from the Planck function	145
Figure 10-9: Magnified photo of the sensing tip of an optical fiber thermometer	146
Figure 10-10: Spectral signals from coated and bare fibers inside and in front a blackbody radiator at 975°C.....	147
Figure 10-11: Experimental setup used to determine the spectral absorption coefficient of the silica optical fiber	148
Figure 10-12: Spectral signals from blackbody radiator at 1144 °C through different fiber lengths	151
Figure 10-13: Experimental value of the spectral absorption coefficient of fused silica optical fibers compared to reported measured values of silica glass	153

Figure 10-14: Experimental setup used to calibrate the optical fiber thermometer.....	154
Figure 10-15: Spectral signals from the OFT at different temperatures.....	157
Figure 10-16: Time-dependent thermocouple measurements in candle flame.....	159
Figure 10-17: Time-dependent thermocouple measurements in Bunsen burner flame.....	160

NOMENCLATURE

A	dimensionless gauge parameter
A	area
A	detector response coefficient
a	constant governing exponential fin shape
B	dimensionless irradiation
B	detector response coefficient
b	fin width
C	detector response coefficient
c	constant
c	specific heat
c	speed of light
D	diameter
D	detector response coefficient
E	emissive power
E	detector response coefficient
F	instrument response function
f	function
G	irradiation
h	convection heat transfer coefficient
I	radiative intensity
IRF	instrument response function
k	thermal conductivity
L	length
L	TBC thickness
M	measured signals
m	roots of auxiliary equation
N	dimensionless number
N	conduction-to-radiation parameter
n	refractive index
P	perimeter
P	function of z , λ , and μ
P	spectral variation due to optical path
Q	energy generation term
Q	function of z , λ , and μ
Q	detector response coefficient
q	heat flux
R	radius of heat flux gauge foil
R	function of λ and μ
R	detector response coefficient
R	ratio of instrument response function slopes
r	radial coordinate
S	detector response coefficient
\hat{s}	direction vector
T	temperature

t	flux gauge foil thickness
U	speed of moving pin fin
v	solution for VOP
W	Wronskian
X	dimensionless axial coordinate
X	detector response coefficient
x	axial coordinate
x	independent variable
Y	detector response coefficient
y	dependent variable
z	Cartesian coordinate

Greek

α	thermal diffusivity
α	absorptance
ε	emittance
θ	dimensionless temperature
θ	polar angle
κ	absorption coefficient
λ	constant governing thermal conductivity
λ	wavelength
μ	cosine of intensity direction
ν	frequency
ρ	dimensionless radial coordinate
ρ	density
ρ	reflectance
τ	transmittance
σ	scattering coefficient
σ	Stefan-Boltzmann constant
Φ	scattering phase function
ϕ	azimuthal angle
Ω	solid angle

Subscripts

0	at left boundary
a	surroundings of moving fin
b	emerging from furnace or die
b	at fin base
b	blackbody
C	cavity
c	complementary solution
c	convection-conduction number
c	cross-sectional area
D	detector
f	fiber
H	heat source

L	at right boundary
i	critical angle
i, m, n	indices
p	particular solution
R	radiative
R	temperature of heat sink
r	radiation-conduction number
s	surface area
s	in the \hat{s} direction
λ	spectral dependence, wavelength
μ	directional dependence
ν	spectral dependence, frequency

Superscripts

+	forward direction
−	backward direction
'	integrating variable
'	first derivative
"	second derivative

1 INTRODUCTION

The three physical mechanisms, or modes, by which thermal energy is transferred are conduction, convection, and radiation. In most practical heat transfer applications, multiple modes of heat transfer must be accounted for simultaneously. In such cases, the energy equation often reduces to a nonlinear differential equation. The method of variation of parameters is a relatively simple and easy to implement technique for solving many nonlinear differential equations. In this work, variation of parameters is used to solve the nonlinear equations that govern direct and inverse multimode heat transfer problems.

1.1 Multimode Heat Transfer

When the effects of two or three modes of heat transfer are significant in a system, the problem is said to be a multimode, or conjugate, heat transfer problem. This is the case for most practical heat transfer applications. There are conduction problems in which convection and radiation provide the thermal boundary conditions, such as the analysis of extended surfaces, or fins. Some problems deal with heat transfer by simultaneous convection and conduction, such as that which occurs in heat exchangers. Multimode heat transfer can also occur in radiatively participating media combined with conduction, such as in translucent coatings, or combined with convection, such as in boundary layers in flows at high temperatures.

1.2 Nonlinear Heat Transfer Problems

In multimode heat transfer problems, the governing equations are often highly nonlinear. The nonlinearity of these problems can be caused by a number of phenomena. If the temperature is one of the unknowns in the problem, the fundamental radiation terms involve temperature to the fourth power while conduction depends on the first power of temperature and its derivatives. Modeling the dependence of the convective heat transfer coefficient on temperature can introduce nonlinearities. Variations in the system properties and parameters with temperature can add further nonlinearities. When a radiatively participating medium is analyzed, the energy equation must be coupled with the total radiative heat flux resulting in a nonlinear integro-differential equation.

Almost all multimode heat transfer problems are solved numerically because of the highly nonlinear nature of the governing equations [1]. Examples of the traditional numerical methods used to solve these problems include finite-difference methods, finite-element methods, the zonal method, and the Monte Carlo method [2]. More recent techniques used to solve nonlinear problems include the variational iteration method, the homotopy perturbation method, and the parameter expansion method [3]. Each of these methods has advantages and drawbacks. The method of variation of parameters is a relatively simple, analytical method for solving some nonlinear differential equations that has the potential to be very useful in many heat transfer analyses.

1.3 Variation of Parameters

In many multimode heat transfer applications, the energy equation reduces to a second order differential equation with a nonlinear forcing function that is a function of both the independent variable and the dependent variable and its derivatives. Specifically, application of

an energy balance to a system frequently results in a nonlinear differential equation that governs the temperature field in the system. A common method of obtaining analytical solutions to second order, nonhomogeneous differential equations is the method of variation of parameters in which the particular solution is assumed to be the sum of the products of unknown variable parameters and functions that make up a fundamental solution set to the corresponding homogeneous equation. The method entails determining these unknown variable parameters. This common method can be extended to differential equations in which the nonhomogeneity is nonlinear. Variation of parameters can provide analytical solutions to nonlinear equations and its relative simplicity and ease of implementation make it an attractive alternative to traditional numerical methods. This method has not previously been applied to nonlinear heat transfer problems. In this work, variation of parameters is used to solve the nonlinear governing equations associated with various extended surface applications as well as applications of radiatively participating media.

1.4 Radiatively Participating Media

The interaction of thermal radiation with an absorbing, emitting, and scattering medium is often significant in the analysis of a system. Such a medium is said to be radiatively participating. Examples of these media include molecular gases such as water vapor and carbon dioxide, particulate media such as smoke and ash, and semitransparent media such as ceramics and foams. Modeling the radiative heat transfer through radiatively participating media is important in analyzing and optimizing engineering systems in which these media play a significant role.

Analysis of the radiative transfer in participating media involves the coupling of two objectives; 1. determining the radiative properties of the medium, and 2. deriving and solving the

governing equations for radiative transport in such media [4]. Once these objectives are achieved, a system can be modeled and analyzed. For example, when the radiative properties are known, the governing equations can be used to find other important parameters of the system such as the temperature field in the medium, the properties of surfaces surrounding the medium, or the heat flux through the medium. Because it is generally difficult to directly measure the radiative properties of a medium, they must be calculated based on parameters that are more easily measured. In order to deduce radiative properties from measurable parameters, an inverse analysis is required [5].

1.5 Inverse Radiative Heat Transfer Problems

A forward, or direct, radiative heat transfer problem is one in which the necessary geometry, temperatures, and properties of the system are known, allowing for the direct calculation of radiative intensity and fluxes. Inverse radiative problems are those in which unknown system parameters are found from a known intensity field. The goal of inverse analyses is to deduce parameters that are difficult to measure (such as radiative properties and temperature distributions) based on radiative measurements that are easier to obtain (such as radiative intensity or flux) [5]. The solution to an inverse problem is generally found by using optimization methods to minimize an objective function, which compares measured data values, such as radiative intensity or flux, with the corresponding values estimated from the direct, or forward, analysis. The difference between these values is minimized based on an optimized set of unknown parameters such as radiative properties. The method of variation of parameters can be a useful tool in efficiently solving the forward problem associated with inverse radiative heat transfer problems. In this work, variation of parameters will be implemented in inverse analyses

to determine the properties and parameters of two examples of radiatively participating media: thermal barrier coatings and optical fiber thermometers.

1.5.1 Thermal Barrier Coatings

There is a growing reliance on the use of thermal barrier coatings (TBCs) as insulation of metallic components, such as vanes and blades, from large and extended heat loads in power generation and aerospace turbines. These coatings allow for an increased inlet temperature, which is accompanied by an increased efficiency, and results in a reduction in the requirements for cooling air [6]. Thermal barrier coatings consist of a thin layer of ceramic oxide which adheres to the super alloy turbine component [7]. The ceramic topcoat is exposed to the hot combustion gases in the turbine, shielding the super alloy substrate from the elevated temperatures. Knowledge of the system properties and the temperature profile within the TBC is critical for evaluating the TBC performance and monitoring its health [8]. Non-contact, non-destructive techniques for finding these temperature profiles are highly desirable. Inverse radiative heat transfer methods can be used to determine the system properties and temperatures from measurements of the radiative intensity from the TBC. In this work, the method of variation of parameters is used to calculate the temperature profile in a thermal barrier coating and inverse methods are then used in the development of a non-contact method of measuring the properties and temperatures within the TBC. Numerical experiments are conducted to assess the effectiveness of the method.

1.5.2 Optical Fiber Thermometers

A blackbody optical fiber thermometer (OFT) consists of an optical fiber whose sensing tip is coated with a highly conductive, opaque material. This forms an isothermal cavity at the tip

of the fiber. The tip temperature can be inferred from the cavity emission, which is transmitted along the optical fiber to a detector [9]. The radiation detected also includes the effects of emission and absorption by the fiber itself and the standard two-color approach cannot be used to accurately determine the temperature of the sensing tip [10, 11]. The temperature of the tip can be inferred from measurements of the radiative intensity incident on the detector using an inverse analysis. In this work, variation of parameters is used to determine the temperature profile along the fiber. Inverse methods are then used to infer the tip temperature from spectral measurements of the radiative intensity from the fiber. Numerical experiments are conducted to assess the accuracy with which the tip temperature can be determined. Finally, preliminary experiments are performed in the development of a high temperature OFT system.

1.6 Overview

This dissertation presents the solutions to nonlinear analytical models of direct and inverse multimode heat transfer problems solved using the method of variation of parameters. The direct problems include extended surface applications and the combined conduction-radiation problem in a radiatively participating medium. The inverse problem applications include the analysis and numerical experimentation of a problem designed to determine the properties of a thermal barrier coating and the theoretical and experimental evaluation of a problem designed to measure the sensing tip temperature of an optical fiber thermometer. Relevant prior work and research in these topics is addressed in Chapter 2. Chapter 3 outlines the method of variation of parameters for linear and nonlinear differential equations. In Chapter 4, the method of variation of parameters is used to solve the nonlinear equations governing three extended surface applications: 1. a radiating annular fin, 2. convective and radiative exchange between the surface of a continuously moving strip and its surroundings, and 3. convection from

a fin with temperature-dependent thermal conductivity and variable cross-sectional area. Chapter 5 discusses the principles of radiatively participating media and introduces the relevant mathematical formulas, governing equations, and methods used to model these media. In Chapter 6, the method of variation of parameters is used to analytically solve the nonlinear governing equations presented in Chapter 5 to determine the temperature profile in a planar, emitting/absorbing, non-gray medium surrounded by non-gray boundaries. Chapter 7 discusses the basic concepts of inverse radiative heat transfer problems and the optimization methods used in their implementation. Chapters 8 and 9 present the inverse analyses used to determine the properties and parameters of a thermal barrier coating and an optical fiber thermometer, respectively, and show the results of numerical experimentation performed using these models. Chapter 10 includes the methods and results of experiments designed to determine the temperature of an optical fiber thermometer system using the model developed in Chapter 9. Finally, Chapter 11 presents a summary of the research presented in this work and the contributions made.

2 PRIOR WORK

This chapter provides a general overview of previous research conducted in the field of solutions to nonlinear equations that govern multimode heat transfer problems. It also addresses the research done for thermal barrier coatings and optical fiber thermometers.

2.1 Nonlinear Multimode Heat Transfer Problems

This work focuses on solutions to second order, nonlinear, nonhomogeneous differential equations. Such equations are prevalent in multimode heat transfer applications due to the second order spatial derivatives that represent diffusion terms in the differential energy equation [12]. In many cases, these equations have a nonhomogeneous forcing function that results from the effects of radiation and/or convection. Phenomena that give rise to nonlinear differential equations include radiative exchange between surfaces, temperature-dependent properties, modeling the dependence of a convective heat transfer coefficient on temperature, and the coupling of the energy equation with the total radiative heat flux in radiatively participating media. One of the most common nonlinear heat transfer problems comes from the analysis of extended surfaces. Abbasbandy and Shivanian [13] obtained an exact analytical solution to the convective fin problem in which the local convection coefficient along the fin surface has a power-law-type dependence on the local temperature difference between the fin and the surrounding fluid. Arslanturk [14] used the Adomian decomposition method (ADM) to analyze a

convective fin with temperature-dependent thermal conductivity while Moradi and Ahmadikia [15] solved a similar problem for fins of variable cross-sectional area using the differential transformation method (DTM). Aziz and Khani [16] used the homotopy analysis method (HAM) to solve the nonlinear equation describing the temperature distribution in a continuously moving radiating-convective fin with temperature-dependent thermal conductivity. The temperature distribution in convective annular fins with temperature-dependent thermal conductivity has been found by Ganji et al. [17] using the homotopy perturbation method (HPM) while that of radiating annular fins has been found using a Green's function approach by Jones and Solovjov [18] and Liechty et al. [19].

In addition to extended surfaces, nonlinear differential equations arise when solving the energy equation in a radiatively participating medium. These problems are highly nonlinear because the energy equation requires the total radiative heat flux, which is found by solving the integro-differential radiative transfer equation [5]. These problems are encountered in the analysis of combustion chambers, rocket nozzles, high-temperature heat exchangers, translucent glass or ceramic coatings, porous insulation, heat treatment of glass plates, and the drawing of optical fibers. Applications in this work include the simultaneous conduction and radiation in a radiatively participating medium. The combined conduction-radiation problem has been solved using an integral transformation method [20, 21], the finite element method [22, 23], the finite difference method [24, 25], the finite volume method [26, 27], the lattice Boltzmann method [28-30], and finite strip theory [31].

2.2 Variation of Parameters for Nonlinear Problems

The method of variation of parameters, or variation of constants, is a general method that has been used to solve nonhomogeneous, linear, ordinary differential equations since the

beginning of the 19th century [32]. More recently, it has been shown that this method can also be used to solve nonlinear differential equations [33-37]. In 1946, Kečkić first showed that variation of parameters could be extended to certain nonlinear differential equations [35]. In 2010, Mohyud-Din et al. [33] successfully applied the method of variation of parameters to various initial and boundary value problems and in 2013, Rahmatullah and Mohyud-Din [34] used variation of parameters to solve nonlinear diffusion equations. The method has been extended to apply to nonlinear equations of higher order [36]. The method of variation of parameters has not been applied previously to nonlinear heat transfer applications.

2.3 Inverse Heat Transfer Problems

The earliest inverse heat transfer problems date back to about 1960 and were only concerned with heat conduction [38-40]. It wasn't until the late 1980's that investigations into inverse radiative heat transfer began to appear [5]. Most of these papers deal with radiative transfer in participating media in which radiation is the only mode of heat transfer treated. Inverse methods were used to determine the temperature profile and properties of participating media [41-43]. Fewer inverse analyses have dealt with problems in which conduction are combined with radiative heat transfer [44, 45]. Most of these methods require knowledge of the temperature profile or heat flux, are only applicable to gray media, and require the use of numerical methods such as the Lattice Boltzmann method and the finite volume method [46-48]. Even fewer studies have investigated the combined convection and radiation problem [49].

2.4 Thermal Barrier Coatings

Various experimental methods have been employed to determine the temperatures within thermal barrier coatings. Infrared pyrometry has been used to determine the topcoat surface

temperature [50]. This process is complicated by the fact that the pyrometer will measure radiation from the hot environment reflected off of the TBC surface [51]. In addition, the translucency of the TBC at conventional pyrometer wavelengths allows radiation from well below the TBC surface to reach the pyrometer [51]. It has been proposed that Raman spectroscopy be used as a non-contact method of determining the temperature in thermal barrier coatings [50]. This, however, becomes increasingly difficult as the temperature increases because of the low intensity of the anti-Stokes Raman signal [50]. Luminescence spectroscopy is used to measure the temperature at the surface or at any desired depth of the TBC by utilizing the temperature dependence of the fluorescence decay time [52, 53]. Current techniques are limited in that they cannot measure the entire temperature profile of the TBC along with its radiative properties. Efforts have been made to measure various radiative properties of TBC systems [54-65]. These measurement techniques rely on reflectance and transmittance measurements of TBC samples and require carefully controlled experimental setups with known sample temperatures and, therefore, cannot be made *in situ*.

2.5 Optical Fiber Thermometers

The concept of the optical fiber thermometer was initially proposed in 1977 [66] and successfully proved in 1982 [9]. Since then, various investigations have been made in an attempt to advance the technology [67, 68]. These OFTs are either restricted to relatively low temperatures or require the use of two color pyrometry to determine the sensing tip temperature. If only the sensing tip and a small length of the optical fiber are exposed to the high temperature environment, then it may be an acceptable approximation to assume that all of the radiation detected is emitted by the blackbody cavity [9]. However, if a significant portion of the optical fiber is exposed to elevated temperatures, then the radiation detected also includes the effects of

emission and absorption by the fiber itself and the standard two-color approach cannot be used to accurately determine the temperature of the sensing tip [11, 69]. Barker and Jones have shown that inverse heat transfer methods can be used to accurately determine the temperature profile along the optical fiber of an OFT [70]. They used inverse heat transfer methods to account for the emission and absorption of the optical fiber and obtained accurate temperature measurements of the sensing tip as well as the temperature profile along the fiber [71]. Their model did not account for multiple modes of heat transfer in the fiber.

3 THE METHOD OF VARIATION OF PARAMETERS

The method of variation of parameters, or variation of constants, is a general technique taught in elementary differential equations courses that is used to solve nonhomogeneous, linear, ordinary differential equations [72]. It has been shown that this method can also be used to solve nonlinear differential equations [33-37]. This method has not previously been used to solve nonlinear heat transfer problems.

3.1 Method Overview

The method of variation of parameters [72] is generally used to solve nonhomogeneous second-order, linear, ordinary differential equations of the form

$$y''(x) + Ay'(x) + By(x) = f(x) \quad (3-1)$$

If the complementary, or general, solution to the associated homogeneous equation is

$$y_c(x) = c_1y_{c,1}(x) + c_2y_{c,2}(x) \quad (3-2)$$

where c_1 and c_2 are constants and $y_{c,1}$ and $y_{c,2}$ form a fundamental set of solutions of the homogeneous equation, then a particular solution to Equation (3-1) with the following form is desired.

$$y_p(x) = v_1(x)y_{c,1}(x) + v_2(x)y_{c,2}(x) \quad (3-3)$$

If Equation (3-3) and its derivatives are substituted into Equation (3-1), then Equation (3-1) has the following form.

$$y_p''(x) + Ay_p'(x) + By_p(x) = \frac{d}{dx}(y_{c,1}v_1' + y_{c,2}v_2') + A(y_{c,1}v_1' + y_{c,2}v_2') + y_{c,1}'v_1' + y_{c,2}'v_2' = f(x) \quad (3-4)$$

Two equations are required to find the two unknown functions v_1 and v_2 . By setting $y_{c,1}v_1' + y_{c,2}v_2' = 0$ in Equation (3-4), the two required equations are

$$y_{c,1}v_1' + y_{c,2}v_2' = 0 \quad (3-5)$$

$$y_{c,1}'v_1' + y_{c,2}'v_2' = f(x) \quad (3-6)$$

Solving these equations for the unknowns gives

$$v_1(x) = - \int \frac{f(x)y_{c,2}(x)}{W(y_{c,1}, y_{c,2})} dx \quad (3-7)$$

$$v_2(x) = \int \frac{f(x)y_{c,1}(x)}{W(y_{c,1}, y_{c,2})} dx \quad (3-8)$$

In Equations (3-7) and (3-8), $W(y_{c,1}, y_{c,2})$ is the Wronskian of $y_{c,1}$ and $y_{c,2}$.

$$W(y_{c,1}, y_{c,2}) = \begin{vmatrix} y_{c,1} & y_{c,2} \\ y_{c,1}' & y_{c,2}' \end{vmatrix} \quad (3-9)$$

The general solution to Equation (3-1) is

$$y(x) = y_c(x) + y_p(x) \quad (3-10)$$

The constants of integration from the indefinite integrals in Equations (3-7) and (3-8) are incorporated into the constants in the complementary solution. Because of the presence of the indefinite integrals in Equations (3-7) and (3-8), it may appear that the method of variation of parameters is only applicable to problems in which the antiderivatives can be computed analytically. However, recall that the antiderivatives of $G(t)$ are simply obtained by $\int_{t_0}^t G(w)dw$, where (t_0, t) is in the domain of G [73]. Therefore, variation of parameters can be used to find a

particular solution even when the integrals cannot be evaluated analytically. In such cases, Equations (3-7) and (3-8) become

$$v_1(x) = - \int_{x_1}^x \frac{f(x')y_{c,2}(x')}{W(y_{c,1}, y_{c,2})} dx' \quad (3-11)$$

$$v_2(x) = \int_{x_1}^x \frac{f(x')y_{c,1}(x')}{W(y_{c,1}, y_{c,2})} dx' \quad (3-12)$$

where the definite integrals are performed from a fixed point x_1 to an arbitrary point x .

Although historically this method has been primarily used to solve linear differential equations, the method of variation of parameters can be extended to solve nonlinear differential equations, particularly those in which the nonhomogeneity is a function of the dependent variable and its derivative in addition to the independent variable [33-37]. The general form of the nonlinear equation is

$$y''(x) + Ay'(x) + By(x) = f(x, y, y') \quad (3-13)$$

The solution procedure is the same as that outlined above for the linear equation such that

$$y(x) = c_1y_{c,1}(x) + c_2y_{c,2}(x) + v_1y_{c,1}(x) + v_2y_{c,2}(x) \quad (3-14)$$

where

$$v_1 = - \int_{x_1}^x \frac{f(x', y, y')y_{c,2}(x')}{W(y_{c,1}, y_{c,2})} dx' \quad (3-15)$$

$$v_2 = \int_{x_1}^x \frac{f(x', y, y')y_{c,1}(x')}{W(y_{c,1}, y_{c,2})} dx' \quad (3-16)$$

Because y appears on both sides of Equation (3-14), an iterative approach is required to solve for y . Although not a closed-form solution because of the iteration required, the solution can still be considered exact if f is only a function of x and y because the numerical integration required by Equations (3-15) and (3-16) can be performed to an arbitrary degree of accuracy. If f

is also a function of the derivatives of y , finite difference equations must be used to approximate these derivatives.

3.2 Verification of the Method of Variation of Parameters with a Simple Problem

The method will be demonstrated on a simple example which will be solved using traditional methods and using the method of variation of parameters. Consider the differential equation

$$y'' - y = x \quad (3-17)$$

subject to the boundary conditions

$$y(x_1) = y_1 \quad (3-18)$$

$$y(x_2) = y_2 \quad (3-19)$$

Note that Equation (3-17) is a linear, nonhomogeneous differential equation. However, if the y term is moved to the right side of the equation, the nonhomogeneity becomes a function of both the dependent variable, y , and the independent variable, x .

$$y'' = x + y = f(x, y) \quad (3-20)$$

First, Equation (3-17) will be solved using traditional methods and the solution will be compared to the solution of Equation (3-20) using variation of parameters. The complementary function of Equation (3-17) can be found using an auxiliary equation and a particular solution can be found using the method of undetermined coefficients. The auxiliary equation is

$$m^2 - 1 = 0 \quad (3-21)$$

The roots of the auxiliary equation are $m = \pm 1$ and the general solution of the homogeneous equation is

$$y_c = c_1 \cosh x + c_2 \sinh x \quad (3-22)$$

The method of undetermined coefficients yields a particular solution $y_p = -x$. The general solution is, therefore, given by the following equation.

$$y = y_c + y_p = c_1 \cosh x + c_2 \sinh x - x \quad (3-23)$$

Applying the boundary conditions and solving for the constants c_1 and c_2 gives

$$c_1 = \frac{1}{\cosh x_2 - \coth x_1 \sinh x_2} \left(y_2 + x_2 - (y_1 + x_1) \frac{\sinh x_2}{\sinh x_1} \right) \quad (3-24)$$

and

$$c_2 = \frac{y_1 + x_1}{\sinh x_1} - c_1 \coth x_1 \quad (3-25)$$

The method of variation of parameters is now used to solve Equation (3-20). The corresponding homogeneous equation is

$$\frac{d^2 y}{dx^2} = 0 \quad (3-26)$$

Equation (3-26) can be separated and integrates twice, yielding the following complementary function.

$$y_c = c_3 x + c_4 \quad (3-27)$$

Therefore, according to Equation (3-2),

$$y_{c,1} = x \quad (3-28)$$

$$y_{c,2} = 1 \quad (3-29)$$

and the Wronskian is

$$W(x, 1) = \begin{vmatrix} x & 1 \\ 1 & 0 \end{vmatrix} = -1 \quad (3-30)$$

The particular solution given by Equations (3-3) through (3-8) is

$$y_p = x \int_{x_1}^x (x' + y) dx' - \int_{x_1}^x x' (x' + y) dx' \quad (3-31)$$

This can be expanded to

$$y_p = \frac{1}{6}x^3 - \frac{1}{2}xx_1^2 + \frac{1}{3}x_1^3 + x \int_{x_1}^x y dx' - \int_{x_1}^x x' y dx' \quad (3-32)$$

The general solution is the sum of the complementary and particular solutions and is given by

$$y = c_3x + c_4 + \frac{1}{6}x^3 - \frac{1}{2}xx_1^2 + \frac{1}{3}x_1^3 + x \int_{x_1}^x y dx' - \int_{x_1}^x x' y dx' \quad (3-33)$$

The constant c_3 and c_4 are found by applying the boundary conditions given in Equations (3-18) and (3-19).

$$c_3 = \frac{1}{x_2 - x_1} \left(y_2 - y_1 - \frac{1}{6}x_2^3 + \frac{1}{2}x_2x_1^2 - \frac{1}{3}x_1^3 - x_2 \int_{x_1}^{x_2} y dx' + \int_{x_1}^{x_2} x' y dx' \right) \quad (3-34)$$

$$c_4 = y_1 - c_3x_1 \quad (3-35)$$

Equation (3-33) is then solved iteratively as follows. An initial guess for y is made over the desired domain. This guess is used to numerically integrate the integrals on the right side of Equation (3-33). Equation (3-33) is then used to calculate a new y function. This process is repeated until convergence is achieved. Figure 3-1 and Figure 3-2 compare the results of the solution to Equation (3-20) using the method of variation of parameters described above to those of the traditional methods used to solve Equation (3-17) given by Equation (3-23) over different domains. Two different solutions with different boundary conditions are shown in each figure. This solution was calculated from a MATLAB program which can be found in Appendix A.1.

While the method of variation of parameters is certainly excessive for a simple case such as that demonstrated above, it is a useful tool when solving many nonlinear differential governing equations that arise in heat transfer applications.

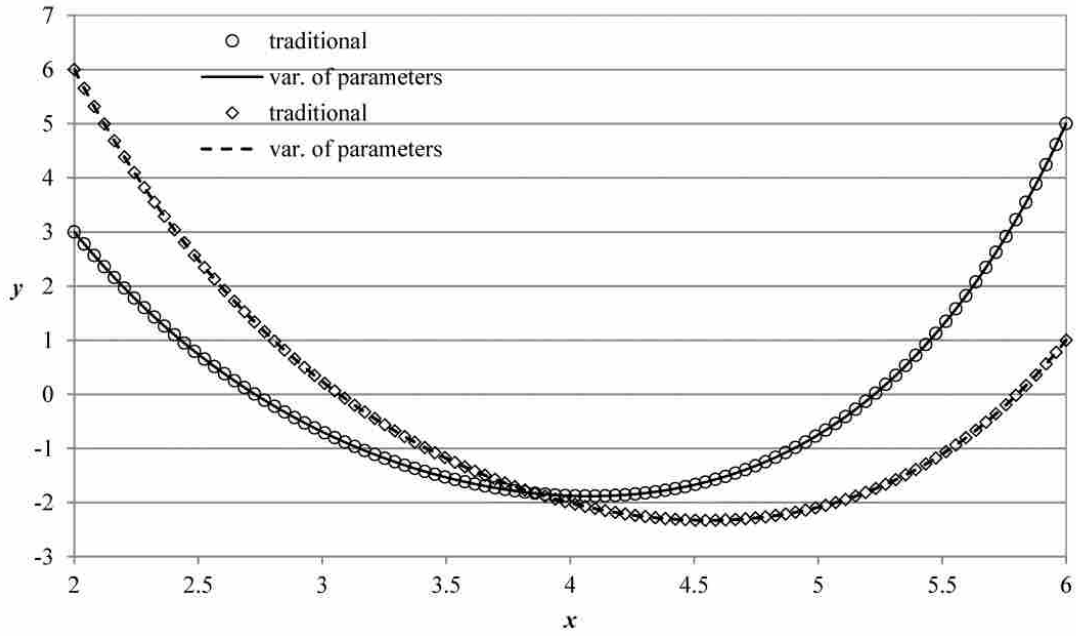


Figure 3-1: Comparison of traditional method and variation of parameters over $x = 2$ to $x = 6$

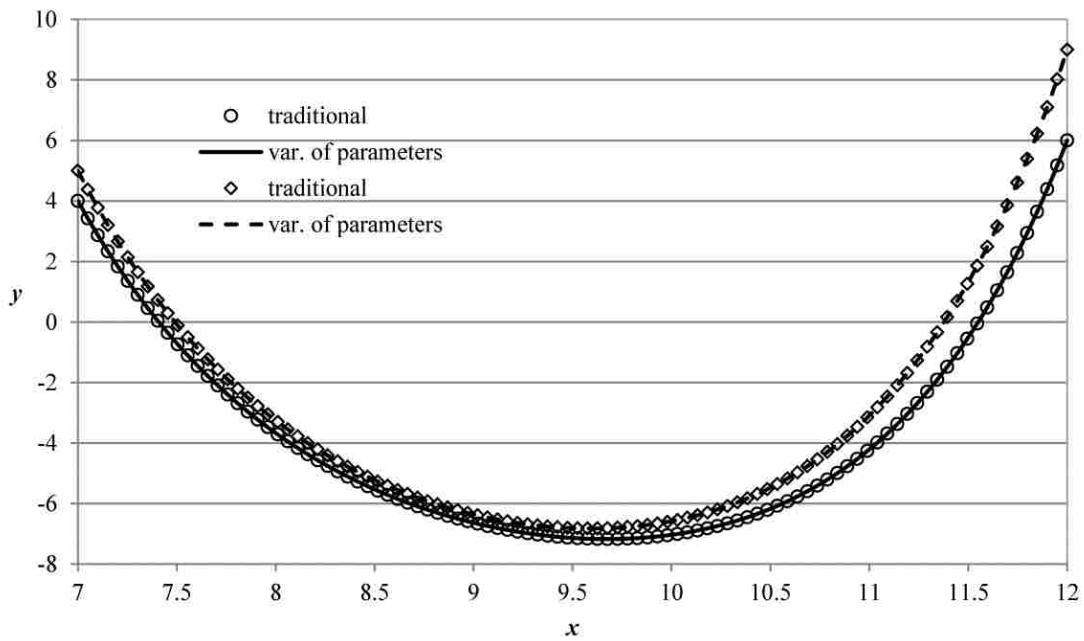


Figure 3-2: Comparison of traditional method and variation of parameters over $x = 7$ to $x = 12$

4 SOLVING NONLINEAR EXTENDED SURFACE HEAT TRANSFER PROBLEMS USING VARIATION OF PARAMETERS

The method of variation of parameters is shown to be useful for solving nonlinear differential equations that arise in multimode heat transfer problems. These types of problems frequently occur in the analysis of extended surfaces, or fins. In this chapter, variation of parameters is used to solve the energy equation for three specific applications: 1. a radiating annular fin, 2. convective and radiative exchange between the surface of a continuously moving strip and its surroundings, and 3. convection from a fin with temperature-dependent thermal conductivity and variable cross-sectional area. The results for each of these examples are compared to those obtained using other analytical and numerical methods and excellent agreement between them was found in all cases. The method of variation of parameters is less complex and relatively easy to implement compared to these other methods.

In Section 3.1, variation of parameters was shown to be useful for solving some nonlinear differential equations. In the following sections, the method of variation of parameters will be used to solve nonlinear differential equations that arise from the analysis of extended surfaces in various applications. The solutions to each of these problems are not closed-form analytical solutions because an iterative approach and numerical iteration are required. However, since numerical integration can be performed to an arbitrary degree of precision, the solutions to the first two problems are exact. The last example requires finite difference approximations of derivatives. For each example, the accuracy of the solution methodology is verified by

comparing the results to those of the direct numerical solution as well as other analytical methods.

4.1 Radiating Annular Fin

Heat flux measurements are important in many processes and procedures. These include monitoring ovens, furnaces, and kilns, flammability testing, measuring the thermal properties of materials, assessing heating, ventilation, and air conditioning systems, and validation of numerical models of combustion processes. Circular foil heat flux gauges can be modeled as radiating annular fins. Liechty et al. [19] presented a thermal model of a copper-constantan circular foil heat flux gauge exposed to a blackbody source in a vacuum environment. Such a setup is typically used to calibrate the heat flux gauge. A schematic of a typical copper-constantan circular foil heat flux gauge is shown in Figure 4-1.

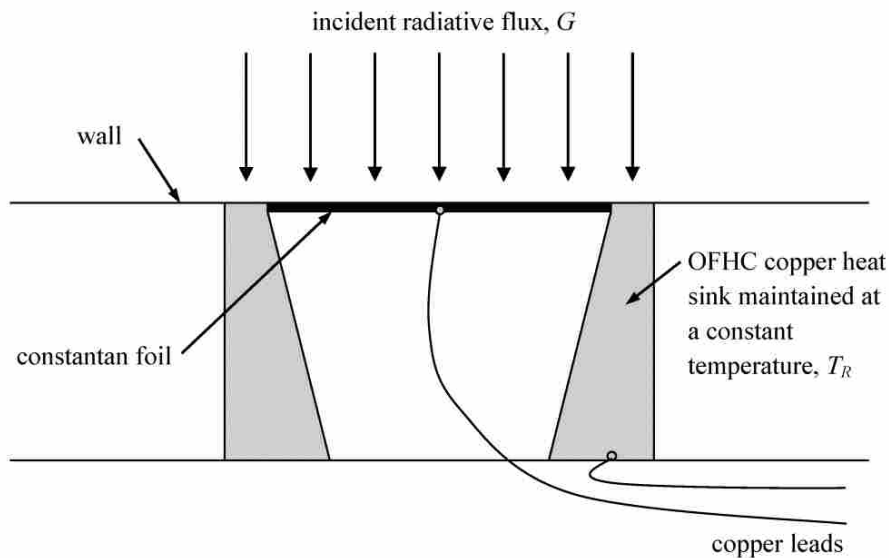


Figure 4-1: Schematic diagram of a typical circular foil heat flux gauge.

A circular constantan foil is attached to an oxygen-free, high-conductivity (OFHC) copper heat sink, which is maintained at a constant temperature. The constantan foil has a diffuse, highly absorbing coating. The design of the gauge is such that the heat loss from the back of the foil is minimized. The gauge is press-fit or threaded and screwed into a wall. Copper leads are attached to the center of the foil and to the copper heat sink. This results in copper-constantan thermocouple junctions at the center of the foil and at the interface between the foil and the heat sink. The voltage difference between the leads is proportional to the temperature difference between the center and the edge of the foil. A model of the heat transfer occurring in the foil can be used to develop a relationship between the measured temperature difference and the incident radiative heat flux. With the assumptions that a one-dimensional, radial temperature profile exists in the foil, the irradiation, G , is uniform over the gauge, the heat losses from the back of the gauge are negligible, the temperature gradients across the thickness, t , of the foil are negligible, the thermal conductivity, k , is constant, and the surface of the foil is diffuse and gray, the governing equation and boundary conditions for the temperature profile are given as follows [19].

$$\frac{1}{r} \frac{d}{dr} \left(r \frac{dT}{dr} \right) = \frac{\varepsilon \sigma}{kt} \left(T^4 - \frac{G}{\sigma} \right) \quad (4-1)$$

$$T(R) = T_R \quad (4-2)$$

$$\left. \frac{dT}{dr} \right|_{r=0} = 0 \quad (4-3)$$

The nondimensional governing equation for the dimensionless temperature profile and the boundary conditions for this model are given below.

$$\frac{1}{\rho} \frac{d}{d\rho} \left(\rho \frac{d\theta}{d\rho} \right) = A\theta^4 - AB \quad (4-4)$$

$$\theta(1) = 1 \quad (4-5)$$

$$\left. \frac{d\theta}{d\rho} \right|_{\rho=0} = 0 \quad (4-6)$$

In Equation (4-4), $\theta = T/T_R$ is the dimensionless temperature, $\rho = r/R$ is the dimensionless radial coordinate, $A = \varepsilon\sigma R^2 T_R^3 / kt$ is the dimensionless gauge parameter, and $B = G/\sigma T_R^4$ is the dimensionless irradiation. The solution to the homogeneous equation corresponding to Equation (4-4) is found by separating and integrating twice.

$$\theta_c = c_1 \ln \rho + c_2 \quad (4-7)$$

The particular solution is found by using the method of variation of parameters as outlined in Section 3.1. The solutions that form a fundamental set of solutions to the homogeneous equation are

$$\theta_{c,1} = \ln \rho \quad (4-8)$$

$$\theta_{c,2} = 1 \quad (4-9)$$

The unknown parameters are

$$v_1(\rho) = - \int_0^\rho \frac{f(\rho') \theta_{c,2}(\rho')}{W(\theta_{c,1}, \theta_{c,2})} d\rho' = \int_0^\rho \rho' (A\theta^4 - AB) d\rho' \quad (4-10)$$

$$v_2(\rho) = \int_0^\rho \frac{f(\rho') \theta_{c,1}(\rho')}{W(\theta_{c,1}, \theta_{c,2})} d\rho' = - \int_0^\rho \rho' (A\theta^4 - AB) (\ln \rho') d\rho' \quad (4-11)$$

Therefore, the particular solution is

$$\theta_p(\rho) = \theta_{c,1}v_1 + \theta_{c,2}v_2 = \ln \rho \int_0^\rho \rho'(A\theta^4 - AB)d\rho' - \int_0^\rho \rho'(A\theta^4 - AB)(\ln \rho')d\rho' \quad (4-12)$$

The dimensionless temperature profile is the sum of the complementary and particular solutions.

$$\theta = c_1 \ln \rho + c_2 + \ln \rho \int_0^\rho \rho'(A\theta^4 - AB)d\rho' - \int_0^\rho \rho'(A\theta^4 - AB)(\ln \rho')d\rho' \quad (4-13)$$

Applying the boundary conditions provides expressions for the constants c_1 and c_2 . Applying the boundary condition given by Equation (4-5) yields

$$\theta(1) = 1 = c_2 - \int_0^1 \rho'(A\theta^4 - AB)(\ln \rho')d\rho' \Rightarrow c_2 = 1 + \int_0^1 \rho'(A\theta^4 - AB)(\ln \rho')d\rho' \quad (4-14)$$

The first derivative of Equation (4-13) is

$$\frac{d\theta}{d\rho} = \frac{c_1}{\rho} + \frac{1}{\rho} \int_0^\rho \rho'(A\theta^4 - AB)d\rho' \quad (4-15)$$

Note that in differentiating the integral terms of Equation (4-13), a useful way of stating the fundamental theorem of calculus is $\frac{d}{dx} \int_a^x f(t)dt = f(x)$. Applying the boundary condition given in Equation (4-6) gives

$$\left. \frac{d\theta}{d\rho} \right|_{\rho=0} = 0 = \frac{c_1}{0} \Rightarrow c_1 = 0 \quad (4-16)$$

Substituting the constants into Equation (4-13) provide the final expression for the dimensionless temperature profile in the foil.

$$\begin{aligned} \theta(\rho) = 1 + \int_0^1 \rho'(A\theta^4 - AB)(\ln \rho')d\rho' + \ln \rho \int_0^\rho \rho'(A\theta^4 - AB)d\rho' \\ - \int_0^\rho \rho'(A\theta^4 - AB)(\ln \rho')d\rho' \end{aligned} \quad (4-17)$$

Because θ appears on both sides of Equation (4-17), an iterative approach is required. An initial guess for the temperature profile is plugged into the right side of Equation (4-17). The

integrals are evaluated numerically and a new temperature profile is computed. This process is repeated until convergence is achieved. Because numerical integration can be performed to an arbitrary degree of precision, the solution can be considered exact. Figure 4-2 shows a comparison of the dimensionless temperature profiles calculated from Equation (4-17) to those found using the Green's function method used by Liechty et al. [19] and to those found from a direct numerical solution using commercial software [74] for various values of the parameters A and B . This solution was calculated from a MATLAB program which can be found in Appendix A.2.

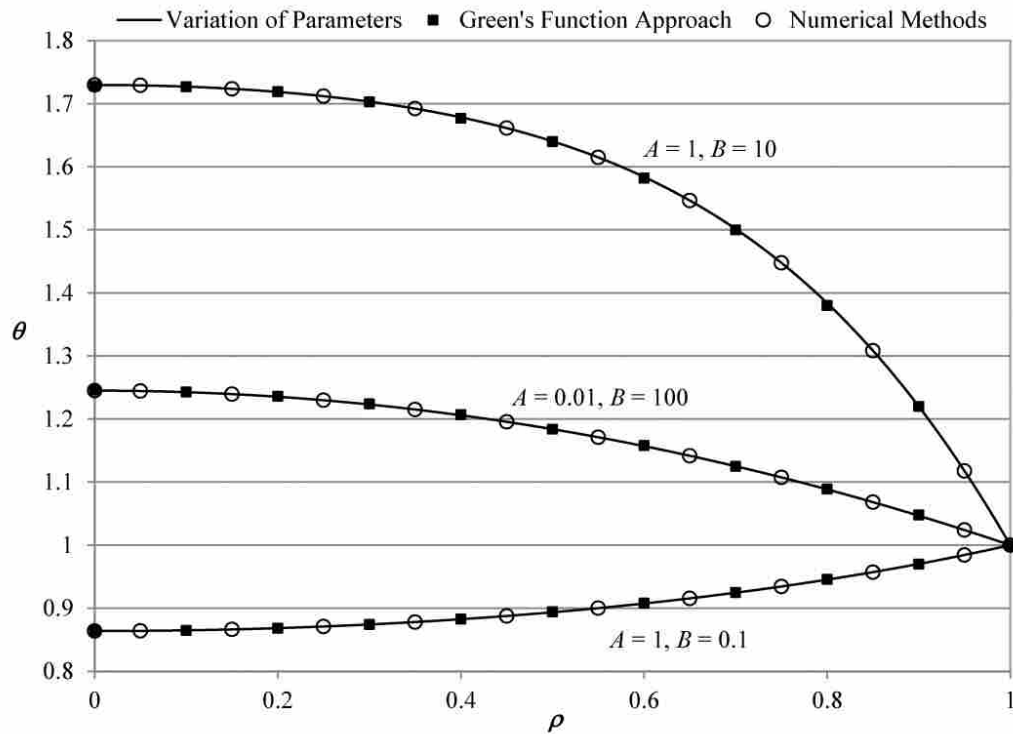


Figure 4-2: Comparison of the dimensionless temperature profiles found from variation of parameters to those found from a Green's function approach and numerical methods for various values of the parameters A and B .

4.2 Continuously Moving Convective-Radiating Pin Fin

In processes such as extrusion, hot rolling, and casting, the manufactured material loses heat to its surroundings by convection and radiation while in continuous motion. This heat transfer process is designed to cool the material to a specified temperature before it is spooled or removed. Aziz and Khani [16] used the homotopy analysis method (HAM) to find an analytic solution for heat transfer in a continuously moving strip which is losing heat to its surrounding by simultaneous convection and radiation.

Consider a solid bar with a cross-sectional area A and perimeter P that is moving horizontally at a constant speed U . The bar emerges from a die or furnace at a constant temperature T_b and is exposed to a colder surrounding medium at T_a and loses heat by radiation and convection. With the assumptions that the thermal conductivity, k , is constant, the material is gray and diffuse with a constant emittance, ε , and a constant heat transfer coefficient, h , over the entire surface of the moving material, the steady state energy balance may be written as [16]

$$\frac{d^2T}{dx^2} - \frac{hP}{kA}(T - T_a) - \frac{\varepsilon\sigma P}{kA}(T - T_a^4) - \frac{1}{\alpha}U \frac{dT}{dX} = 0 \quad (4-18)$$

where $\alpha = k/\rho c$ is the thermal diffusivity of the material, ρ is the density, and c is the specific heat. The axial coordinate x is measured from the slot from which the material emerges. The following dimensionless variables are introduced.

$$\theta = \frac{T}{T_b} \quad \theta_a = \frac{T_a}{T_b} \quad L^* = \frac{PL}{A} \quad X = \frac{xL^*}{L} \quad (4-19)$$

$$a = \beta T_b \quad N_c = \frac{hA}{Pk} \quad N_r = \frac{\varepsilon\sigma T_b^3}{Pk} \quad Pe = \frac{UA}{\alpha P} \quad (4-20)$$

where L is the length between the point of emergence and the point where the temperature gradient is zero, N_c is the convection-conduction number (commonly known as the Biot number), N_r is the radiation-conduction number, Pe is the Peclet number (which represents the

dimensionless speed of the moving strip), and L^* is a parameter that allows the length of the strip exposed to the surrounding fluid to be adjusted. The nondimensional governing equation and boundary conditions to this problem are given as follows.

$$\frac{d^2\theta}{dX^2} - N_c(\theta - \theta_a) - N_r(\theta^4 - \theta_a^4) - Pe \frac{d\theta}{dX} = 0 \quad (4-21)$$

$$\theta(0) = 1 \quad (4-22)$$

$$\left. \frac{d\theta}{dX} \right|_{X=L^*} = 0 \quad (4-23)$$

Equation (4-21) can be rearranged so that it has a nonlinear, nonhomogeneous function as specified by Equation (3-1).

$$\frac{d^2\theta}{dX^2} - Pe \frac{d\theta}{dX} - N_c\theta = N_r(\theta^4 - \theta_a^4) - N_c\theta_a \quad (4-24)$$

The procedure used to solve this equation is exactly the same as that used to solve the heat flux gauge problem in Section 4.1, and so the details are omitted here. The homogeneous equation corresponding to Equation (4-24) can be solved using an auxiliary equation [72] such that

$$\theta_c = c_1 e^{m_1 X} + c_2 e^{m_2 X} \quad (4-25)$$

where the roots of the auxiliary equation are given by

$$m_1 = \frac{Pe + \sqrt{(Pe)^2 + 4N_c}}{2} \quad (4-26)$$

$$m_2 = \frac{Pe - \sqrt{(Pe)^2 + 4N_c}}{2} \quad (4-27)$$

Variation of parameters is used as outlined in Section 3.1 to find the particular solution, which is

$$\theta_p(X) = -e^{m_1 X} \int_0^X \frac{(N_r(\theta^4 - \theta_a^4) - N_c\theta_a)e^{m_2 t}}{(m_2 - m_1)e^{(m_1+m_2)t}} dt + e^{m_2 X} \int_0^X \frac{(N_r(\theta^4 - \theta_a^4) - N_c\theta_a)e^{m_1 t}}{(m_2 - m_1)e^{(m_1+m_2)t}} dt \quad (4-28)$$

The dimensionless temperature profile is the sum of the complementary and particular solutions. Applying the boundary conditions provides expressions for the constants and the dimensionless temperature profile is

$$\begin{aligned} \theta(X) = & c_1 e^{m_1 X} + c_2 e^{m_2 X} - e^{m_1 X} \int_0^X \frac{(N_r(\theta^4 - \theta_a^4) - N_c \theta_a) e^{m_2 t}}{(m_2 - m_1) e^{(m_1 + m_2)t}} dt \\ & + e^{m_2 X} \int_0^X \frac{(N_r(\theta^4 - \theta_a^4) - N_c \theta_a) e^{m_1 t}}{(m_2 - m_1) e^{(m_1 + m_2)t}} dt \end{aligned} \quad (4-29)$$

where

$$\begin{aligned} c_1 = & \frac{1}{m_2 e^{m_2 L^*} - m_1 e^{m_1 L^*}} \left(m_2 e^{m_2 L^*} - m_1 e^{m_1 L^*} \int_0^{L^*} \frac{(N_r(\theta^4 - \theta_a^4) - N_c \theta_a) e^{m_2 t}}{(m_2 - m_1) e^{(m_1 + m_2)t}} dt \right. \\ & \left. + m_2 e^{m_2 L^*} \int_0^{L^*} \frac{(N_r(\theta^4 - \theta_a^4) - N_c \theta_a) e^{m_1 t}}{(m_2 - m_1) e^{(m_1 + m_2)t}} dt \right) \end{aligned} \quad (4-30)$$

$$c_2 = 1 - c_1 \quad (4-31)$$

Although not a closed-form solution because it requires an iterative approach, Equation (4-29) is exact. Figure 4-3 shows a comparison of the dimensionless temperature profiles calculated from Equation (4-29) to those found using HAM used by Aziz and Khani [16] and to those found from a direct numerical solution using commercial software [74] for $N_c = 4$, $N_r = 4$, $Pe = 3$, and $L^* = 1$. This solution was calculated from a MATLAB program which can be found in Appendix A.3.

4.3 Exponential Convective Fin with Temperature-Dependent Thermal Conductivity

Heat transfer through extended surfaces is used in many industrial applications. An extensive review of this subject is given by Kraus et al. [75]. The use of fins with constant cross-sectional area and the assumption of constant thermophysical properties over the length of the fin allow for some closed-form analytical solutions to the energy equation [75]. However, fins

optimized for specific purposes often have variable cross-sectional area and, if a large temperature difference exists within the fin, the thermal conductivity of the fin may vary over the length of the fin as a function of the temperature. These complexities can significantly complicate the governing energy balance, which becomes a nonlinear differential equation. Moradi and Ahmadikia [15] used the differential transformation method (DTM) to find an analytical solution to the energy equation for fins with different profiles and with temperature-dependent thermal conductivity.

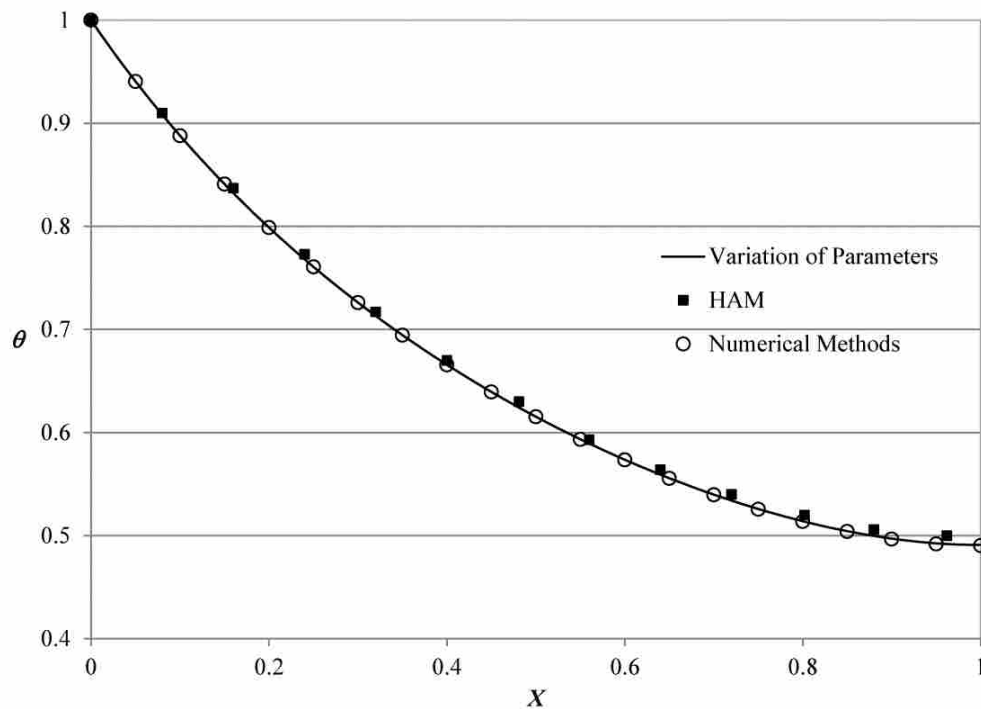


Figure 4-3: Comparison of dimensionless temperature profiles found from variation of parameters to those found from HAM and numerical methods for $N_c = 4$, $N_r = 4$, $Pe = 3$, and $L^* = 1$.

Here, variation of parameters is used to calculate the temperature profile in a fin with an exponential profile and a thermal conductivity that varies linearly with temperature. Consider a fin of length L and with a cross-sectional area $A(x)$ that varies as a function of axial position, x .

The fin surface is exposed to a convective environment at temperature T_∞ . The heat transfer coefficient, h , is constant over the length of the fin and the thermal conductivity, k , varies with the fin temperature. The one-dimensional energy equation reduces to [15]

$$\frac{d}{dx} \left(k(T)A(x) \frac{dT}{dx} \right) - A_s h(T - T_\infty) = 0 \quad (4-32)$$

where A_s is the total surface area of the fin. The thermal conductivity of the fin varies linearly with temperature according to

$$k(T) = k_\infty [1 + \lambda(T - T_\infty)] \quad (4-33)$$

where k_∞ is the thermal conductivity of the fin at the ambient temperature and λ is a constant. If b is the width of the fin, then the cross-sectional area of an exponentially varying fin is given by

$$A(x) = bt_b e^{a(x/L)} \quad (4-34)$$

where x is measured from the tip of the fin, t_b is the thickness at the base of the fin and a is a constant. The following dimensionless parameters are introduced

$$\theta = \frac{T - T_\infty}{T_b - T_\infty} \quad X = \frac{x}{L} \quad N = \left(\frac{hA_s L^2}{k_\infty A_b} \right)^{\frac{1}{2}} \quad (4-35)$$

where A_b is the area of the base of the fin and T_b is the base temperature. If $\beta = \lambda(T_b - T_\infty)$ and the base temperature is known and the tip is insulated, then the nondimensional governing equation and boundary conditions are given by

$$\frac{d}{dX} \left(e^{aX} (1 + \beta\theta) \frac{d\theta}{dX} \right) - N^2 \theta = 0 \quad (4-36)$$

$$\theta(1) = 1 \quad (4-37)$$

$$\left. \frac{d\theta}{dX} \right|_{X=0} = 0 \quad (4-38)$$

Equation (4-36) can be expanded and rearranged such that it is in the form of Equation (3-1).

$$\frac{d^2\theta}{dX^2} = \frac{1}{e^{aX}(1 + \beta\theta)} \left(N^2\theta - e^{aX}\beta \left(\frac{d\theta}{dX} \right)^2 \right) - a \frac{d\theta}{dX} \quad (4-39)$$

Note that the $a(d\theta/dX)$ term could remain on the left side of the equation as part of the homogeneous equation which could be solved using an auxiliary equation as was done in Section 4.2. However, this would make finding the particular solution using variation of parameters much more complicated and gives no added benefit because of the presence of the $(d\theta/dX)^2$ term in the nonhomogeneity, which will have to be solved using finite difference methods. Because the derivative is approximate, this solution cannot be considered exact, unlike the first two extended surface applications. The procedure used to solve Equation (4-39) is exactly the same as that used to solve the heat flux gauge problem in Section 4.1, and so the details are omitted here. The homogeneous equation corresponding to Equation (4-39) is separated and integrated twice, yielding the complementary solution.

$$\theta_c = c_1X + c_2 \quad (4-40)$$

The particular solution is found using the method of variation of parameters and is given as

$$\theta_p(X) = X \int_0^X f(t, \theta, \theta') dt - \int_0^X t f(t, \theta, \theta') dt \quad (4-41)$$

where

$$f(X, \theta, \theta') = \frac{1}{e^{aX}(1 + \beta\theta)} (N^2\theta - e^{aX}\beta(\theta')^2) - a\theta' \quad (4-42)$$

The dimensionless temperature profile is the sum of the complementary and particular solutions. The constants in Equation (4-40) are found by applying the boundary conditions so that the nondimensional temperature profile is given as follows.

$$\theta(X) = 1 - \int_0^1 f(t, \theta, \theta') dt + \int_0^1 t f(t, \theta, \theta') dt + X \int_0^X f(t, \theta, \theta') dt - \int_0^X t f(t, \theta, \theta') dt \quad (4-43)$$

Like the first two fin examples, an iterative approach is necessary to find θ . However, in this example finite difference methods must be used approximate θ' , so the solution is not exact. Figure 4-4 compares the temperature profile calculated from Equation (4-43) to that calculated using DTM [15] and that found from the direct numerical solution of Equation (4-36) [74] for various values of β with $a = 1$ and $N = 1$. This solution was calculated from a MATLAB program which can be found in Appendix A.4.

4.4 Conclusion

The method of variation of parameters was shown to be a useful tool for solving nonlinear differential equations that arise in extended surface problems. It was used to solve the energy equation for three specific applications: 1. a radiating annular fin, 2. convective and radiative exchange between the surface of a continuously moving strip and its surroundings, and 3. a convective fin with temperature-dependent thermal conductivity and variable cross-sectional area. Although the method requires an iterative approach and numerical integration, the solutions to the first two examples can be considered exact because numerical integration can be performed to an arbitrary degree of precision. The last example requires finite difference approximations of derivatives. The results for each of these examples were compared to those of

other analytical and numerical methods and there is excellent agreement between them. The method is relatively easy to implement and generally less involved than other analytical and numerical solutions.

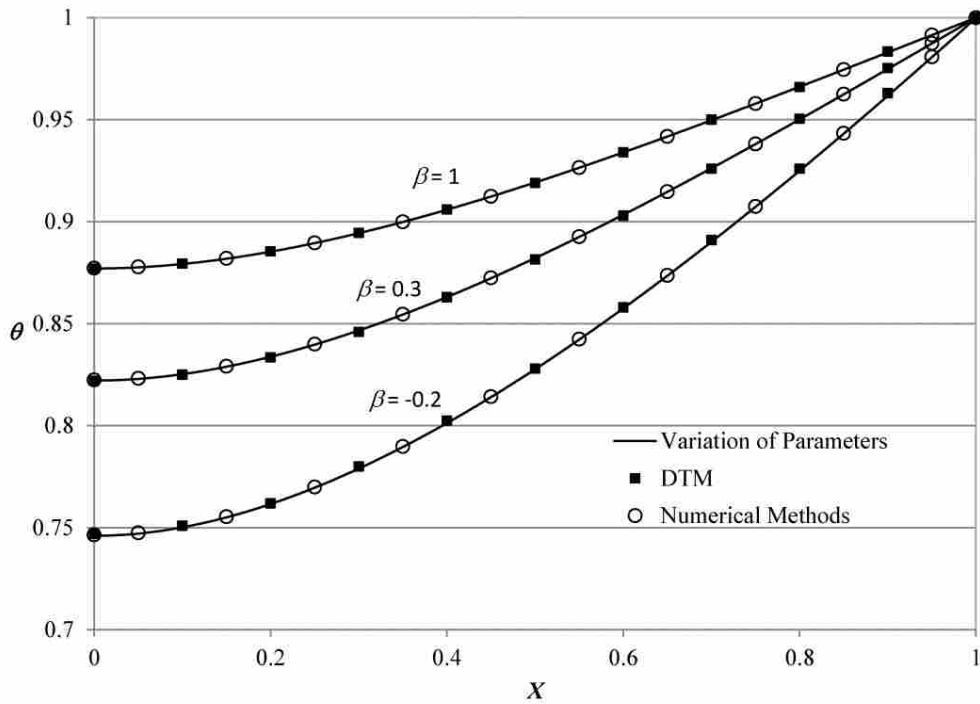


Figure 4-4: Comparison of the dimensionless temperature profiles found from variation of parameters to those found from DTM and numerical methods for $\alpha = 1$ and $N = 1$ for various values of β .

5 RADIATIVELY PARTICIPATING MEDIA

In addition to the analyses of extended surfaces, as shown in the Chapter 4, nonlinear equations also arise when solving the overall energy balance in radiatively participating media because the energy equation requires the total radiative heat flux, which is dependent on the temperature profile of the medium. This chapter describes the fundamental concepts of radiative heat transfer in participating media and the mathematical formulas and governing equations that are used when analyzing such media.

5.1 Semitransparent Media

When an electromagnetic wave penetrates a medium, attenuation of the wave may occur. If there is complete attenuation such that none of the penetrating radiation reemerges, the medium is said to be opaque. If the wave passes through the medium with no attenuation, the medium is referred to as transparent or radiatively non-participating. Many substances can be approximated as transparent in order to simplify analysis. However, in many cases the interaction of thermal radiation with the medium is significant. A radiatively participating medium is one in which the absorption, emission, and/or scattering of thermal radiation by the medium is significant. Examples of participating media include smoke, combustion gases, fibrous insulating layers, and foams. This research will apply to a particular class of radiatively participating media, namely, semitransparent media. A semitransparent medium is any solid or liquid into which electromagnetic waves are allowed to penetrate a significant distance. The two

semitransparent media that are investigated in this research are ceramics that are used in thermal barrier coatings and crystalline media (such as SiO₂) that optical fibers are made of in optical fiber thermometers.

5.2 Radiative Properties

The extent to which a radiatively participating medium interacts with thermal radiation is dependent upon the characteristics of the medium. Naturally, the thickness of the medium affects the degree to which incident radiation is attenuated. Additionally, the absorption and scattering characteristics of a participating medium can be described by its radiative properties such as its absorption coefficient, κ , scattering coefficient, $\sigma_{s,\lambda}$, and scattering phase function, Φ . The absorption coefficient represents the fraction of energy absorbed by a participating medium. Similarly, the scattering coefficient is the fraction of energy scattered by the medium. The scattering phase function describes the probability that a ray from one direction will be scattered into a specific direction in a participating medium. The emittance of a medium, ε , is the fraction of blackbody energy emitted by the medium at a given temperature. The reflectance, ρ , absorptance, α , and transmittance, τ , represent the fraction of radiation incident on a medium that will be reflected, absorbed, and transmitted, respectively. The refractive index, n , dictates the degree to which radiation is refracted by a medium.

5.3 Radiative Transfer Equation (RTE)

Accurate prediction of the heat transfer of a system with a radiatively participating medium requires simultaneously the solution to the governing equations and the determination of the radiative properties of the medium [76]. The equation that governs the behavior of radiative heat transfer in the presence of an absorbing, emitting, and/or scattering medium is known as the

Radiative Transfer Equation (RTE). This equation describes the radiative intensity field as a function of location, direction (fixed by a unit direction vector $\hat{\mathbf{s}}$), and spectral variable (such as wavelength, λ) [5]. The RTE is an integro-differential equation that can be derived by performing a radiative energy balance on a differential volume element along a single line of sight. The radiative transport equation can be expressed in terms of the spectral intensity I_λ of radiation propagating in the direction $\hat{\mathbf{s}}$ as [5]

$$\frac{1}{c} \frac{\partial I_\lambda}{\partial t} + \frac{\partial I_\lambda}{\partial s} = \kappa_\lambda I_{b,\lambda} - (\kappa_\lambda + \sigma_{s,\lambda}) I_\lambda + \frac{\sigma_{s,\lambda}}{4\pi} \int_{4\pi} I_\lambda(\hat{\mathbf{s}}_i) \Phi_\lambda(\hat{\mathbf{s}}_i, \hat{\mathbf{s}}) d\Omega_i \quad (5-1)$$

The first term on the left side of Equation (5-1) is the transient term where c is the speed of light. The first term on the right side represents emission from the participating medium in the direction $\hat{\mathbf{s}}$ where κ_λ is the spectral absorption coefficient. The second term represents attenuation of the intensity in the direction $\hat{\mathbf{s}}$ by absorption and “out-scattering” (scattering away from the direction of consideration) where $\sigma_{s,\lambda}$ is the spectral scattering coefficient. The last term represents “in-scattering” (augmentation of the intensity in the direction of interest due to scattering from all directions) and contains the scattering phase function Φ which represents the probability that the radiation propagating in a direction $\hat{\mathbf{s}}_i$ will be scattered into the direction $\hat{\mathbf{s}}$. There are a number of simplifying assumptions that were applied in the development of Equation (5-1): 1. the participating medium is at rest (as compared to the speed of light), 2. the medium is nonpolarizing and the state of polarization is neglected, 3. the medium is at local thermodynamic equilibrium and 4. the medium has a constant index of refraction [5].

5.4 Overall Energy Conservation

In a semitransparent medium, energy can be transferred internally by conductive and convective heat transfer in addition to thermal radiation. In order to determine the temperature

profile in the semitransparent medium, the energy conservation equation must include all three modes of heat transfer. In a semitransparent medium, radiative energy is deposited locally by absorption and leaves by local emission. The net energy transfer by radiative effects can be treated as a local energy source in a control volume. Therefore, the overall energy conservation equation for a stationary semitransparent medium is given by [5, 2]

$$\rho c_p \frac{\partial T}{\partial t} = \nabla \cdot (k \nabla T) - \nabla \cdot \mathbf{q}_R'' + \dot{Q}''' \quad (5-2)$$

The left side of Equation (5-2) represents the energy storage term. The first term on the right side is the divergence of the conduction flux vector, which is given by Fourier's law, and represents the net contribution to the control volume by heat conduction. Similarly, the net contribution of radiant energy is given by the negative of the divergence of the total radiative heat flux vector, \mathbf{q}_R'' . Finally, \dot{Q}''' is the local energy generation term.

5.5 Total Radiative Heat Flux

The radiative intensity depends on the temperature profile and so the energy equation (Equation (5-2)) and the RTE (Equation (5-1)) must be solved simultaneously. The radiative intensity is related to the total radiative heat flux vector inside a radiatively participating medium, \mathbf{q}_R'' , by the following equation [5].

$$\mathbf{q}_R'' = \int_0^\infty \int_{4\pi} I_\lambda(\hat{\mathbf{s}}) \hat{\mathbf{s}} d\Omega d\lambda \quad (5-3)$$

The total radiative heat flux is expressed in terms of the incident and outgoing spectral intensity integrated over all directions and over all wavelengths.

6 TEMPERATURE PROFILE IN A NON-GRAY MEDIUM SURROUNDED BY NON-GRAY BOUNDARIES

In a radiatively participating medium, the energy equation contains the divergence of the total radiative heat flux vector, as shown in Equation (5-2). The total radiative heat flux is a function of the intensity field, which is dependent upon the temperature profile in the medium to the fourth power. Therefore, the energy equation becomes a nonlinear, nonhomogeneous differential equation. In this chapter, an exact solution to the conduction-radiation problem in a one-dimensional, planar, absorbing, emitting, non-gray medium between non-gray boundaries is presented. The method uses an integrating factor to solve the Radiative Transfer Equation and variation of parameters is used to solve the energy equation. The model is verified by comparing the temperature profiles calculated from the presented approach to those found using numerical methods for both gray and non-gray cases.

6.1 Introduction

Systems in which both conduction and radiation are the dominant modes of heat transfer can be found in many practical engineering applications. These include fiber and foam insulations, the manufacture of glass, the study and design of furnaces and internal-combustion engines, filler and cover for windows and solar collectors, thermal barrier coatings, and many others. The wide variety of applications has resulted in several numerical and experimental studies of methods for analyzing systems with simultaneous conduction and radiation.

The analysis of such systems is inherently difficult because of the integro-differential nature of the radiative transfer equation [5]. The pioneering theoretical analysis for this problem was presented by Viskanta and Grosh in 1962 in which the temperature profile of a one-dimensional, gray medium bounded on both sides by opaque surfaces was obtained by transforming the governing integro-differential equation into a non-linear integral equation that was solved iteratively [20]. The same authors investigated the effects of different emittances of the bounding surfaces on the heat transfer in the gray medium [21]. The results of these analyses are often used as benchmark solutions to which other methods are compared.

More recent approaches to solving the combined conduction-radiation problem include the use of the finite element method [22, 23], the finite difference method [24, 25], the finite volume method [26, 27], and the lattice Boltzmann method [28-30]. The radiation portion of the problem has been solved using the discrete ordinates method [29], the discrete transfer method [5, 30], the method of spherical harmonics [5, 77], the Monte Carlo method [78], and the finite volume method [28, 79]. Each of these methods has advantages and disadvantages.

Most of the published solutions deal with heat transfer in gray media [31]. Fewer investigations have been conducted for the case of combined conduction-radiation heat transfer in non-gray media. Heinemann et al. used theoretical and experimental methods to analyze conduction-radiation heat transfer in non-gray silica aerogels [80] while Manohar et al. investigated conduction-radiation heat transfer in non-gray plastics [81]. More recently, Marques et al. developed a computationally efficient numerical model based on finite strip theory to determine the temperature profile and heat flux in absorbing, emitting, non-scattering, non-gray media [31].

Previous efforts to solve combined conduction and radiation heat transfer problems have relied on numerical methods to solve the governing equations. This chapter outlines an exact solution to the equations governing the simultaneous conduction and radiation heat transfer in a one-dimensional, plane parallel, absorbing, emitting, non-scattering, non-gray medium surrounded by diffuse, opaque surfaces. The particular solution to the governing differential equation is obtained using the method of variation of parameters while the spectral intensities required to calculate the total radiative heat flux are found by solving the RTE using an integrating factor. This approach results in an integral equation that is solved for the temperature profile. The temperature profile is obtained using iterative, numerical integration, and a closed-form solution is not obtained. However, since numerical integration can be performed to an arbitrary degree of precision, the solution is exact. The model is verified by comparing the results for various cases to those calculated using different numerical methods and to CFD simulations performed using commercial software [82], which employs the discrete ordinates method to model the radiative heat transfer.

6.2 Problem Formulation

A one-dimensional, plane-parallel, homogeneous, isotropic, non-gray, participating medium bounded by two surfaces is shown in Figure 6-1. The medium is absorbing, emitting, and non-scattering and the bounding surfaces are opaque and diffuse. The temperature of the boundaries are denoted by T_0 and T_L at $z = 0$ and $z = L$, respectively. The material properties of both the participating medium and the boundaries are independent of temperature.

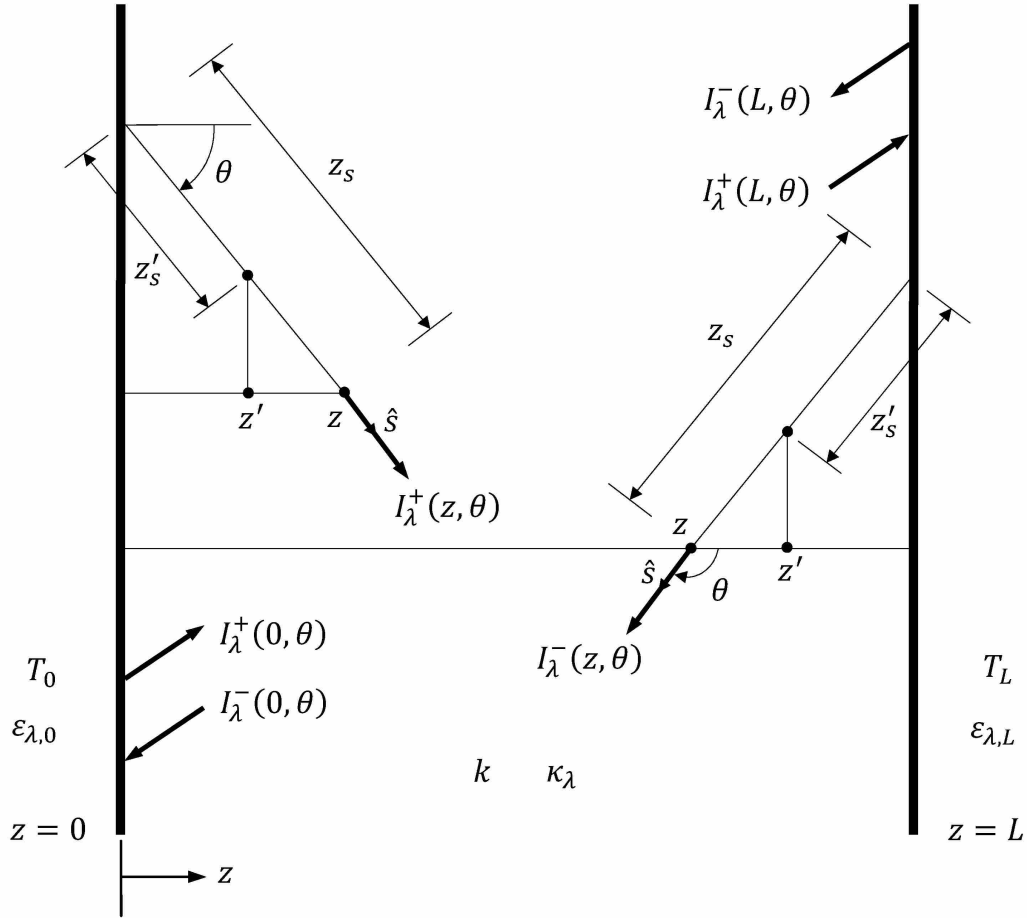


Figure 6-1: Absorbing-emitting medium between two diffuse boundaries. Coordinates used in the theoretical analysis are shown

Heat transfer in the medium occurs by both conduction and radiation. The energy equation for simultaneous conduction and radiation in a participating medium is [5]

$$\rho c_p \frac{\partial T}{\partial t} = \nabla \cdot (k \nabla T) - \nabla \cdot \mathbf{q}_R'' + \dot{Q}''' \quad (6-1)$$

For a one-dimensional, planar medium at steady state with constant thermal conductivity and without internal heat generation, Equation (6-1) reduces to

$$\frac{d^2 T}{dz^2} = \frac{1}{k} \frac{dq_R''}{dz} \quad (6-2)$$

This equation is subject to the following boundary conditions.

$$T(0) = T_0 \quad (6-3)$$

$$T(L) = T_L \quad (6-4)$$

This differential equation can be solved to determine the temperature profile in the participating medium. In order to solve the differential equation, the total radiative heat flux, q_R , must be determined. This heat flux is given by [1]

$$q_R'' = \int_0^\infty \int_{4\pi} I_\lambda(\hat{\mathbf{s}}) \hat{\mathbf{s}} d\Omega d\lambda \quad (6-5)$$

Using the definition of the solid angle, $d\Omega = \sin\theta d\theta d\phi$, and expressing the direction vector, $\hat{\mathbf{s}}$ in terms of z and θ , Equation (6-5) becomes

$$q_R'' = \int_0^\infty \int_0^{2\pi} \int_0^\pi I_\lambda(z, \theta) \cos\theta \sin\theta d\theta d\phi d\lambda \quad (6-6)$$

Integrating over ϕ , employing the direction cosine, $\mu = \cos\theta$, and noting that $\sin\theta d\theta = -d\mu$, Equation (6-6) becomes

$$q_R'' = 2\pi \int_0^\infty \int_{-1}^{+1} I(z, \mu) \mu d\mu d\lambda \quad (6-7)$$

$$= 2\pi \int_0^\infty \left[\int_{-1}^0 I_\lambda^-(z, \mu) \mu d\mu + \int_0^{+1} I_\lambda^+(z, \mu) \mu d\mu \right] d\lambda \quad (6-8)$$

$$= 2\pi \int_0^\infty \left[\int_0^1 I_\lambda^+(z, \mu) \mu d\mu - \int_0^1 I_\lambda^-(z, -\mu) \mu d\mu \right] d\lambda \quad (6-9)$$

6.3 Analytical Solution

The Radiative Transfer Equation (RTE) can be used to find $I^+(z, \mu)$ and $I^-(z, -\mu)$ required by the equation for the total radiative heat flux shown in Equation (6-9). The RTE

represents the conservation of energy along a line of sight in a radiatively participating medium.

The RTE is given by [5]

$$\frac{1}{c} \frac{\partial I_\lambda}{\partial t} + \frac{\partial I_\lambda}{\partial s} = \kappa_\lambda I_{b,\lambda} - (\kappa_\lambda + \sigma_{s,\lambda}) I_\lambda + \frac{\sigma_{s,\lambda}}{4\pi} \int_{4\pi} I_\lambda(\hat{\mathbf{s}}_i) \Phi_\lambda(\hat{\mathbf{s}}_i, \hat{\mathbf{s}}) d\Omega_i \quad (6-10)$$

For a non-scattering medium and looking in the z_s direction, Equation (6-10) reduces to

$$\frac{dI_\lambda^+}{dz_s} = \kappa_\lambda I_{b,\lambda}(z_s) - \kappa_\lambda I_\lambda^+ \quad (6-11)$$

Note that the + superscript on the spectral intensity indicates that the intensity is traveling in the “positive” direction (for which $0 < \theta < \pi/2$). Multiplying both sides of Equation (6-11) by the integrating factor $e^{\kappa_\lambda z_s}$ and rearranging gives

$$\frac{dI_\lambda^+}{dz_s} e^{\kappa_\lambda z_s} + \kappa_\lambda I_\lambda^+ e^{\kappa_\lambda z_s} = \kappa_\lambda I_{b,\lambda}(z_s) e^{\kappa_\lambda z_s} \quad (6-12)$$

Taking advantage of the product rule of differentiation, Equation (6-12) becomes

$$\frac{d}{dz_s} (e^{\kappa_\lambda z_s} I_\lambda^+) = \kappa_\lambda I_{b,\lambda}(z_s) e^{\kappa_\lambda z_s} \quad (6-13)$$

Integrating both sides of Equation (6-13) from the left boundary to an arbitrary point z_s gives

$$e^{\kappa_\lambda z_s} I_\lambda^+(z_s) - I_\lambda^+(0) = \int_0^{z_s} \kappa_\lambda I_{b,\lambda}(z'_s) e^{\kappa_\lambda z'_s} dz'_s \quad (6-14)$$

Finally, Equation (6-14) can be solved for the intensity at an arbitrary point z_s as follows.

$$I_\lambda^+(z_s) = I_\lambda^+(0) e^{-\kappa_\lambda z_s} + \kappa_\lambda \int_0^{z_s} I_{b,\lambda}(T(z'_s)) e^{-\kappa_\lambda(z_s - z'_s)} dz'_s \quad (6-15)$$

This equation is put in terms of z and θ by using the relation $z_s = z/\cos\theta$ such that

$$I_\lambda^+(z, \theta) = I_\lambda^+(0, \theta) e^{-\kappa_\lambda z/\cos\theta} + \kappa_\lambda \int_0^z I_{b,\lambda}(T(z')) e^{-\kappa_\lambda(z-z')/\cos\theta} \frac{dz'}{\cos\theta} \quad (6-16)$$

In order to find $I_{\lambda}^{-}(z, \theta)$, the same process as outlined above is followed except that the integration is now performed from an arbitrary point z_s to the right boundary. This results in the following equation.

$$I_{\lambda}^{-}(z, \theta) = I_{\lambda}^{-}(L, \theta)e^{\kappa_{\lambda}(L-z)/\cos \theta} - \kappa_{\lambda} \int_z^L I_{b,\lambda}(T(z'))e^{\kappa_{\lambda}(z'-z)/\cos \theta} \frac{dz'}{\cos \theta} \quad (6-17)$$

Note that, in this case, the intensity is traveling in the “negative” direction (for which $\pi/2 < \theta < \pi$). Equations (6-16) and (6-17) can be written in terms of the direction cosine $\mu = \cos \theta$ as follows.

$$I_{\lambda}^{+}(z, \mu) = I_{\lambda}^{+}(0, \mu)e^{-\kappa_{\lambda}z/\mu} + \frac{\kappa_{\lambda}}{\mu} \int_0^z I_{b,\lambda}(T(z'))e^{-\kappa_{\lambda}(z-z')/\mu} dz' \quad 0 < \mu < 1 \quad (6-18)$$

$$I_{\lambda}^{-}(z, \mu) = I_{\lambda}^{-}(L, \mu)e^{\kappa_{\lambda}(L-z)/\mu} - \frac{\kappa_{\lambda}}{\mu} \int_z^L I_{b,\lambda}(T(z'))e^{-\kappa_{\lambda}(z-z')/\mu} dz' \quad -1 < \mu < 0 \quad (6-19)$$

In order for $I_{\lambda}^{-}(z, \mu)$ to have limits of integration from 0 to 1 as required in Equation (6-9), μ must be negative in Equation (6-19).

$$I_{\lambda}^{-}(z, -\mu) = I_{\lambda}^{-}(L, -\mu)e^{-\kappa_{\lambda}(L-z)/\mu} + \frac{\kappa_{\lambda}}{\mu} \int_z^L I_{b,\lambda}(T(z'))e^{-\kappa_{\lambda}(z'-z)/\mu} dz' \quad 0 < \mu < 1 \quad (6-20)$$

The unknowns in Equations (6-18) and (6-20) are $I_{\lambda}^{+}(0, \mu)$ and $I_{\lambda}^{-}(L, -\mu)$, respectively. $I_{\lambda}^{+}(0, \mu)$ represents the intensity coming from the left boundary, which is due to both emission and reflection and is represented by Equation (6-21).

$$I_{\lambda}^{+}(0, \mu) = \varepsilon_{\lambda,0}I_{b,\lambda}(T(0)) + \rho_{\lambda,0}I_{\lambda}^{-}(0, -\mu) \quad (6-21)$$

The first term on the right side of Equation (6-21) represents the diffuse emission from the wall while the second term is the diffuse reflection of the incident intensity on the wall where $\rho_{\lambda,0}$ is the spectral, directional-hemispherical reflectance. The incident intensity, $I_{\lambda}^{-}(0, -\mu)$, is a result of the emission and reflection from the opposite wall as well as the emission from the medium

itself and is therefore dependent on direction. $I_{\lambda}^{-}(0, -\mu)$ is found by letting $z = 0$ in Equation (6-20).

$$I_{\lambda}^{-}(0, -\mu) = I_{\lambda}^{-}(L, -\mu)e^{-\kappa_{\lambda}L/\mu} + \frac{\kappa_{\lambda}}{\mu} \int_0^L I_{b,\lambda}(T(z'))e^{-\kappa_{\lambda}z'/\mu} dz' \quad (6-22)$$

$I_{\lambda}^{-}(L, -\mu)$ represents the intensity emitted and reflected by the right surface.

$$I_{\lambda}^{-}(L, -\mu) = \varepsilon_{\lambda,L}I_{b,\lambda}(T(L)) + \rho_{\lambda,L}I_{\lambda}^{+}(L, \mu) \quad (6-23)$$

The intensity incident on the left boundary, $I_{\lambda}^{+}(L, \mu)$, is found by letting $z = L$ in Equation (6-18).

$$I_{\lambda}^{+}(L, \mu) = I_{\lambda}^{+}(0, \mu)e^{-\kappa_{\lambda}L/\mu} + \frac{\kappa_{\lambda}}{\mu} \int_0^L I_{b,\lambda}(T(z'))e^{-\kappa_{\lambda}(L-z')/\mu} dz' \quad (6-24)$$

Making the appropriate substitutions results in expressions for $I_{\lambda}^{+}(0, \mu)$ and $I_{\lambda}^{-}(L, -\mu)$.

$$I_{\lambda}^{+}(0, \mu) = \frac{1}{(1 - \rho_{\lambda,0}\rho_{\lambda,L}e^{-2\kappa_{\lambda}L/\mu})} \left[\varepsilon_{\lambda,0}I_{b,\lambda}(T(0)) + \rho_{\lambda,0}\varepsilon_{\lambda,L}I_{b,\lambda}(T(L))e^{-\kappa_{\lambda}L/\mu} \right. \\ \left. + \frac{\rho_{\lambda,0}\rho_{\lambda,L}\kappa_{\lambda}}{\mu} \int_0^L I_{b,\lambda}(T(z'))e^{-\kappa_{\lambda}(2L-z')/\mu} dz' + \frac{\rho_{\lambda,0}\kappa_{\lambda}}{\mu} \int_0^L I_{b,\lambda}(T(z'))e^{-\kappa_{\lambda}z'/\mu} dz' \right] \quad (6-25)$$

$$I_{\lambda}^{-}(L, -\mu) = \varepsilon_{\lambda,L}I_{b,\lambda}(T(L)) \\ + \frac{\rho_{\lambda,L}e^{-\kappa_{\lambda}L/\mu}}{(1 - \rho_{\lambda,0}\rho_{\lambda,L}e^{-2\kappa_{\lambda}L/\mu})} \left[\varepsilon_{\lambda,0}I_{b,\lambda}(T(0)) + \rho_{\lambda,0}\varepsilon_{\lambda,L}I_{b,\lambda}(T(L))e^{-\kappa_{\lambda}L/\mu} \right. \\ \left. + \frac{\rho_{\lambda,0}\rho_{\lambda,L}\kappa_{\lambda}}{\mu} \int_0^L I_{b,\lambda}(T(z'))e^{-\kappa_{\lambda}(2L-z')/\mu} dz' + \frac{\rho_{\lambda,0}\kappa_{\lambda}}{\mu} \int_0^L I_{b,\lambda}(T(z'))e^{-\kappa_{\lambda}z'/\mu} dz' \right] \\ + \frac{\rho_{\lambda,L}\kappa_{\lambda}}{\mu} \int_0^L I_{b,\lambda}(T(z'))e^{-\kappa_{\lambda}(L-z')/\mu} dz' \quad (6-26)$$

Substituting Equations (6-25) and (6-26) into Equations (6-18) and (6-20), respectively, provides expressions for $I_{\lambda}^{+}(z, \mu)$ and $I_{\lambda}^{-}(z, -\mu)$.

$$\begin{aligned}
I_{\lambda}^{+}(z, \mu) = & R_{\lambda, \mu} e^{-\kappa_{\lambda} z / \mu} \left[\varepsilon_{\lambda, 0} I_{b, \lambda}(T(0)) + \rho_{\lambda, 0} \varepsilon_{\lambda, L} I_{b, \lambda}(T(L)) e^{-\kappa_{\lambda} L / \mu} \right. \\
& + \frac{\rho_{\lambda, 0} \rho_{\lambda, L} \kappa_{\lambda}}{\mu} \int_0^L I_{b, \lambda}(T(z')) e^{-\kappa_{\lambda}(2L-z') / \mu} dz' \\
& \left. + \frac{\rho_{\lambda, 0} \kappa_{\lambda}}{\mu} \int_0^L I_{b, \lambda}(T(z')) e^{-\kappa_{\lambda} z' / \mu} dz' \right] + \frac{\kappa_{\lambda}}{\mu} \int_0^z I_{b, \lambda}(T(z')) e^{-\kappa_{\lambda}(z-z') / \mu} dz'
\end{aligned} \tag{6-27}$$

$$\begin{aligned}
I_{\lambda}^{-}(z, -\mu) = & \varepsilon_{\lambda, L} I_{b, \lambda}(T(L)) e^{-\kappa_{\lambda}(L-z) / \mu} \\
& + R_{\lambda, \mu} \rho_{\lambda, L} e^{-\kappa_{\lambda}(2L-z) / \mu} \left[\varepsilon_{\lambda, 0} I_{b, \lambda}(T(0)) + \rho_{\lambda, 0} \varepsilon_{\lambda, L} I_{b, \lambda}(T(L)) e^{-\kappa_{\lambda} L / \mu} \right. \\
& + \frac{\rho_{\lambda, 0} \rho_{\lambda, L} \kappa_{\lambda}}{\mu} \int_0^L I_{b, \lambda}(T(z')) e^{-\kappa_{\lambda}(2L-z') / \mu} dz' + \frac{\rho_{\lambda, 0} \kappa_{\lambda}}{\mu} \int_0^L I_{b, \lambda}(T(z')) e^{-\kappa_{\lambda} z' / \mu} dz' \left. \right] \\
& + \frac{\rho_{\lambda, L} \kappa_{\lambda}}{\mu} \int_0^L I_{b, \lambda}(T(z')) e^{-\kappa_{\lambda}(2L-z-z') / \mu} dz' + \frac{\kappa_{\lambda}}{\mu} \int_z^L I_{b, \lambda}(T(z')) e^{-\kappa_{\lambda}(z'-z) / \mu} dz'
\end{aligned} \tag{6-28}$$

where

$$R_{\lambda, \mu} = \frac{1}{(1 - \rho_{\lambda, 0} \rho_{\lambda, L} e^{-2\kappa_{\lambda} L / \mu})} \tag{6-29}$$

The total radiative heat flux, q_R , is found by substituting Equations (6-27) and (6-28) into Equation (6-9), which can be expressed as

$$q_R'' = 2\pi \sum_{i=1}^{12} A_i \tag{6-30}$$

where

$$A_1 = \int_0^{\infty} \int_0^1 R_{\lambda, \mu} \varepsilon_{\lambda, 0} I_{b, \lambda}(0) e^{-\kappa_{\lambda} z / \mu} \mu d\mu d\lambda \tag{6-31}$$

$$A_2 = \int_0^{\infty} \int_0^1 R_{\lambda, \mu} \rho_{\lambda, 0} \varepsilon_{\lambda, L} I_{b, \lambda}(T(L)) e^{-\kappa_{\lambda}(L+z) / \mu} \mu d\lambda \tag{6-32}$$

$$A_3 = \int_0^\infty \int_0^1 R_{\lambda,\mu} \rho_{\lambda,0} \rho_{\lambda,L} \kappa_\lambda e^{-\kappa_\lambda(2L+z)/\mu} \int_0^L I_{b,\lambda}(T(z')) e^{\kappa_\lambda z'/\mu} dz' d\mu d\lambda \quad (6-33)$$

$$A_4 = \int_0^\infty \int_0^1 R_{\lambda,\mu} \rho_{\lambda,0} \kappa_\lambda e^{-\kappa_\lambda z/\mu} \int_0^L I_{b,\lambda}(T(z')) e^{-\kappa_\lambda z'/\mu} dz' d\mu d\lambda \quad (6-34)$$

$$A_5 = \int_0^\infty \int_0^1 \kappa_\lambda e^{-\kappa_\lambda z/\mu} \int_0^z I_{b,\lambda}(T(z')) e^{\kappa_\lambda z'/\mu} dz' d\mu d\lambda \quad (6-35)$$

$$A_6 = - \int_0^\infty \int_0^1 \varepsilon_{\lambda,L} I_{b,\lambda}(T(L)) e^{-\kappa_\lambda(L-z)/\mu} \mu d\mu d\lambda \quad (6-36)$$

$$A_7 = - \int_0^\infty \int_0^1 R_{\lambda,\mu} \rho_{\lambda,L} \varepsilon_{\lambda,0} I_{b,\lambda}(T(0)) e^{-\kappa_\lambda(2L-z)/\mu} \mu d\mu d\lambda \quad (6-37)$$

$$A_8 = - \int_0^\infty \int_0^1 R_{\lambda,\mu} \rho_{\lambda,0} \rho_{\lambda,L} \varepsilon_{\lambda,L} I_{b,\lambda}(T(L)) e^{-\kappa_\lambda(3L-z)/\mu} \mu d\mu d\lambda \quad (6-38)$$

$$A_9 = - \int_0^\infty \int_0^1 R_{\lambda,\mu} \rho_{\lambda,0} \rho_{\lambda,L}^2 \kappa_\lambda e^{-\kappa_\lambda(4L-z)/\mu} \int_0^L I_{b,\lambda}(T(z')) e^{\kappa_\lambda z'/\mu} dz' d\mu d\lambda \quad (6-39)$$

$$A_{10} = - \int_0^\infty \int_0^1 R_{\lambda,\mu} \rho_{\lambda,0} \rho_{\lambda,L} \kappa_\lambda e^{-\kappa_\lambda(2L-z)/\mu} \int_0^L I_{b,\lambda}(T(z')) e^{-\kappa_\lambda z'/\mu} dz' d\mu d\lambda \quad (6-40)$$

$$A_{11} = - \int_0^\infty \int_0^1 \rho_{\lambda,L} \kappa_\lambda e^{-\kappa_\lambda(2L-z)/\mu} \int_0^L I_{b,\lambda}(T(z')) e^{\kappa_\lambda z'/\mu} dz' d\mu d\lambda \quad (6-41)$$

$$A_{12} = - \int_0^\infty \int_0^1 \kappa_\lambda e^{\kappa_\lambda z/\mu} \int_z^L I_{b,\lambda}(T(z')) e^{-\kappa_\lambda z'/\mu} dz' d\mu d\lambda \quad (6-42)$$

Equation (6-30) is then substituted into Equation (6-2) which is the equation governing the temperature profile in the participating medium.

$$\frac{d^2 T}{dz^2} = \frac{2\pi}{k} \sum_{i=1}^{12} \frac{dA_i}{dz} = f(z, T) \quad (6-43)$$

Equation (6-43) is a second order, linear, non-homogeneous differential equation. This equation can be solved for the temperature profile $T(z)$ in the medium by finding both the complementary and particular solutions.

$$T(z) = T_c + T_p \quad (6-44)$$

The complementary solution is the solution to the homogeneous equation.

$$\frac{d^2T}{dz^2} = 0 \quad (6-45)$$

Separating and integrating Equation (6-45) twice results in the following complementary solution.

$$T_c = c_1z + c_2 \quad (6-46)$$

The particular solution to Equation (6-43) is solved using the method of variation of parameters as described in Chapter 3. From the complementary solution,

$$T_1 = z \quad (6-47)$$

$$T_2 = 1 \quad (6-48)$$

The particular solution is given by

$$T_p = u_1T_1 + u_2T_2 = u_1z + u_2 \quad (6-49)$$

where

$$u_1 = \int \frac{2\pi}{k} \sum_{i=1}^{12} \frac{dA_i}{dz} dz \Rightarrow u_1 = \frac{2\pi}{k} \sum_{i=1}^{12} A_i \quad (6-50)$$

$$u_2 = - \int \frac{2\pi}{k} z \sum_{i=1}^{12} \frac{dA_i}{dz} dz \quad (6-51)$$

To find u_2 , integration by parts is employed on Equation (6-51), resulting in the following equation.

$$u_2 = -\frac{2\pi}{k} z \sum_{i=1}^{12} A_i + \int \frac{2\pi}{k} \sum_{i=1}^{12} A_i dz \quad (6-52)$$

Equations (6-50) and (6-52) are substituted into Equation (6-49), so the particular solution is

$$T_p = \frac{2\pi}{k} z \sum_{i=1}^{12} A_i - \frac{2\pi}{k} z \sum_{i=1}^{12} A_i + \int \frac{2\pi}{k} \sum_{i=1}^{12} A_i dz = \frac{2\pi}{k} \int \sum_{i=1}^{12} A_i dz \quad (6-53)$$

An equation for the temperature profile of the participating medium is found by substituting Equations (6-46) and (6-53) into Equation (6-44).

$$T(z) = c_1 z + c_2 + \frac{2\pi}{k} \int \sum_{i=1}^{12} A_i dz \quad (6-54)$$

Each of the A terms in Equation (6-54) is integrated with respect to z so that the temperature profile has the following form.

$$T(z) = c_1 z + c_2 + \frac{2\pi}{k} \sum_{i=1}^{12} B_i(z) \quad (6-55)$$

where

$$B_1 = - \int_0^\infty \int_0^1 \frac{R_{\lambda,\mu} \varepsilon_{\lambda,0}}{\kappa_\lambda} I_{b,\lambda}(T(0)) e^{-\kappa_\lambda z / \mu} \mu^2 d\mu d\lambda \quad (6-56)$$

$$B_2 = - \int_0^\infty \int_0^1 \frac{R_{\lambda,\mu} \rho_{\lambda,0} \varepsilon_{\lambda,L}}{\kappa_\lambda} I_{b,\lambda}(T(L)) e^{-\kappa_\lambda(L+z) / \mu} \mu^2 d\mu d\lambda \quad (6-57)$$

$$B_3 = - \int_0^\infty \int_0^1 R_{\lambda,\mu} \rho_{\lambda,0} \rho_{\lambda,L} e^{-\kappa_\lambda(2L+z) / \mu} \mu \int_0^L I_{b,\lambda}(T(z')) e^{\kappa_\lambda z' / \mu} dz' d\mu d\lambda \quad (6-58)$$

$$B_4 = - \int_0^\infty \int_0^1 R_{\lambda,\mu} \rho_{\lambda,0} e^{-\kappa_\lambda z / \mu} \mu \int_0^L I_{b,\lambda}(T(z')) e^{-\kappa_\lambda z' / \mu} dz' d\mu d\lambda \quad (6-59)$$

Evaluating the integral of A_5 is not as straightforward as the previous terms because the variable z is in the definite integral. The integration is performed as follows.

$$B_5 = \int \int_0^\infty \int_0^1 \int_0^z \kappa_\lambda I_{b,\lambda}(T(z')) e^{-\kappa_\lambda(z-z')/\mu} dz' d\mu d\lambda dz = \int \int_0^\infty \int_0^1 \kappa_\lambda e^{-\kappa_\lambda z/\mu} g(z, \lambda, \mu) d\mu d\lambda dz \quad (6-60)$$

In the above equation,

$$g(z, \lambda, \mu) = \int_0^z I_{b,\lambda}(T(z')) e^{\kappa_\lambda z'/\mu} dz' \quad (6-61)$$

The order of integration in Equation (6-60) is changed such that

$$B_5 = \int_0^\infty \int_0^1 \int \kappa_\lambda e^{-\kappa_\lambda z/\mu} g(z, \lambda, \mu) dz d\mu d\lambda \quad (6-62)$$

and integration by parts is used on the inner integral of Equation (6-62) with

$$u = g(z, \lambda, \mu) \quad (6-63)$$

$$du = \frac{\partial g}{\partial z} dz \quad (6-64)$$

$$dv = \kappa_\lambda e^{-\kappa_\lambda z/\mu} dz \quad (6-65)$$

$$v = \int \kappa_\lambda e^{-\kappa_\lambda z/\mu} dz = -\mu e^{-\kappa_\lambda z/\mu} \quad (6-66)$$

so that

$$B_5 = \int_0^\infty \int_0^1 \mu \left[-g(z, \lambda, \mu) e^{-\kappa_\lambda z/\mu} + \int e^{-\kappa_\lambda z/\mu} \frac{\partial g}{\partial z} dz \right] d\mu d\lambda \quad (6-67)$$

$\partial g/\partial z$ is now evaluated.

$$\frac{\partial g}{\partial z} = \frac{\partial}{\partial z} \int_0^z I_{b,\lambda}(T(z')) e^{\kappa_\lambda z'/\mu} dz' \quad (6-68)$$

If the function $f(z', z)$ is defined as

$$f(z', z) = I_{b,\lambda}(T(z'))e^{\kappa\lambda z'/\mu} \quad (6-69)$$

then

$$\frac{\partial g}{\partial z} = \frac{\partial}{\partial z} \int_0^z f(z', z) dz' \quad (6-70)$$

From the fundamental theorem of calculus,

$$\frac{\partial g}{\partial z} = I_{b,\lambda}(T(z))e^{\kappa\lambda z/\mu} \quad (6-71)$$

Finally, Equations (6-61) and (6-71) are substituted into Equation (6-67).

$$B_5 = - \int_0^\infty \int_0^1 \int_0^z I_{b,\lambda}(T(z'))e^{\kappa\lambda(z'-z)/\mu} \mu dz' d\mu d\lambda + \int \int_0^\infty \int_0^1 \mu I_{b,\lambda}(T(z)) d\mu d\lambda dz \quad (6-72)$$

Continuing with the integration of the A terms from Equation (6-54),

$$B_6 = - \int_0^\infty \int_0^1 \frac{\varepsilon_{\lambda,L}}{\kappa_\lambda} I_{b,\lambda}(T(L))e^{-\kappa_\lambda(L-z)/\mu} \mu^2 d\mu d\lambda \quad (6-73)$$

$$B_7 = - \int_0^\infty \int_0^1 \frac{R_{\lambda,\mu} \rho_{\lambda,L} \varepsilon_{\eta,0}}{\kappa_\lambda} I_{b,\lambda}(T(0))e^{-\kappa_\lambda(2L-z)/\mu} \mu^2 d\mu d\lambda \quad (6-74)$$

$$B_8 = - \int_0^\infty \int_0^1 \frac{R_{\lambda,\mu} \rho_{\lambda,0} \rho_{\lambda,L} \varepsilon_{\lambda,L}}{\kappa_\lambda} I_{b,\lambda}(T(L))e^{-\kappa_\lambda(3L-z)/\mu} \mu^2 d\mu d\lambda \quad (6-75)$$

$$B_9 = - \int_0^\infty \int_0^1 R_{\lambda,\mu} \rho_{\lambda,0} \rho_{\lambda,L}^2 e^{-\kappa_\lambda(4L-z)/\mu} \mu \int_0^L I_{b,\lambda}(T(z'))e^{\kappa_\lambda z'/\mu} dz' d\mu d\lambda \quad (6-76)$$

$$B_{10} = - \int_0^\infty \int_0^1 R_{\lambda,\mu} \rho_{\lambda,0} \rho_{\lambda,L} e^{-\kappa_\lambda(2L-z)/\mu} \mu \int_0^L I_{b,\lambda}(T(z'))e^{-\kappa_\lambda z'/\mu} dz' d\mu d\lambda \quad (6-77)$$

$$B_{11} = - \int_0^\infty \int_0^1 \rho_{\lambda,L} e^{-\kappa_\lambda(2L-z)/\mu} \mu \int_0^L I_{b,\lambda}(T(z'))e^{\kappa_\lambda z'/\mu} dz' d\mu d\lambda \quad (6-78)$$

Because z is in the definite integral in A_{12} , the same process used to integrate A_5 is to evaluate the integral of A_{12} . The result is

$$B_{12} = - \int_0^\infty \int_0^1 \int_z^L I_{b,\lambda}(T(z')) e^{-\kappa_\lambda(z'-z)/\mu} \mu dz' d\mu d\lambda - \int \int_0^\infty \int_0^1 \mu I_{b,\lambda}(T(z)) d\mu d\lambda dz \quad (6-79)$$

Note that in the summation of Equation (6-55), the second term of B_5 cancels with the second term of B_{12} and that all constants of integration are combined with those of the complementary solution. The constants c_1 and c_2 in Equation (6-55) are found by applying the boundary conditions shown in Equations (6-3) and (6-4).

After finding the constants and multiplying the π term by the spectral intensities according to the equation $\pi I_{b,\lambda} = E_{b,\lambda}$, the final expression for the temperature profile in a one-dimensional, plane-parallel, non-gray, absorbing, emitting, and non-scattering medium bounded by two opaque surfaces can be written as

$$T(z) = \left(\frac{T_L}{L} - \frac{T_0}{L} \right) z + T_0 + \frac{2}{k} \sum_{i=1}^{12} \int_0^\infty \int_0^1 C_i(z, \lambda, \mu) d\mu d\lambda \quad (6-80)$$

where

$$C_1 = \frac{R_{\lambda,\mu} \varepsilon_{\lambda,0}}{\kappa_\lambda} E_{b,\lambda}(T(0)) P(z, \lambda, \mu) \mu^2 \quad (6-81)$$

$$C_2 = \frac{R_{\lambda,\mu} \rho_{\lambda,0} \varepsilon_{\lambda,L}}{\kappa_\lambda} E_{b,\lambda}(T(L)) e^{-\kappa_\lambda L/\mu} P(z, \lambda, \mu) \mu^2 \quad (6-82)$$

$$C_3 = R_{\lambda,\mu} \rho_{\lambda,0} \rho_{\lambda,L} e^{-2\kappa_\lambda L/\mu} P(z, \lambda, \mu) \mu \int_0^L E_{b,\lambda}(T(z')) e^{\kappa_\lambda z'/\mu} dz' \quad (6-83)$$

$$C_4 = R_{\lambda,\mu} \rho_{\lambda,0} P(z, \lambda, \mu) \mu \int_0^L E_{b,\lambda}(T(z')) e^{-\kappa_\lambda z'/\mu} dz' \quad (6-84)$$

$$C_5 = \frac{z}{L} e^{-\kappa_\lambda L/\mu} \mu \int_0^L E_{b,\lambda}(T(z')) e^{\kappa_\lambda z'/\mu} dz' \quad (6-85)$$

$$C_6 = -e^{-\kappa\lambda z/\mu} \mu \int_0^z E_{b,\lambda}(T(z')) e^{\kappa\lambda z'/\mu} dz' \quad (6-86)$$

$$C_7 = R_{\lambda,\mu} \frac{\varepsilon_{\lambda,L}}{\kappa\lambda} E_{b,\lambda}(T(L)) Q(z, \lambda, \mu) \mu^2 \quad (6-87)$$

$$C_8 = \frac{R_{\lambda,\mu} \rho_{\lambda,L} \varepsilon_{\lambda,0}}{\kappa\lambda} E_{b,\lambda}(T(0)) e^{-\kappa\lambda L/\mu} Q(z, \lambda, \mu) \mu^2 \quad (6-88)$$

$$C_9 = R_{\lambda,\mu} \rho_{\lambda,L} e^{-\kappa\lambda L/\mu} \mu Q(z, \lambda, \mu) \int_0^L E_{b,\lambda}(T(z')) e^{\kappa\lambda z'/\mu} dz' \quad (6-89)$$

$$C_{10} = R_{\lambda,\mu} \rho_{\lambda,L} \rho_{\lambda,0} e^{-\kappa\lambda L/\mu} Q(z, \lambda, \mu) \mu \int_0^L E_{b,\lambda}(T(z')) e^{-\kappa\lambda z'/\mu} dz' \quad (6-90)$$

$$C_{11} = \left(1 - \frac{z}{L}\right) \int_0^L E_{b,\lambda}(T(z')) e^{-\kappa\lambda z'/\mu} \mu dz' \quad (6-91)$$

$$C_{12} = -e^{\kappa\lambda z/\mu} \mu \int_z^L E_{b,\lambda}(T(z')) e^{-\kappa\lambda z'/\mu} dz' \quad (6-92)$$

In Equations (6-81) through (6-92), recall that $R_{\lambda,\mu}$ is given by Equation (6-29) and $P(z, \lambda, \mu)$ and $Q(z, \lambda, \mu)$ are given by

$$P(z, \lambda, \mu) = \frac{z}{L} (e^{-\kappa\lambda L/\mu} - 1) + (1 - e^{-\kappa\lambda z/\mu}) \quad (6-93)$$

$$Q(z, \lambda, \mu) = \frac{z}{L} (1 - e^{-\kappa\lambda L/\mu}) + e^{-\kappa\lambda L/\mu} (1 - e^{\kappa\lambda z/\mu}) \quad (6-94)$$

6.4 Evaluation

The solution for the temperature profile given in Equation (6-80) is not a closed-form solution, so evaluation of the temperature profile requires an iterative approach involving the numerical integration of the $C_i(z, \lambda, \mu)$ terms over direction and wavelength. Although numerical integration is used in the iterative approach, it can be performed to an arbitrary degree of precision, so the solution is exact.

The iterative solution begins with an initial guess of the temperature profile. In this study, the linear temperature profile that results from neglecting the radiative transfer is used as the initial guess. With this initial guess, the spectral emissive power is calculated, and the temperature profile is updated using Equation (6-80). This updated temperature profile is then used to recalculate the spectral emissive power as needed and the process is repeated until convergence is obtained. Convergence is considered achieved when the Euclidean norm of the difference between the calculated temperature profile of the current iteration and that of the previous iteration reaches a specified tolerance. In cases where the radiation heat transfer is dominant, under-relaxation is required to obtain convergence.

When numerically evaluating the integrals in Equation (6-80), both the spatial dimension, z , and the direction cosine, μ , are discretized and each integral is expressed as a summation. For example, the eleventh term in the summation is approximated as

$$\begin{aligned}
 C_{11} &= \left(1 - \frac{z}{L}\right) \int_0^\infty \int_0^1 \int_0^L E_{b,\lambda}(T(z')) e^{-\kappa_\lambda z'/\mu} \mu dz' d\mu d\lambda \\
 &\approx \left(1 - \frac{z}{L}\right) \int_0^\infty \sum_m \sum_n E_{b,\lambda}(T(z_n)) e^{-\kappa_\lambda z_n/\mu_m} \mu_m \Delta z \Delta \mu d\lambda
 \end{aligned} \tag{6-95}$$

Again, although numerical integration is used to evaluate the integrals, the degree of precision is based on the step sizes Δz and $\Delta \mu$ and, therefore, the solution can still be considered exact. For gray media, the Stefan-Boltzmann Law [5] may be used to evaluate the integral of the spectral blackbody emissive power over all wavelengths. For non-gray media, the spectrally varying properties are discretized into bands and assumed to be constant over each band. The spectral emissive power in each band is calculated using a curve fit to the fractional blackbody emissive power function [5, 83].

6.5 Results and Discussion

The evaluation methodology discussed in Section 6.4 was implemented as a program in Matlab, which can be found in Appendix A.5. The accuracy of the method is verified by comparing the results for various cases to those calculated using different numerical methods and to CFD simulations in which the discrete-ordinates method is used to model the radiative heat transfer [82]. The conduction-to-radiation parameter is defined as

$$N = \frac{k\kappa}{4\sigma T_0^3} \quad (6-96)$$

For optically thick slabs, this parameter provides a good estimate for the relative importance of conduction heat transfer relative to radiation heat transfer [5]. The simplest case presented here is a gray material with $\kappa = 1 \text{ m}^{-1}$ surrounded by black surfaces ($\varepsilon_0 = \varepsilon_L = 1$) with $T_L = 0.5T_0$. For this simple case, the non-dimensional temperature profiles calculated using Equation (6-80) are compared to those calculated using a finite difference method [5], the collapsed dimension method implemented by Talukdar and Mishra [84], and the discrete ordinates method [82]. Figure 6-2 shows these comparisons for different values of N . The average difference between the results of the present method and the numerical methods is 0.89%. The number of iterations required by the collapsed dimension method for $N = 0.1$ and $N = 0.01$ was 80 and 120 [84], respectively, while that of the method presented here was 7 and 37, respectively. The computational time required for the present method was, on average, about 3.5 times faster than that of the finite element method but was, on average, about three times slower than that of the CFD simulations.

A somewhat more complicated case is a gray medium surrounded by non-black surfaces. Figure 6-3 compares the temperature profiles found using the present method to those found using finite strip theory [31] for a gray medium with $\kappa = 1 \text{ m}^{-1}$ and $N = 0.001$ with boundary

emittances of $\varepsilon_0 = \varepsilon_L = 1$ and $\varepsilon_0 = \varepsilon_L = 0.1$. Figure 6-4 and Figure 6-5 compare the results from this work to those found from CFD simulations for cases in which the boundary emittances are different. Figure 6-4 shows the case of a gray medium with $\kappa = 0.1 \text{ m}^{-1}$ and boundary emittances of $\varepsilon_0 = 0.75$ and $\varepsilon_L = 0.1$ while Figure 6-5 shows the case of a gray medium with $\kappa = 1 \text{ m}^{-1}$ and boundary emittances of $\varepsilon_0 = 0.2$ and $\varepsilon_L = 0.9$. The bounding surfaces are assumed to be diffuse, so $\rho = 1 - \varepsilon$ in each of these cases. The average difference between the results of the present method and the numerical methods is 1.2%. The computational time required for the present method was, on average, about eight times greater than that of the CFD simulations.

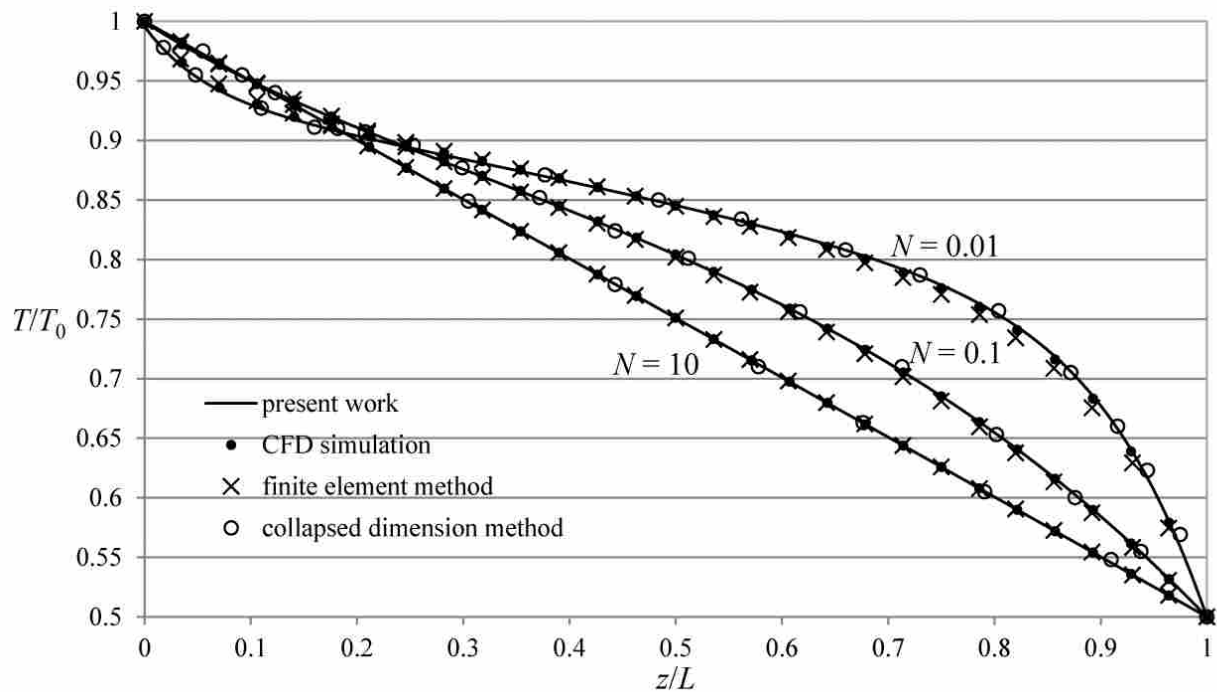


Figure 6-2: Comparison of present method to numerical methods for case of gray medium ($\kappa = 1$) with black boundaries for various conduction-to-radiation parameters

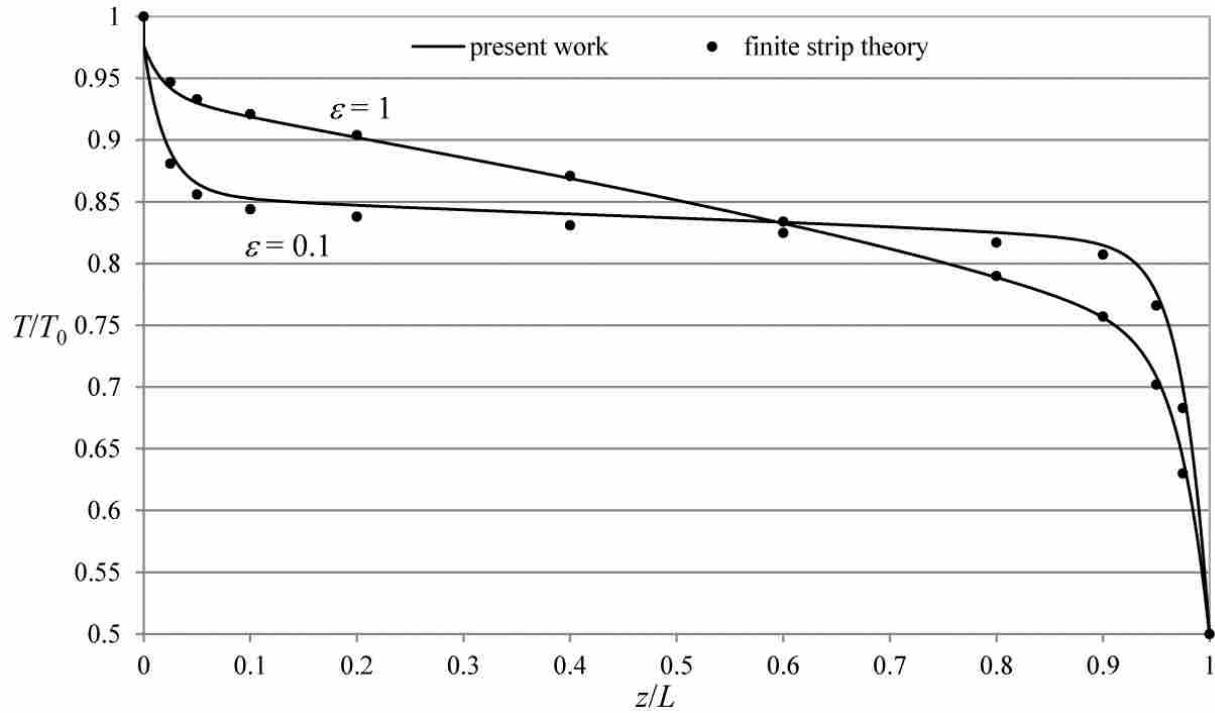


Figure 6-3: Comparison of present method to finite strip method for case of gray medium ($\kappa = 1$) with $\varepsilon_0 = \varepsilon_L = 1$ and $\varepsilon_0 = \varepsilon_L = 0.1$ for $N = 0.001$

Finally, the most complex case is that of a non-gray medium bounded by spectrally selective surfaces. Two scenarios are considered. The spectrally dependent properties of the medium and boundaries are divided into three bands over each of which the properties are assumed to be constant. Table 6-1 shows the values of these spectrally dependent properties for the two cases and the results of these cases are compared to CFD simulations and shown in Figure 6-6 and Figure 6-7 for various values of the thermal conductivity. Again, the bounding surfaces are assumed to be diffuse, so $\rho_\lambda = 1 - \varepsilon_\lambda$. The average difference between the results of the present method and the CFD solutions is 1.67%. The computational time required for the present method was, on average, about 55 times greater than that of the CFD simulations.

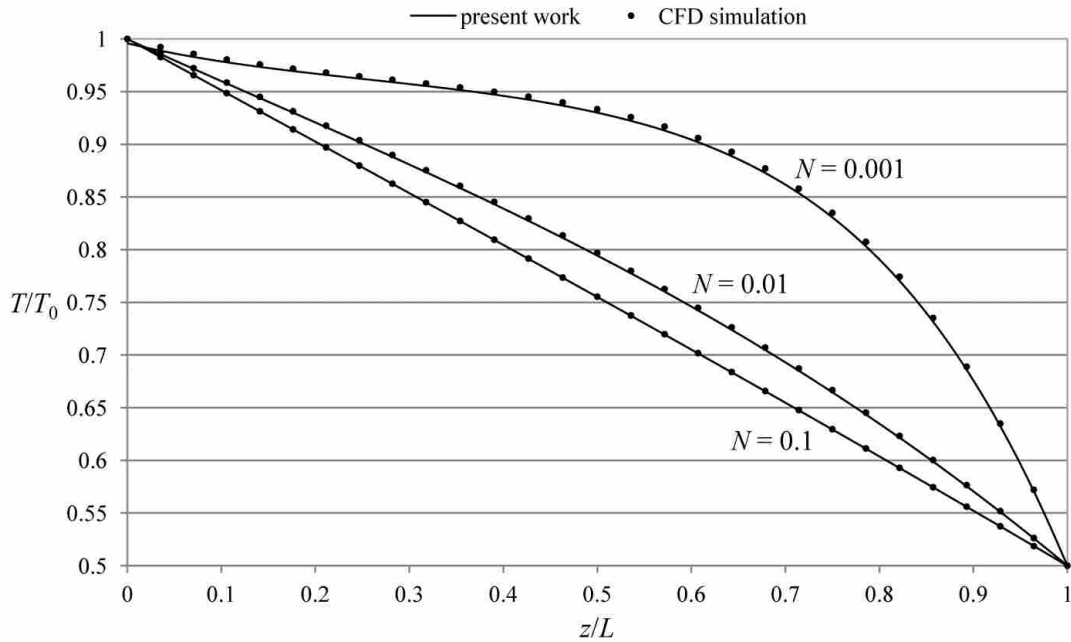


Figure 6-4: Comparison of present method to CFD solutions for case of gray medium ($\kappa = 0.1$) with $\varepsilon_0 = 0.75$ and $\varepsilon_L = 0.1$ for various conduction-to-radiation parameters

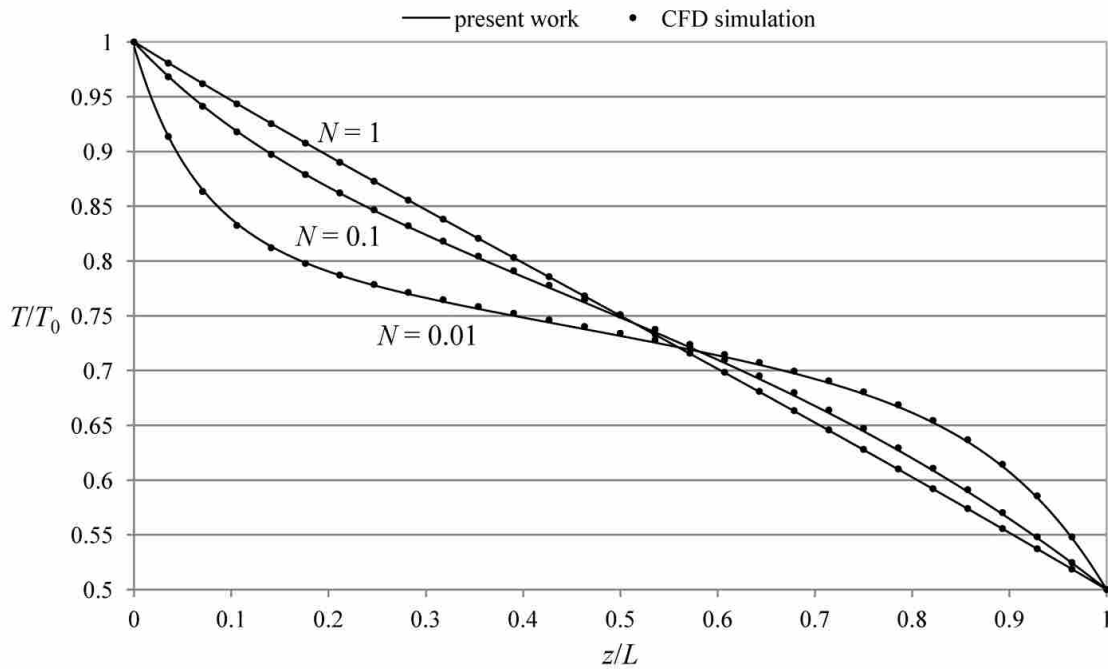


Figure 6-5: Comparison of present method to CFD solutions for case of gray medium ($\kappa = 1$) with $\varepsilon_0 = 0.2$ and $\varepsilon_L = 0.9$ for various conduction-to-radiation parameters

Table 6-1: Spectral properties for two non-gray cases.

Case 1: $T_0 = 800 \text{ K}, T_L = 400 \text{ K}$			
Band	$0 - 10 \mu\text{m}$	$10 - 20 \mu\text{m}$	$20 - \infty \mu\text{m}$
$\varepsilon_{\lambda,0}$	0.25	0.5	0.75
$\varepsilon_{\lambda,L}$	0.3	0.85	1
κ_{λ}	10	1	0.1
Case 2: $T_0 = 1400 \text{ K}, T_L = 900 \text{ K}$			
Band	$0 - 2 \mu\text{m}$	$2 - 7 \mu\text{m}$	$7 - \infty \mu\text{m}$
$\varepsilon_{\lambda,0}$	0.5	0.1	0.3
$\varepsilon_{\lambda,L}$	0.65	0.9	0.8
κ_{λ}	5	0.2	2

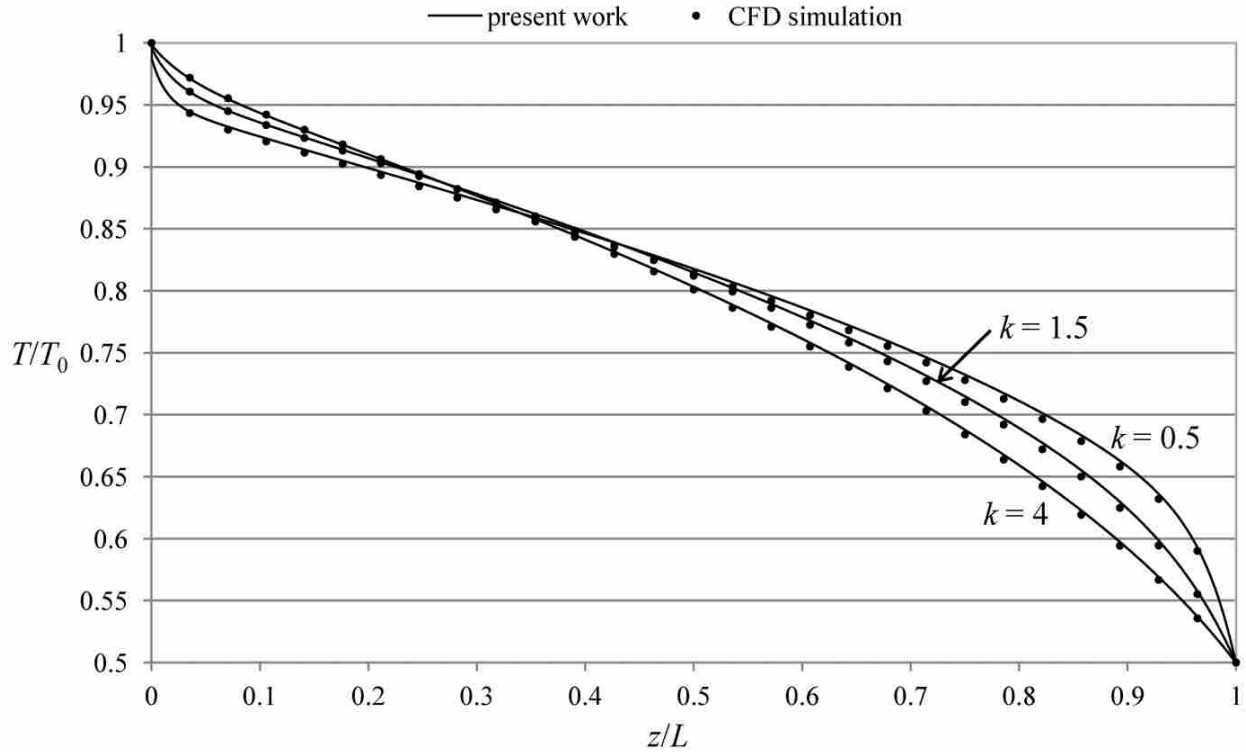


Figure 6-6: Comparison of present method to CFD solutions for various thermal conductivities with non-gray properties corresponding to Case 1 in Table 6-1

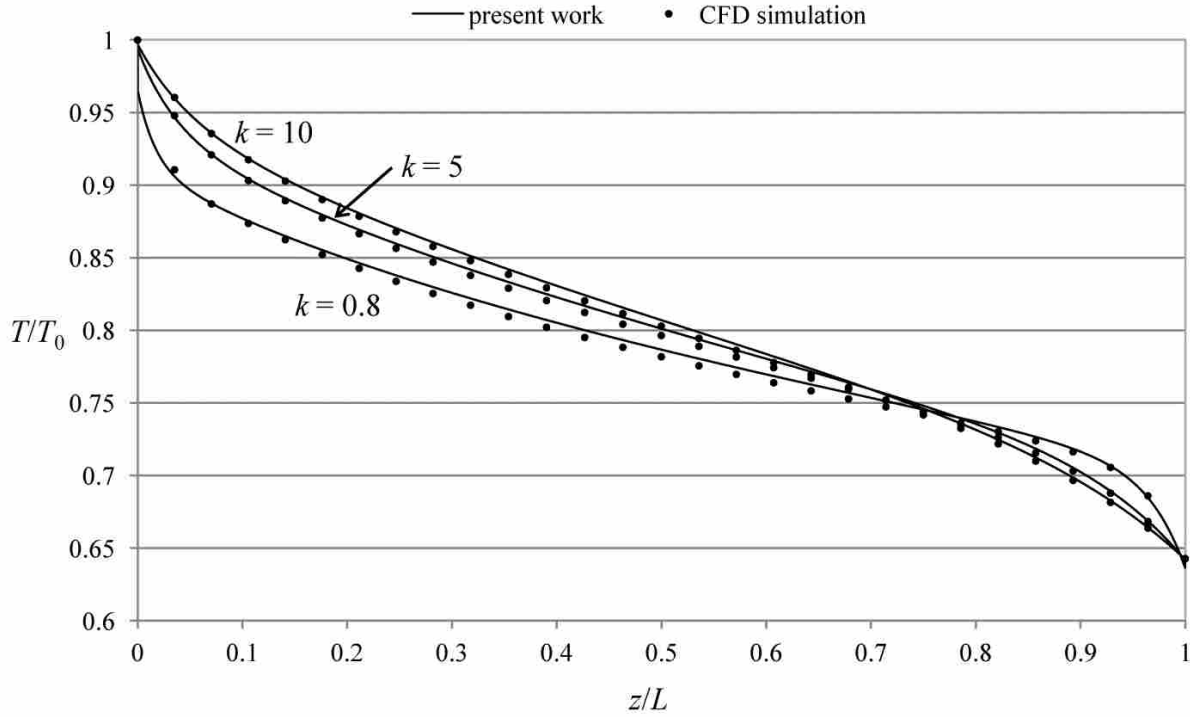


Figure 6-7: Comparison of present method to CFD solutions for various thermal conductivities with non-gray properties corresponding to Case 2 in Table 6-1

As can be seen from the figures above, there is excellent agreement between the model presented in this work and other methods for determining the temperature profile in a gray or non-gray one-dimensional, plane-parallel medium surrounded by two gray or non-gray diffuse, opaque surfaces. The average difference between the results of the present method and the numerical methods tested was 1.25%. The time required for the present model to reach convergence was often greater than that required for the other methods, especially the CFD simulations. This was most apparent in the non-gray cases. This was, in part, due to the need to use an under-relaxation factor that decreased as the conduction-to-radiation parameter decreased and as the thermal conductivity of the medium decreased. The time required for convergence may be improved by using a dynamic under-relaxation factor. Additionally, a large number of points were required in the discretization of the spatial coordinate in order to fully capture the

effects of the radiative heat transfer at the left boundary, which significantly increased the time required to achieve convergence. The use of a non-uniform spatial discretization would significantly improve the computational efficiency of the exact solution. The model presented here is, in theory, more accurate than the numerical methods and may be used as a benchmark solution for validation of other numerical methods.

6.6 Conclusion

An exact, analytical method of determining the temperature profile in a one-dimensional, planar, absorbing, emitting, non-gray medium in which both radiation and conduction heat transfer are significant has been presented. The method utilizes an integrating factor to solve the Radiative Transfer Equation to determine the spectral intensities required in the total radiative heat flux. The method of variation of parameters is employed to solve the energy equation in which the divergence of the radiative heat flux is the source of thermal energy. Comparison of results obtained using the proposed method with results obtained using various numerical techniques has verified the method. Cases with gray and non-gray media and gray and non-gray boundaries were considered. Since the proposed method is exact, it may be used to obtain benchmark solutions.

7 INVERSE RADIATIVE HEAT TRANSFER ANALYSES

In the preceding chapters, the method of variation of parameters was used to solve direct heat transfer problems. A direct, or forward, heat transfer analysis is one in which the required geometry, radiative properties, and temperatures are known, allowing for the calculation of radiative intensities and fluxes [5]. For example, one might wish to find the rate at which radiation is transferred from a surface based on knowledge of the surface properties. In contrast, the corresponding inverse problem would entail determining the properties of the surface based on measurements of the radiative intensity or flux emerging from the surface. There are many important problems in which one or more unknown input parameters which cause a certain radiative intensity field are desired. The goal of inverse radiative analyses is to deduce parameters that are difficult to measure (such as radiative properties and temperature distributions) based on various types of radiation measurements (such as radiative intensity or flux) [5].

In general, the solution to an inverse problem is found by minimizing an objective function which is a weighted least squares norm representing the difference between measured data values and corresponding values calculated from a direct analysis. The measured data values are radiation measurements such as radiative flux or intensity. The solution to the direct problem requires the unknown parameters, such as temperature distribution or radiative properties, which

are to be determined. Various optimization techniques can be used to find these unknown parameters such that the objective function is minimized.

7.1 Genetic Algorithm

One optimization method that has been used to solve inverse heat transfer problems is the genetic algorithm [85]. Genetic algorithms are based on the principle of natural selection or survival of the fittest. Figure 7-1 shows a simple flowchart representing the steps taken in a genetic algorithm.

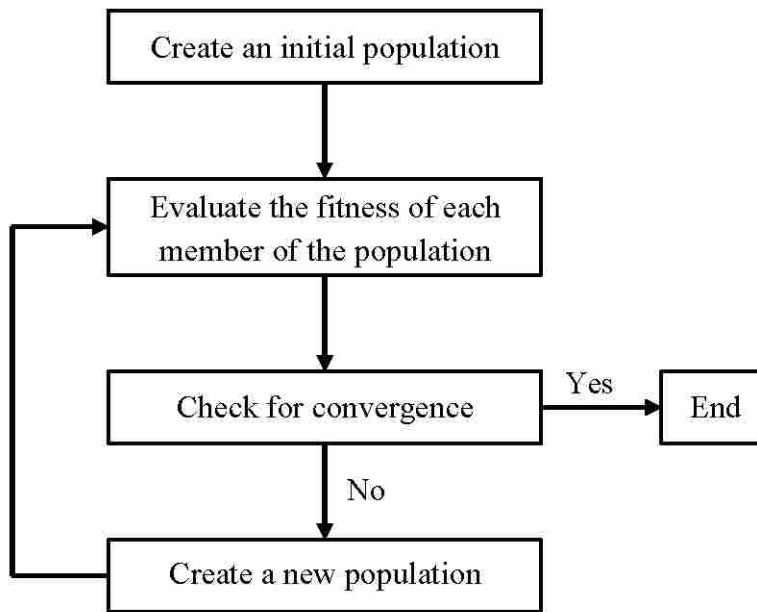


Figure 7-1: Basic flowchart of a genetic algorithm

In this research, the population consists of sets of the unknown parameters that are to be determined. The forward problem is solved for each of these sets, or individuals, resulting in theoretical measurements of the radiative intensity. The fitness of each individual is evaluated by

comparing the theoretical measurements calculated from the forward problem to actual measurements made experimentally. The individuals in the population with the best fitness values are used to create a new population. This process is repeated until some convergence criterion is met. The optimum provides a set of parameters that correspond to the measurements made.

7.2 Generalized Reduced Gradient Algorithm

Another optimization method used in this research is the Generalized Reduced Gradient (GRG) Algorithm which is implemented as a solver tool in Microsoft Excel. This is an iterative numerical approach for optimizing nonlinear problems. The constraint and optimum cells are functions of the adjustable cells. Finite difference methods are used to approximate the derivatives of the optimum value with respect to each of the adjustable values, which represents the gradient of the function. The gradient information at each iteration is used to determine the values of the adjustable cells for the following iteration. When the gradient is nominally zero and all the constraints are satisfied, the optimum has been achieved. In this research, the adjustable cells represent the unknown parameters to be determined while the optimum cell is the least squares norm representing the difference between the measured data values and the corresponding values calculated from the direct analysis.

7.3 Ill-Posed Problems

One of the major difficulties associated with inverse problems is that they are often ill-posed or ill-conditioned. An inverse problem is not well posed if a solution to the problem does not exist, the solution is not unique, or the solution is unstable (i.e., small changes in the problem parameters cause large changes in the solution) [5]. Efforts can be made in the optimization

process to regularize the problem or to stabilize the problem by adding more constraints. However, the inverse solution may be insensitive to some of the system parameters. If this is the case, changes in these parameters will have little or no effect on the solution and the inverse problem will not be able to accurately predict them.

8 A NON-CONTACT METHOD OF MEASURING THE PROPERTIES OF THERMAL BARRIER COATINGS

In this chapter, an experimental, non-contact method of measuring the bond coat temperature of a thermal barrier coating (TBC) is proposed. The forward problem models the spectral measurements of the radiation coming from the TBC surface. The energy equation is solved using the method of variation of parameters to determine the temperature profile in the TBC in an analysis similar to that shown in Chapter 6. A genetic algorithm is used to solve the inverse problem. Numerical experiments are performed to assess the accuracy of the model.

8.1 Introduction

There is a growing reliance on the use of thermal barrier coatings (TBCs) as insulation of metallic components, such as vanes and blades, from large and extended heat loads in power generation and aerospace turbines. These coatings allow for increased inlet temperatures, which are accompanied by an increased efficiency, and result in a reduction in the requirements for cooling air [6]. They can also extend part life by reducing oxidation and thermal fatigue [86]. Thermal barrier coatings are generally composed of two layers: a ceramic oxide top layer followed by a metallic bond coat which adheres to the super alloy turbine component [87]. The ceramic topcoat is exposed to the hot combustion gases in the turbine. It is usually composed of yttria-stabilized zirconia (YSZ) which, because of its low thermal conductivity, provides thermal insulation. The metallic bond coat, located between the ceramic top and the super alloy substrate,

is most commonly made of MCrAlY (M=Ni, Co) and improves adherence to the ceramic topcoat while providing environmental protection from hot corrosion and oxidation [87].

Knowledge of the temperature gradients through the coating and the properties of the TBC and bond coat are critical for evaluating TBC performance and monitoring its health, as well as for accurate simulation and modeling. Of particular interest is the temperature at the interface of the bond coat and the super alloy substrate. Non-contact, non-destructive techniques for finding these temperatures and properties are highly desirable. Infrared pyrometry has been employed to determine the topcoat surface temperature [50]. This process is complicated by the fact that the pyrometer will measure radiation from the hot environment reflected from the TBC surface [51]. In addition, the translucency of the TBC at conventional pyrometer wavelengths allows radiation from well below the TBC surface to reach the pyrometer [51]. Luminescence spectroscopy is used to measure the temperature at the surface or at a desired depth of the TBC by utilizing the temperature dependence of the fluorescence decay time [52, 53]. This requires the use of thermal barrier sensor coatings [59 - 61].

In this chapter, a method of determining the bond coat temperature and other TBC properties by measuring the radiative intensity from the TBC surface is proposed. This method requires a mathematical model of the heat transfer in the TBC. Various models of thermal barrier coatings have been developed in order to study the effects of thermal radiation on the coating and substrate. Both Siegel [88] and Lim [89] combined radiation and conductive heat transfer models to determine the steady-state temperature profile in YSZ coatings. Siegel used the two-flux method to model the radiative heat flux in the TBC while Lim incorporated the radiative intensities into a differential control volume. In this chapter, the top coat of the TBC is modeled as a one-dimensional, absorbing and emitting layer. Radiative intensity measurements from the

TBC are found by solving the Radiative Transfer Equation using an integrating factor. The temperature profile in the top coat is found by solving the energy equation using the method of variation of parameters.

The proposed method uses the developed mathematical model, or forward problem, with inverse heat transfer techniques to infer the desired TBC temperatures and properties from the measured intensities. An inverse problem is solved by iteratively solving the forward problem in order to optimize the objective function. This chapter demonstrates the use of a genetic algorithm to determine the bond coat temperature as well as the TBC refractive index and bond coat emittance by minimizing the error between measured TBC surface intensities and those calculated from the forward problem. A spectral band over which measurements are to be made is determined based on TBC properties and a sensitivity analysis. Numerical experiments are performed to assess the accuracy of the proposed method.

8.2 Problem Overview

An inverse heat transfer problem is generally solved by iteratively solving a forward problem in order to optimize some objective function. The forward problem is a mathematical model of the phenomenon of interest. In this investigation, the forward problem consists of a model of the spectral measurements, M_ν , of the radiative intensity, I_ν , exiting the top surface of the thermal barrier coating. A schematic of the basic experimental setup is shown below in Figure 8-1.

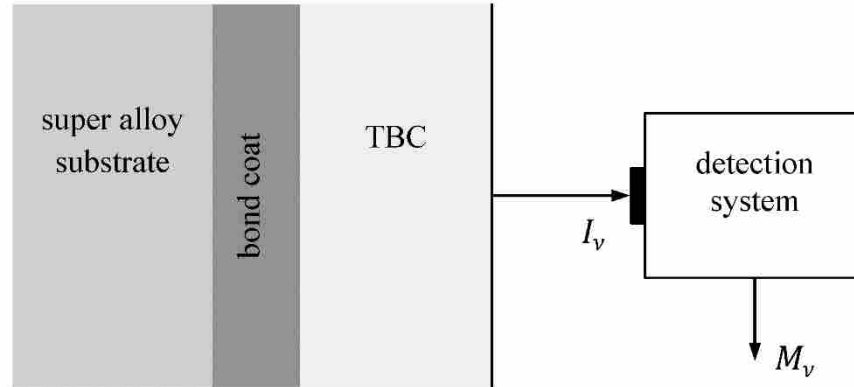


Figure 8-1: Schematic of the proposed experimental setup

A thermal barrier coating is a radiatively participating medium. Therefore, the intensity exiting the TBC accounts for the emission from the bond coat as well as the emission, absorption, and scattering of the TBC itself. The exiting intensity is intercepted by a detector and converted to a spectral signal, M_ν . The forward problem is an equation which relates this signal to the TBC parameters. The inverse problem is solved by using optimization techniques to determine the desired parameters such that the error between the experimentally measured signals and those calculated from the forward problem is minimized. Because the forward problem deals with radiative energy propagating through materials with different indices of refraction, frequency is used as the spectral variable. Unlike wavelength or wavenumber, frequency does not change with changes in the refractive index.

8.3 Temperature Profile

In order to calculate M_ν from the forward problem, the temperature profile in the TBC, $T(z)$, must be known. The temperature profile depends on both conduction and radiation in the TBC. Determining the temperature profile in the TBC is very similar to the problem solved in Chapter 6. The difference is at the right boundary. While the right boundary was an opaque

surface in the problem in Chapter 6, here it is an interface between the TBC and air. Therefore, if the radiation from the combustion gases is neglected, the boundary condition at the right boundary is

$$I_v^-(L, -\mu) = \rho_{v,L} I_v^+(L, \mu) \quad (8-1)$$

Note that Equation (8-1) is similar to Equation (6-23), except that emission from the boundary surface is not present. The same procedure that was used in Chapter 6 was used here, resulting in the following equation for the temperature profile in the TBC.

$$T(z) = \left(\frac{T_L}{L} - \frac{T_0}{L} \right) z + T_0 + \frac{2}{k} \sum_{i=1}^{10} D_i(z) \quad (8-2)$$

where

$$D_1 = \int_0^\infty \int_0^1 \frac{\epsilon_{v,0}}{\kappa_v} E_{b,v}(T(0)) P(z, \nu, \mu) \mu d\mu dv \quad (8-3)$$

$$D_2 = \int_0^\infty \int_0^1 \rho_{v,0} \rho_{v,L} e^{-2\kappa_v L/\mu} P(z, \nu, \mu) \int_0^L E_{b,\nu}(T(z')) e^{\kappa_\nu z'/\mu} dz' d\mu dv \quad (8-4)$$

$$D_3 = \int_0^\infty \int_0^1 \rho_{v,0} P(z, \nu, \mu) \int_0^L E_{b,\nu}(T(z')) e^{-\kappa_\nu z'/\mu} dz' d\mu dv \quad (8-5)$$

$$D_4 = \frac{z}{L} \int_0^\infty \int_0^1 \int_0^L E_{b,\nu}(T(z')) e^{\kappa_\nu(z'-L)/\mu} \mu dz' d\mu dv \quad (8-6)$$

$$D_5 = - \int_0^\infty \int_0^1 \int_0^z E_{b,\nu}(T(z')) e^{\kappa_\nu(z'-z)/\mu} \mu dz' d\mu dv \quad (8-7)$$

$$D_6 = \int_0^\infty \int_0^1 \frac{\rho_{v,L} \epsilon_{v,0}}{\kappa_v} E_{b,\nu}(T(0)) Q(z, \nu, \mu) \mu d\mu dv \quad (8-8)$$

$$D_7 = \int_0^\infty \int_0^1 \rho_{v,0} \rho_{v,L} Q(z, \nu, \mu) \int_0^L E_{b,\nu}(T(z')) e^{-\kappa_\nu z'/\mu} dz' d\mu dv \quad (8-9)$$

$$D_8 = \int_0^\infty \int_0^1 \rho_{v,L} Q(z, \nu, \mu) \int_0^L E_{b,\nu}(T(z')) e^{\kappa_\nu z'/\mu} dz' d\mu dv \quad (8-10)$$

$$D_9 = \left(1 - \frac{z}{L}\right) \int_0^\infty \int_0^1 \int_0^L E_{b,\nu}(T(z')) e^{-\kappa_\nu z'/\mu} \mu dz' d\mu dv \quad (8-11)$$

$$D_{10} = - \int_0^\infty \int_0^1 \int_z^L E_{b,\nu}(T(z')) e^{-\kappa_\nu(z'-z)/\mu} \mu dz' d\mu dv \quad (8-12)$$

and

$$P(z, \nu, \mu) = R_{\nu,\mu} \mu \left(\frac{z}{L} (e^{-\kappa_\nu L/\mu} - 1) + (1 - e^{-\kappa_\nu z/\mu}) \right) \quad (8-13)$$

$$Q(z, \nu, \mu) = R_{\nu,\mu} \mu e^{-\kappa_\nu L/\mu} \left(\frac{z}{L} (1 - e^{-\kappa_\nu L/\mu}) + e^{-\kappa_\nu L/\mu} (1 - e^{\kappa_\nu z/\mu}) \right) \quad (8-14)$$

where

$$R_{\nu,\mu} = \frac{1}{(1 - \rho_{\nu,0} \rho_{\nu,L} e^{-2\kappa_\nu L/\mu})} \quad (8-15)$$

Note that this equation is almost identical to that found in Chapter 6, except for the absence of two of the terms, namely, those associated with emission from the right boundary.

8.3.1 Interfacial Reflectance at a Diffuse Boundary

The spectral reflectance at the interface between the thermal barrier coating and the air, $\rho_{\nu,L}$, is required to determine the temperature profile. The reflectance at the interface between two media is determined by the indices of refraction of the media. When electromagnetic waves propagate from a medium of a given index of refraction into a second medium with a different refractive index, both reflection and refraction of the wave may occur. Figure 8-2 shows a ray traveling in the \vec{s} direction from a semi-transparent medium a with refractive index n_a to another semi-transparent b with refractive index n_b .

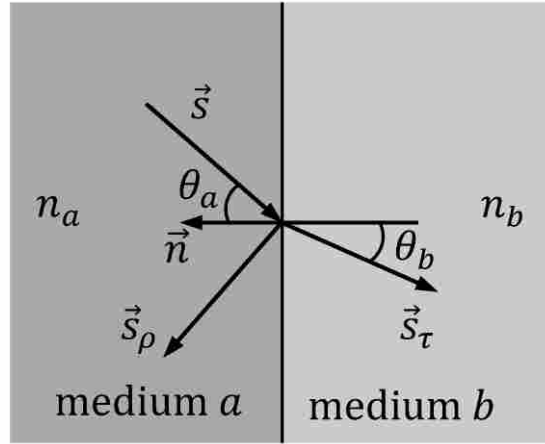


Figure 8-2: Reflection and transmission of radiation at the interface of two semi-transparent media

The Fresnel equations describe what fraction of the radiation is reflected and what fraction is refracted. The interface reflectance on side a represents the fraction of incident energy transferred from \vec{s} to \vec{s}_ρ and is given by Equation (8-16) [5].

$$\rho_a(\vec{s}) = \frac{1}{2} \left(\frac{n_a \cos \theta_b - n_b \cos \theta_a}{n_a \cos \theta_b + n_b \cos \theta_a} \right)^2 + \frac{1}{2} \left(\frac{n_a \cos \theta_a - n_b \cos \theta_b}{n_b \cos \theta_b + n_b \cos \theta_a} \right)^2 \quad (8-16)$$

A convenient assumption is that the reflected radiation is diffuse, or that it is reflected with the same intensity in all directions. For diffuse reflection, the interfacial reflectance is equal to the hemispherically averaged value shown in Equations (8-17) and (8-18) where $n = n_A/n_B > 1$ [90].

$$\rho_a = 1 - \frac{(1 - \rho_b)}{n^2} \quad (8-17)$$

where

$$\rho_b = \frac{1}{2} + \frac{(3n + 1)(n - 1)}{6(n + 1)^2} + \frac{n^2(n^2 - 1)^2}{(n + 1)^3} \ln \left(\frac{n - 1}{n + 1} \right) - \frac{2n^3(n^2 + 2n - 1)}{(n^2 + 1)(n^4 - 1)} + \frac{8n^4(n^4 + 1)}{(n^2 + 1)(n^4 - 1)^2} \ln(n) \quad (8-18)$$

The diffuse reflections given in Equations (8-16) through (8-18) are not given on a spectral basis. Therefore, the spectral reflectance at the right boundary of the thermal barrier

coating must be assumed to be constant over the entire spectrum. This assumption is consistent with the fact that the Planck function is only valid if the index of refraction is spectrally independent [5].

8.3.2 Verification of Temperature Profile Model

In order to verify the mathematical model used to calculate the temperature profile in a thermal barrier coating, temperature profiles found using this model with various parameters were compared to those found from CFD simulations [82]. Table 8-1 shows the different parameters used in three cases and the results are shown in Figure 8-3. In Case A, the TBC was treated as gray while in Cases B and C, some of the properties were considered constant over three spectral bands. The Matlab source code used to calculate the temperature profiles can be found in Appendix A.6.

Table 8-1: Properties used in three cases to verify the model

Case A			
k (W/m·K)	0.2	n	3
κ_V (m ⁻¹)	10	ϵ_0	0.7
Case B			
k (W/m·K)	0.5	n	2
band	0 - 5×10^{13} Hz	5×10^{13} - 7.5×10^{13} Hz	7.5×10^{13} - ∞ Hz
κ_V (m ⁻¹)	15	20	5
ϵ_0	0.7	0.9	0.4
Case C			
k (W/m·K)	12	n	1.9
band	0 - 5×10^{13} Hz	5×10^{13} - 7.5×10^{13} Hz	7.5×10^{13} - ∞ Hz
κ_V (m ⁻¹)	5	20	15
ϵ_0	0.7	0.9	0.4

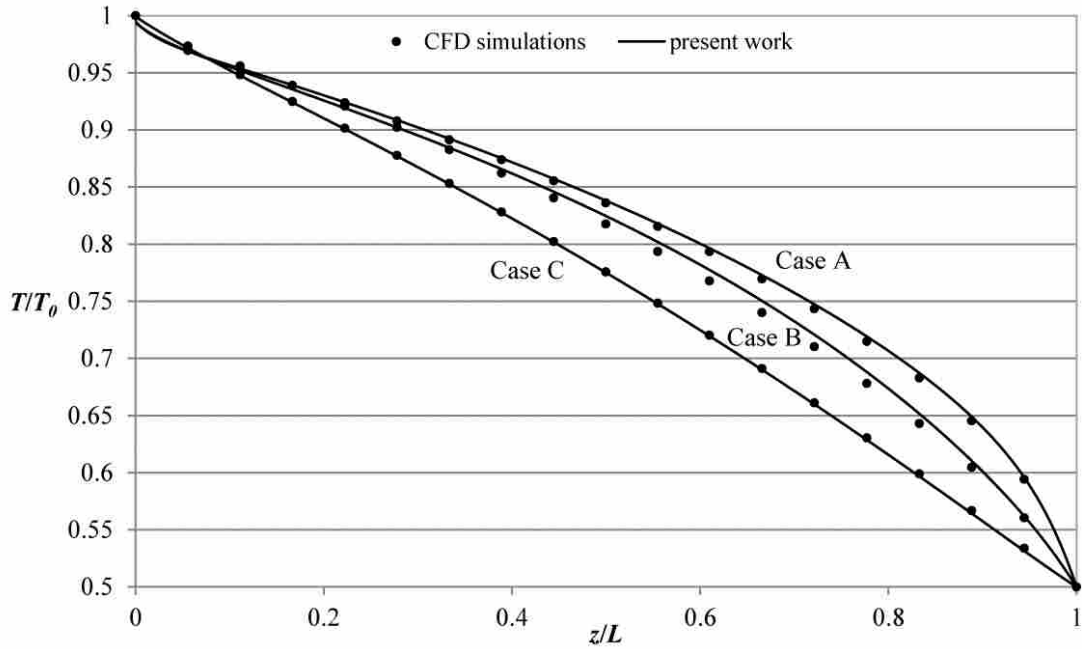


Figure 8-3: Comparison of present method to CFD solutions for properties shown in Table 8-1

8.3.3 Temperature Profile of an Actual TBC

Efforts have been made to measure various radiative properties of TBC systems [62-65]. Using these measured properties and typical TBC thicknesses to solve Equation (8-2) reveals that the temperature profile within the top coat of a thermal barrier coating is linear. This finding is consistent with other analyses of TBCs [62, 88, 89, 91-93]. This knowledge removes the thermal conductivity of the TBC as a variable in the forward problem and makes the boundary temperatures, T_0 and T_L , the only unknowns required for the temperature profile.

8.4 Forward Problem

The forward problem is a mathematical model of the physical phenomenon of interest. In order to infer the desired properties of a thermal barrier coating from the radiative intensity at the

TBC surface, a forward problem, which relates the intensity to these properties, is required. This section shows the development of the forward problem. The TBC is modeled as a one-dimensional, plane-parallel medium of thickness L bounded by two surfaces, as shown in Figure 8-5. The goal of this work is to determine if TBC properties and parameters can be accurately determined from measurements of the surface intensity. Therefore, for the purposes of this work, the hot gases between the detector and the TBC are neglected and it is assumed that the space beyond the TBC is a cold vacuum. The primary temperature of interest is that of the super alloy substrate. The temperature difference across the metallic bond coat is small and it will be assumed that the substrate is at the same temperature as the bond coat [88, 54].

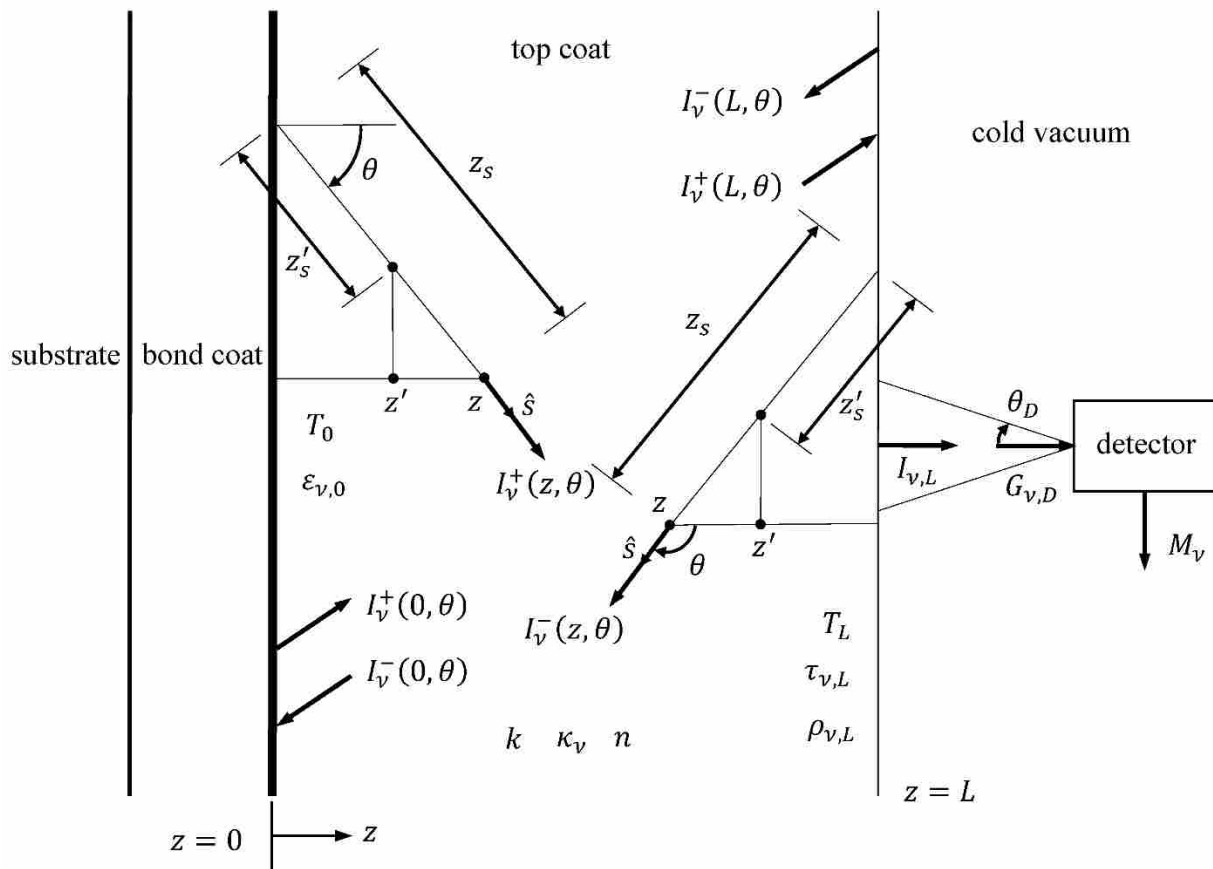


Figure 8-4: Coordinates used in the theoretical analysis of a TBC

The left boundary ($z = 0$) is the interface between the bond coat and the TBC while the right boundary ($z = L$) represents the outer surface of the TBC. The objective is to relate the spectral signal from the detection system, M_ν , to the spectral irradiation incident on the detector, $G_{\nu,D}$.

$$M_\nu = f(G_{\nu,D}) \quad (8-19)$$

The irradiation is equal to the portion of the spectral intensity incident on the right TBC boundary, $I_\nu^+(L, \theta)$, that is transmitted through the surface, integrated over the hemisphere.

$$G_{\nu,D} = \int_{2\pi} \tau_{\nu,L} I_\nu^+(L, \theta) \cos \theta_D d\Omega \quad (8-20)$$

Note that in Equation (8-20) there are two angles: θ is measured from the normal to the TBC surface while θ_D is the acceptance angle of the detector and is measured from the normal to the detector. If it is assumed that radiation from the TBC is the only source of radiation on the detector and that the solid angle from which the TBC surface is viewed by the detector, $\Delta\Omega_{D-TBC}$, is small, then Equation (8-20) reduces to

$$G_{\nu,D} = \tau_{\nu,L} I_\nu^+(L, \theta) \Delta\Omega_{D-TBC} \quad (8-21)$$

The approach used to find $I_\nu^+(L, \theta)$ here is exactly the same as that used in Chapter 6. The only difference is that the boundary condition at $z = L$ does not include emission from the boundary surface (as shown in Equation (8-1)). The resulting expression for $I_\nu^+(L, \mu)$ is given by

$$\begin{aligned} I_\nu^+(L, \mu) = & R_{\nu,\mu} \varepsilon_{\nu,0} I_{b,\nu}(T(0)) e^{-\kappa_\nu L/\mu} + R_{\nu,\mu} \frac{\rho_{\nu,0} \kappa_\nu}{\mu} \int_0^L I_{b,\nu}(T(z')) e^{-\kappa_\nu(L+z')/\mu} dz' \\ & + R_{\nu,\mu} \frac{\kappa_\nu}{\mu} \int_0^L I_{b,\nu}(T(z')) e^{-\kappa_\nu(L-z')/\mu} dz' \end{aligned} \quad (8-22)$$

In the above equation, $R_{\nu,\mu}$ is given by

$$R_{\nu,\mu} = \frac{1}{(1 - \rho_{\nu,0}\rho_{\nu,L}e^{-2\kappa_{\nu}L/\mu})} \quad (8-23)$$

Equation (8-22) is substituted into Equation (8-21) to provide an expression for the spectral irradiation on the detector.

$$G_{\nu,D} = \tau_{\nu,L} \left(R_{\nu,\mu} \varepsilon_{\nu,0} I_{b,\nu}(T(0)) e^{-\kappa_{\nu}L/\mu} + R_{\nu,\mu} \frac{\rho_{\nu,0}\kappa_{\nu}}{\mu} \int_0^L I_{b,\nu}(T(z')) e^{-\kappa_{\nu}(L+z')/\mu} dz' \right. \\ \left. + R_{\nu,\mu} \frac{\kappa_{\nu}}{\mu} \int_0^L I_{b,\nu}(T(z')) e^{-\kappa_{\nu}(L-z')/\mu} dz' \right) \Delta\Omega_{D-TBC} \quad (8-24)$$

If it is assumed that the acceptance angle of the detector is small, then the approximation $\mu \approx 1$ can be made in Equation (8-24) so that $I_{\nu}^+(L, \mu) \approx I_{\nu}^+(L, 1)$. Equation (8-21) becomes

$$G_{\nu,D} = \tau_{\nu,L} R_{\nu} \left(\varepsilon_{\nu,0} I_{b,\nu}(T(0)) e^{-\kappa_{\nu}L} + \rho_{\nu,0}\kappa_{\nu} \int_0^L I_{b,\nu}(T(z')) e^{-\kappa_{\nu}(L+z')} dz' \right. \\ \left. + \kappa_{\nu} \int_0^L I_{b,\nu}(T(z')) e^{-\kappa_{\nu}(L-z')} dz' \right) \Delta\Omega_{D-TBC} \quad (8-25)$$

The irradiation on the detector, $G_{\nu,D}$, is related to the detection system measurements, M_{λ} , by a spectral instrument response function, IRF_{ν} . The instrument response function is dependent on the detection system and is determined by a calibration procedure. Equation (8-26) is the forward problem, which is a model of the measurements made by a detection system of the spectral radiative intensity exiting the surface of the thermal barrier coating. Note that the solid angle, $\Delta\Omega_{D-TBC}$, the spectral transmittance at the end of the fiber, $\tau_{\nu,L}$, and the R_{ν} term have been combined with the instrument response function and that the spectral reflectance of the bond coat is written in terms of the spectral emittance as $\rho_{\nu,0} = 1 - \varepsilon_{\nu,0}$.

$$M_{\nu} = IRF_{\nu} \left(\varepsilon_{\nu,0} I_{b,\nu}(T(0)) e^{-\kappa_{\nu}L} + (1 - \varepsilon_{\nu,0})\kappa_{\nu} \int_0^L I_{b,\nu}(T(z')) e^{-\kappa_{\nu}(L+z')} dz' + \kappa_{\nu} \int_0^L I_{b,\nu}(T(z')) e^{-\kappa_{\nu}(L-z')} dz' \right) \quad (8-26)$$

In Equation (8-26), the first term in the parentheses represents emission from the bond coat, the second term represents the sum of the radiative intensity emitted by the TBC which is reflected off of the bond coat back to the surface, and the third term represents the sum of the radiative intensity emitted by the TBC to the surface.

8.5 Unknown Parameters

There are five unknowns in the forward problem: 1. the bond coat temperature, T_0 , 2. the top coat surface temperature, T_L , 3. the index of refraction of the top coat, n , which is required in the Planck function to calculate the spectral intensities in Equation (8-26), 4. the spectral absorption coefficient of the top coat, κ_ν , and 5. the spectral emittance of the bond coat, $\epsilon_{\nu,0}$. The number of spectral measurements must be equal to or greater than the number of unknowns to be determined. Therefore, it must be assumed that the spectral absorption coefficient of the top coat and the spectral emittance of the bond coat can be approximated as constant over the spectral band at which measurements are made.

8.6 Measurement Band Selection

In order to determine the best frequencies at which measurements should be taken, available data of thermal barrier coating properties were examined. Figure 8-5 shows measurements of the spectral absorption coefficient of 8YSZ [55] at room temperature, YSZ TBCs at 1633 K [56] and 1573 K [57], and zirconia [8]. On the secondary vertical axis, the spectral emittance of a NiCrAlY bond coat is shown [58]. Measurements at a single frequency show that the bond coat emittance is essentially constant over a wide temperature range [64]. The spectral refractive index of YSZ is nominally a constant over a band from 6×10^{13} to 3×10^{14} Hz (1 to 5 μm) [92, 65].

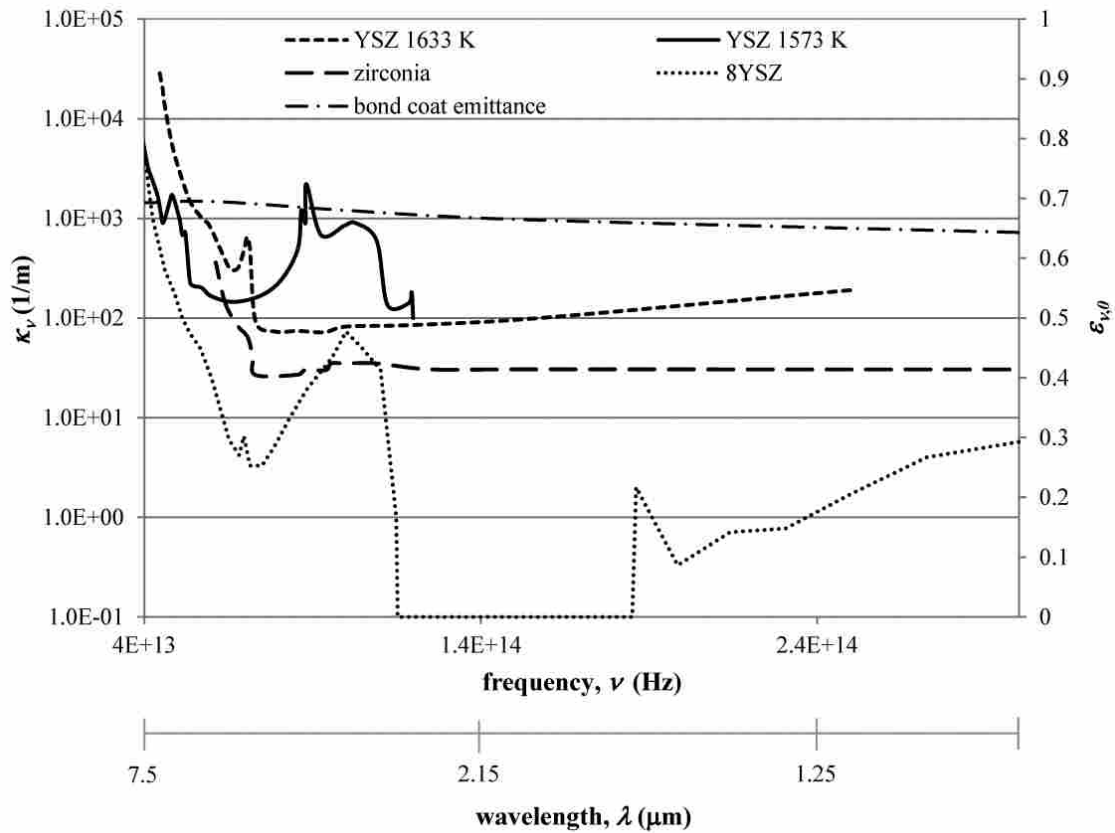


Figure 8-5: Measured spectral absorption coefficients of YSZ, 8YSZ, zirconia, and the spectral emittance of a NiCrAlY bond coat

A sensitivity analysis was performed to determine how sensitive the spectral signals are to changes in each of the five parameters. A single parameter was adjusted while all other parameters were held constant. The forward problem was solved for each case and the changes in the spectral irradiation on the detector were plotted. Figure 8-6 and Figure 8-7 show the sensitivity of the spectral irradiation on the detector to changes in the bond coat temperature and TBC surface temperature, respectively. The sensitivity plots for the other parameters were similar.

For all of the parameters, the maximum sensitivity occurs between 7.5×10^{13} and 1.5×10^{14} Hz (2 to 4 μm). The spectral signals were largely insensitive over all frequencies to changes in the TBC surface temperature, T_L , and the spectral absorption coefficient of the TBC, κ_ν . The insensitivity of the spectral measurements to changes in some of the system parameters shows that the inverse problem is not well posed. In other words, there are multiple solutions to the forward problem that will result in the same set of spectral measurements. Based on the data available in the literature and the sensitivity analysis, the best spectral band over which the spectral properties can be assumed to be constant lies between 1.2×10^{14} and 1.5×10^{14} Hz (2 to 2.5 μm).

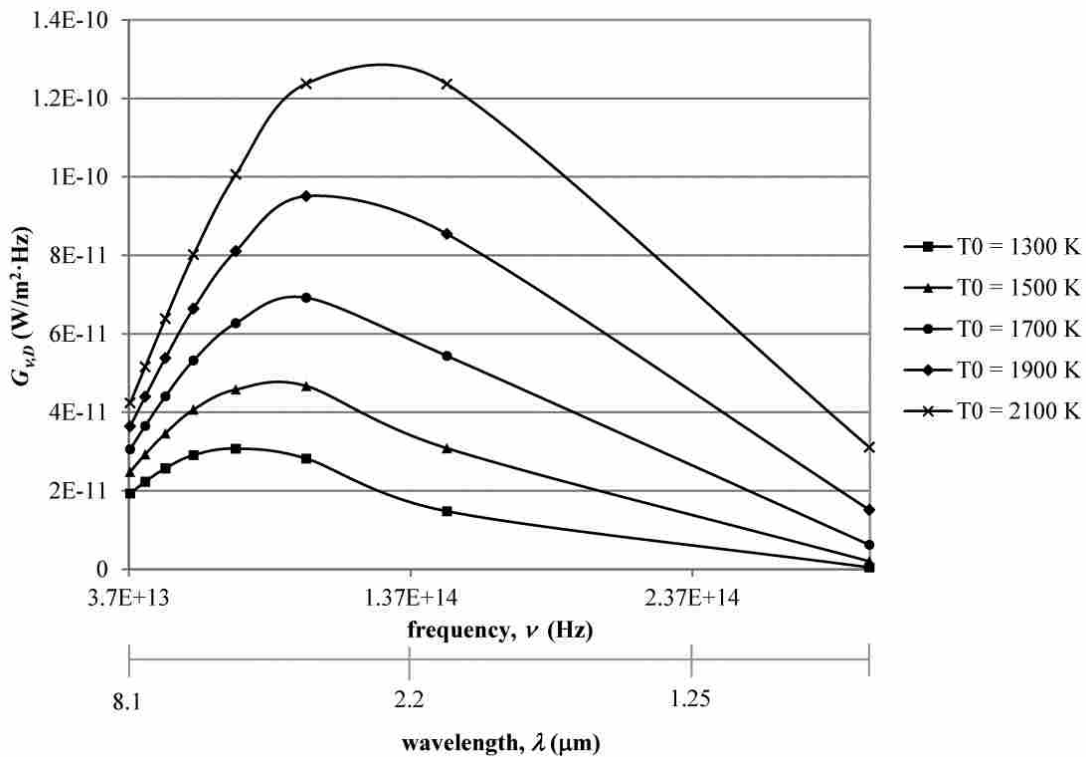


Figure 8-6: Sensitivity of spectral irradiation on detector to changes in the substrate temperature

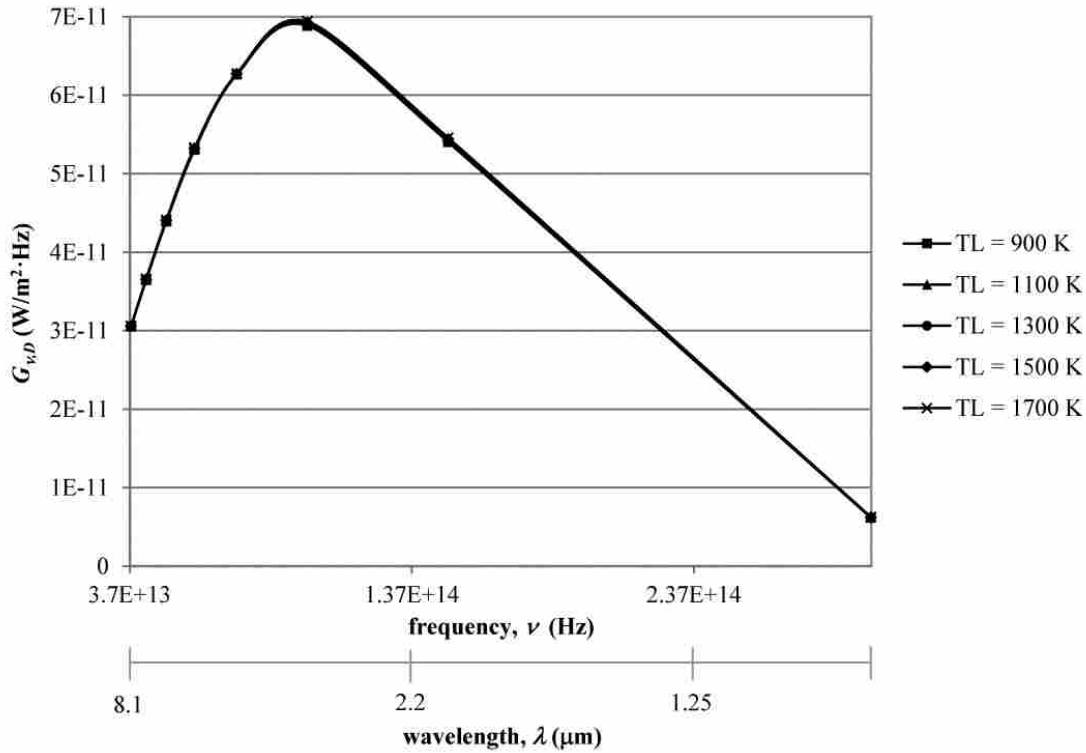


Figure 8-7: Sensitivity of spectral irradiation on detector to changes in the TBC surface temperature

8.7 Inverse Problem

The forward problem consists of calculating the spectral signals from the detection system based on known values of the system parameters, T_0 , T_L , κ_ν , n , and $\varepsilon_{\nu,0}$. The corresponding inverse problem involves inferring these system parameters from known spectral measurements. The inverse problem is solved by using optimization methods to determine the unknown parameters of the system by minimizing the error between the experimentally measured signals and those calculated from the forward problem.

A genetic algorithm was used to solve the inverse problem. In the genetic algorithm, a population of sets of the parameters to be determined is created. The forward problem is solved for each set in the population. The resulting spectral signals for each set are compared to the measured

signals. The parameter sets that result in spectral signals which are closest to the measured signals are used to create a new population of sets of parameters. This process is repeated until the error between the experimentally measured signals and those calculated from the forward problem is minimized.

Each parameter in a set is represented by a binary string. The strings for every parameter in a given set are concatenated to form a single binary string which represents that set of parameters, or individual, in the population. An initial population of a specified number of individuals is created by randomly generating binary strings. Each individual in the population is converted from a binary string into a set of real valued parameters. The spectral measurements corresponding to each of the sets of parameters are calculated from the forward problem using Equation (8-26). The fitness of each individual in the population is evaluated by calculating the Euclidean norm of the differences between the spectral signals calculated from the forward problem and the measured spectral signals.

The individual with the best fitness from the entire population is copied directly into the new generation of individuals. The rest of the individuals in the new generation are created by tournament selection as follows. Two subsets of the initial population are selected as groups of potential pools of “mothers” and “fathers.” Each subset consists of a group of randomly selected individuals. The size of the subset is specified as a percentage of the entire population. The individuals in both pools with the best fitness are selected as the mother and father. Segments of the binary strings of the mother and father are used at a specified number of arbitrarily selected crossover points to create a new individual. This process is repeated until the new generation is filled. In order to promote diversity in the population, mutation may occur in some individuals by changing random bits in the binary strings. The fitness of the individuals in the new

population are calculated and the process is repeated until either the best fitness reaches a specified value or the best fitness value does not change significantly over a specified number of generations. Once one of these criteria is met, the parameters corresponding to the individual with the best fitness value in the current generation are considered the optimized solution to the inverse problem.

8.8 Results of Numerical Experiments

Because the objective of this work was only to develop and assess the method by which the inverse problem can be solved, no actual physical experiments were conducted. Simulated measurements were used to assess the accuracy of the method. In order to determine the simulated measurements, the forward problem was solved at five selected frequencies for a theoretical TBC for which the five system parameters, T_0 , T_L , κ_ν , n , and $\varepsilon_{\nu,0}$ were assumed to be known. The selected frequencies were in the spectral band between 1.2×10^{14} and 1.5×10^{14} Hz (2 to 2.5 μm), over which the spectral properties are assumed to be constant. The inverse problem was then solved using the genetic algorithm to determine the accuracy with which the system parameters could be inferred from the simulated measurements. In order to assess the robustness of the inverse problem, it was solved for various theoretical TBCs with different properties and thicknesses. The source code for the genetic algorithm can be found in Appendix A.7. Table 8-2 shows the settings used in the genetic algorithm in one of the cases.

Table 8-2: Example of setting used in the genetic algorithm

TBC thickness (m)	0.0001
number points in temperature profile	100
lower temperature bound (K)	1300
upper temperature bound (K)	1900
lower κ_v bound (1/m)	0.1
upper κ_v bound (1/m)	150
lower $\varepsilon_{v,0}$ bound	0.1
upper $\varepsilon_{v,0}$ bound	1
lower n bound	1.6
upper n bound	2.2
ν_1 (Hz)	1.25×10^{14} (2.4 μm)
ν_2 (Hz)	1.30×10^{14} (2.3 μm)
ν_3 (Hz)	1.36×10^{14} (2.2 μm)
ν_4 (Hz)	1.43×10^{14} (2.1 μm)
ν_5 (Hz)	1.50×10^{14} (2.0 μm)
parameter binary string size	10
number of individuals in population	200
% of population used for tournament	10
% chance of mutation	70
number of crossover points	3

Some example results are shown in Table 8-3. Because the problem is ill-posed, the optimum parameter sets found from the inverse problem are never exactly the same. This issue can be addressed to some extent by putting tighter upper and lower bounds on the possible values of the parameters for which data is available. Examples of these bounds are shown in Table 8-2 for each of the unknowns. As expected, the parameters to which changes in the spectral signals are most sensitive were determined with greater accuracy. The bond coat temperature was found with excellent accuracy in every case tested. The average error between the optimum value and the actual value for the bond coat temperature was about 0.2%. This corresponds to an average error of about 3.5 K. The index of refraction and spectral emittance of the bond coat were calculated from the inverse problem with a reasonable level of accuracy with average errors of about 7% and 18%, respectively. The measurements were insensitive to the TBC surface temperature and the spectral absorption coefficient. Therefore, the accuracy with which they

were found by the inverse problem was very low. The average error of the absorption coefficient was 88%. The average error of the TBC surface temperature was about 5%, which represents an average deviation of 85 K from the actual temperature value. However, because the temperature profile is linear, the TBC surface temperature could be calculated using the bond coat temperature if the thermal conductivity of the top coat is known.

Table 8-3: Example of optimum parameter values found from the genetic algorithm

	actual	optimum 1	% error	optimum 2	% error
T_o (K)	1550	1551	0.06	1548	0.13
T_L (K)	1700	1723	1.4	1795	5.6
ϵ_o	0.5	0.59	18	0.57	14
κ (m ⁻¹)	35	74	111	69	97
n	1.9	1.74	8.4	1.78	6.3

In order to assess the potential impact of measurement error on the results of the inverse problem, error was introduced into the simulated measurements. Table 8-4 and Table 8-5 show typical results for cases in which 10% and 20% error were added to the measurements, respectively. Even with 20% measurement error, the bond coat temperature was inferred from the inverse problem with an average error of only about 0.2%.

Table 8-4: Example of optimum parameter values found from the genetic algorithm with 10% measurement error

	actual	optimum 1	% error	optimum 2	% error
T_o (K)	1750	1748	0.11	1746	0.23
T_L (K)	1855	1914	3.2	1989	7.2
ϵ_o	0.32	0.33	3.1	0.29	9.4
κ (m ⁻¹)	67	11	84	49	27
n	1.75	1.84	5.1	1.95	11

Table 8-5: Example of optimum parameter values found from the genetic algorithm with 20% measurement error

	actual	optimum 1	% error	optimum 2	% error
T_o (K)	1300	1304	0.31	1302	0.15
T_L (K)	1500	1430	3.2	1620	8
ϵ_0	0.8	0.95	19	0.89	11
κ (m ⁻¹)	100	22	78	25	75
n	2.1	2.12	0.95	2.2	4.8

8.9 Future Work

The results of the numerical experiments show that the proposed experimental method is capable of accurately predicting the bond coat temperature of a thermal barrier coating based on measurements of the radiative intensity from the TBC surface. The primary limitation of the analytical model described here comes from neglecting the radiation from the combustion gases that are present between the surface of the TBC and the detection system. These hot gases are radiatively participating and their effects on the detector signal described by the forward problem would likely be significant. These effects include the emission from the gases into the detection system, absorption and scattering of the radiation coming from the TBC surface, and reflection off of the TBC surface. Each of these effects should be investigated by adding another participating medium into the forward problem between the TBC surface and the detector that represents the combustion gases. Scattering of radiation within the TBC top coat may also be significant and should be added to the analysis.

8.10 Conclusion

An inverse radiative heat transfer method capable of accurately determining the bond coat temperature, the bond coat emittance, and the top coat refractive index of a thermal barrier coating has been proposed. The forward problem is a mathematical model of the measurements of the intensity from the TBC surface and accounts for the emission from the bond coat as well as the emission and absorption of the TBC itself. The TBC was approximated as a one-dimensional, plane-parallel, non-scattering medium. The RTE was solved using an integrating factor and the temperature profile in the top coat was found by solving the energy equation using the method of variation of parameters. The inverse method consists of using a genetic algorithm to determine the desired TBC parameters by minimizing the error between actual intensity measurements and those calculated from the forward problem. The spectral band over which measurements should be made was determined. Numerical experiments were performed using a number of simulated measurements calculated from the forward problem based on theoretical TBCs with known properties. The inverse problem was solved with and without simulated measurement error. Even with 20% measurement error introduced, the bond coat temperature was determined with only an average error of 0.2% while the average error in the refractive index was 7% and that in the spectral emittance of the bond coat was 18%. The spectral measurements were insensitive to changes in the spectral absorption coefficient and the TBC surface temperature and, therefore, cannot be determined by the inverse method with any accuracy.

9 OPTICAL FIBER THERMOMETER: THEORETICAL ANALYSIS

This chapter discusses the development of an analytical model that can be used to determine the temperature of the sensing tip of an optical fiber thermometer. This model includes the forward problem, which relates the properties and temperature profile of the fiber to spectral measurements of the radiant energy from the OFT made by a detection system. The temperature profile is calculated using the method of variation of parameters to solve the overall energy equation. An inverse model is developed to infer the unknown temperature and properties of the OFT system from known spectral measurements. Numerical experiments are performed to assess the accuracy of the model.

9.1 Introduction

An optical fiber thermometer (OFT) consists of an optical fiber whose sensing tip is coated with a highly conductive, opaque material. This forms an isothermal cavity at the tip of the fiber. The tip temperature can be inferred from the cavity emission, which is transmitted along the optical fiber to a detector [9]. Some advantages of OFTs include long-term stability, wider dynamic range, high sensitivity, fast response, the ability to withstand harsh environments, and imperviousness to electromagnetic interference [94]. These advantages make OFT's a more attractive option than existing temperature measurement techniques, such as thermocouples, for many applications such as measuring the temperature in oxy-coal combustion environments.

An optical fiber is a radiatively participating medium and, as such, the radiation detected from the fiber includes the effects of emission and absorption of the fiber itself in addition to the emission from the cavity and conduction in the fiber. If only the sensing tip and a small length of the optical fiber are exposed to the high temperature environment, then it is an acceptable approximation to assume that all of the radiation detected is emitted by the blackbody cavity [9]. However, if a significant portion of the optical fiber is exposed to elevated temperatures, then the standard two-color approach cannot be used to accurately determine the temperature of the sensing tip [10, 11].

In this chapter, an equation for the spectral irradiation from an OFT incident on a detection system is found by solving the RTE using an integrating factor. This equation requires knowledge of the temperature profile along the fiber. A differential equation that can be solved for the temperature profile is developed from an energy balance on a differential element of the optical fiber. This energy balance includes conduction along the fiber, emission and absorption of radiation within the fiber, convection heat transfer between the fiber and the surrounding gas, and radiation heat transfer between the outer surface of the fiber and the surroundings. Various simplifications to the model are made and their effects are analyzed. It is shown that for the small diameters of optical fibers, a constant thermal conductivity in the fiber can be assumed, the internal radiation component of the heat rate down the fiber is negligible, and the nonlinear portion of the governing differential equation can be linearized with little loss in accuracy. The inverse problem is solved using the GRG optimization algorithm that is implemented by the Solver application in Microsoft Excel. Numerical experiments are performed to assess the accuracy of the model.

9.2 Forward Problem

The forward problem is a mathematical model of the physical phenomenon of interest. This section shows the development of an equation representing the signal from a detection system as a function of the system parameters. Figure 9-1 shows the geometry and coordinate system used in the development of the forward problem. The left boundary consists of the cavity while the right boundary is the interface between the fiber and the air. Because the fiber is thin, variations of the properties and temperature in the radial direction are neglected and the optical fiber is modeled as a one-dimensional medium of length L .

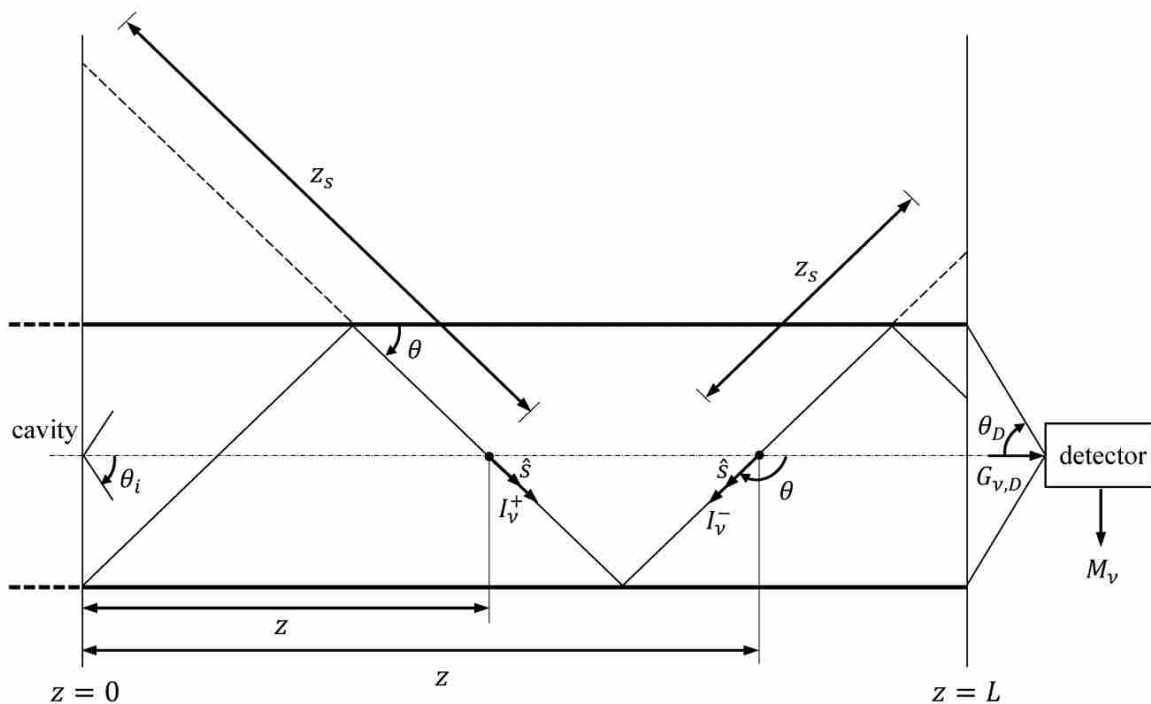


Figure 9-1: Coordinates used in the theoretical analysis of the optical fiber thermometer

Optical fibers consist of a core and a cladding. The refractive index of the core is greater than that of the cladding. As illustrated in Figure 9-2, when light passes from a medium with one

refractive index to another medium with a lower refractive index, it refracts away from the normal (the line perpendicular to the interface of the two media). As the angle of the incident beam decreases, the refracted light bends further away from the normal. At some critical angle, θ_i , the refracted light will travel along the interface. Radiant energy incident at an angle smaller than the critical angle is not refracted but entirely reflected back into the core. This is known as total internal reflection. Radiation that enters the fiber within the acceptance cone of the critical angle will experience total internal reflection and be transmitted along the fiber.

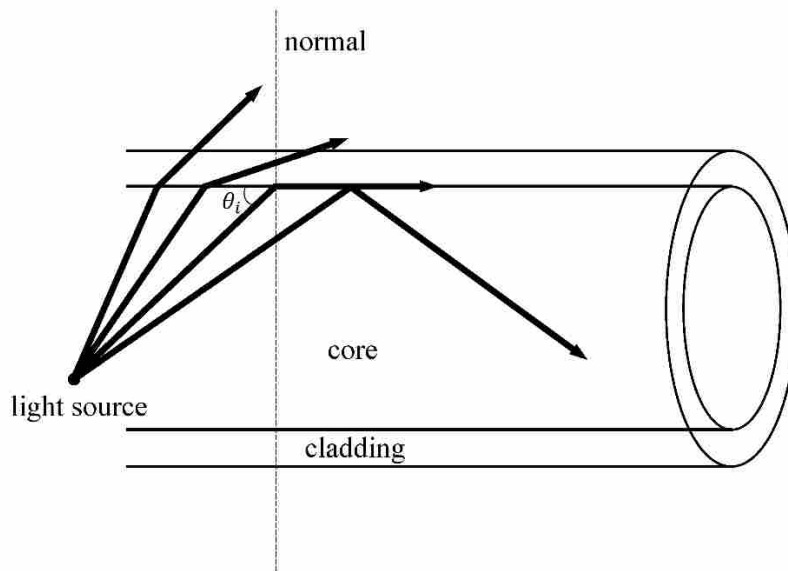


Figure 9-2: Illustration of total internal reflection

In order to account for the multiple reflections of a beam which occur within the fiber, it is easier to consider the intensity at a given point z in the \hat{s} direction from a point source in the fiber as that coming from an image of this point projected onto the boundary a distance z_s from the reception point, as shown in Figure 9-1 [95]. Just like the thermal barrier coating problem,

the spectral variable here will be frequency because frequency remains constant when moving between media with different refractive indices.

The objective is to determine the spectral irradiation incident on the detector, $G_{v,D}$ in terms of the parameters of the system. This irradiation is equal to the portion of intensity incident on the right boundary, $I_v^+(L, \theta)$, that is transmitted through the outer surface of the fiber at $z = L$ integrated over the solid angle from which the end of the fiber is viewed by the detector, $\Delta\Omega_{D-F}$.

$$G_{v,D} = \int_{\Delta\Omega_{D-F}} \tau_{v,L} I_v^+(L, \theta) \cos \theta_D d\Omega \quad (9-1)$$

Note that in Equation (9-1) there are two angles: θ is measured from the normal to the fiber face while θ_D is the acceptance angle of the detector and is measured from the normal to the detector. If this angle is assumed to be small, then $\cos \theta_D \approx 1$ and Equation (9-1) becomes

$$G_{v,D} \approx \tau_{v,L} I_v^+(L, \theta) \Delta\Omega_{D-F} \quad (9-2)$$

In order to find $I_v^+(L, \theta)$, the same process as that used in Chapter 6 is followed. The only difference is at the boundaries. In the Chapter 6 problem, the boundaries were opaque surfaces that emitted and reflected radiation. Here, the left boundary consists of the cavity at the end of the fiber which only emits radiation such that

$$I_v^+(0, \mu) = \varepsilon_C I_{b,v}(T_C) \quad (9-3)$$

In Equation (9-3), ε_C is the effective emittance of the cavity. If the space beyond the right boundary of the fiber is approximated as a cold vacuum, the intensity coming from the right surface consists only of the intensity reflected off of that surface as shown below.

$$I_v^-(L, -\mu) = \rho_{v,L} I_v^+(L, \mu) \quad (9-4)$$

Continuing the process as outlined in Chapter 6 yields the following expressions for $I_v^+(z, \mu)$ and $I_v^-(z, -\mu)$.

$$I_v^+(z, \mu) = \varepsilon_C I_{b,v}(T_C) e^{-\kappa_v z / \mu} + \frac{\kappa_v}{\mu} \int_0^z I_{b,v}(T(z')) e^{-\kappa_v(z-z')/\mu} dz' \quad (9-5)$$

$$I_v^-(z, -\mu) = \rho_{v,L} \varepsilon_C I_{b,v}(T_C) e^{-\kappa_v(2L-z)/\mu} + \frac{\rho_{v,L} \kappa_v}{\mu} \int_0^L I_{b,v}(T(z')) e^{-\kappa_v(2L-z-z')/\mu} dz' \\ + \frac{\kappa_v}{\mu} \int_z^L I_{b,v}(T(z')) e^{-\kappa_v(z'-z)/\mu} dz' \quad (9-6)$$

Evaluating Equation (9-5) at $z = L$ and substituting it into Equation (9-1) provides the following expression for the spectral irradiation on the detector.

$$G_{v,D} = \tau_{v,L} \left(\varepsilon_C I_{b,v}(T_C) e^{-\kappa_v L / \mu} + \frac{\kappa_v}{\mu} \int_0^L I_{b,v}(T(z')) e^{-\kappa_v(L-z')/\mu} dz' \right) \Delta\Omega_{D-F} \quad (9-7)$$

The spectral intensity at $z = L$ depends on the path that the radiation follows within the optical fiber, as indicated by the presence of the direction cosine $\mu = \cos \theta$ in Equation (9-7). Here, the total radiant energy incident on the detector is desired, so the spectral intensity exiting the fiber in all directions must be considered. This can be done by integrating over the direction cosine in Equation (9-7). The shortest possible distance traveled by a beam is the length of the fiber, L , when the angle of the incident beam is zero. The longest possible distance traveled by a beam in the fiber occurs when the angle of the incident beam is the critical angle. Integrating over this range of direction cosines from $\mu_i = \cos \theta_i$ to $\mu_0 = \cos 0 = 1$,

$$G_{v,D} = \tau_{v,L} \Delta\Omega_{D-F} \int_{\mu_i}^1 \left(\varepsilon_C I_{b,v}(T_C) e^{-\kappa_v L / \mu} + \frac{\kappa_v}{\mu} \int_0^L I_{b,v}(T(z')) e^{-\kappa_v(L-z')/\mu} dz' \right) d\mu \quad (9-8)$$

Just as in Chapter 6 and Chapter 8, the integral over μ requires numerical integration.

The irradiation on the detector is related to the detection system measurements, M_ν , by a spectral instrument response function, IRF_ν , as shown in Equation (9-9). The instrument response function is dependent on the detection system and includes the solid angle $\Delta\Omega_{D-F}$ as well as the spectral transmittance at the end of the fiber, $\tau_{\nu,L}$. It is determined by a calibration procedure. The spectral signal from the detector is

$$M_\nu = IRF_\nu \left[\int_{\mu_i}^1 \left(\varepsilon_C I_{b,\nu}(T_C) e^{-\kappa_\nu L/\mu} + \frac{\kappa_\nu}{\mu} \int_0^L I_{b,\nu}(T(z')) e^{-\kappa_\nu(L-z')/\mu} dz' \right) d\mu \right] \quad (9-9)$$

Equation (9-9) models the measurements made by a detection system of the spectral radiative intensity exiting the optical fiber.

9.3 Temperature Profile along the Fiber

In order to calculate M_ν using the forward problem in Equation (9-9) for a given frequency, the temperature profile along the fiber, $T(z)$, must be known. The temperature profile depends on both conduction and radiation within the fiber as well as convection and radiation at the fiber's outer surface. The temperature profile can be found by performing a total energy balance (both thermal and radiative) on a differential volume of the fiber. Temperature variations in the radial direction of the fiber are neglected. All of the heat transfer interactions with the cylindrical differential volume are shown in Figure 9-3. These include the heat transfer at the outer surface of the fiber due to convection, q_{conv} , and radiation exchange with the surrounding environment, q_{rad} , as well as the total heat rate along the fiber, q_z . It is assumed that both convection and radiation transfer heat out of the control volume.

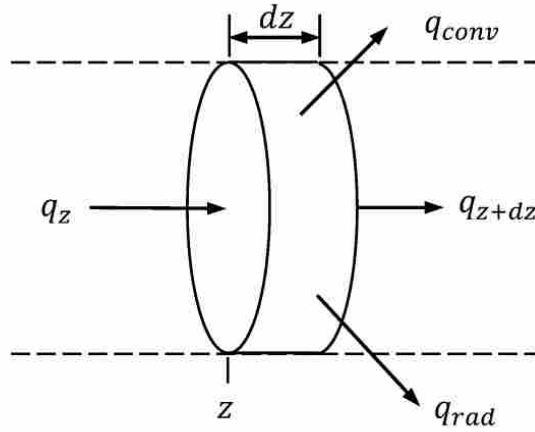


Figure 9-3: Differential volume of optical fiber with energy interactions

The thermal energy balance has the form

$$\dot{E}_{in} - \dot{E}_{out} + \dot{E}_{gen} = \dot{E}_{st} \quad (9-10)$$

There is no stored energy because the system is assumed to be in steady state and there is no energy generated. Substituting the heat transfer interactions shown in Figure 9-3 into the energy balance results in the following equation.

$$q_z - q_{z+dz} = q_{conv} + q_{rad} \quad (9-11)$$

The rate of heat transferred by convection is

$$q_{conv} = \bar{h}A(T(z + dz/2) - T_{\infty}) \quad (9-12)$$

where \bar{h} is the average heat transfer coefficient over the fiber and $A = \pi D dz$ is the surface area of the differential volume that is exposed to the surroundings. Similarly, the rate of radiation exchange between the outer fiber surface and the surroundings can be expressed as follows where ε_f is the emittance of the fiber.

$$q_{rad} = A\varepsilon_f\sigma(T^4(z + dz/2) - T_{sur}^4) \quad (9-13)$$

This equation carries the assumption that the surroundings are isothermal and large compared to the optical fiber. Substituting Equations (9-12) and (9-13) into Equation (9-11) and dividing both sides by dz gives

$$-\frac{q_{z+dz} - q_z}{dz} = \pi D \bar{h}(T(z + dz/2) - T_\infty) + \pi D \varepsilon_f \sigma (T^4(z + dz/2) - T_{sur}^4) \quad (9-14)$$

Making use of the difference quotient by taking the limit of Equation (9-14) as dz approaches zero gives

$$-\frac{d}{dz}(q) = \pi D \bar{h}(T(z) - T_\infty) + \pi D \varepsilon_f \sigma (T^4(z) - T_{sur}^4) \quad (9-15)$$

The total heat rate along the fiber results from both conduction, q_{cond} , and from radiation within the fiber, q_R . The q_R term represents the net radiative energy deposited into (or withdrawn from) the volume element due to emission and absorption within the volume.

$$-\frac{d}{dz}(q_{cond} + q_R) = \pi D \bar{h}(T(z) - T_\infty) + \pi D \varepsilon_f \sigma (T^4(z) - T_{sur}^4) \quad (9-16)$$

The conduction rate is given by Fourier's law.

$$-\frac{d}{dz}\left(-kA_c \frac{dT}{dz}\right) - \frac{d}{dz}(A_c q_R'') = \pi D \bar{h}(T(z) - T_\infty) + \pi D \varepsilon_f \sigma (T^4(z) - T_{sur}^4) \quad (9-17)$$

In Equation (9-17), k is the thermal conductivity of the optical fiber, q_R'' is the total radiative heat flux in the fiber, and $A_c = \pi D^2/4$ is the cross-sectional area normal to the direction of heat transfer. If the thermal conductivity is assumed to be constant over z , the resulting equation is

$$\frac{d^2T}{dz^2} = \frac{1}{k} \frac{dq_R''}{dz} + \frac{4}{kD} \left(\bar{h}(T(z) - T_\infty) + \varepsilon_f \sigma (T^4(z) - T_{sur}^4) \right) \quad (9-18)$$

In order to solve this differential equation for the temperature profile in the fiber, the total radiative heat flux, q_R'' , must be determined. This heat flux is given by [5]

$$q_R'' = \int_0^\infty \int_{4\pi} I_\nu(\hat{\mathbf{s}}) \hat{\mathbf{s}} d\Omega d\nu \quad (9-19)$$

Using the definition of the solid angle, $d\Omega = \sin \theta d\theta d\phi$, and expressing the direction vector, \hat{s} in terms of z and θ , Equation (9-19) becomes

$$q_R'' = \int_0^\infty \int_0^{2\pi} \left[\int_0^{\theta_i} I_v^+(z, \theta) \cos \theta \sin \theta d\theta + \int_{\pi-\theta_i}^\pi I_v^-(z, \theta) \cos \theta \sin \theta d\theta \right] d\phi dv \quad (9-20)$$

In this equation, θ_i represents the critical angle below which total internal reflection occurs in the optical fiber, as shown in Figure 9-1. Integrating over ϕ , employing the direction cosine, $\mu = \cos \theta$, and noting that $\sin \theta d\theta = -d\mu$, Equation (9-20) becomes

$$q_R = 2\pi \int_0^\infty \left[\int_{\mu_i}^1 I_v^+(z, \mu) \mu d\mu + \int_{\mu_i}^1 I_v^-(z, -\mu) \mu d\mu \right] dv \quad (9-21)$$

where $\mu_i = \cos \theta_i$. The total radiative heat flux is found by substituting Equations (9-5) and (9-6) into Equation (9-21).

$$q_R'' = 2\pi \sum_{i=1}^5 A_i \quad (9-22)$$

where

$$A_1 = \int_0^\infty \int_0^1 \varepsilon_{v,c} I_{b,v}(T_c) e^{-\kappa_v z / \mu} \mu d\mu dv \quad (9-23)$$

$$A_2 = \int_0^\infty \int_0^1 \kappa_v \int_0^z I_{b,v}(T(z')) e^{-\kappa_v(z-z')/\mu} dz' d\mu dv \quad (9-24)$$

$$A_3 = - \int_0^\infty \int_0^1 \rho_{v,L} \varepsilon_{v,c} I_{b,v}(T_c) e^{-\kappa_v(2L-z)/\mu} \mu d\mu dv \quad (9-25)$$

$$A_4 = - \int_0^\infty \int_0^1 \rho_{v,L} \kappa_v \int_0^L I_{b,v}(T(z')) e^{-\kappa_v(2L-z-z')/\mu} dz' d\mu dv \quad (9-26)$$

$$A_5 = - \int_0^\infty \int_0^1 \kappa_v \int_z^L I_{b,v}(T(z')) e^{-\kappa_v(z'-z)/\mu} dz' d\mu dv \quad (9-27)$$

Equation (9-21) is then substituted into Equation (9-18).

$$\frac{d^2T}{dz^2} = \frac{2\pi}{k} \sum_{i=1}^5 \frac{dA_i}{dz} + \frac{4}{kD} \left(\bar{h}(T(z) - T_\infty) + \varepsilon_f \sigma (T^4(z) - T_{sur}^4) \right) \quad (9-28)$$

This second order, nonlinear, nonhomogeneous differential equation can be solved for the temperature profile $T(z)$ in the fiber by finding both the complementary and particular solutions.

$$T(z) = T_c + T_p \quad (9-29)$$

The complementary solution is the solution to the homogeneous equation.

$$\frac{d^2T}{dz^2} = 0 \quad (9-30)$$

which is found by separating and integrating twice.

$$T_c = c_1 z + c_2 \quad (9-31)$$

The particular solution is solved using the method of variation of parameters and is given by

$$T_p = u_1 T_1 + u_2 T_2 = u_1 z + u_2 \quad (9-32)$$

where

$$u_1 = \int_0^z \left(\frac{2\pi}{k} \sum_{i=1}^5 \frac{dA_i}{dz'} + \frac{4}{kD} \left(\bar{h}(T(z') - T_\infty) + \varepsilon_f \sigma (T^4(z') - T_{sur}^4) \right) \right) dz' \quad (9-33)$$

$$u_2 = \int_0^z \left(-\frac{2\pi}{k} z' \sum_{i=1}^5 \frac{dA_i}{dz'} - \frac{4z'}{kD} \left(\bar{h}(T(z') - T_\infty) + \varepsilon_f \sigma (T^4(z') - T_{sur}^4) \right) \right) dz' \quad (9-34)$$

Integration by parts is used on Equation (9-34) and the particular solution reduces to

$$\begin{aligned} T_p = & \frac{2\pi}{k} \int_0^z \sum_{i=1}^5 A_i dz' + \frac{4z}{kD} \int_0^z \left(\bar{h}(T(z') - T_\infty) + \varepsilon_f \sigma (T^4(z') - T_{sur}^4) \right) dz' \\ & - \frac{4}{kD} \int_0^z z' \left(\bar{h}(T(z') - T_\infty) + \varepsilon_f \sigma (T^4(z') - T_{sur}^4) \right) dz' \end{aligned} \quad (9-35)$$

An equation for the temperature profile along the fiber is found by substituting Equations (9-31) and (9-35) into Equation (9-29).

$$T(z) = c_1 z + c_2 + \frac{2\pi}{k} \int_0^z \sum_{i=1}^5 A_i dz' + \frac{4z}{kD} \int_0^z \left(\bar{h}(T(z') - T_\infty) + \varepsilon_f \sigma (T^4(z') - T_{sur}^4) \right) dz' - \frac{4}{kD} \int_0^z z' \left(\bar{h}(T(z') - T_\infty) + \varepsilon_f \sigma (T^4(z') - T_{sur}^4) \right) dz' \quad (9-36)$$

Each of the A terms in Equation (9-36) is integrated with respect to z and evaluated from 0 to z so that the temperature profile has the following form.

$$T(z) = c_1 z + c_2 + \frac{2\pi}{k} \sum_{i=1}^5 B_i(z) + \frac{4z}{kD} \int_0^z \left(\bar{h}(T(z') - T_\infty) + \varepsilon_f \sigma (T^4(z') - T_{sur}^4) \right) dz' - \frac{4}{kD} \int_0^z z' \left(\bar{h}(T(z') - T_\infty) + \varepsilon_f \sigma (T^4(z') - T_{sur}^4) \right) dz' \quad (9-37)$$

where

$$B_1 = \int_0^\infty \int_0^1 \frac{\varepsilon_{v,C}}{\kappa_v} I_{b,v}(T_C) (1 - e^{-\kappa_v z / \mu}) \mu^2 d\mu dv \quad (9-38)$$

$$B_2 = - \int_0^\infty \int_0^1 \int_0^z I_{b,v}(T(z')) e^{\kappa_v(z'-z)/\mu} \mu dz' d\mu dv \quad (9-39)$$

$$B_3 = \int_0^\infty \int_0^1 \frac{\rho_{v,L} \varepsilon_{v,C}}{\kappa_v} I_{b,v}(T_C) e^{-\kappa_v 2L/\mu} (1 - e^{\kappa_v z / \mu}) \mu^2 d\mu dv \quad (9-40)$$

$$B_4 = \int_0^\infty \int_0^1 \rho_{v,L} \mu e^{-\kappa_v 2L/\mu} (1 - e^{\kappa_v z / \mu}) \int_0^L I_{b,v}(T(z')) e^{\kappa_v z' / \mu} dz' d\mu dv \quad (9-41)$$

$$B_5 = - \int_0^\infty \int_0^1 \int_z^L I_{b,v}(T(z')) e^{-\kappa_v(z'-z)/\mu} \mu dz' d\mu dv + \int_0^\infty \int_0^1 \int_0^L I_{b,v}(T(z')) e^{-\kappa_v z' / \mu} \mu dz' d\mu dv \quad (9-42)$$

The terms B_2 and B_5 were calculated using the same method as terms B_5 and B_{12} in Section 6.3.

The constants c_1 and c_2 in Equation (9-37) are found by applying the boundary conditions.

At $z = 0$, the temperature of the fiber is that of the cavity, T_C so that

$$c_2 = T_C \quad (9-43)$$

At $z = L$ the temperature is assumed to be that of the ambient air, T_∞ which gives

$$\begin{aligned} c_1 = & \frac{T_\infty - T_C}{L} - \frac{2\pi}{kL} \sum_{i=1}^5 B_i(L) - \frac{4}{kD} \int_0^L \left(\bar{h}(T(z')) - T_\infty + \varepsilon_f \sigma (T^4(z') - T_{sur}^4) \right) dz' \\ & + \frac{4}{kLD} \int_0^L z' \left(\bar{h}(T(z')) - T_\infty + \varepsilon_f \sigma (T^4(z') - T_{sur}^4) \right) dz' \end{aligned} \quad (9-44)$$

These constants are substituted into Equation (9-37) and the π term is multiplied by the spectral intensities so that $\pi I_{b,\nu} = E_{b,\nu}$. Adding all of the summation terms provides the following expression for the temperature profile in the fiber.

$$\begin{aligned} T(z) = & \left(\frac{T_\infty}{L} - \frac{T_C}{L} \right) z + T_C + k \sum_{i=1}^7 H_i(z) \\ & - \frac{4z}{kD} \int_0^L \left(\bar{h}(T(z')) - T_\infty + \varepsilon_f \sigma (T^4(z') - T_{sur}^4) \right) dz' \\ & + \frac{4z}{LkD} \int_0^L z' \left(\bar{h}(T(z')) - T_\infty + \varepsilon_f \sigma (T^4(z') - T_{sur}^4) \right) dz' \\ & + \frac{4z}{kD} \int_0^z \left(\bar{h}(T(z')) - T_\infty + \varepsilon_f \sigma (T^4(z') - T_{sur}^4) \right) dz' \\ & - \frac{4}{kD} \int_0^z z' \left(\bar{h}(T(z')) - T_\infty + \varepsilon_f \sigma (T^4(z') - T_{sur}^4) \right) dz' \end{aligned} \quad (9-45)$$

where

$$H_1 = \int_0^\infty \int_0^1 \frac{\varepsilon_{\nu,C}}{\kappa_\nu} E_{b,\nu}(T_C) P(z, \nu, \mu) d\mu d\nu \quad (9-46)$$

$$H_2 = \frac{z}{L} \int_0^\infty \int_0^1 \int_0^L E_{b,\nu}(T(z')) e^{\kappa_\nu(z'-L)/\mu} \mu dz' d\mu d\nu \quad (9-47)$$

$$H_3 = - \int_0^\infty \int_0^1 \int_0^z E_{b,\nu}(T(z')) e^{\kappa_\nu(z'-z)/\mu} \mu dz' d\mu dv \quad (9-48)$$

$$H_4 = \int_0^\infty \int_0^1 \frac{\rho_{\nu,L} \epsilon_{\nu,C}}{\kappa_\nu} E_{b,\nu}(T_C) Q(z, \nu, \mu) \mu d\mu dv \quad (9-49)$$

$$H_5 = \int_0^\infty \int_0^1 \rho_{\nu,L} Q(z, \nu, \mu) \int_0^L E_{b,\nu}(T(z')) e^{\kappa_\nu z'/\mu} dz' d\mu dv \quad (9-50)$$

$$H_6 = \left(1 - \frac{z}{L}\right) \int_0^\infty \int_0^1 \int_0^L E_{b,\nu}(T(z')) e^{-\kappa_\nu z'/\mu} \mu dz' d\mu dv \quad (9-51)$$

$$H_7 = - \int_0^\infty \int_0^1 \int_z^L E_{b,\nu}(T(z')) e^{-\kappa_\nu(z'-z)/\mu} \mu dz' d\mu dv \quad (9-52)$$

In the above equations, $P(z, \nu, \mu)$ and $Q(z, \nu, \mu)$ are given as follows.

$$P(z, \nu, \mu) = \mu^2 \left(\frac{z}{L} (e^{-\kappa_\nu L/\mu} - 1) + (1 - e^{-\kappa_\nu z/\mu}) \right) \quad (9-53)$$

$$Q(z, \nu, \mu) = \mu e^{-\kappa_\nu L/\mu} \left(\frac{z}{L} (1 - e^{-\kappa_\nu L/\mu}) + e^{-\kappa_\nu L/\mu} (1 - e^{\kappa_\nu z/\mu}) \right) \quad (9-54)$$

Equation (9-45) is used to determine the temperature profile along the fiber. Because the temperature profile is found in the integrals on the right side of Equation (9-45), an iterative solution approach is required.

9.4 Heat Source Temperature

It is important to note that the temperature of the cavity may differ significantly from the temperature of the heat source which is to be measured. The relationship between the cavity temperature and the heat source temperature can be found by performing an energy balance on the cavity. Figure 9-4 shows all of the energy interactions with the cavity. These include convection heat transfer between the heat source and the outer surface of the cavity, q_{conv} , radiation exchange between the large, isothermal surroundings and the outer surface of the

cavity, q_{rad} , conduction down the optical fiber, q_{cond} , and emission from the cavity down the fiber, q_{cav} .

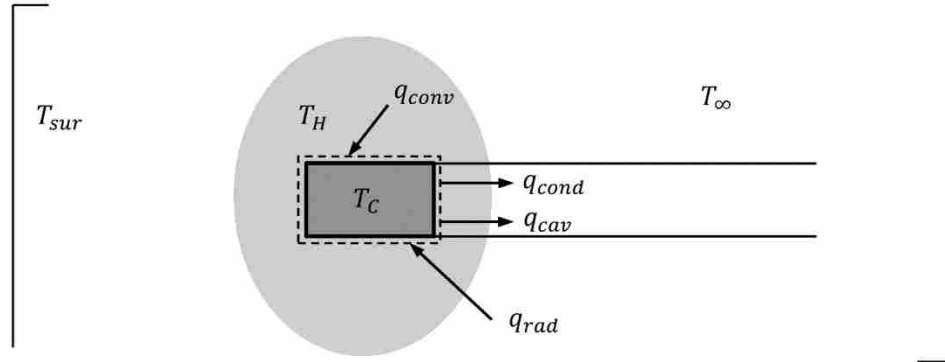


Figure 9-4: Energy interactions with the OFT sensing tip

An energy balance on the cavity reduces to

$$\dot{E}_{in} = \dot{E}_{out} \quad (9-55)$$

or

$$q_{conv} + q_{rad} = q_{cond} + q_{cav} \quad (9-56)$$

The rate of heat transferred by convection is

$$q_{conv} = \bar{h}_H A_s (T_H - T_C) \quad (9-57)$$

where \bar{h}_H is the average convection heat transfer coefficient between the hot surroundings and the outer cavity surface, T_H is the temperature of the heat source, and A_s is the surface area of the cavity. If the surroundings are considered large and isothermal compared to the cavity, the rate of radiation exchange between the outer cavity surface and the surroundings can be expressed as

$$q_{rad} = A_s \varepsilon_{cav} \sigma (T_{sur}^4 - T_C^4) \quad (9-58)$$

In the above equation, ε_{cav} is the emittance of the outer surface of the cavity. The conduction term at the tip is given by Fourier's Law.

$$q_{cond} = -A_c k \left. \frac{dT}{dz} \right|_{z=0} \quad (9-59)$$

where A_c is the cross-sectional area of the fiber and k is the fiber thermal conductivity. The cavity emission is given by

$$q_{cav} = A_c \varepsilon_c \sigma T_C^4 \quad (9-60)$$

where ε_c is the effective emittance of the cavity. Substituting these four heat rates into the energy balance gives

$$\bar{h}_H A_s (T_H - T_C) + A_s \varepsilon_{cav} \sigma (T_{sur}^4 - T_C^4) = -A_c k \left. \frac{dT}{dz} \right|_{z=0} + A_c \varepsilon_c \sigma T_C^4 \quad (9-61)$$

The derivative at $z = 0$ can be approximated as

$$\left. \frac{dT}{dz} \right|_{z=0} \approx \frac{T(\Delta z) - T_C}{\Delta z} \quad (9-62)$$

Therefore, the heat source temperature, T_H , can be calculated from the following equation.

$$T_H = T_C + \frac{\varepsilon_{cav} \sigma}{\bar{h}_H} (T_C^4 - T_{sur}^4) + \frac{A_c k}{\bar{h}_H A_s \Delta z} (T_C - T(\Delta z)) + \frac{A_c}{\bar{h}_H A_s} \varepsilon_c \sigma T_C^4 \quad (9-63)$$

9.5 Simplifications to the Forward Problem

The forward problem is given by Equation (9-9), which is an expression for the signal output by a detector due to irradiation on the detector from an optical fiber. This expression requires knowledge of the temperature profile along the fiber, which can be calculated from Equation (9-45). This section describes various simplifications that are made in calculating the temperature profile along the fiber.

9.5.1 Constant Thermal Conductivity

One of the primary approximations made in solving Equation (9-17) was that the thermal conductivity of the fiber was constant over the length of fiber. Because of the large range of temperatures that could exist within the fiber, the thermal conductivity could vary significantly over the fiber and, therefore, the effects of this approximation on the temperature profile must be assessed. The temperature profile was calculated for a set of system properties and parameters over a wide range of thermal conductivity values. These parameters are shown in Table 9-1.

Table 9-1: System parameters for hypothetical OFT system.

T_c	1100 K	L	0.5 m
T_{sur}	300 K	L_{cav}	0.004 m
T_∞	300 K	\bar{h}	20 W/m ² ·K
ε_c	0.8	\bar{h}_H	100 W/m ² ·K
ε_f	0.5	n	1.8
θ_i	30°	κ	10 m ⁻¹

The temperature profile for these system parameters are shown Figure 9-5 and Figure 9-6 for various fiber diameters and at relatively low and relatively high thermal conductivity values.

The results in Figure 9-5 and Figure 9-6 show that as the diameter of the fiber decreases, differences in the fiber thermal conductivity have a smaller impact on the temperature profile in the fiber. The average percent error between the signals calculated from Equation (9-9) for the two cases shown in Figure 9-5 was 14% while the average error between the signals of the two cases shown in Figure 9-6 was 0.3%. Because optical fibers generally have very small diameters (optical fiber diameters range from 10 to 500 μm), it is a reasonable approximation to assume a constant thermal conductivity.

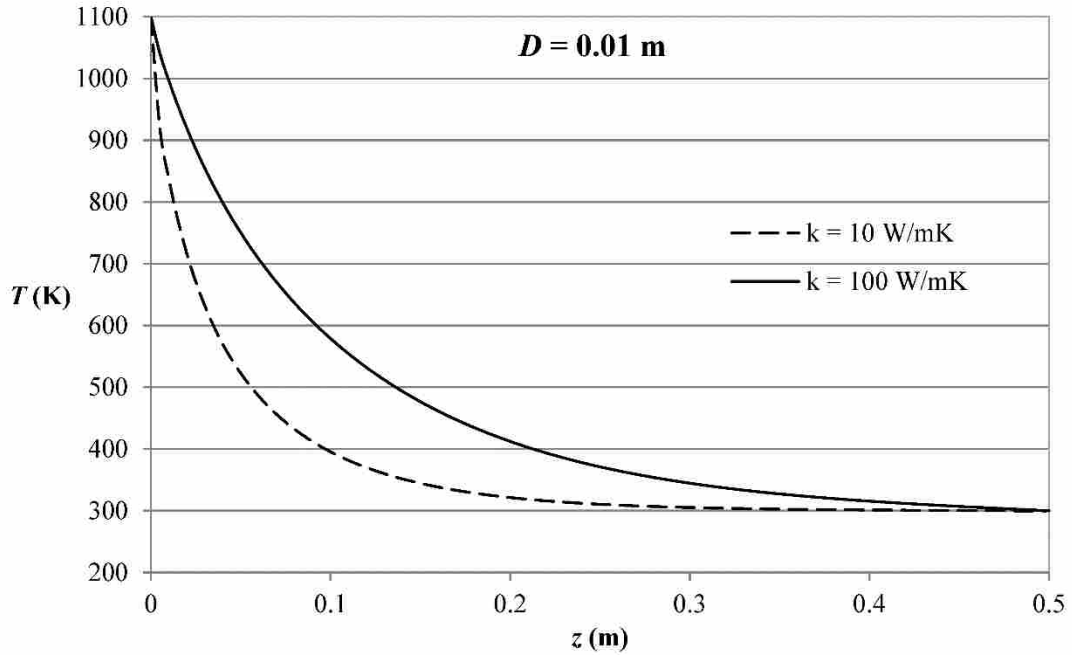


Figure 9-5: Temperature profiles in a fiber of diameter 0.01m at two different values of k for the parameters shown in Table 9-1

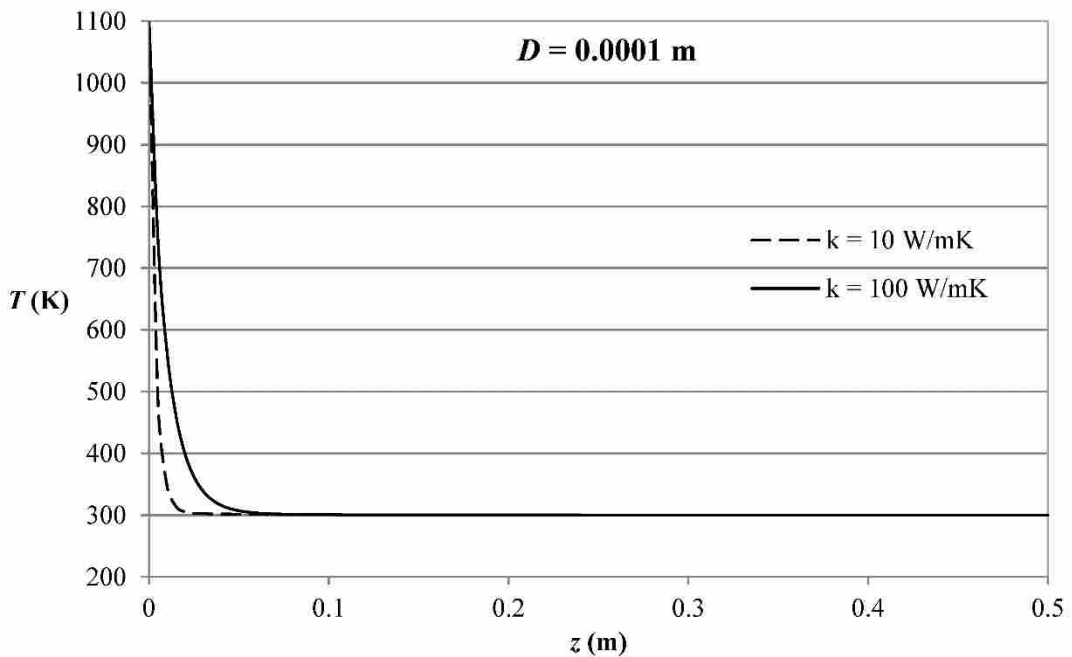


Figure 9-6: Temperature profiles in a fiber of diameter 0.0001m at two different values of k for the parameters shown in Table 9-1

The iterative approach to finding the temperature profile along with the high number of terms and numerical integrations required in Equation (9-45) make solving the forward problem computationally expensive. This computational cost is heightened by the use of small under relaxation factors required in the iterative process. For example, convergence of the temperature profile shown in Figure 9-6 with a thermal conductivity value of 10 W/m·K required an under relaxation factor of 0.0003 and over 22,000 iterations in 11 minutes.

9.5.2 Neglect Internal Radiation

Because the inverse problem calls for the forward problem to be solved many times, it would be computationally beneficial to simplify the forward problem. The effects of the radiative component of the heat rate down the optical fiber were assessed solving Equation (9-18) without the radiative component and comparing the results to those found from Equation (9-18). Without the radiative transfer within the optical fiber, the differential equation required to find the temperature profile becomes

$$\frac{d^2T}{dz^2} = \frac{4}{kD} \left(\bar{h}(T(z) - T_{\infty}) + \varepsilon_f \sigma (T^4(z) - T_{sur}^4) \right) \quad (9-64)$$

The complementary solution is again found by separating and integrating the homogeneous equation twice.

$$T_c = c_3 z + c_4 \quad (9-65)$$

As before, the particular solution can be solved using the method of variation of parameters and is given by

$$T_p = u_1 T_1 + u_2 T_2 = u_1 z + u_2 \quad (9-66)$$

In this equation,

$$u_1 = \frac{4}{kD} \int_0^z \left(\bar{h}(T(z') - T_\infty) + \varepsilon_f \sigma (T^4(z') - T_{sur}^4) \right) dz' \quad (9-67)$$

$$u_2 = -\frac{4}{kD} \int_0^z z' \left(\bar{h}(T(z') - T_\infty) + \varepsilon_f \sigma (T^4(z') - T_{sur}^4) \right) dz' \quad (9-68)$$

Combining the complementary and particular solutions provides the following equation for the temperature profile in the fiber.

$$T = c_3 z + c_4 + \frac{4z}{kD} \int_0^z \left(\bar{h}(T(z') - T_\infty) + \varepsilon_f \sigma (T^4(z') - T_{sur}^4) \right) dz' - \frac{4}{kD} \int_0^z z' \left(\bar{h}(T(z') - T_\infty) + \varepsilon_f \sigma (T^4(z') - T_{sur}^4) \right) dz' \quad (9-69)$$

The constants are found by applying the boundary conditions $T(0) = T_C$ and $T(L) = T_\infty$.

$$c_4 = T_C \quad (9-70)$$

$$c_3 = \frac{T_\infty}{L} - \frac{T_C}{L} - \frac{4}{kD} \int_0^L \left(\bar{h}(T(z') - T_\infty) + \varepsilon_f \sigma (T^4(z') - T_{sur}^4) \right) dz' + \frac{4}{LkD} \int_0^L z' \left(\bar{h}(T(z') - T_\infty) + \varepsilon_f \sigma (T^4(z') - T_{sur}^4) \right) dz' \quad (9-71)$$

Figure 9-7 and Figure 9-8 compare the temperature profiles found using Equation (9-69) to those found using Equation (9-45) for various fiber diameters. The system properties and parameters used are those found in Table 9-1 and the thermal conductivity was 10 W/m·K. The results in Figure 9-7 and Figure 9-8 show that as the diameter of the fiber decreases, the effects of the internal radiation component of the heat rate down the fiber become negligible. Physically, this means that for small diameters, the temperature profile is primarily dependent upon the convection and radiation heat transfer between the outer surface of the fiber and the environment.

The average percent error between the signals calculated from Equation (9-9) for the two cases shown in Figure 9-7 was 0.09% while the average error between the signals of the two cases shown in Figure 9-8 was $8.3 \times 10^{-5}\%$. Again, because optical fibers generally have very small diameters it is a reasonable approximation to exclude the internal fiber radiation to increase the computational efficiency of the forward problem. In Figure 9-8, the temperature profile calculated with the internal fiber radiation took about 11 minutes to converge while the profile without internal radiation took about 21 seconds to converge. Both profiles required an under relaxation factor of 0.0003 and about 22,000 iterations for convergence.

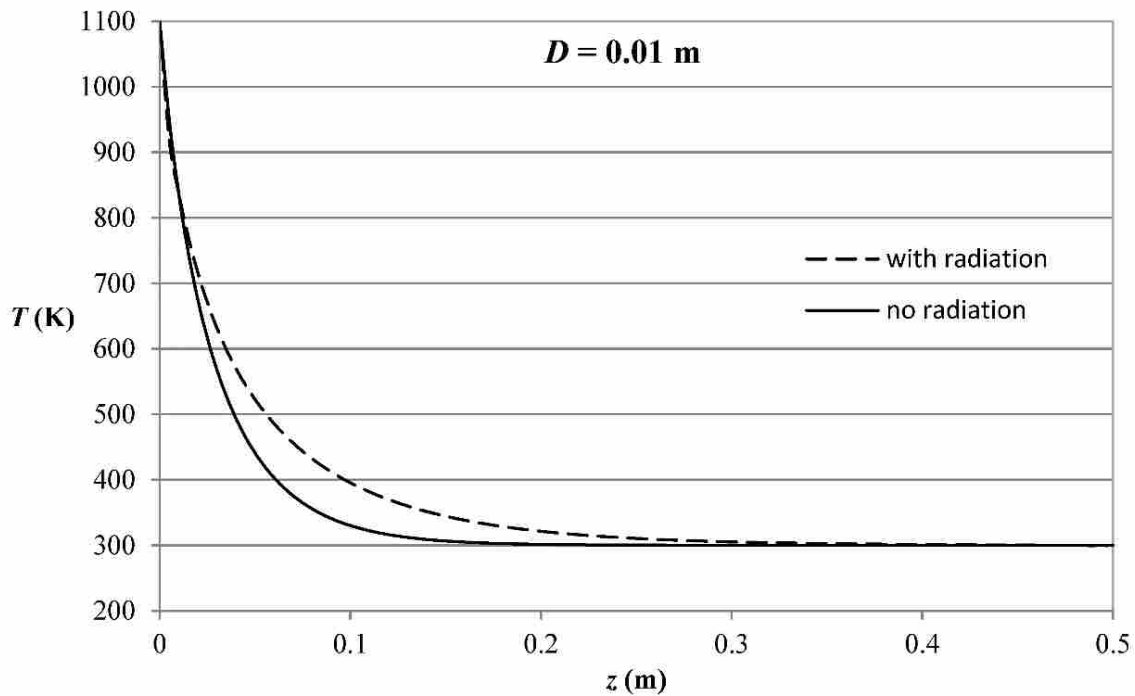


Figure 9-7: Temperature profiles in a fiber of diameter 0.01m with and without internal radiation

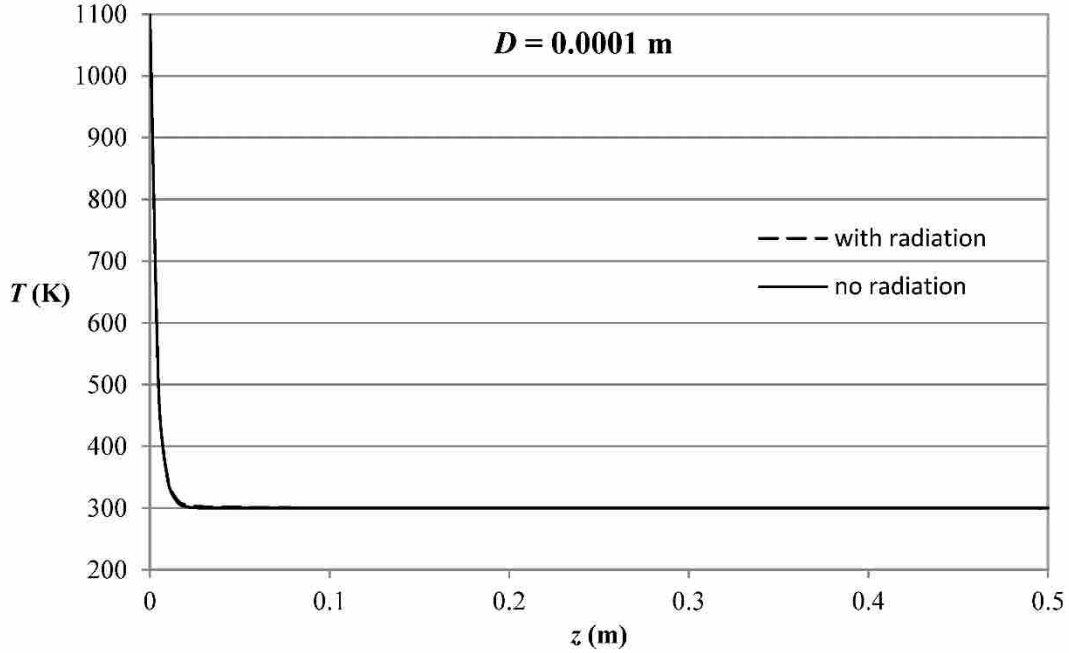


Figure 9-8: Temperature profiles in a fiber of diameter 0.0001m with and without internal radiation

9.5.3 Linearized Solution

Even without the effects of radiation within the fiber, the model still requires an iterative solution because of the nonlinear nature of the external radiation term and very small under relaxation factors are still required for convergence to be achieved. Therefore, in order to further simplify the forward problem, the nonlinear term is linearized using the surroundings temperature as shown in Equation (9-72) so that Equation (9-64) can be solved exactly without iteration.

$$T^4(z) \approx T_{sur}^3 T(z) \quad (9-72)$$

Substituting the linearized term into Equation (9-72) and rearranging results in the following linear differential equation.

$$\frac{d^2 T}{dz^2} - \frac{4}{kD} (\bar{h} + \epsilon_f \sigma T_{sur}^3) T(z) = -\frac{4}{kD} (\bar{h} T_\infty + \epsilon_f \sigma T_{sur}^4) \quad (9-73)$$

The complementary solution is found by solving the following homogeneous equation.

$$\frac{d^2T}{dz^2} - \frac{4}{kD} (\bar{h} + \varepsilon_f \sigma T_{sur}^3) T = 0 \quad (9-74)$$

Equation (9-74) can be written as

$$\frac{d^2T}{dz^2} - p^2 T = 0 \quad (9-75)$$

where

$$p = \sqrt{\frac{4}{kD} (\bar{h} + \varepsilon_f \sigma T_{sur}^3)} \quad (9-76)$$

The auxiliary equation associated with Equation (9-75) is

$$m^2 - p^2 = 0 \quad (9-77)$$

and the roots of the auxiliary equation are $m = \pm p$, so the complementary solution is

$$T_c(z) = c_5 e^{pz} + c_6 e^{-pz} \quad (9-78)$$

The particular solution can be found using the method of undetermined coefficients and is given

by

$$T_p = \frac{\bar{h} T_\infty + \varepsilon_f \sigma T_{sur}^4}{\bar{h} + \varepsilon_f \sigma T_{sur}^3} \quad (9-79)$$

The solution to Equation (9-73) is

$$T(z) = c_5 e^{pz} + c_6 e^{-pz} + T_p \quad (9-80)$$

The constants are found by applying of the boundary conditions $T(0) = T_C$ and $T(L) = T_\infty$.

$$c_5 = T_C - T_p - \frac{T_\infty - T_p + (T_p - T_C) e^{pL}}{e^{-pL} - e^{pL}} \quad (9-81)$$

$$c_6 = \frac{T_\infty - T_p + (T_p - T_C) e^{pL}}{e^{-pL} - e^{pL}} \quad (9-82)$$

Figure 9-9 and Figure 9-10 compare the temperature profiles found using Equation (9-80) to those found using Equation (9-45) for different fiber diameters. The system properties and parameters used are again those found in Table 9-1.

The results in Figure 9-9 and Figure 9-10 show that as the diameter of the fiber decreases, the linearized model becomes more accurate. The average percent error between the signals calculated from Equation (9-9) for the two cases shown in Figure 9-9 was 2% while the average error between the signals of the two cases shown in Figure 9-10 was 0.0006%. It is therefore a reasonable approximation to use Equation (9-80) in order to determine the temperature profile in the forward problem. In Figure 9-10, the temperature profile calculated with the internal fiber radiation took about 11 minutes to converge while the linearized profile is calculated from an exact, closed-form solution that was calculated in 0.01 seconds.

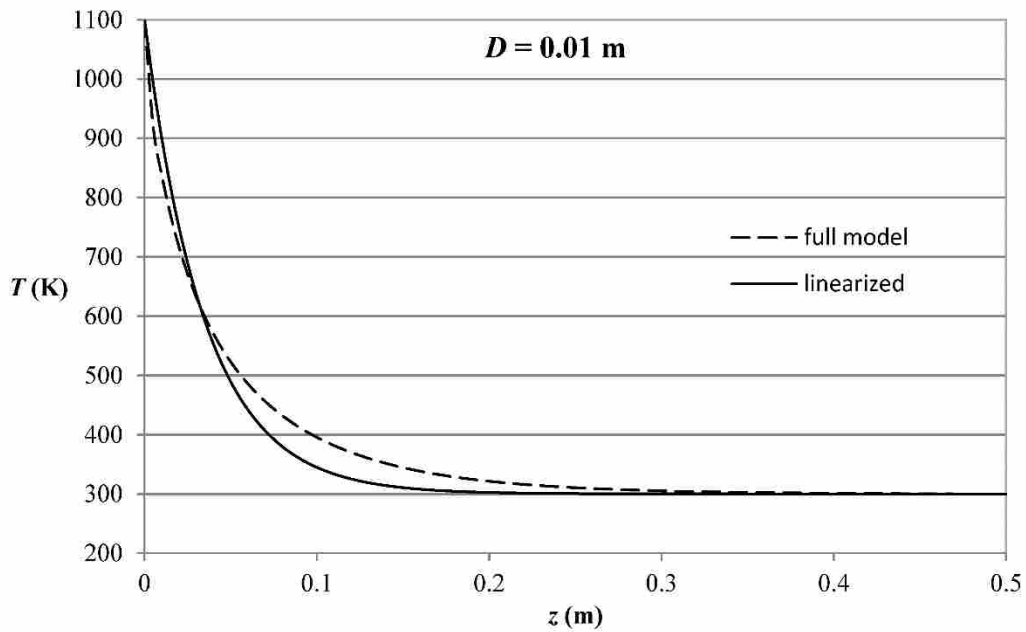


Figure 9-9: Temperature profiles in a fiber of diameter 0.01m with linearized and non-linearized models

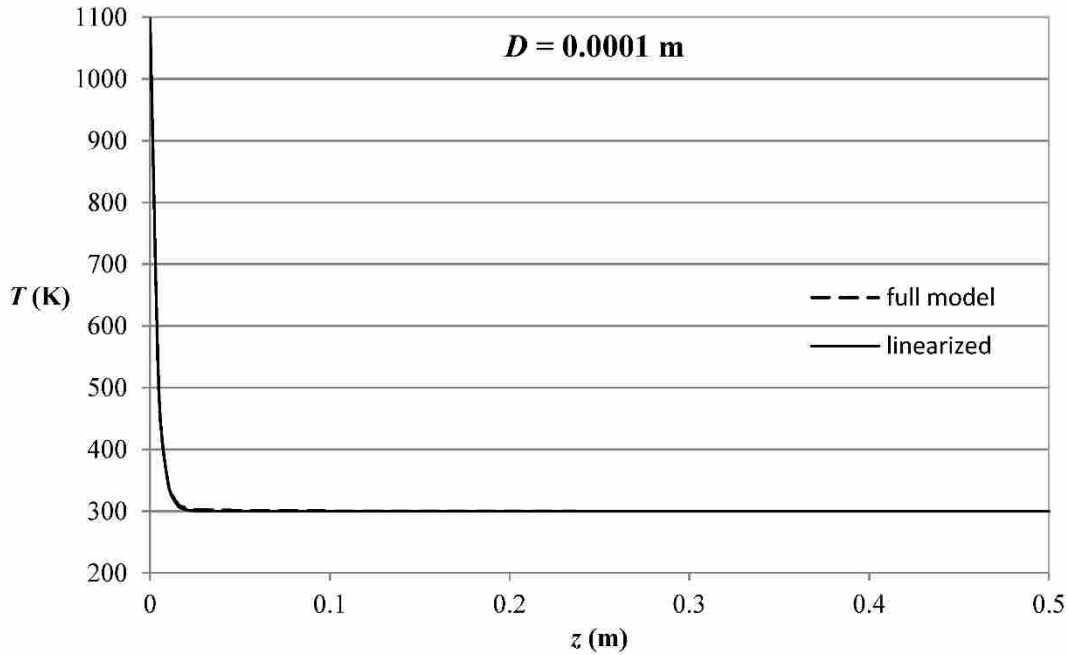


Figure 9-10: Temperature profiles in a fiber of diameter 0.0001m with linearized and non-linearized models

9.6 Summary of the Forward Problem

The forward problem is given by Equation (9-9), which provides a relation between the spectral signal from the detector and the parameters and properties of the OFT system. The forward problem requires the temperature profile along the fiber. For fibers with small diameters, a simplified model for the temperature profile is given in Equation (9-80). This model assumes a constant fiber thermal conductivity at an elevated temperature, neglects the internal radiation in the fiber, and linearizes the nonlinear external radiation term. The temperature of the heat source can be calculated from the cavity temperature and other system parameters using Equation (9-63).

9.7 Measurement Band Selection

The forward problem requires various properties and parameters of the optical fiber thermometer system in order to calculate the signal from the detector. These include the effective emittance of the cavity, the emittance of the outer surface of the cavity, the absorption coefficient, thermal conductivity, refractive index, and emittance of the fiber, as well as the convection heat transfer coefficient along the fiber. Spectral variations in the absorption coefficient can have a significant impact on the calculations of the forward problem in Equation (9-9). Therefore, a measurement band must be specified over which the spectral properties can be considered constant.

Optical fibers can be made of a number of materials, such as fluorozirconate, fluoroaluminate, and chalcogenide glasses [96]. However, they are primarily made from silicon dioxide (SiO_2), commonly known as silica. For higher temperature applications, other crystalline materials, like aluminum oxide (Al_2O_3), also known as sapphire, can be used. The spectral absorption coefficient of silica is low and relatively constant at frequencies lower than about 1.2×10^{14} Hz (above $2.5 \mu\text{m}$) and similar trends are seen for sapphire at frequencies lower than about 8.6×10^{13} Hz (above $3.5 \mu\text{m}$) [97-99]. It is important to note that, in Equation (9-9), as the spectral absorption coefficient κ_ν increases, the contribution of the radiation from the cavity to the spectral signal decreases exponentially. Therefore, in order to accurately predict the cavity temperature, it is important to make measurements over frequencies at which the absorption coefficient of the fiber is as low as possible. Numerical experiments with the forward problem show that the spectral measurements become insensitive to the cavity temperature at absorption coefficients above about $\kappa_\nu = 10 \text{ m}^{-1}$. From measurements reported in the literature, the spectral absorption coefficient of silica increases above 10 m^{-1} at about 1.15×10^{14} Hz ($2.6 \mu\text{m}$)

[99, 100]. The refractive index of silica varies from 1.43 at 1.2×10^{14} Hz ($2.5 \mu\text{m}$) to 1.5 at 1.2×10^{15} Hz ($0.25 \mu\text{m}$) [101].

A sensitivity analysis was performed to determine how sensitive the spectral signals calculated from Equation (9-9) are to changes in the system properties and parameters. A single parameter was adjusted while all other parameters were held constant. The forward problem was solved for each case and the changes in the spectral irradiation on the detector were plotted. Figure 9-11 and Figure 9-12 show the sensitivity of the spectral irradiation on the detector to changes in the cavity temperature and the convection coefficient at the heated section of the fiber, respectively. The sensitivity plots for the other parameters were similar.

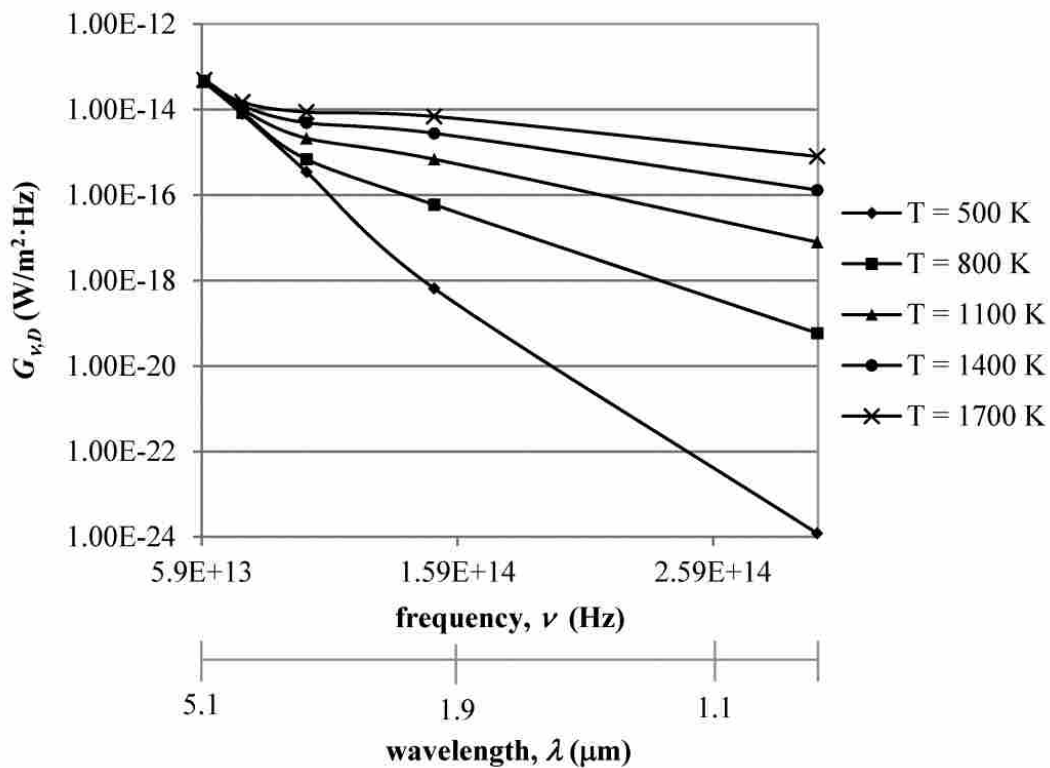


Figure 9-11: Sensitivity of spectral irradiation on detector to changes in the cavity temperature

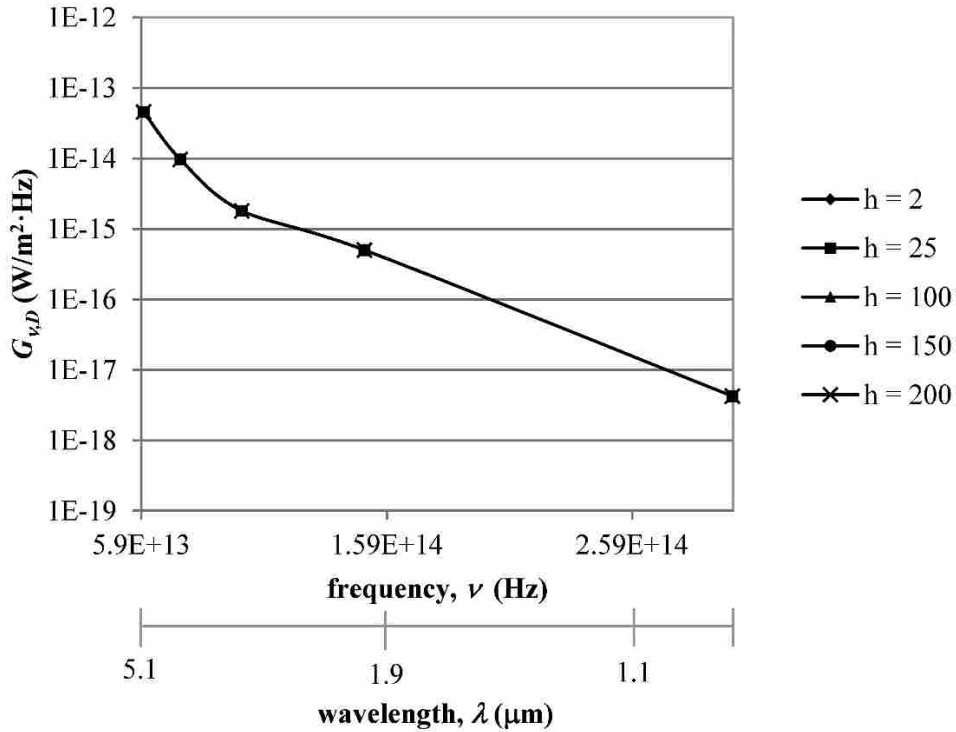


Figure 9-12: Sensitivity of spectral irradiation on the detector to changes in the convection coefficient in the heated section of the fiber

The sensitivity analysis revealed that detector measurements are highly sensitive to the cavity temperature, the absorption coefficient of the fiber, and the refractive index of the fiber and that the sensitivity is greater at higher frequencies (lower wavelengths). The measurements are largely insensitive to changes in the thermal conductivity and emittance of the fiber as well as to the convection coefficient along the fiber. Based on the spectral properties of the fiber and on the sensitivity analysis, measurements should be made in a small band anywhere between 1.0×10^{14} Hz and 3×10^{14} Hz (1 to 3 μm). The spectral range of the detector might also limit the band over which measurements can be made.

9.8 Inverse Problem

The forward problem consists of calculating the spectral signals from the detection system based on known values of the system parameters. The corresponding inverse problem entails determining these system parameters from known spectral measurements. The inverse problem is solved by using optimization methods to determine the unknown parameters of the system by minimizing the error between the experimentally measured signals and those calculated from the forward problem.

The inverse problem was solved using the Solver application in Microsoft Excel, which uses the Generalized Reduced Gradient (GRG) Algorithm as explained in Section 7.2. The forward problem was implemented in Excel as outlined in Section 9.6. The integral terms were evaluated numerically. The optimum cell was the Euclidean norm of the difference between the actual spectral measurements and those calculated from the forward problem. The adjustable cells included the cavity temperature, the average convection coefficients along the fiber, and the absorption coefficient, emittance, refractive index, and thermal conductivity of the optical fiber. The optimization algorithm minimizes the optimum cell by changing the values in the adjustable cells.

9.9 Numerical Experiments

Simulated measurements were used to assess the accuracy of the inverse solution and to address the feasibility of using inverse methods to determine OFT sensing tip temperature from experimental measurements of the spectral radiative intensity from the fiber. In order to determine the simulated measurements, the forward problem was solved over the spectral band between 1.33×10^{14} Hz and 1.5×10^{14} Hz (2 to 2.25 μm) for a theoretical OFT system for which the system properties and parameters were assumed to be known. In order to assess the

robustness of the inverse solution, various values of the system properties and parameters were used. The GRG algorithm in the Excel solver was used to minimize the error between the spectral measurements calculated from the forward problem and the simulated measurements from the theoretical OFT system. Table 9-2 shows the known parameters used in the GRG algorithm in one of the cases. The only constraint applied to the optimization algorithm was that the refractive index of the fiber be greater than one.

Table 9-2: Example of known parameters used in the GRG algorithm

D (m)	0.0002
L (m)	1
number points	100
T_{∞} (K)	300
T_{sur} (K)	300
ν_1 (Hz)	1.33×10^{14} (2.25 μm)
ν_2 (Hz)	1.36×10^{14} (2.20 μm)
ν_3 (Hz)	1.39×10^{14} (2.15 μm)
ν_4 (Hz)	1.43×10^{14} (2.10 μm)
ν_5 (Hz)	1.46×10^{14} (2.05 μm)
ν_6 (Hz)	1.50×10^{14} (2.00 μm)

The GRG algorithm requires an initial guess for each of the adjustable cells. Table 9-3 shows example results from the optimization algorithm for two sets of initial values. As demonstrated by the sensitivity analysis in Section 9.7, the inverse problem was insensitive to changes in the emittance and thermal conductivity of the fiber as well as the convection coefficient along the fiber. These parameters did not change significantly from the initial guessed values during the optimization process. Therefore, these values cannot be accurately predicted by the inverse analysis. Because the problem is ill-posed, the optimum parameter sets found from

the inverse problem are somewhat dependent upon the initial guess values of the parameters. The average error between the optimum value and the actual value for the cavity temperature was 0.05%. The average error for the absorption coefficient was 3.5% and that of the refractive index was 52%.

Table 9-3: Example of optimum unknown parameter values found from the GRG algorithm

	actual	initial 1	optimum 1	% error	initial 2	optimum 2	% error
T_c (K)	1250	1500	1250.03	0.00	800	1249.97	0.00
h (W/m ² K)	5	10	10.00	100.00	25	25.00	399.99
κ (m ⁻¹)	5	1	4.58	8.44	1	4.61	7.88
ε	0.7	0.3	0.30	57.14	1	1.00	42.86
n	1.7	1.2	3.10	82.34	2	3.00	76.47
k (W/mK)	20	5	5.00	75.01	30	29.81	49.06

In order to assess the potential impact of measurement error on the results of the inverse problem, error was introduced into the simulated measurements. Table 9-4 and Table 9-5 show typical results for cases in which 10% and 20% error were added to the measurements, respectively.

Table 9-4: Example of optimum unknown parameter values found from the GRG algorithm with 10% measurement error

	actual	initial 1	optimum 1	% error	initial 2	optimum 2	% error
T_c (K)	750	1500	749.99	0.00	500	749.98	0.00
h (W/m ² K)	5	10	10.00	100.00	1	1.00	80.00
κ (m ⁻¹)	2	5	1.94	3.09	1	1.95	2.56
ε	0.3	0.5	0.50	66.67	0.1	0.10	66.67
n	1.3	1.5	1.46	12.47	1.1	1.33	2.61
k (W/mK)	15	10	10.00	33.33	5	5.00	66.67

Table 9-5: Example of optimum unknown parameter values found from the GRG algorithm with 20% measurement error

	actual	initial 1	optimum 1	% error	initial 2	optimum 2	% error
T_c (K)	1100	1500	1098.99	0.09	800	1096.80	0.29
h (W/m ² K)	10	5	5.00	50.00	25	25.04	150.36
κ (m ⁻¹)	10	5	9.88	1.16	1	9.57	4.32
ε	0.5	0.3	0.30	40.00	0.8	0.73	45.71
n	1.5	1.2	1.09	27.58	2	3.00	99.97
k (W/mK)	8	5	5.00	37.50	20	129.46	1518.30

As would be expected, increases in the length of the fiber decreases the accuracy with which the unknown parameters can be predicted using the inverse problem. Table 9-6 compares the results of the inverse problem for two cases in which all of the parameters are the same except the fiber has a length of 1 meter in the first case and 2 meters in the second case.

Table 9-6: Comparison of optimums found with differing fiber lengths

	actual	optimum, $L = 1$ m	optimum, $L = 2$ m
T_c (K)	1100	1100.04	1104.03
h (W/m ² K)	10	5.00	5.00
κ (m ⁻¹)	10	10.00	10.01
ε	0.5	0.70	0.70
n	1.5	1.50	1.50
k (W/mK)	10	5.73	5.00

Table 9-7 shows the average error between the parameter values determined from the inverse problem and the actual parameter values for all cases run with and without measurement error.

Table 9-7: Average error between optimum values and actual values with and without measurement error

	measurement error		
	0%	10%	20%
T_C (K)	0.05	0.04	0.07
κ (m ⁻¹)	3.47	5.42	7.55
n	51.91	50.26	48.68

Based on the numerical experiments conducted above, the tip temperature of the optical fiber thermometer can be accurately inferred from spectral measurements of the radiant energy from the fiber using the inverse methods described.

9.10 Determining the Heat Source Temperature

As demonstrated in Section 9.9, the inverse analysis can accurately predict the cavity temperature of the optical fiber thermometer system. However, as shown in Section 9.4, the temperature of the cavity can differ significantly from the temperature of the heat source which is to be measured. The relationship between the cavity temperature and the heat source temperature is shown in Equation (9-63). It is dependent upon the convection heat transfer coefficient at the cavity, the surface emittance of the cavity, the effective emittance of the cavity, and the thermal conductivity of the fiber. A sensitivity analysis was performed in order to assess the effects of each of these parameters on the calculation of the heat source temperature. For a known cavity temperature of $T_C = 1050$ K, Equation (9-63) was used to calculate the heat source temperature T_H for different values of h_H , ϵ_C , ϵ_{cav} , and k . Some of the results are plotted in Figure 9-13 and Figure 9-14.

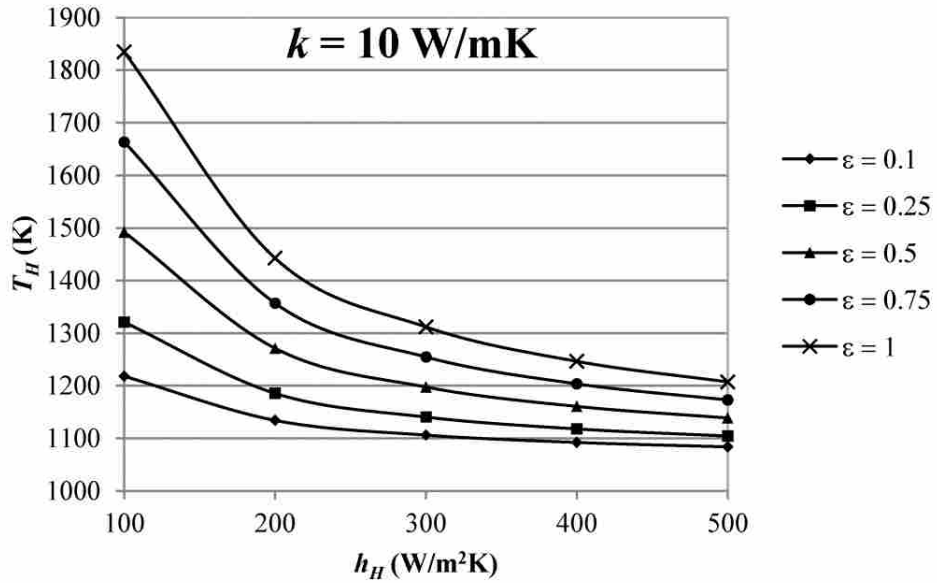


Figure 9-13: Sensitivity of the heat source temperature to changes in the convection coefficient and the surface emittance of the cavity at $k = 10 \text{ W/mK}$

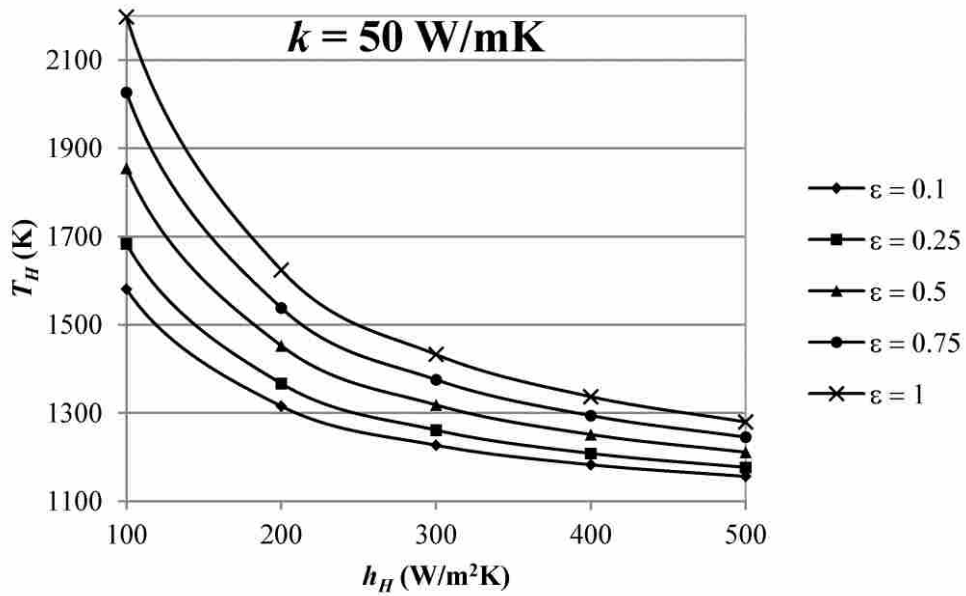


Figure 9-14: Sensitivity of the heat source temperature to changes in the convection coefficient and the surface emittance of the cavity at $k = 50 \text{ W/mK}$

The sensitivity analysis shows that the heat source temperature is highly dependent on the values of h_H , ε_{cav} , and k . The calculated heat source temperature can vary significantly (up to hundreds of degrees) based on the values of these parameters. Therefore, in order to accurately measure the temperature of the heat source, accurate estimates of these parameters must be determined. Thermal conductivity measurements as functions of temperature for silica are well documented [102]. Measurements of the emittance of the cavity surface depend on the cavity material. Lower values of the emittance of the cavity surface result in less heat lost to radiation exchange with the surroundings and smaller variations in the heat source temperature with changes in the other parameters. The convection coefficient may be evaluated from a correlation or experimentally. Changes in the effective emittance of the cavity ε_c had almost no impact on the heat source temperature.

9.11 Heated Fiber

The analysis described in Sections 9.2 through 9.8 above applies to an optical fiber thermometer system in which only the cavity which forms the sensing tip is heated. This analysis can be extended to the case in which a significant portion of the fiber is also exposed to an elevated temperature. In this case, the heated part of the fiber will provide a greater contribution to the total radiant energy exiting the fiber. In the following sections, the analysis described in the sections above will be extended to account for a heated section and an unheated section as shown in Figure 9-15. An application of this case could be inserting the OFT into a furnace or a reactor.

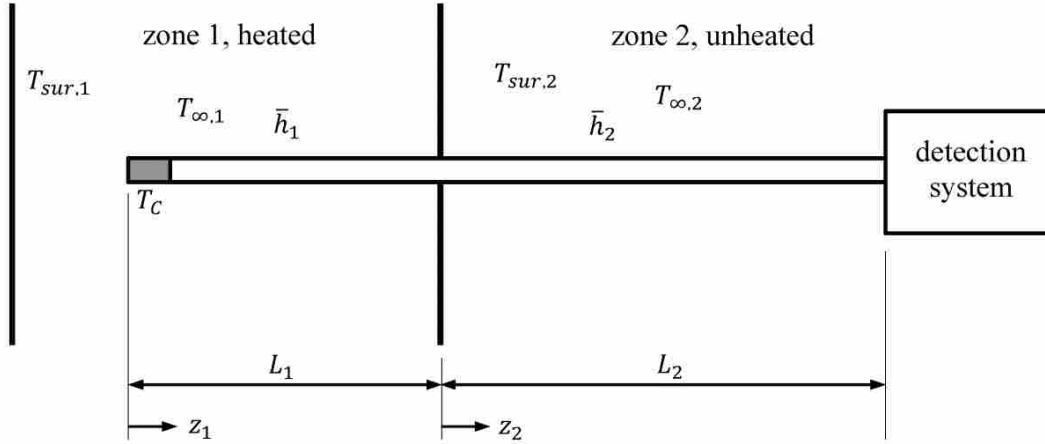


Figure 9-15: Schematic of two-zone OFT system

9.11.1 Forward Problem

The forward problem is exactly the same as that developed in Section 9.2 and is given by Equation (9-9). This equation requires knowledge of the temperature profile in the fiber. As was done in Section 9.3, an energy balance is performed on a differential volume of the fiber. In this case, however, there are two zones which have different convection and radiation exchange rates with the surroundings. An energy balance on the differential volumes in both the heated and unheated sections of the fiber gives the following differential equations that govern the temperature profiles.

$$\frac{d^2 T_1}{dz_1^2} - \frac{4}{k_1 D} (\bar{h}_1 + \epsilon_{f,1} \sigma T_{sur,1}^3) T_1(z) = -\frac{4}{k_1 D} (\bar{h}_1 T_{\infty,1} + \epsilon_{f,1} \sigma T_{sur,1}^4) \quad (9-83)$$

$$\frac{d^2 T_2}{dz_2^2} - \frac{4}{k_2 D} (\bar{h}_2 + \epsilon_{f,2} \sigma T_{sur,2}^3) T_2(z) = -\frac{4}{k_2 D} (\bar{h}_2 T_{\infty,2} + \epsilon_{f,2} \sigma T_{sur,2}^4) \quad (9-84)$$

Note that two coordinate systems are used for convenience and the same simplifications that were made in Section 9.5 were used. Solving these equations using the methods described in Section 9.5.3 results in the following expressions for the temperature profiles.

$$T_1(z_1) = c_7 e^{p_1 z_1} + c_8 e^{-p_1 z_1} + T_{p,1} \quad (9-85)$$

$$T_2(z_2) = c_9 e^{p_2 z_2} + c_{10} e^{-p_2 z_2} + T_{p,2} \quad (9-86)$$

where

$$p_1 = \sqrt{\frac{4}{k_1 D} (\bar{h}_1 + \varepsilon_{f,1} \sigma T_{sur,1}^3)} \quad (9-87)$$

$$p_2 = \sqrt{\frac{4}{k_2 D} (\bar{h}_2 + \varepsilon_{f,2} \sigma T_{sur,2}^3)} \quad (9-88)$$

$$T_{p,1} = \frac{\bar{h}_1 T_{\infty,1} + \varepsilon_{f,1} \sigma T_{sur,1}^4}{\bar{h}_1 + \varepsilon_{f,1} \sigma T_{sur,1}^3} \quad (9-89)$$

$$T_{p,2} = \frac{\bar{h}_2 T_{\infty,2} + \varepsilon_{f,2} \sigma T_{sur,2}^4}{\bar{h}_2 + \varepsilon_{f,2} \sigma T_{sur,2}^3} \quad (9-90)$$

The matching boundary conditions given below require that the temperature and the temperature gradient be the same at the point where the two sections meet.

$$T_1(L_1) = T_2(0) \quad (9-91)$$

$$\left. \frac{dT_1}{dz_1} \right|_{z_1=L_1} = \left. \frac{dT_2}{dz_2} \right|_{z_2=0} \quad (9-92)$$

The other boundary conditions are the same as those used in the previous analysis.

$$T_1(0) = T_c \quad (9-93)$$

$$T_2(L_2) = T_{\infty,2} \quad (9-94)$$

The following system of equations was found by applying the boundary conditions given in the above equations. and can be solved for the constants in Equations (9-85) and (9-86).

$$c_8 = T_C - T_{p,1} - c_7 \quad (9-95)$$

$$c_9 = (T_{\infty,2} - T_{p,2})e^{-p_2L_2} - c_{10}e^{-2p_2L_2} \quad (9-96)$$

$$c_7e^{p_1L_1} + c_8e^{-p_1L_1} + T_{p,1} = c_9 + c_{10} + T_{p,c} \quad (9-97)$$

$$c_7p_1e^{p_1L_1} - c_8p_1e^{-p_1L_1} = c_9p_2 - c_{10}p_2 \quad (9-98)$$

This set of four equations and four unknowns can be solved for the constants found in Equations (9-85) and (9-86). An example of the temperature distribution calculated from the model described above for the system parameters given in Table 9-8 is shown in Figure 9-16. Note that the temperature profile is primarily a function of the surrounding temperatures in both the heated and unheated zones. The small diameter of the fiber results in a steep temperature gradient between the heated portion and the cooler surroundings.

Table 9-8: Parameters used in example temperature distribution in two-zone system

T_C (K)	1700	h_1 (W/m ² K)	100
$T_{sur,1}$ (K)	1600	h_2 (W/m ² K)	10
$T_{\infty,2}$ (K)	300	κ (m ⁻¹)	20
$T_{sur,2}$ (K)	300	ϵ_1	0.7
L_1 (m)	0.4	ϵ_2	0.5
L_2 (m)	1.6	k_1 (W/mK)	10
D (m)	0.0004	k_2 (W/mK)	30
n	1.5		

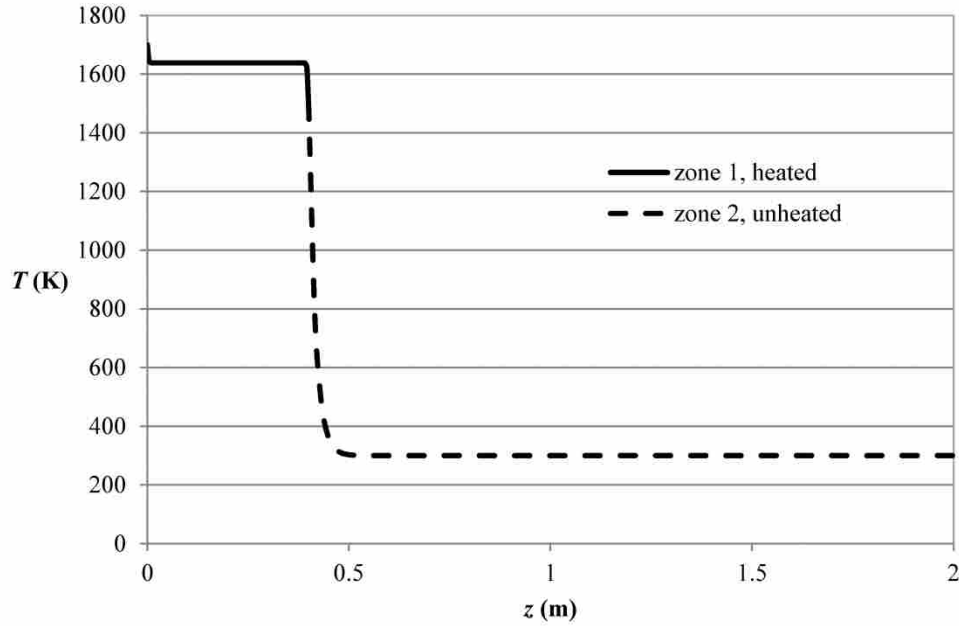


Figure 9-16: Example of a two-zone temperature distribution with parameters shown in Table 9-8

9.11.2 Inverse Problem

The inverse problem was solved using the Solver application in Microsoft Excel, which uses the Generalized Reduced Gradient (GRG) Algorithm as explained in Section 7.2. The forward problem was implemented in Excel as outlined in Section 9.11.1. The integral terms were evaluated numerically. The optimum cell was the Euclidean norm of the difference between the actual spectral measurements and those calculated from the forward problem. The adjustable cells included the cavity temperature, the convection coefficients in the heated and unheated sections of the fiber, the thermal conductivity and emittance of the fiber in the heated and unheated sections, and the absorption coefficient and the refractive index of the fiber. The optimization algorithm minimizes the optimum cell by changing the values in the adjustable cells.

9.11.3 Numerical Experiments

As was done in Section 9.9, simulated measurements were used to assess the accuracy of the inverse solution. In order to determine the simulated measurements, the forward problem was solved over the spectral band between 1.15×10^{14} Hz and 1.5×10^{14} Hz for a theoretical OFT system for which the system properties and parameters were assumed to be known. In order to assess the robustness of the inverse solution, various values of the system properties and parameters were used. The GRG algorithm in the Excel Solver was used to minimize the error between the spectral measurements calculated from the forward problem and the simulated measurements from the theoretical OFT system.

A sensitivity analysis revealed that, as was the case for the system in Section 9.7, the detector measurements are highly sensitive to the cavity temperature, the absorption coefficient of the fiber, and the refractive index of the fiber and insensitive to the other system parameters. Accordingly, the inverse problem can very accurately predict the absorption coefficient and the refractive index. Its ability to predict the cavity temperature was not as accurate as the case when only the cavity was heated. As the length of the heated portion of the fiber increases, the accuracy with which the inverse problem can predict the cavity temperature decreases. Table 9-9 shows a comparison of the optimums found for a given OFT system with different lengths of the heated portion of the fiber. The values of the other parameters correspond to those shown in Table 9-8. Because heating a significant portion of the fiber decreases the accuracy with which the sensing tip temperature is determined, it is better that only the sensing tip be exposed to the heat source to be measured. In some applications, this could require a heat shield or a cooled sheath around the fiber.

Table 9-9: Comparison of optimums found with differing lengths of the heated portion of the fiber

	actual	initial	optimum		
			$L_1 = 0.1 \text{ m}$	$L_1 = 0.3 \text{ m}$	$L_1 = 0.7 \text{ m}$
$T_c \text{ (K)}$	1700	1900.00	1717.55	1727.64	1733.95
$h_1 \text{ (W/m}^2\text{K)}$	150	100.00	99.27	98.60	97.92
$h_2 \text{ (W/m}^2\text{K)}$	10	25.00	24.93	23.74	24.31
$\kappa \text{ (m}^{-1}\text{)}$	20	10.00	19.90	19.90	19.89
ϵ_1	0.6	0.50	0.50	0.51	0.51
ϵ_2	0.4	0.50	0.50	0.53	0.49
n	1.7	1.20	1.70	1.70	1.70
$k_1 \text{ (W/mK)}$	10	20.00	20.08	20.08	20.05
$k_2 \text{ (W/mK)}$	30	20.00	19.94	20.15	19.95

As mentioned before, the cavity temperature may differ significantly from that of the heat source that is to be measured, $T_{\infty,1}$, depending on the heat transferred between the cavity and the surroundings. Therefore, accurate prediction of $T_{\infty,1}$ is dependent upon knowledge of the emittance of the cavity surface, the convection heat transfer coefficient, and the thermal conductivity of the fiber.

9.12 Conclusion

This chapter presented a rigorous mathematical model of an optical fiber thermometer system. This included a model of the temperature profile along the fiber, which accounted for conduction and radiation within the fiber as well as convection and radiation exchange with the surroundings. It was shown that as the fiber diameter decreases, a simplified model is as accurate as the full model. A forward problem was developed which relates the properties and temperature profile of the fiber to the spectral measurements of the radiant energy from the OFT made by a detection system. An inverse model was used to infer the unknown temperature and

properties of the OFT system from known spectral measurements. Numerical experiments were performed in which the OFT sensing tip temperature and properties were inferred from simulated measurements. The results of these experiments show that an inverse analysis can be used to accurately measure the temperature of an optical fiber thermometer if the fiber properties are known.

10 OPTICAL FIBER THERMOMETER: EXPERIMENTAL METHODS

This chapter outlines the preliminary experimental methods required for the development of an optical fiber thermometer system. This includes a discussion of the materials used to coat the sensing tip of the fiber and the process by which the coating is applied. A calibration procedure is outlined in which a blackbody radiator is the source and an FTIR spectrometer is used to detect the radiant energy from the OFT. The inverse problem developed in Chapter 9 was used to determine the sensing tip temperature of the OFT in the blackbody radiator and to measure the temperature of the OFT heated by a heat gun, a candle flame, and a Bunsen burner flame.

10.1 Introduction

A number of optical fiber thermometer systems have been proposed and developed [9, 66-68]. These have used a sapphire rod with a thin film of platinum or iridium sputtered on the end to form the sensing tip. Sputtering deposition is a process in which atoms are ejected from a target source material due to bombardment of the target by energetic particles onto a substrate material. In this case, the target is the platinum or iridium and the substrate is the sapphire rod. Sputtering can be expensive and the sputtering chambers are generally small and cannot accommodate long optical fibers. In addition to verifying the inverse analysis developed in Chapter 9, the primary purpose of the experiments performed in this research was to determine a

more cost effective and practical coating material and method of coating to create the sensing tip of the optical fiber thermometer.

10.2 Optical Fiber

For the purposes of this research, standard silica fibers were used to test the coating materials and processes. The fibers used were purchased from FiberTech Optica. As shown in the schematic in Figure 10-1, the optical fibers used in this research consist of three layers: 1. a 400 μm diameter pure fused silica core, 2. a 440 μm diameter fluorine doped fused silica cladding, and 3. a 470 μm diameter coating made of either polyamide which can withstand temperatures up to 385°C or Acrylate, which can withstand temperatures up to 85°C. The fused silica core has a refractive index of 1.43 over the measurement band [104]. The numerical aperture of the fiber is 0.22, which results in an acceptance cone angle of 8.8°. The fibers are classified as having low OH content.

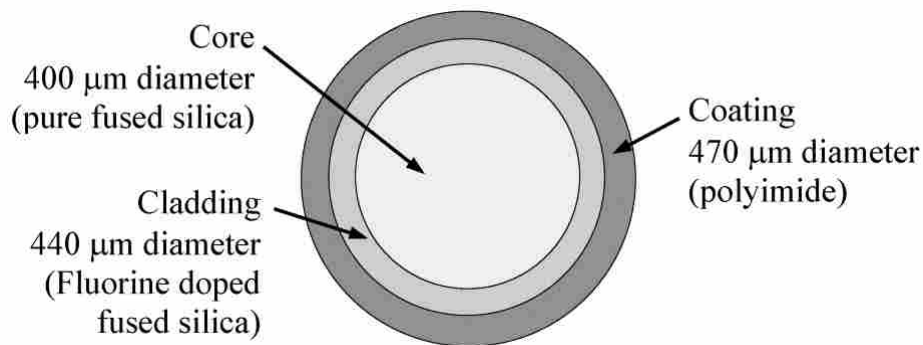


Figure 10-1: Schematic of the layers of an optical fiber

10.3 Cavity

In order for the radiation emitted by a cavity at the end of the fiber to experience total internal reflection and travel along the fiber, the cavity must be adhered to the fiber core. Therefore, the coating and the cladding must be removed from the end of the fiber before the thin coating which forms the cavity is applied. As the length of the cavity increases, the emission from the cavity approaches that of a blackbody [2]. This is independent of the emittance of the inside surface of the cavity. In order for the effective emittance of the cavity to approach unity, the length of the cavity must be at least ten times the cavity diameter [2]. The cavity wall must be thick enough to be opaque to incident radiation, but thin enough to be isothermal and to reach a steady state temperature quickly.

10.4 Coating Material

The ideal material used to form the sensing tip of an optical fiber thermometer has a high thermal conductivity, is opaque even when very thin, has a high melting temperature, is easily applied to the end of the fiber, and remains adhered to the fiber through many thermal cycles. Sauereisen Electrotemp Cement No. 8 [106] is a zircon based cement primarily used for electrical insulation where high thermal conductivities are desired. The thermal conductivity varies from 0.97 – 1.2 W/m·K. The cement cures by a chemical-set and is designed to withstand high temperatures and thermal shock. The maximum service temperature is 1426°C. It is non-corrosive and is compatible for applications with ceramics, glass, and most metals. In order to increase the opacity and the thermal conductivity of the cement, it is mixed with nickel oxide (NiO). The thermal conductivity of NiO at elevated temperatures varies from 3 – 10 W/m·K [107].

10.5 Coating Process

Sauereisen No. 8 is supplied in powder form and can be mixed with nickel oxide powder. Water is mixed with the powder mixture which causes the cement to begin to set. Trial and error experimentation was performed to determine the proper amount of Sauereisen No. 8 powder, NiO powder, and water required to create a mixture that could successfully be applied as thin coatings to the ends of optical fibers. Prior to mixing, both the Sauereisen No. 8 powder and the NiO powder are sifted through a sieve with 43.2 μm openings to prevent clumping. One gram of the Sauereisen No. 8 powder is thoroughly mixed with 0.1 grams of the nickel oxide powder in a clean mixing container. Five drops of water are added to the powder and mixing is continued until a smooth, uniform consistency is obtained. The end of the fiber is inserted horizontally into the mixture and rotated and then pulled out. This process is repeated multiple times until there is a thin, even coating on the end of the fiber. Failure of the cement to adhere to the fiber indicates that setting has begun and the cement can no longer be used.

10.6 Detection System

The optical fiber with a cavity at the sensing tip must be coupled with a detection system to measure the radiant energy from the fiber. In this work, the coated fiber was connected to a coupler/collimator by an SMA connector. The coupler/collimator collimates the radiative energy from the coated end of the fiber and directs it into an external port on an FTIR spectrometer. This optical path is shown in Figure 10-2.

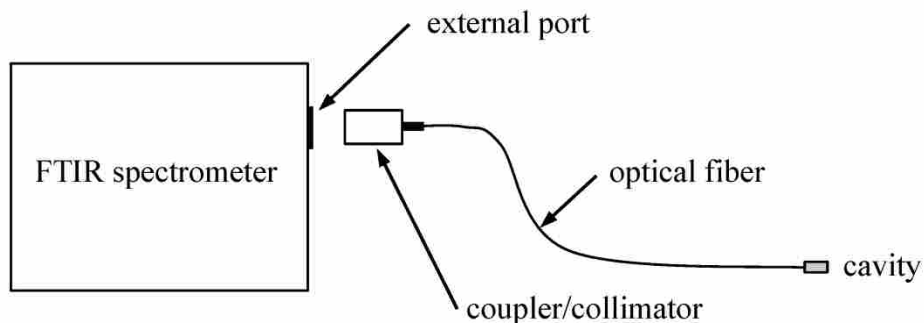


Figure 10-2: Optical path used to direct radiant energy from fiber to detection system

10.6.1 FTIR Spectrometer

In the experimental research discussed in this chapter, a Fourier transform infrared (FTIR) spectrometer was used to detect the radiative energy from the OFT system. An FTIR spectrometer is an instrument which collects the entire radiant energy from a source [103]. A schematic of the components inside an FTIR spectrometer is shown in Figure 10-3.

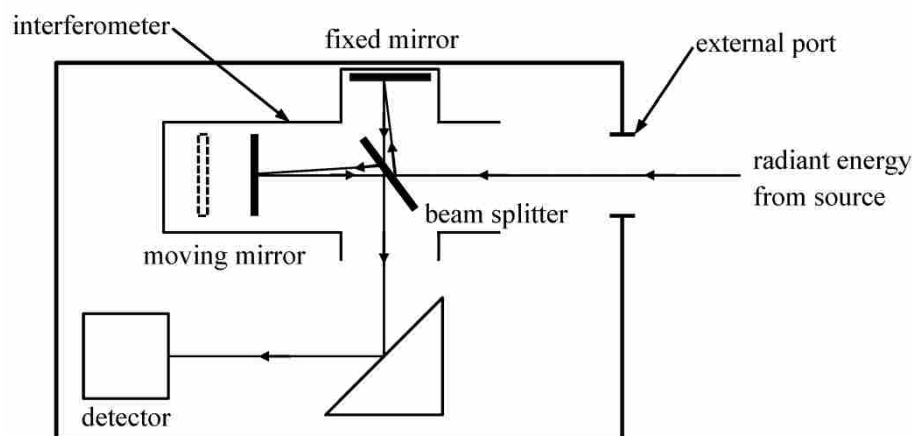


Figure 10-3: Basic components in an FTIR spectrometer

The energy from the radiation source enters the spectrometer through an external port and enters the interferometer. An interferometer consists of a beam splitter, a stationary mirror and a moving mirror. The incoming radiant energy is divided by the beam splitter. The intensity measured by the detector depends on the position of the moving mirror based on the constructive and destructive interference of the combined radiant energy returning from the mirrors [103]. The result is an interferogram, which represents the intensity of the recombined light as a function of the position of the moving mirror. The interferogram is the Fourier transform of the light intensity as a function of wavenumber. The FTIR spectrometer performs the required inverse Fourier transform calculations and provides a plot of the detector signal as a function of wavenumber. The spectral variable can be changed to frequency as required by the forward analysis in Section 9.2.

There are two detectors in the FTIR spectrometer, the MCT detector and the DTGS detector. The mercury cadmium telluride (HgCdTe), or MCT [105], detector consists of a semiconductor made from an alloy of mercury, cadmium, and telluride. Photons are absorbed by the detector element resulting in electrons being promoted from the valence band to the conduction band. Electrons in the conduction band respond to an applied voltage, resulting in an electrical current. This current is directly proportional to the number of photons hitting the detector and is, therefore, a direct measure of the radiative intensity. One major drawback of the MCT detector is that heat given off by the detector element itself is detected, resulting in a large noise signal. Therefore, the element must be cooled with liquid nitrogen. The MCT detector used in this work has a spectral range from about 2×10^{13} Hz (15 μm) to 2×10^{14} Hz (1.5 μm).

The other detector in the FTIR spectrometer is a deuterated triglycine sulfate, or DTGS [105], pyroelectric detector. Infrared radiation incident on the detector increases the detector

temperature which changes the dielectric constant of the deuterated triglycine sulfate. The change in capacitance with temperature is measured as a voltage across the detector element [108]. The DTGS detector has a greater spectral range than the MCT detector but is much less sensitive.

10.6.2 Experimental Characterization of the Detector Response

An experimental procedure was performed in order to characterize the spectral response of both the DTGS and MCT detectors. A relationship between the spectral irradiation on the detector, $G_{\nu,D}$, and the spectral signal output by the FTIR spectrometer, M_{ν} , is desired.

$$G_{\nu,D} = f(M_{\nu}) \quad (10-1)$$

A blackbody radiator was placed in front of the external access port of the FTIR spectrometer so that the blackbody radiation entered the FTIR optical path as shown in Figure 10-4. A blackbody radiator was used because its temperature can be accurately controlled and its spectral emittance is known to nominally equal unity.

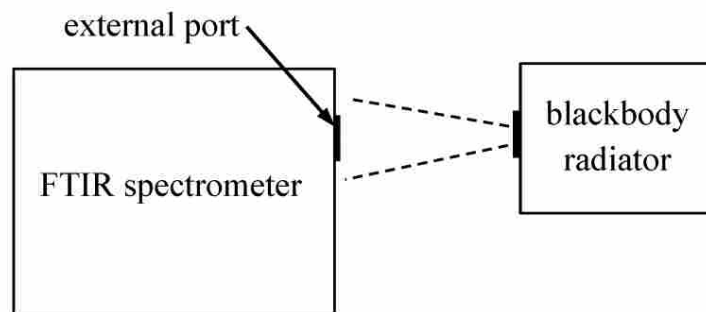


Figure 10-4: Experimental setup used to characterize the response of the FTIR detectors

The spectral irradiation on the detector is given by

$$G_{\nu,D} = P_{\nu} \int_{2\pi} I_{\nu}(T_S) \cos \theta_D d\Omega \quad (10-2)$$

where T_S is the temperature of the source, θ_D is the angle measured from the normal to the detector, and P_{ν} represents the spectral variation of the source intensity due to the optical path inside of the FTIR spectrometer. The spectral radiative intensity incident on the detector can be modeled according to the following equation.

$$I_{\nu}(T_S) = \begin{cases} I_{b,\nu}(T_B) & \text{if } \Delta\Omega = \Delta\Omega_{D \rightarrow B} \\ 0 & \text{if } \Delta\Omega \neq \Delta\Omega_{D \rightarrow B} \end{cases} \quad (10-3)$$

Equation (10-3) states that the radiative intensity incident on the detector is equal to the blackbody radiative intensity at the temperature of the blackbody radiator, T_B , over the solid angle with which the radiator is seen from the detector, $\Delta\Omega_{D \rightarrow B}$. It is assumed that outside of this solid angle, there are no other sources of radiation incident on the detector. Therefore, Equation (10-2) reduces to

$$G_{\nu,D} = P_{\nu} \int_{\Delta\Omega_{D \rightarrow B}} I_{b,\nu}(T_B) \cos \theta_D d\Omega \quad (10-4)$$

If the solid angle of the blackbody radiator seen by the detector is small, then the spectral irradiation incident on the detector can be approximated as

$$G_{\nu,D} \approx P_{\nu} I_{b,\nu}(T_B) \Delta\Omega_{D \rightarrow B} \quad (10-5)$$

Spectra were collected using both DTGS and MCT detectors over a wide range of blackbody temperatures (from 300°C to 1100°C). For a given frequency, the spectral intensity of the blackbody source, $I_{b,\nu}$, which can be calculated using the Planck function for the specified blackbody temperature, can be plotted as a function of the FTIR signal, M_{ν} . A curve fit to the

data provides a relationship between $I_{b,\nu}$ and M_ν for a given frequency. Figure 10-5 shows the data and the corresponding curves for five different frequencies for the DTGS detector.

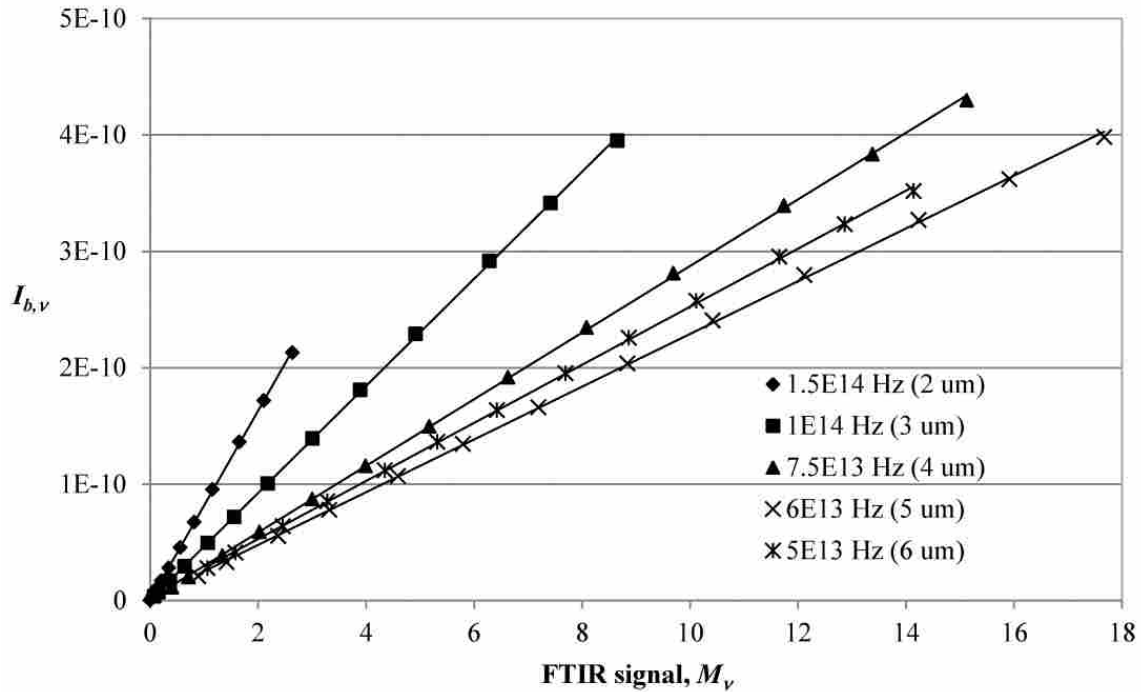


Figure 10-5: Spectral blackbody emissive power at various temperatures as a function of the FTIR signal from the DTGS detector for five different frequencies

Based on the curves fit to the data shown in Figure 10-5, the response of the DTGS detector can be approximated as linear. This is consistent with the results of experiments found in the literature [109-111]. Therefore, the relationship between the spectral irradiation on the DTGS detector, $G_{\nu,D}$, and the spectral signal output by the FTIR spectrometer, M_ν , from Equation (10-1) can be written as

$$G_{\nu,D} = C_{\nu,1}M_\nu + C_{\nu,2} \quad (10-6)$$

In the above equation, $C_{v,1}$ and $C_{v,2}$ are functions of the detector. Substituting Equation (10-5) into Equation (10-6) gives the relationship between the spectral blackbody intensity and the spectral FTIR signal,

$$I_{b,v} = \left(\frac{C_{v,1}}{P_v \Delta \Omega_{D \rightarrow B}} \right) M_v + \frac{C_{v,2}}{P_v \Delta \Omega_{D \rightarrow B}} = A_v M_v + B_v \quad (10-7)$$

where

$$A_v = \frac{C_{v,1}}{P_v \Delta \Omega_{D \rightarrow B}} \quad (10-8)$$

$$B_v = \frac{C_{v,2}}{P_v \Delta \Omega_{D \rightarrow B}} \quad (10-9)$$

In Equation (10-7), A_v is the slope of the line for a given frequency in Figure 10-5 and B_v is the offset from the origin. The offset term includes the radiation emitted by the collecting optical system and by the detector itself [109-111]. Equation (10-7) is the instrument response function for the experimental setup shown in Figure 10-4 for the DTGS detector. Calibration consists of determining A_v and B_v for each frequency. To test the instrument response function, Equation (10-7) was used to calculate the blackbody spectral intensity based on the spectral FTIR signal collected from the blackbody radiator at a temperature that was not used in the determination of A_v and B_v . Figure 10-6 shows a comparison of the spectral intensity calculated using Equation (10-7) from an FTIR signal using the DTGS detector collected from the blackbody radiator at 969°C to that calculated from the Planck function at 969°C. To illustrate the importance of the offset term in the instrument response function, Figure 10-6 also shows the spectral intensity calculated from Equation (10-7) without the B_v term. Figure 10-7 shows the spectral intensity of the blackbody source, $I_{b,v}$, as a function of the FTIR signal, M_v , using the MCT detector for four frequencies. The curves fit to the data are also shown.

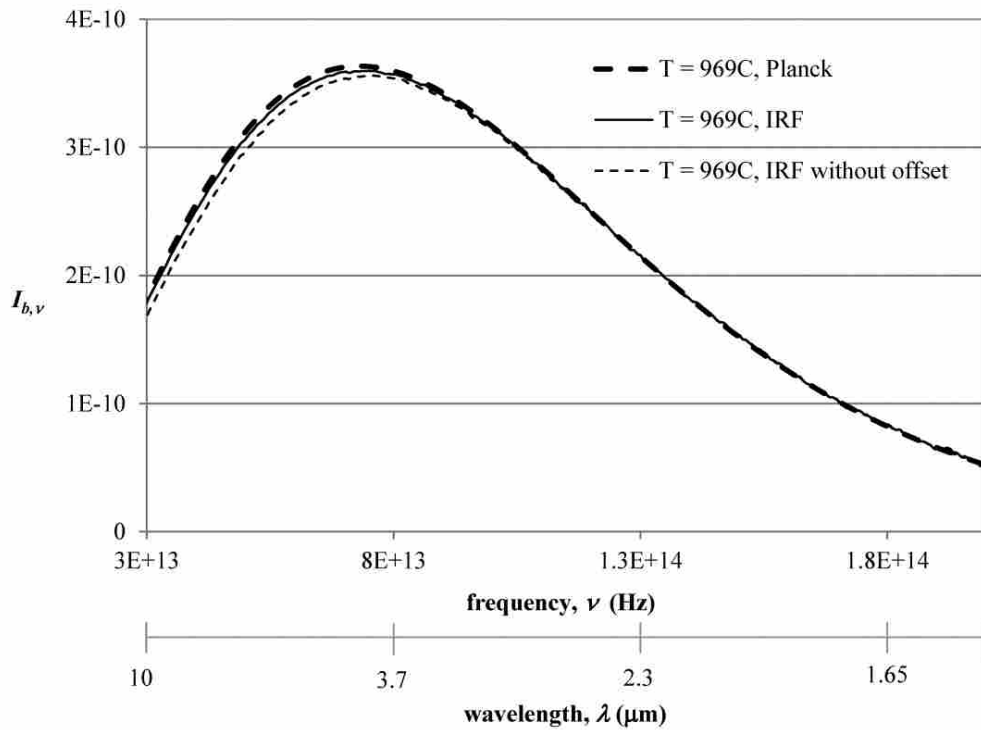


Figure 10-6: Comparison of the blackbody spectral intensity at 969°C calculated from the instrument response function of the DTGS detector to that calculated from the Planck function

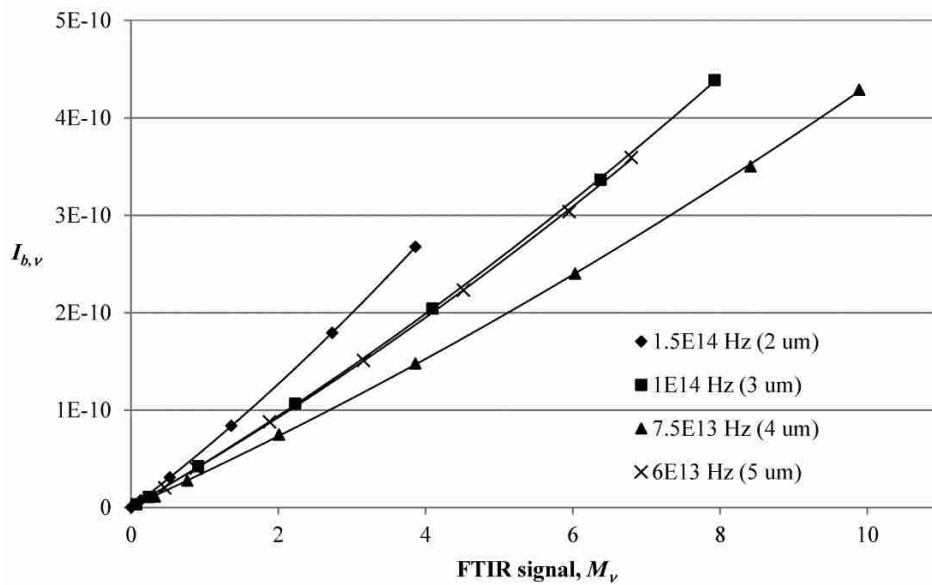


Figure 10-7: Spectral blackbody emissive power at various temperatures as a function of the FTIR signal from the MCT detector for four different frequencies

Unlike the response of the DTGS detector, the MCT detector cannot be approximated as linear [112-114]. As shown in Figure 10-7, a second order polynomial is a good fit to the data [112, 115]. Therefore, the relationship between the FTIR signal and the irradiation on the MCT detector from Equation (10-1) can be written as

$$G_{\nu,D} = C_{\nu,3}M_{\nu}^2 + C_{\nu,4}M_{\nu} + C_{\nu,5} \quad (10-10)$$

where $C_{\nu,3}$, $C_{\nu,4}$, and $C_{\nu,5}$ are functions of the detector. Substituting Equation (10-5) into Equation (10-10) gives the relationship between the spectral blackbody intensity and the spectral FTIR signal,

$$I_{b,\nu} = \left(\frac{C_{\nu,3}}{P_{\nu}\Delta\Omega_{D \rightarrow B}} \right) M_{\nu}^2 + \left(\frac{C_{\nu,4}}{P_{\nu}\Delta\Omega_{D \rightarrow B}} \right) M_{\nu} + \frac{C_{\nu,5}}{P_{\nu}\Delta\Omega_{D \rightarrow B}} = C_{\nu}M_{\nu}^2 + D_{\nu}M_{\nu} + E_{\nu} \quad (10-11)$$

where

$$C_{\nu} = \frac{C_{\nu,3}}{P_{\nu}\Delta\Omega_{D \rightarrow B}} \quad (10-12)$$

$$D_{\nu} = \frac{C_{\nu,4}}{P_{\nu}\Delta\Omega_{D \rightarrow B}} \quad (10-13)$$

$$E_{\nu} = \frac{C_{\nu,5}}{P_{\nu}\Delta\Omega_{D \rightarrow B}} \quad (10-14)$$

In Equation (10-11), C_{ν} , D_{ν} , and E_{ν} are the spectrally dependent coefficients of the second order polynomial curves in Figure 10-7 for a given frequency. Equation (10-11) is the instrument response function for the experimental setup shown in Figure 10-4 for the MCT detector. In order to assess the accuracy of the instrument response function shown in Equation (10-11), it was used to calculate the blackbody spectral intensity based on the spectral FTIR signal collected from the blackbody radiator at a temperature that was not used in the determination of C_{ν} , D_{ν} , and E_{ν} . Figure 10-8 compares the blackbody spectral intensity calculated using Equation (10-11) from the FTIR signal using the MCT detector collected from the blackbody radiator at 353°C to

that calculated from the Planck function at 353°C. Figure 10-8 also shows the blackbody spectral intensity calculated if the MCT detector response was approximated as linear.

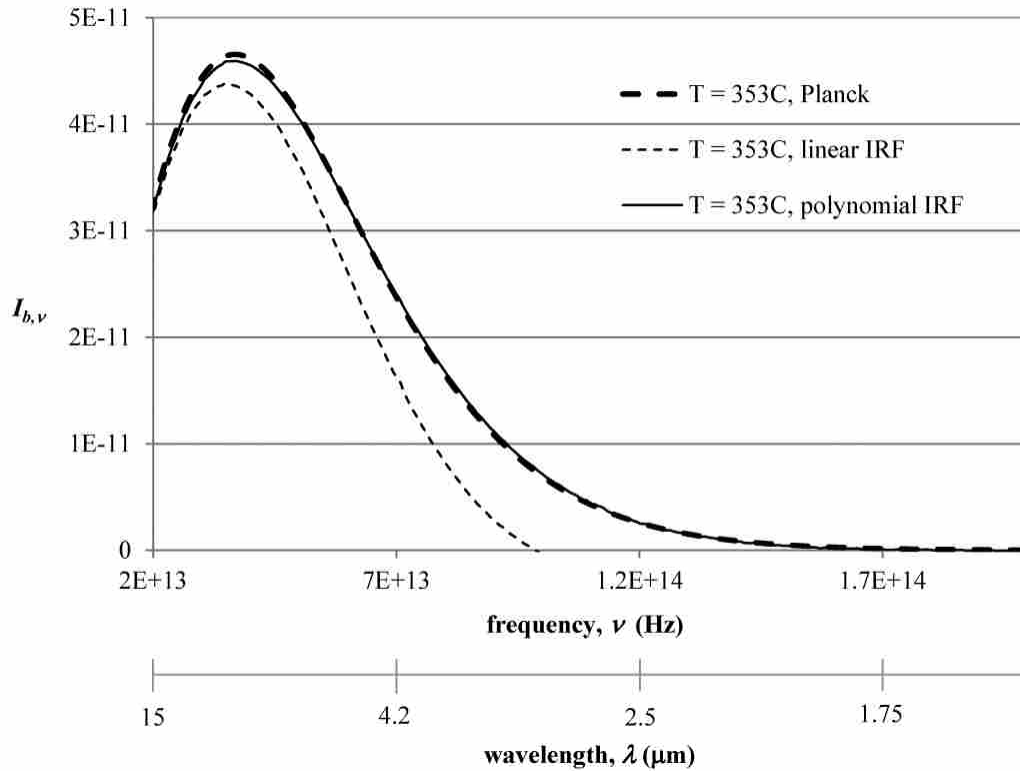


Figure 10-8: Comparison of the blackbody spectral intensity at 353°C calculated from the instrument response function of the MCT detector to that calculated from the Planck function

10.7 Verification of Cavity Formation

To determine if the coating process described in Section 10.5 above successfully formed an opaque cavity that emits like a blackbody at the end of the fiber, various tests were performed. Figure 10-9 shows a picture of the cavity taken with a microscope. Based on visual inspection, the cavity appears to fully cover the end of the fiber. The length of the cavity is at least ten times

the diameter of the fiber core as required for the effective emittance of the cavity to approach unity [2].

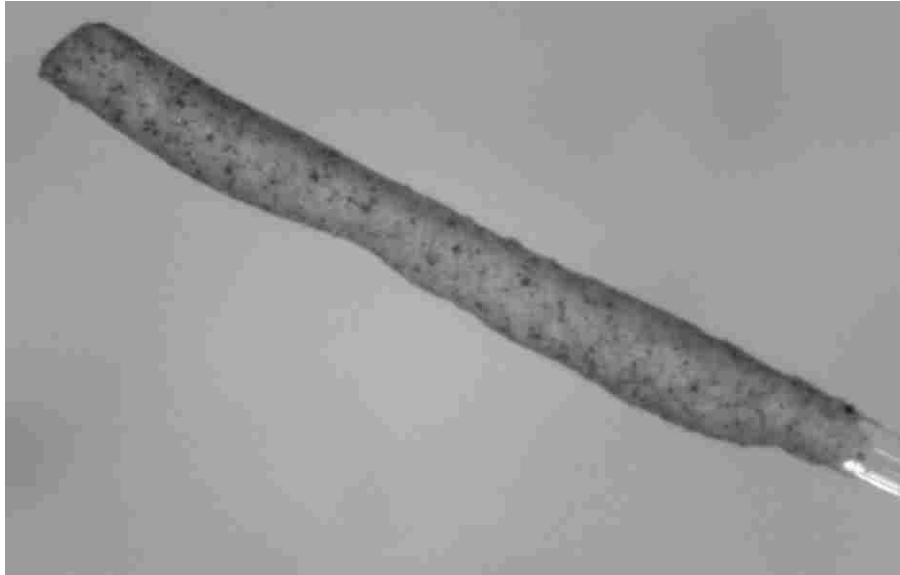


Figure 10-9: Magnified photo of the sensing tip of an optical fiber thermometer

To test if the coating is opaque to incident radiation, spectra from the FTIR spectrometer were collected when the coated end of the fiber was placed inside the cavity of a blackbody radiator and when it was placed in front of the blackbody. When inside the radiator, the temperature of the coating will increase and the OFT cavity will emit radiation down the fiber to the detector. When the cavity on the end of the fiber is placed in front of the blackbody radiator, it is irradiated by the blackbody radiation and, if the cavity is opaque, this radiation will not enter the optical fiber. In Figure 10-10, the spectral signal from the FTIR spectrometer collected when the coated end of the fiber was placed inside the cavity of a blackbody radiator at 975°C is compared to a spectrum collected when the coated end of the fiber was placed in front of the opening of the blackbody radiator at the same temperature. The low signal seen in Figure 10-10

for the case where the fiber is placed in front of the blackbody can be attributed to the heating of the cavity due to the irradiation from the radiator. When there is no cavity on the end of the fiber, the spectral signal is essentially the same when the end of the fiber is inside or in front of the blackbody radiator. The opacity of the coating to visible radiation was tested by shining a laser through the fiber. The laser could not be seen through the coating.

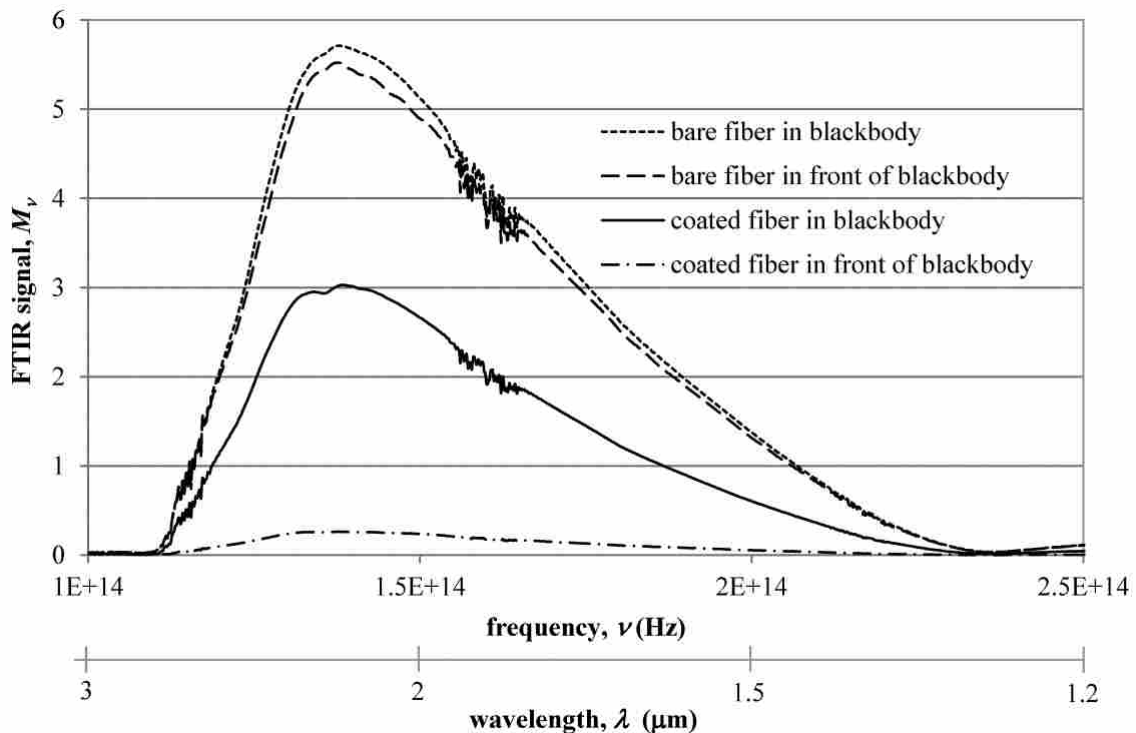


Figure 10-10: Spectral signals from coated and bare fibers inside and in front a blackbody radiator at 975°C.

10.8 OFT Calibration

The forward problem that provides the desired relationship between the cavity temperature and the spectral signal from the detection system was found in Section 9.2. It is repeated below for convenience. A calibration procedure is required to determine the instrument

response function, IRF_ν , which describes the spectral response of the detection system to the irradiation from the optical fiber thermometer system. This section describes the detection system and the method used to determine the instrument response function.

$$M_\nu = IRF_\nu \left[\int_{\mu_i}^1 \left(\epsilon_C I_{b,\nu}(T_C) e^{-\kappa_\nu L/\mu} + \frac{\kappa_\nu}{\mu} \int_0^L I_{b,\nu}(T(z')) e^{-\kappa_\nu(L-z')/\mu} dz' \right) d\mu \right] \quad (10-15)$$

10.8.1 Spectral Absorption Coefficient of the Fiber

Equation (10-15) requires knowledge of the spectral absorption coefficient of the optical fiber. An experiment was performed to measure the spectral absorption coefficient of the silica fibers used in the OFT. The experimental setup is shown in Figure 10-11. Radiative energy from a blackbody calibration source was directed into an optical fiber through a reflective collimator. The collimator consists of a 90° off-axis parabolic mirror with a protected silver coating which collects collimated radiant energy and directs it into the end of the optical fiber. The average reflectance of the mirror is greater than 96% between the wavelengths 0.45 and 20 μm. The fiber connects to the collimator by as SMA connector. The other end of the optical fiber was connected by an SMA connector to another reflective collimator, which collimated the radiation from the fiber and directed it into the external access port of the FTIR spectrometer.

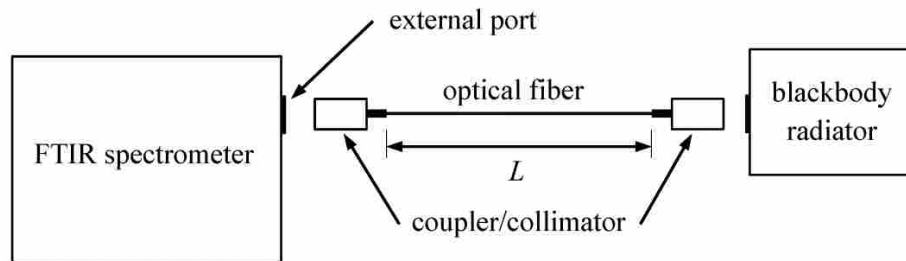


Figure 10-11: Experimental setup used to determine the spectral absorption coefficient of the silica optical fiber

Based on the detector characterization discussed in Section 10.6.2, the instrument response function for the DTGS detector is given by

$$G_{\nu,D} = C_{\nu,1}M_{\nu} + C_{\nu,2} \quad (10-16)$$

where $G_{\nu,D}$ is the spectral irradiation incident on the detector. The detector irradiation can be found from the forward analysis performed in Section 9.2. The difference here is that the boundary condition at $z = 0$ is the spectral intensity from the blackbody radiator instead of from the sensing tip cavity. Therefore, the irradiation on the detector reduces to

$$G_{\nu,D} = P_{\nu}\tau_{\nu,L} \left[\int_{\mu_i}^1 \left(I_{b,\nu}(T_B)e^{-\kappa_{\nu}L/\mu} + \frac{\kappa_{\nu}}{\mu} \int_0^L I_{b,\nu}(T(z'))e^{-\kappa_{\nu}(L-z')/\mu} dz' \right) d\mu \right] \Delta\Omega_{D-F} \quad (10-17)$$

where T_B is the temperature of the blackbody radiator and P_{ν} represents the spectral variation due to the optical path. This path includes the coupler/collimators as well as all of the components inside of the FTIR spectrometer. The entire fiber is at room temperature, T_{∞} , so Equation (10-17) can be reduced to

$$G_{\nu,D} = P_{\nu}\tau_{\nu,L} \left[\int_{\mu_i}^1 \left(I_{b,\nu}(T_B)e^{-\kappa_{\nu}L/\mu} + I_{b,\nu}(T_{\infty})(1 - e^{-\kappa_{\nu}L/\mu}) \right) d\mu \right] \Delta\Omega_{D-F} \quad (10-18)$$

Substituting Equation (10-18) into Equation (10-16) provides the following relationship between the spectral blackbody intensity $I_{b,\nu}(T_B)$ and the spectral FTIR measurements M_{ν} .

$$\int_{\mu_i}^1 \left(I_{b,\nu}(T_B)e^{-\kappa_{\nu}L/\mu} + I_{b,\nu}(T_{\infty})(1 - e^{-\kappa_{\nu}L/\mu}) \right) d\mu = X_{\nu}M_{\nu} + Y_{\nu} \quad (10-19)$$

Note that P_{ν} , $\tau_{\nu,L}$, and $\Delta\Omega_{D-F}$ have been incorporated into the instrument response function to form the new spectrally and path dependent terms X_{ν} and Y_{ν} . Equation (10-19) can be rearranged as

$$I_{b,\nu}(T_B) = \frac{X_{\nu}}{\int_{\mu_i}^1 e^{-\kappa_{\nu}L/\mu} d\mu} M_{\nu} + \frac{Y_{\nu}}{\int_{\mu_i}^1 e^{-\kappa_{\nu}L/\mu} d\mu} - \frac{I_{b,\nu}(T_{\infty})}{\int_{\mu_i}^1 e^{-\kappa_{\nu}L/\mu} d\mu} \int_{\mu_i}^1 (1 - e^{-\kappa_{\nu}L/\mu}) d\mu \quad (10-20)$$

This equation can be simplified to

$$I_{b,\nu}(T_B) = \left(\frac{X_\nu}{\int_{\mu_i}^1 e^{-\kappa_\nu L/\mu} d\mu} \right) M_\nu + Z_\nu \quad (10-21)$$

where

$$Z_\nu = \frac{Y_\nu}{\int_{\mu_i}^1 e^{-\kappa_\nu L/\mu} d\mu} - \frac{I_{b,\nu}(T_\infty)}{\int_{\mu_i}^1 e^{-\kappa_\nu L/\mu} d\mu} \int_{\mu_i}^1 (1 - e^{-\kappa_\nu L/\mu}) d\mu \quad (10-22)$$

is an offset term which varies with frequency and with the length of the fiber. The spectral absorption coefficient can be determined by taking spectral measurements through two different lengths of optical fibers at different temperatures of the blackbody radiator. For each fiber, lines are fit through the blackbody emissive power and FTIR measurement data to determine $X_\nu/\int_{\mu_i}^1 e^{-\kappa_\nu L/\mu} d\mu$ and Z_ν . At a given frequency, the ratio of the slopes of the lines for the different lengths of fibers is

$$R_\nu = \frac{\frac{X_\nu}{\int_{\mu_i}^1 e^{-\kappa_\nu L_1/\mu} d\mu}}{\frac{X_\nu}{\int_{\mu_i}^1 e^{-\kappa_\nu L_2/\mu} d\mu}} = \frac{\int_{\mu_i}^1 e^{-\kappa_\nu L_2/\mu} d\mu}{\int_{\mu_i}^1 e^{-\kappa_\nu L_1/\mu} d\mu} \quad (10-23)$$

If both fibers have the same spectral absorption coefficient, then Equation (10-23) can be solved to find the absorption coefficient. Optical fibers of lengths 0.5, 1, 1.5, and 2 meters were used in the experimental setup shown in Figure 10-11 to determine the spectral absorption coefficient of the fibers. Spectral signals were collected through each of these fibers at six blackbody temperatures ranging from 500°C to 1200°C using the DTGS detector. Each of these spectra represents an average of 32 scans taken by the FTIR spectrometer at a resolution of 32 cm^{-1} . In order to account for variability in the experiments, at each blackbody temperature each of the fibers was secured between the two reflective collimators and measurements made five

separate times. The average of these five signals at each temperature was used to create the instrument response function for each fiber length. Figure 10-12 shows the average FTIR signals collected from each of the four fibers at a blackbody radiator temperature of 1144 °C. As the fiber length increases, the signal strength decreases due to absorption within the fiber.

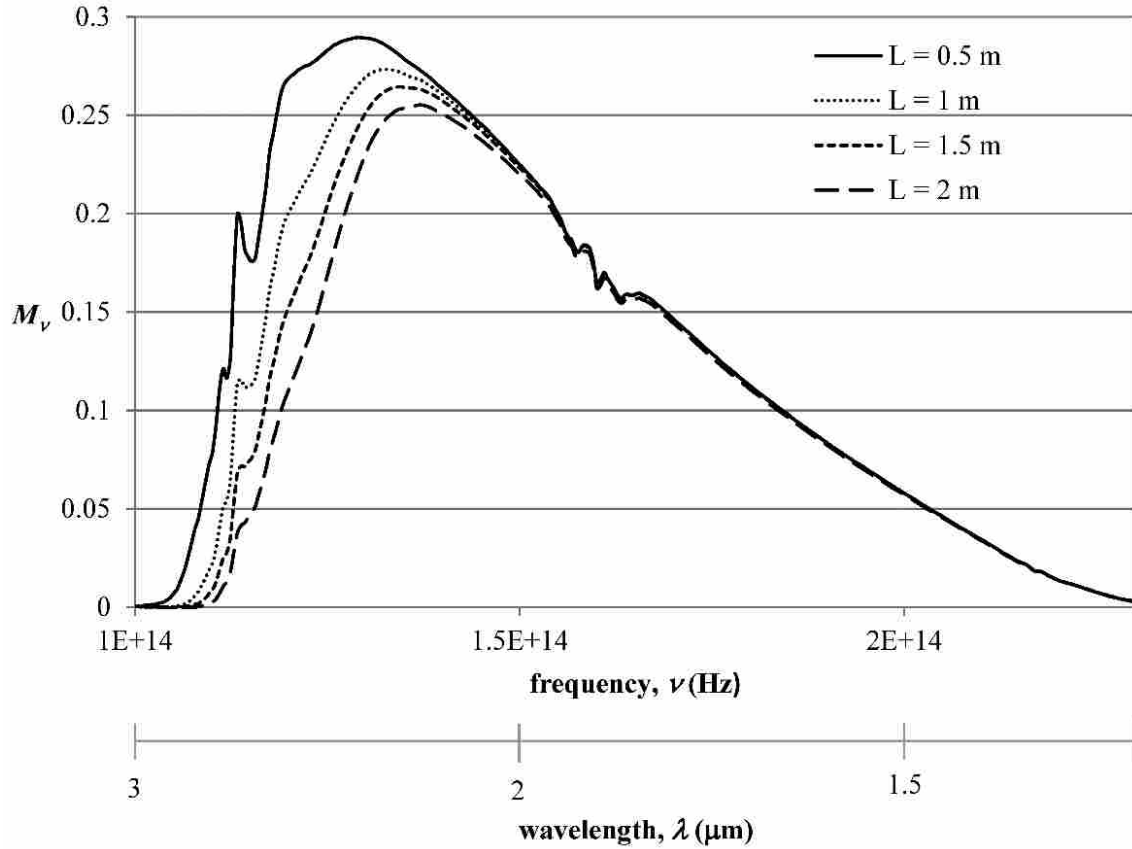


Figure 10-12: Spectral signals from blackbody radiator at 1144 °C through different fiber lengths

An instrument response function was calculated for each of the fibers by fitting linear curves to the spectral blackbody intensity as a function of the average FTIR measurement data. The Solver function in Microsoft Excel was used to find the spectral absorption coefficient of the optical fibers by minimizing the Euclidean norm of the difference between the ratio of slopes

calculated from Equation (10-23) and those found from the curve fits. The absorption coefficient was calculated using the ratios of the slopes from all combinations of the different fiber lengths. Figure 10-13 shows the average absorption coefficient of the fused silica optical fibers. Error bars indicate one standard deviation from the average. The spectral measurements were made between 1.2×10^{14} Hz (2.5 μm), which is the lower limit of the transmission range of the fibers, and 2×10^{14} Hz (1.5 μm), which is the upper limit of the detector range. Figure 10-13 also shows spectral absorption coefficient measurements of low OH fused silica made by Izawa [116, 117], which compare favorably with those made in this work. The measurements made in this work are also consistent with the measured value of 0.0018 m^{-1} at 2.83×10^{14} Hz (1.06 μm) made by Yoshida *et al* [118] and the reported value of 0.001 m^{-1} at 3×10^{14} Hz (1 μm) [119].

For reference, Figure 10-13 also shows measured values of the spectral absorption coefficient of K1 silica glass at 1400°C [99], quartz at 700°C [100], and fused quartz at 500°C [120] as reported in the literature. The absorption coefficient of the low OH fused silica fibers measured here follows the same trends as that of the quartz and fused quartz but is significantly lower. This is most likely due to the water content in the glass. Moisture present in the manufacturing process results in hydroxyl groups chemically bonded to the silica network (SiOH), which increase the transmission loss in the fibers [121]. Additionally, as shown by research performed on fused quartz, the spectral absorption coefficient of glasses increases with increasing temperature [120, 122].

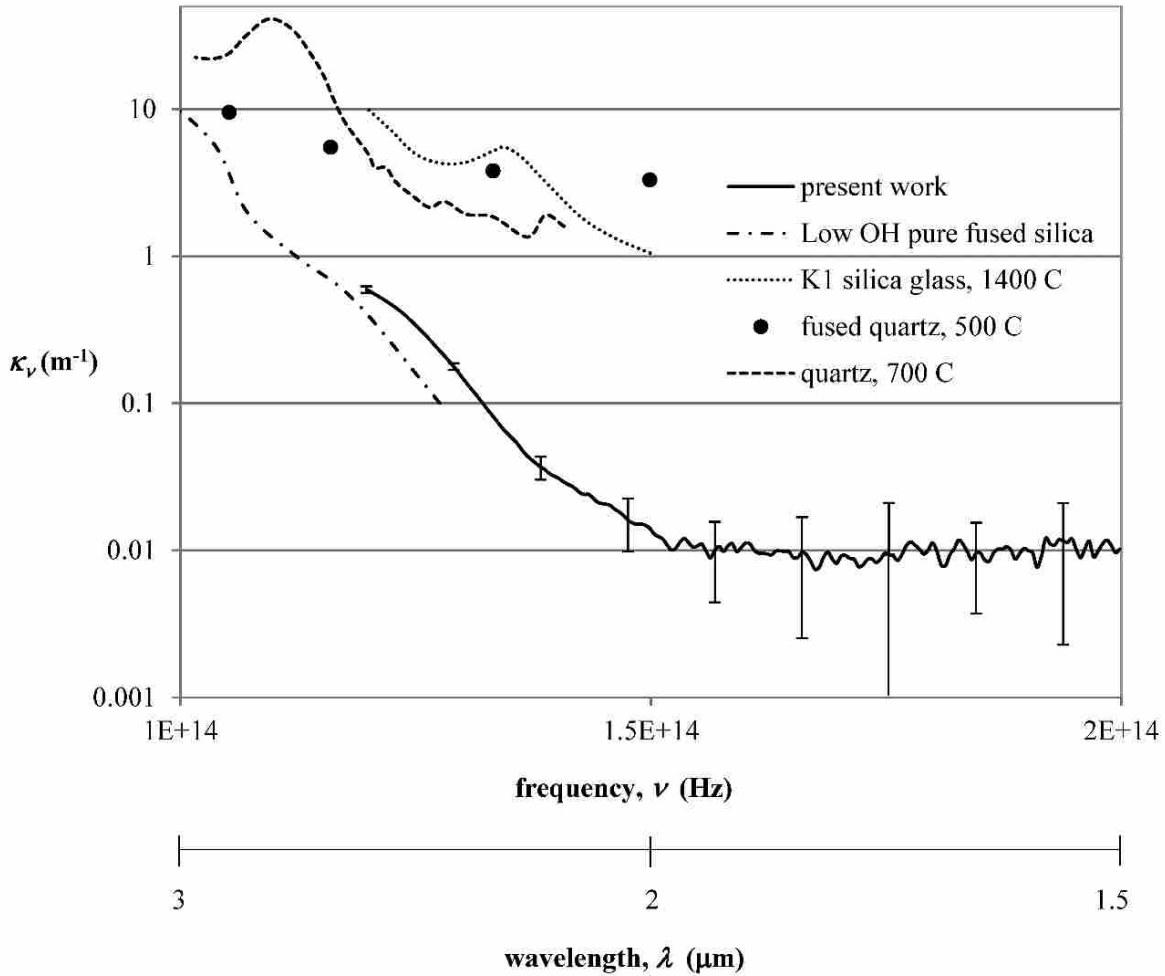


Figure 10-13: Experimental value of the spectral absorption coefficient of fused silica optical fibers compared to reported measured values of silica glass

10.8.2 Instrument Response Function for the OFT

An instrument response function similar to that given in Equation (10-11) is required to calibrate the optical fiber thermometer system. Because of the small size of the optical fiber, the radiative intensity from the optical fiber thermometer to the FTIR spectrometer detector is relatively weak. Therefore, the MCT detector was used because it is much more sensitive to

incident radiation than the DTGS detector. From Equation (9-8), the spectral irradiation on the detector is given by

$$G_{\nu,D} = P_{\nu} \tau_{\nu,L} \Delta\Omega_{D-F} \int_{\mu_i}^1 \left(\epsilon_C I_{b,\nu}(T_C) e^{-\kappa_{\nu}L/\mu} + \frac{\kappa_{\nu}}{\mu} \int_0^L I_{b,\nu}(T(z')) e^{-\kappa_{\nu}(L-z')/\mu} dz' \right) d\mu \quad (10-24)$$

From Equation (10-10), the relationship between the irradiation on the detector and the output signal is

$$G_{\nu,D} = C_{\nu,3} M_{\nu}^2 + C_{\nu,4} M_{\nu} + C_{\nu,5} \quad (10-25)$$

Substituting Equation (10-24) into Equation (10-25) and simplifying yields

$$\int_{\mu_i}^1 \left(\epsilon_C I_{b,\nu}(T_C) e^{-\kappa_{\nu}L/\mu} + \frac{\kappa_{\nu}}{\mu} \int_0^L I_{b,\nu}(T(z')) e^{-\kappa_{\nu}(L-z')/\mu} dz' \right) d\mu = Q_{\nu} M_{\nu}^2 + R_{\nu} M_{\nu} + S_{\nu} \quad (10-26)$$

where P_{ν} , $\tau_{\nu,L}$, and $\Delta\Omega_{D-F}$ have been combined with the detector spectral response coefficients, $C_{\nu,3}$, $C_{\nu,4}$, and $C_{\nu,5}$ to form the new coefficients Q_{ν} , R_{ν} , and S_{ν} . These constants can be determined for the optical fiber thermometer using the experimental setup shown in Figure 10-14.

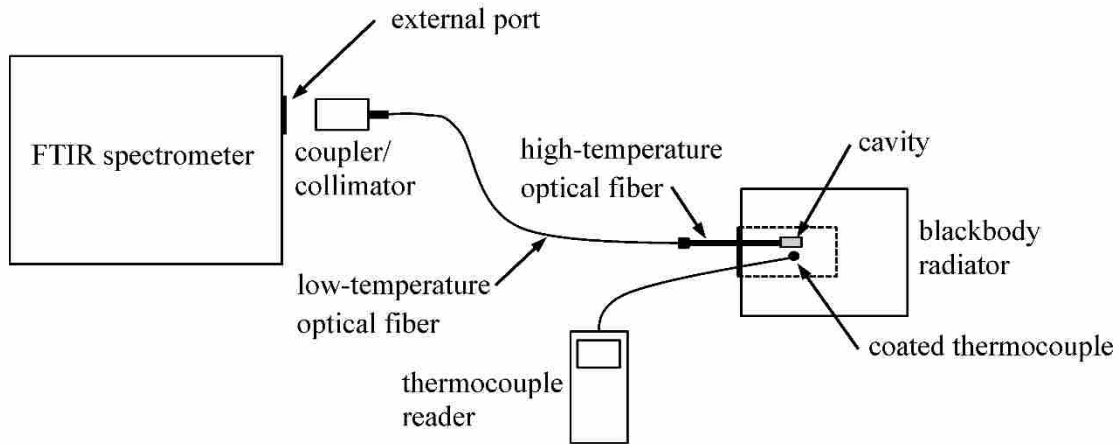


Figure 10-14: Experimental setup used to calibrate the optical fiber thermometer

The sensing tip of the OFT is placed into the cavity of a blackbody radiator. A thermocouple is also placed in the blackbody radiator close to the sensing tip of the OFT. The thermocouple is coated in the Sauereisen #8 cement so that it has the same emittance as the OFT sensing tip. The blackbody radiator is set to a wide range of temperatures and spectra are collected using the MCT detector in the FTIR spectrometer. It is assumed that the OFT sensing tip and the thermocouple are at the same temperature. The left side of Equation (10-26) can be calculated for each cavity temperature and a second-order polynomial curve can be fit to this data as a function of the FTIR measurements for each frequency. The coefficients of the polynomial are the calibration constants Q_v , R_v , and S_v in Equation (10-26).

10.8.3 Measuring Temperature using the OFT

Once the instrument response function is calculated according to the procedure described above, the inverse problem described in Section 9.8 can be used to determine the temperature of the cavity from any given spectral signal. The Solver function in Microsoft Excel is used to minimize the Euclidean norm of the difference between the measured FTIR signal and that calculated from the forward problem. From Equation (10-26), the forward problem can be solved for the spectral measurements using the quadratic equation.

$$M_v = -\frac{R_v}{2Q_v} + \frac{1}{2Q_v} \left(R_v^2 - 4Q_v \left(S_v - \int_{\mu_i}^1 \left(\varepsilon_C I_{b,v}(T_C) e^{-\kappa_v L/\mu} + \frac{\kappa_v}{\mu} \int_0^L I_{b,v}(T(z')) e^{-\kappa_v(L-z')/\mu} dz' \right) d\mu \right) \right)^{\frac{1}{2}} \quad (10-27)$$

10.9 Experiments

Experiments were performed to assess the effectiveness of the optical fiber thermometer. A high temperature optical fiber of length 1.9 meters was connected by an FC connector to a low temperature fiber of length 1 meter. The high and low temperature optical fibers differ only in

the coating material. The coating and cladding were removed from the end of the high temperature fiber and a Sauereisen #8 coating was placed on the fiber core to form the cavity according to the procedure described in Section 10.5. The end of the low-temperature fiber was connected by an SMA connector to the coupler/collimator, which directs the radiant energy from the fiber into the FTIR spectrometer.

The Sauereisen OFT sensing tip and a coated thermocouple were placed inside the cavity of the blackbody radiator as shown in Figure 10-14. In order to determine the instrument response function, the blackbody radiator was heated to five different temperatures between 300°C and 1100°C. On average, the thermocouple measured about 30°C cooler than the blackbody radiator cavity. Figure 10-15 shows an example of the spectral signals from the FTIR at different blackbody temperatures during the calibration process. A program written in Matlab was used to determine the calibration constants Q_ν , R_ν , and S_ν in Equation (10-26) according to the procedure outlined in the previous section. The Matlab code can be found in Appendix A.8.

In order to calculate the left side of Equation (10-26) in determining the calibration constants, the absorption coefficient of the fiber and the temperature profile along the fiber are required. The spectral absorption coefficient of the fiber was measured in Section 10.8.1 and a value of $\kappa_\nu = 0.01 \text{ m}^{-1}$ was used. It was assumed that the spectral absorption coefficient was constant over the measurement band. The temperature profile along the fiber was calculated from the linearized model given in Equation (9-80). This model requires values for the cavity temperature, the emittance of the fiber, the average convection coefficient along the fiber, and the thermal conductivity of the fiber. The Planck function, which requires knowledge of the refractive index of the fiber, was used to calculate the spectral intensity required in the left side of Equation (10-26). Measured values from the literature were used for the thermal conductivity

and refractive index of the silica fiber. A thermal conductivity of 2 W/m·K was assumed for the fiber [123-126]. The refractive index of the fiber was assumed to be 1.43 [104, 127-128]. The sensitivity analysis performed in Section 9.7 revealed that the values of the fiber emittance and the average convection coefficient along the optical fiber had little to no impact on the temperature profile of the fiber. A value of 0.5 was used for the fiber emittance and a typical low value for free convection of 2 W/m²·K was used for the average convection coefficient along the fiber length [12].

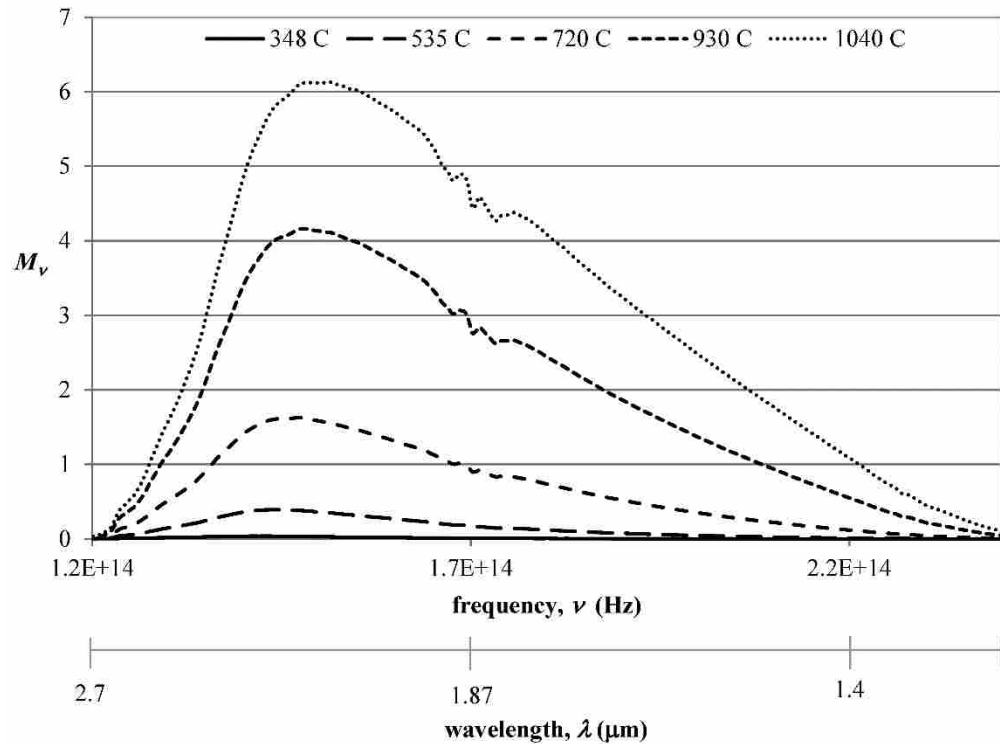


Figure 10-15: Spectral signals from the OFT at different temperatures

Spectral measurements were made at six frequencies within the measurement band specified in Section 9.7: 1.33×10^{14} Hz (2.25 μm), 1.36×10^{14} Hz (2.2 μm), 1.39×10^{14} Hz (2.15 μm), 1.43×10^{14} Hz (2.1 μm), 1.46×10^{14} Hz (2.05 μm), and 1.5×10^{14} Hz (2 μm). This

measurement band was used because the spectral properties are relatively constant and the sensitivity is high. After the spectral calibration constants Q_ν , R_ν , and S_ν were determined by fitting the calculated values of the left side of Equation (10-26) to the FTIR signal for each frequency, the OFT and coated thermocouple were placed back into the blackbody radiator and spectra were collected at various blackbody temperatures over a wide temperature range. Optimization methods were used to determine the OFT sensing tip temperature based on the measured spectral signal by solving the inverse problem outlined in Section 9.8. The Solver function in Microsoft Excel was used to minimize the difference between the spectral measurements taken by the FTIR and those calculated from Equation (10-27) by adjusting the value of the OFT sensing tip temperature, T_c . To assess the accuracy of the OFT, the temperature calculated from the inverse problem was compared to the temperature measured by the coated thermocouple. The average difference between the thermocouple temperature and the OFT temperature was 5°C. The maximum difference was 10°C.

To further test the accuracy of the optical fiber thermometer outside of the controlled environment of the blackbody cavity, both the OFT sensing tip and the coated thermocouple were heated with a heat gun and placed in a candle flame and a Bunsen burner flame. Spectra were collected from the OFT and time-dependent thermocouple measurements were recorded simultaneously. The OFT sensing tip temperature was inferred from the spectral measurements using the inverse problem and compared to the thermocouple measurements. It is difficult to compare the OFT and thermocouple measurements because of the significant variation of temperature with position in front of the heat gun and in the candle and Bunsen burner flames. Very small changes in the position of the OFT sensing tip resulted in significant changes in the FTIR signal strength, indicating large spatial temperature variations. The fact that the

thermocouple was close to, but not at, the same position as the OFT sensing tip most likely resulted in the two being at different temperatures. Furthermore, there were large variations in the temperature over time while spectra were being collected in the candle and Bunsen burner, due to the unsteady nature of the flames. This, along with the fact that the temporal response of the OFT is different than that of the thermocouple, make it difficult to compare their measured temperatures. Figure 10-16 shows some examples of the time-dependent temperature of the thermocouple temperature measurement in the candle flame. The temperatures shown in the legend are the corresponding temperatures calculated from the OFT. Figure 10-17 shows similar examples from the Bunsen burner flame. The average difference between the time-averaged thermocouple measurement and the OFT temperature measurement being heated by the heat gun was 30°C. The average temperature difference in the candle flame was 46°C and the average temperature difference in the Bunsen burner flame was 31°C.

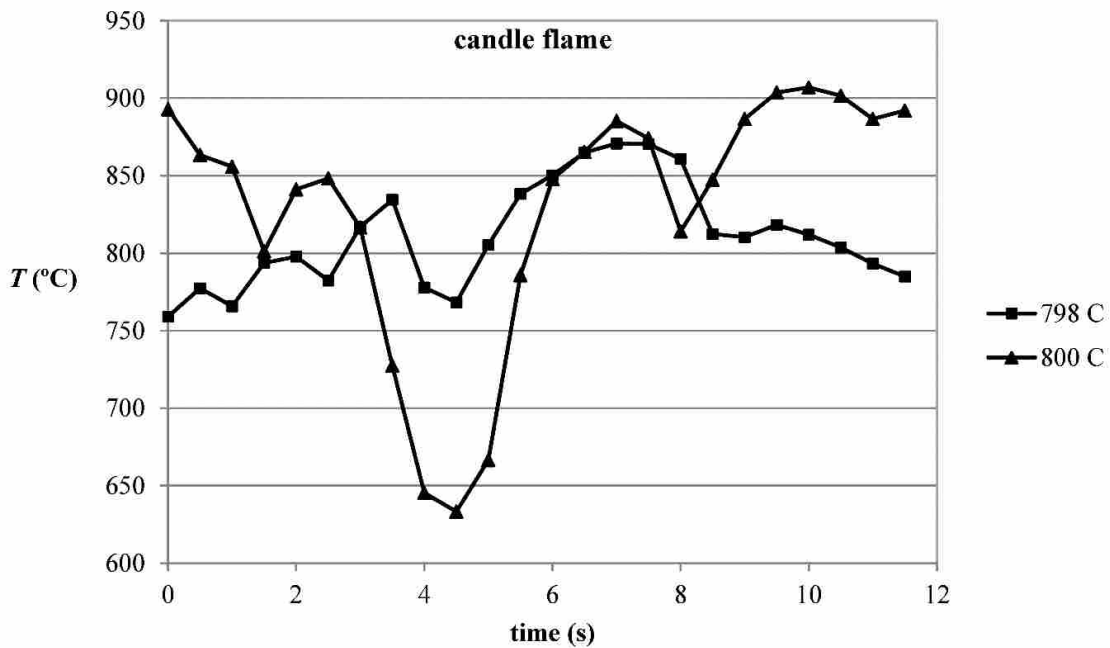


Figure 10-16: Time-dependent thermocouple measurements in candle flame

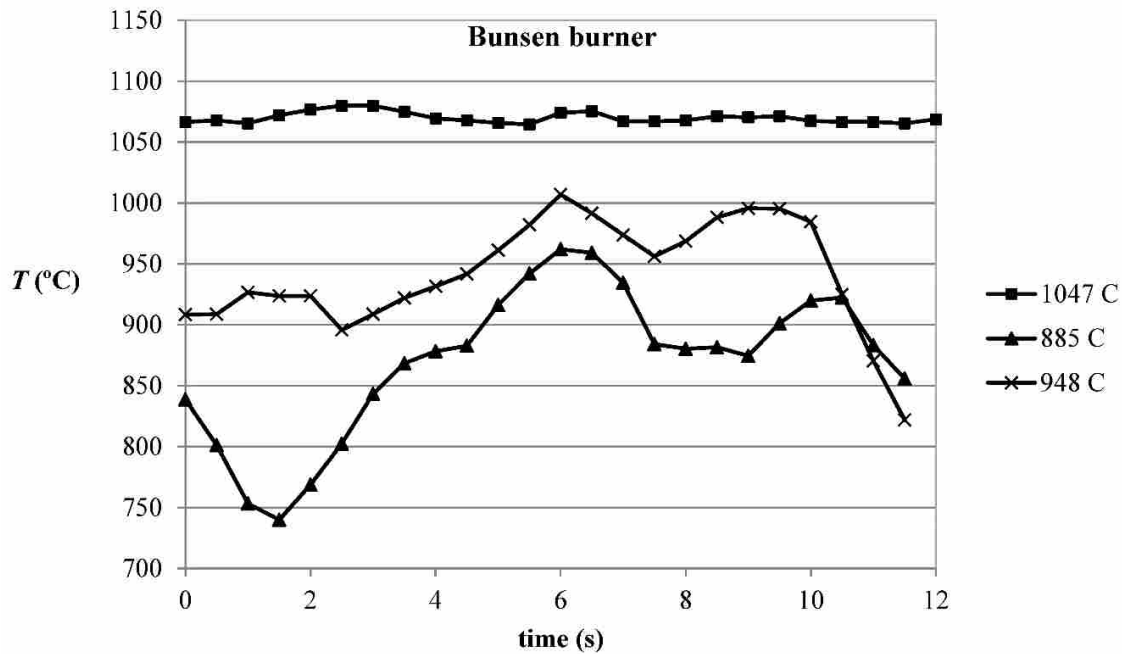


Figure 10-17: Time-dependent thermocouple measurements in Bunsen burner flame

The results of the sensitivity analysis performed in Section 9.7 were confirmed by assuming different values of the fiber emittance and the average convection coefficient along the fiber. Changes in these parameters had no impact on the results of the inverse analysis. Assuming different values for the spectral absorption coefficient of the fiber below $\kappa_v = 5 \text{ m}^{-1}$ had no effect on the OFT temperature inferred from the inverse problem. As the absorption coefficient was increased above $\kappa_v = 5 \text{ m}^{-1}$, there began to be significant error in the inferred OFT temperature. This is far out of the range of any variability in the absorption coefficient measurements made in Section 10.8.1.

10.10 Conclusion and Future Work

The purpose of the experiments described in this chapter was to demonstrate the feasibility of a relatively inexpensive optical fiber thermometer system and to test the theoretical analysis and inverse problem developed in Chapter 9. The results of the experiments have shown that an optical fiber thermometer can be made from a standard inexpensive silica optical fiber coated on the end with a high-temperature cement. This is significantly simpler and cheaper than the large diameter sapphire fibers with a sputtered metallic sensing tip that have been used in previous OFT research. The analytical model developed in Chapter 9 was verified in this chapter and the inverse analysis was successfully applied to determine the temperature OFT.

While the basic OFT concept has been proven, more research and development of the system described in this chapter is required to make a sturdy, reliable optical fiber thermometer capable of making accurate temperature measurements in various high-temperature environments. The maximum service temperature of the Sauereisen Electrotemp Cement No. 8 as a cement is 1426°C. It is not known if the Sauereisen sensing tip would remain a viable coating material for the OFT tip above this temperature. Measuring temperatures above this may require a material with a higher service temperature. The primary difficulty associated with the OFT developed in this research is the brittle nature of the core of the optical fiber. The coating must be applied directly to the core of the optical fiber in order for the radiant energy from the cavity to experience total internal reflection and be transmitted along the fiber. This requires that the fiber coating and cladding at the tip be removed before the cavity is applied. The fiber core is very brittle and becomes even more brittle and susceptible to breaking after being heated. This issue must be addressed if the OFT is to be used in a harsh environment such as that found in an oxy-coal combustion environment.

During the calibration procedure, it was assumed that the OFT sensing tip was at the same temperature as the coated thermocouple. However, this may not be an accurate assumption due to the geometry differences between the sensing tip and thermocouple that will affect the convection and radiation heat exchange with the surroundings. Therefore, a more accurate method of calibrating the OFT in which the temperature of the sensing tip is precisely controllable and more accurately known is desired. Finally, using an FTIR spectrometer as a detection device is obviously not ideal because of the high cost and large size. It was used in this research because of the large spectral band over which radiant energy can be collected. A smaller, simpler detection system which collects radiant energy only over the small measurement band would be ideal.

11 SUMMARY AND CONTRIBUTIONS

This work has described the application of the method of variation of parameters to various direct and inverse nonlinear, multimode heat transfer problems. The method of variation of parameters has not previously been used in the evaluation of nonlinear heat transfer applications. This work provides a significant contribution because the methods presented here can provide exact solutions to the overall energy equation for many applications for which only approximate solutions have previously been calculated. Additionally, the methods described in this work are generally less complex and relatively easy to implement compared to other analytical and approximate approaches.

The method of variation of parameters was used to solve the overall energy equation in order to determine the temperature profile in six nonlinear, multimode heat transfer applications: 1. a radiating annular fin, 2. convective and radiative exchange between the surface of a continuously moving strip and its surroundings, 3. convection from a fin with temperature-dependent thermal conductivity and variable cross-sectional area, 4. combined conduction and radiation in a non-gray, plane-parallel medium surrounded by non-gray opaque boundaries, 5. combined conduction and radiation in a ceramic thermal barrier coating, and 6. combined conduction and radiation in an optical fiber with convective and radiative exchange with the surroundings. The temperature profiles calculated in these applications using variation of parameters were compared to those computed using other numerical and analytical methods.

The solution to the thermal barrier coating application was used in conjunction with inverse methods to develop a non-contact technique for measuring the properties and temperatures within the thermal barrier coating from measurements of the radiative intensity exiting the coating surface. Numerical experiments were performed to assess the effectiveness of this measurement technique. The method could accurately predict the substrate temperature of the thermal barrier coating.

The solution to the optical fiber application was used with inverse methods to develop an optical fiber thermometer capable of making accurate temperature measurements in high temperature environments by measuring the radiative energy from a sensing tip that is transmitted along the fiber. Numerical experiments were conducted to assess the effectiveness of the optical fiber thermometer system. Experimental procedures were presented in which the optical fiber thermometer analysis was verified by accurately inferring the sensing tip temperature in various heat sources.

REFERENCES

1. https://www.thermalfluidscentral.org/encyclopedia/index.php/Multimode_heat_transfer_with_radiation
2. Siegel, R. and Howell, J. (2002). *Thermal Radiation Heat Transfer*, 4th ed., Taylor and Francis.
3. Mohyud-Din, S. T., Noor, M. A., and Noor, K. I. (2009). "Some Relatively New Techniques for Nonlinear Problems." *Mathematical Problems in Engineering*, 2009, Article ID 234849, 25 pages.
4. Baillis, D., and Sacadura, J. (2000). "Thermal Radiation Properties of Dispersed Media: Theoretical Prediction and Experimental Characterization." *Journal of Quantitative Spectroscopy & Radiative Transfer*, 67, 327 – 363.
5. Modest, M. F. (2003). *Radiative Heat Transfer*, 2nd ed., Academic Press.
6. Swadzba, L., Mendala, B., and Hetmanczyk, M. (2008). "Characterization of Microstructure and Properties of TBC Systems with Gradient of Chemical Composition and Porosity." *Archives of Metallurgy and Materials*, 53(3), 945 – 954.
7. Nelson, W. A., and Orenstein, R. M. (1997). "TBC Experience in Land-Based Gas Turbines." *Journal of Thermal Spray Technology*, 6(2), 176 – 180.
8. Eldridge, J. I., Allison, S. W., and Beshears, D. L. (2004). "Depth-Penetrating Temperature Measurements of Thermal Barrier Coatings Incorporating Thermographic Phosphors." *Journal of Thermal Spray Technology*, 13(1), 44 – 50.
9. Dils, R. R. (1983). "High-Temperature Optical Fiber Thermometer." *Journal of Applied Physics*, 54 (3), 1198 – 1201.
10. Tsai, B. K., Meyer, C. W., and Lovas, F. J. (2000). "Characterization of Lightpipe Radiation Thermometers for the NIST Test Bed." *8th International Conference on Advanced Thermal Processing of Semiconductors*, Gaithersburg, MD, 83 – 93.

11. Jones, M. R. and Barker, D. G. (2002). "Use of Blackbody Optical Fiber Thermometers in High Temperature Environments." *AIAA. Thermophys. Heat Transfer*, 16(3), 306 – 312.
12. Incropera, F. P., and DeWitt, D. P. (2002). *Fundamentals of Heat and Mass Transfer*, 5th ed., John Wiley & Sons.
13. Abbasbandy, S. and Shivanian, E. (2010). "Exact analytical solution of a nonlinear equation arising in heat transfer," *Physics Letters. A*, 374(4), 567 – 574.
14. Arslanturk, C. (2005). "A decomposition method for fin efficiency of convective straight fins with temperature-dependent thermal conductivity," *International Communications in Heat and Mass Transfer*, 32(6), 831 – 841.
15. Moradi, A. and Ahmadikia, H. (2010). "Analytical Solution for Different Profiles of Fin with Temperature Dependent Thermal Conductivity," *Mathematical Problems in Engineering*, 2010, Article ID 568263, 15 pages.
16. Aziz, A. and Khani, H. (2011). "Convection–radiation from a continuously moving fin of variable thermal conductivity," *Journal of the Franklin Institute*, 348(4), 640 – 651.
17. Ganji, D. D., Ganji, Z. Z., and Ganji, H. D. (2011). "Determination of temperature distribution for annular fins with temperature dependent thermal conductivity by HPM," *Thermal Science*, 15(1), S111 – S115.
18. Jones, M. R., and Solovjov, V. P. (2010). "Green's Function Approach to Nonlinear Conduction and Surface Radiation Problems," *Journal of Heat Transfer*, 132(2), 024502 (5 pages).
19. Liechty, B. C., Clark, M. M., Jones, M. R., Larson, R. S., and Woolford, B. L. (2007). "Nonlinear Thermal Model of Circular Foil Heat Flux Gauges," *Journal of Thermophysics and Heat Transfer*, 21(3), 468 – 474.
20. Viskanta, R., and Grosh, R. J. (1962). "Heat transfer by simultaneous conduction and radiation in an absorbing medium." *Journal of Heat Transfer*, 84(1), 63 – 72.
21. Viskanta, R., and Grosh, R. J. (1962). "Effect of surface emissivity on heat transfer by simultaneous conduction and radiation." *International Journal of Heat and Mass Transfer*, 5, 729 – 734.
22. Sarvari, S. M. H., Howell, J. R., and Mansouri, S. H. (2003). "Inverse boundary design conduction–radiation problem in irregular two-dimensional domains." *Numerical Heat Transfer Part B*, 44(3), 209 – 224.

23. Ruan, L. M., Xie, M., Qi, H., An, W., and Tan, H. P. (2006). “Development of a finite element model for coupled radiative and conductive heat transfer in participating media.” *Journal of Quantitative Spectroscopy and Radiative Transfer*, 102(2), 190 – 202.
24. Asllanaj, F., Milandri, A., Jeandel, G., and Roche, J. R. (2002). “A finite difference solution of non-linear systems of radiative–conductive heat transfer equations.” *International Journal for Numerical Methods in Engineering*, 54(11), 1649 – 1668.
25. Safavisohi, B., Sharbati, E., Aghanajafi, C., and Firoozabadi, R. K. (2009). “Finite difference solution for radiative–conductive heat transfer of a semitransparent polycarbonate layer.” *Journal of Applied Polymer Science*, 112(6), 3313 – 3321.
26. Patankar, S. V. (1980). *Numerical Heat Transfer and Fluid Flow*, 1st ed., Hemisphere Publishing Corp.
27. Birgelis, K., and Raitums, U. (2013). “Convergence of the finite volume method for a conductive-radiative heat transfer problem.” *Mathematical Modeling and Analysis*, 18(2), 274 – 288.
28. Mishra, S. C., and Roy, H. K. (2007). “Solving transient conduction–radiation problems using the lattice Boltzmann method and the finite volume method.” *Journal of Computational Physics*, 223(1), 89 – 107.
29. Mondal, B., and Mishra, S. C. (2007). “Application of the lattice Boltzmann method and discrete ordinate method for solving transient conduction and radiation heat transfer problems.” *Numerical Heat Transfer A*, 52(8), 757 – 775.
30. Mishra, S. C., and Lankadasu, A. (2005). “Transient conduction-radiation heat transfer in participating media using the lattice Boltzmann method and the discrete transfer method.” *Numerical Heat Transfer A*, 47(9), 935 – 954.
31. Marques, S. P. C., Barbero, E. J., and Murillo, J. S. R. (2009). “Analysis of conduction-radiation problem in absorbing and emitting nongray materials.” *International Journal of Numerical Methods for Heat and Fluid Flow*, 19(2), 165 – 181.
32. http://en.wikipedia.org/wiki/Variation_of_parameters
33. Mohyud-Din S. T, Noor, M. A., and Waheed, A. (2010). “Variation of Parameters Method for Initial and Boundary Value Problems.” *World Applied Sciences Journal*, 11(5), 622 – 639.
34. Rahmatullah and Mohyud-Din S. T. (2013). “Variation of parameters method for nonlinear diffusion equations.” *International Journal of Modern Applied Physics*, 3(1), 48 – 56.

35. Kečkić, J. (1976). "Additions to Kamkes treatise VII: Variation of parameters for nonlinear second order differential equations." *Publikacije Elektrotehničkog fakulteta. Serija Matematika i fizika*, 544, 31 – 36.
36. Noor, M. A., Mohyud-Din, S. T., and Waheed, A. (2008). "Variation of parameters method for solving fifth-order boundary value problems." *Applied Mathematics & Information Sciences*, 2(2), 135 – 141.
37. Bogdanova, M. P. (1962). "On a generalization of the method of variation of parameters." *Doklady Akademii nauk BSSR*, 6, 285 – 287.
38. Stolz, G. (1960). "Numerical solutions to an inverse problem of heat conduction for simple shapes." *ASME Journal of Heat Transfer*, 82, 20 – 26.
39. Frank, I. (1963). "An application of least squares method to the solution of the inverse problem of heat conduction." *ASME Journal of Heat Transfer*, 85C, 378 – 379.
40. Burggraf, O. R. (1964). "An exact solution of the inverse problem in heat conduction theory and application." *ASME Journal of Heat Transfer*, 86C, 373 – 382.
41. Li, H. Y., and Özişik, M. N. (1992). "Identification of temperature profile in an absorbing, emitting and isotropically scattering medium by inverse analysis." *ASME Journal of Heat Transfer*, 114, 1060 – 1063.
42. Sacadura, J. –F., and Nicolau, V. P. (1992). "Spectral radiative properties identification of semi-transparent porous media." *3rd UK National & 1st European Conference Thermal Sciences, Birmingham, UK*, 717 – 723.
43. Li, H. Y., and Özişik, M. N. (1993). "Inverse radiation problem for simultaneous estimation of temperature profile and surface reflectivity." *Journal of Thermophysics and Heat Transfer*, 7(1), 88 – 93.
44. Li, H. Y. (1999). "Estimation of thermal properties in combined conduction and radiation." *International Journal of Heat and Mass Transfer*, 42(3), 565 – 572.
45. Park, H. M., and Lee, W. J. (2000). "Solution of the inverse radiation problem using a conjugate gradient method." *International Journal of Heat and Mass Transfer*, 43(10), 1767 – 1776.
46. Verma, S. and Balaji, C. (2007). "Multi-parameter estimation in combined conduction–radiation from a plane parallel participating medium using genetic algorithms." *International Journal of Heat and Mass Transfer*, 50, 1706 – 1714.
47. Ranjan, D., Mishra, S. C., Pavan Kumar, T. B., and Uppaluri, R. (2011). "An inverse analysis for parameter estimation applied to a non-Fourier conduction–radiation problem." *Heat Transfer Engineering*, 32(6), 455 – 466.

48. Ranjan, D., Mishra, S. C., and Uppaluri, R. (2010). "Inverse analysis applied to retrieval of parameters and reconstruction of temperature field in a transient conduction–radiation heat transfer problem involving mixed boundary conditions." *International Communications in Heat and Mass Transfer*, 37, 52 – 57 (2010).
49. Franca, F. H. R., Ezekoye, O. A., and Howell, J. R. (2002). "Inverse boundary design combining radiation and convection heat transfer." *Journal of Quantitative Spectroscopy and Radiative Transfer*, 73, 41 – 54.
50. Gentleman, M., Lugh, V., Nychka, J. A., and Clarke, D. R. (2006). "Noncontact Methods for Measuring Thermal Barrier Coating Temperatures." *International Journal of Applied Ceramic Technology*, 3(2), 105 – 112.
51. Eldridge, J. I., Allison, S. W., and Beshears, D. L. (2004). "Depth-Penetrating Temperature Measurements of Thermal Barrier Coatings Incorporating Thermographic Phosphors." *Journal of Thermal Spray Technology*, 13(1), 44 – 50.
52. Allison, S. W., Beshears, D. L., Cates, M. R., Noel, B. W., and Turley, W. D. (1997). "Taking an Engine's Temperature," *Mech. Eng.*, 119(1), 72 – 74.
53. Feist J. P., and Heyes A. L. (2000). "Development of the Phosphor Thermometry Technique for Applications in Gas Turbines." 10th International Symposium on Applications of Laser Techniques to Fluid Mechanics, Lisbon, Portugal.
54. Klemens, P. G. and Gell, M. (1998). "Thermal conductivity of thermal barrier coatings." *Materials Science and Engineering A*, 245(2), 143 – 149.
55. Eldridge, J. I., Spuckler, C. M., and Markham, J. R. (2008). "Determination of Scattering and Absorption Coefficients for Plasma-Sprayed Yttria-Stabilized Zirconia Thermal Barrier." *Journal of the American Ceramic Society*, 91(5), 1603 – 1611.
56. Eldridge, J. I., Spuckler, C. M., and Markham, J. R. (2009). "Determination of Scattering and Absorption Coefficients for Plasma-Sprayed Yttria-Stabilized Zirconia Thermal Barrier Coatings at Elevated Temperatures." *Journal of the American Ceramic Society*, 92(10), 2276 – 2285.
57. Dombrovsky, L. A., Tagne, H. K., and Baillis, D. (2007). "Near-infrared Radiative Properties of Porous Zirconia Ceramics." *Infrared Physics & Technology*, 51, 44 – 53.
58. Liebert, C. H. (1978). *Emissance and Absorptance of NASA Ceramic Thermal Barrier Coating System*, National Aeronautics and Space Administration, Scientific and Technical Information Office.

59. Heyes, A. L., Feist, J. P., Chen, X., Mutasim, Z., and Nicholls, J. R. (2008). "Optical Nondestructive Condition Monitoring of Thermal Barrier Coatings." *Journal of Engineering for Gas Turbines and Power*, 130(6), 061307.
60. Feist, J. P., Sollazzo, P. Y., Berthier, S., Charnley, B., and Wells, J. (2012). "Application of an Industrial Sensor Coating System on a Rolls-Royce Jet Engine for Temperature Detection." *Journal of Engineering for Gas Turbines and Power*, 135(1), 012101.
61. Steenbakker, R. J. L., Feist, J. P., Wellman, R. G., and Nicholls, J. R. (2009). "Sensor Thermal Barrier Coatings: Remote In Situ Condition Monitoring of EB-PVD Coatings at Elevated Temperatures." *Journal of Engineering for Gas Turbines and Power*, 131(4), 041301.
62. Dombrovsky, L. A., Tagne, H. K., and Baillis, D. (2007). "Near-infrared Radiative Properties of Porous Zirconia Ceramics," *Infrared Physics & Technology*, 51, 44 – 53.
63. Liebert, C. H. (1978). Emittance and Absorptance of NASA Ceramic Thermal Barrier Coating System. National Aeronautics and Space Administration, Scientific and Technical Information Office.
64. Alaruri, S., Bianchini, L., and Brewington, A. (1998). "Effective spectral emissivity measurements of superalloys and YSZ thermal barrier coating at high temperatures using a 1.6 μm single wavelength pyrometer." *Optics and Lasers in Engineering*, 30, 77 – 91.
65. Wood, D. L., and Nassau, K. (1982). "Refractive index of cubic zirconia stabilized with yttria." *Applied Optics*, 21(16), 2978 – 2981.
66. Dakin, J. P., and Kahn, K. A. (1977). "A novel fibre-optic temperature probe." *Optical and Quantum Electronics*, 9(6), 540 – 544.
67. Cheung, W. S. (1989). "The development of an optical fibre thermometer for gas turbine engines." *Sensors and Actuators*, 19(2), 105 – 117.
68. Small, W., Celliers, P. M., Da Silva, L. B., Matthews, D. L., and Soltz, B. A. (1998). "Two-color mid-infrared thermometer with a hollow glass optical fiber." *Applied Optics*, 37(28), 6677 – 6683 (1998).
69. Tsai, B. K., Meyer, C. W., and Lovas, F. J. (2000). "Characterization of Lightpipe Radiation Thermometers for the NIST Test Bed." *8th International Conference on Advanced Thermal Processing of Semiconductors*, Gaithersburg, MD, 83 – 93.
70. Barker, D. G. (2003). *Reconstruction of the Temperature Profile along a Blackbody Optical Fiber Thermometer*, Brigham Young University.

71. Barker, D. G. and Jones, M. R. (2003). "Temperature Measurements Using a High-Temperature Blackbody Optical Fiber Thermometer," *Journal of Heat Transfer*, 125(3), 471 – 477.
72. Zill, D. G. and Cullen, M. R. (2000). *Advanced Engineering Mathematics*, 2nd ed., Jones and Bartlett Publishers, Inc.
73. Prevlite, J. P. (2013). *Essential Differential Equations*, 2nd ed., lulu.com.
74. Maple 16.00, © Maplesoft.
75. Kraus, A. D., Aziz, A., and Welty, J. R. (2002). *Extended Surface Heat Transfer*, Wiley, New York.
76. Viskanta, R., and Mengüç, M. P. (1989). "Radiative Transfer in Dispersed Media," *Applied Mechanics Reviews*, 42(9), 241 – 259.
77. Tsai, J. H. (1991). "Double spherical-harmonics approximation applied to combined conduction-radiation in a planar medium." *International Communications in Heat and Mass Transfer*, 18(5), 741 – 756.
78. Kovtanyuk, A. E., Botkin, N. D., and Hoffmann, K. H. (2012). "Numerical simulations of coupled radiative–conductive heat transfer model using a modified Monte Carlo method." *International Journal of Heat and Mass Transfer*, 55(4), 649 – 654.
79. Chai, J. C., Lee, H. S., and Patankar, S. V. (1994). "Finite volume method for radiation heat transfer." *Journal of Thermophysics and Heat Transfer*, 8(3), 419 – 425.
80. Heinemann, U., Caps, R., and Fricke, J. (1996). "Radiation – conduction interaction: an investigation on silica aerogels." *International Journal of Heat and Mass Transfer*, 39(10), 2115 – 2130.
81. Manohar, S. S., Kulkarni, A. K., and Thynell, S. T. (1995). "In-depth absorption of externally incident radiation in nongray media." *Journal of Heat Transfer*, 117(1), 146 – 151.
82. ANSYS® Academic Research, Release 14.5.0.
83. Wiebelt, J. A. (1966). *Engineering Radiation Heat Transfer*, Holt, Rinehart and Winston, Inc.
84. Talukdar, P., and Mishra, S. C. (2002). "Analysis of conduction-radiation problem in absorbing, emitting and anisotropically scattering media using the collapsed dimension method." *International Journal of Heat and Mass Transfer*, 45(10), 2159 – 2168.

85. Jones, M. R., Brewster, M. Q., and Yamada, Y. (1996). "Application of a genetic algorithm to the optical characterization of propellant smoke." *Journal of Thermophysics and Heat Transfer*, 10(2), 372 – 377.
86. Okazaki, M. (2003). "The Potential for the Improvement of High Performance Thermal Barrier Coatings." *Materials Science Research International*, 9(1), 3 – 8.
87. Nelson, W. A., and Orenstein, R. M. (1997). "TBC Experience in Land-Based Gas Turbines." *Journal of Thermal Spray Technology*, 6(2), 176 – 180.
88. Siegel, R., and Spuckler, C. M. (1998). "Analysis of Thermal Radiation Effects on Temperatures in Turbine Engine Thermal Barrier Coatings." *Materials Science and Engineering A*, 245(2), 150 – 159.
89. Lim, G., and Kar, A. (2009). "Modeling of Thermal Barrier Coating Temperature due to Transmissive Radiative Heating." *Journal of Materials Science*, 44(13), 3589 – 3599.
90. Siegel, R., and Spuckler, C. M. (1994). "Effects of Refractive Index and Diffuse or Specular Boundaries on Radiating Isothermal Layer." *Journal of Heat Transfer*, 116, 787 – 790.
91. Stuke, A., Kassner, H., Marqués, J. –L., Vassen, R., Stöver, D., and Carius, R. (2012). "Suspension and Air Plasma-Sprayed Ceramic Thermal Barrier Coatings with High Infrared Reflectance." *International Journal of Applied Ceramic Technology*, 9(3), 561 – 574.
92. Nychka, J. A., Winter, M. R., Clark, D. R., Naganuma, T., and Kagawa, Y. (2006). "Temperature-Dependent Optical Reflectivity of Tetragonal-Phase Yttria-Stabilized Zirconia." *Journal of the American Ceramic Society*, 89(3), 908 – 913.
93. Wang, D., Huang, X., and Patnaik, P. (2006). "Design and modeling of multiple layered TBC system with high reflectance." *Journal of Materials Science*, 41(19), 6245 – 6255.
94. Yu, Y. B. and Chow, W., K. (2009). "Review on an Advanced High-Temperature Measurement Technology: The Optical Fiber Thermometry." *Journal of Thermodynamics*, 2009, Article ID 823482, 11 pages, doi:10.1155/2009/823482.
95. Yuferev, V. S. (1979). "Radiation-conduction heat transfer in a thin semitransparent cylinder in the light-guide approximation," *Journal of applied mechanics and technical physics*, 20(4), 415 – 418.
96. http://en.wikipedia.org/wiki/Optical_fiber
97. Smakula, A. (1961). "Synthetic crystals and polarizing materials." *International Journal of Optics*, 36(4), 205 – 222.

98. Settarova, Z. S., Sergeev, O. A., and Nikolaeva, Z. D. (1972). "Temperature dependence of absorption coefficients of some grades of quartz glass." *High Temperature*, 10(3), 646 – 648.
99. Dvurechensky, A. V., Petrov, V. A., and Reznik, V. Yu (1979). "Spectral emissivity and absorption coefficient of silica glass at extremely high temperatures in the semitransparent region." *Infrared Physics*, 19(3-4), 465 – 469.
100. Loenen, E., and van der Tempel, L. (1996). *Determination of absorption coefficients of glasses at high temperatures, by measuring the thermal emission*. Philips Electronics N. V.
101. Malitson, I. H. (1965). "Interspecimen Comparison of the Refractive Index of Fused Silica." *Journal of the Optical Society of America*, 55(10), 1205 – 1208.
102. Bitjukov, V. K., and Petrov, V. A. (2000). "Optical quartz glass as a reference substance for the thermal conductivity coefficient for partially transparent materials." *High Temperature*, 38(2), 293 – 299.
103. Giffiths, P. R., and de Haseth, J. A. (2007). *Fourier Transform Infrared Spectrometry*, 2nd ed. John Wiley and Sons, Inc.
104. http://refractiveindex.info/legacy/?group=GLASSES&material=F_SILICA
105. Smith, B. C. (2011). *Fundamentals of Fourier Transform Infrared Spectroscopy*. Taylor and Francis Group, LLC.
106. http://www.sauereisen.com/Portals/0/product_index/8.pdf
107. Keem, J. E., and Honig, J. M. (1978). "Selected electrical and thermal properties of undoped nickel oxide." Center for Information and Numerical Data Analysis and Synthesis (CINDAS), Report 52.
108. Moore, T. J., and Jones, M. R. (2011). "An experimental method for making spectral emittance and surface temperature measurements of opaque surfaces." *Journal of Quantitative Spectroscopy and Radiative Transfer*, 112(7), 1191 – 1196.
109. González-Fernández, L., Pérez-Sáez, R. B., del Campo, L., and Tello, M. J. (2010). "Analysis of calibration methods for direct emissivity measurements." *Applied Optics*, 49(14), 2728 – 2735.
110. Dufour, P. C., Rowell, N. L., and Steele, A. G. (1998). "Fourier-transform radiation thermometry: measurements and uncertainties." *Applied Optics*, 37(25), 5923 – 59314.

111. Lindermeir, E., Haschberger, P., Tank, V., and Dietl, H. (1992). "Calibration of a Fourier transform spectrometer using three blackbody sources." *Applied Optics*, 31(22), 4527 – 4533.
112. Zhang, Z. M., Zhu, C. J., and Hanssen, L. M. (1997). "Absolute detector calibration applied to nonlinearity error correction in FT-IR measurements." *Applied Spectroscopy*, 51(4), 576 – 579.
113. Carter III, R. O., Lindsay, N. E., and Beduhn, D. (1990). "A solution to baseline uncertainty due to MCT detector nonlinearity in FT-IR." *Applied Spectroscopy*, 44(7), 1147 – 1151.
114. Shao, L., and Griffiths, P. R. (2008). "Correcting nonlinear response of mercury cadmium telluride detectors in open path Fourier transform infrared spectrometry." *Analytical Chemistry*, 80(13), 5219 – 5224.
115. Liu, Z. et al. (2008). "Study of the method of FTIR spectrum non linear multiple point calibration." *Guangpuxue yu guangpu fenxi*, 28(9), 2077 – 2080.
116. Izawa, T., Shibata, N., and Takeda, A. (1977). "Optical attenuation in pure and doped fused silica in the IR wavelength region." *Applied Physics Letters*, 31(1), 33 – 34.
117. Izawa, T., and Sudo, S. (1987). *Optical Fibers: Materials and Fabrication*. KTK Scientific Publishers, Tokyo, Japan.
118. Yoshida, S., Reitze, D. H., Tanner, D. B., and Mansell, J. D. (2003). "Method for measuring small optical absorption coefficients with use of a Shack–Hartmann wavefront detector." *Applied Optics*, 42(24), 4835 – 4840.
119. <http://www.crystran.co.uk/optical-materials/silica-glass-sio2>
120. Beder, E. C., Bass, C. D., and Shackleford, W. F. (1971). "Transmissivity and absorption of fused quartz between 0.22 μ 3.5 μ from room temperature to 1500 degrees C." *Applied Optics*, 10(10), 2263 – 2268.
121. Humbach, O., Fabian, H., Grzesik, U., Haken, U., and Heitmann, W. (1996). "Analysis of OH absorption bands in synthetic silica." *Journal of Non-Crystalline Solids*, 203, 19 – 26.
122. Prikhodk, L. V., and Bagdasarov, Kh. S. (1973). "Temperature dependence of IR absorption in fused quartz at high temperatures." *Optika i spektroskopiâ*, 34(6), 1210 – 1211.
123. Sergeev, O. A., Shashkov, A. G., and Umanskii, A. S. (1982). "Thermophysical properties of quartz glass." *Journal of Engineering Physics and Thermophysics*, 43(6), 1375 – 1383.

124. Sugawara, A. (1968). "The precise determination of thermal conductivity of pure fused quartz." *Journal of Applied Physics*, 39(13), 5994 – 5997.
125. Bitukov, V. K., and Petrov, V. A. (1999). "Optical quartz glass as a reference substance for the thermal conductivity coefficient of partially transparent materials." *High Temperature*, 38(2), 293 – 299.
126. http://en.wikipedia.org/wiki/List_of_thermal_conductivities
127. Rodney, W. S., and Spindler, R. J. (1954). "Index of refraction of fused-quartz glass for ultraviolet, visible, and infrared wavelengths." *Journal of Research of the National Bureau of Standards*, 53(3), 185 – 189.
128. Malitson, I. H. (1965). "Interspecimen comparison of the refractive index of fused silica." *Journal of the Optical Society of America*, 55(10), 1205 – 1209.

APPENDIX A. SOURCE CODE

This Appendix contains all of the MATLAB code used in this research.

A.1 Variation of Parameters Example Problem, Section 3.2

Source code file: VOP_example.m

User inputs: system parameters

Source code:

```
clear all;
format('longg');

%This program solves the differential equation solves  $y'' = y + x$ 
%using variation of parameters

%Travis J. Moore, Brigham Young University, 2013

%user inputs
x1 = 2;           %domain start
x2 = 6;           %domain end
y1 = 6;           %boundary condition at  $x = x1$ 
y2 = 1;           %boundary condition at  $x = x2$ 
N = 100;          %number of points in x vector
relax = 0.01;     %under-relaxation factor

dx = (x2-x1)/(N-1); %length of x divisions
compare = 1;      %initialize compare

%create x vector
for i = 1 : N
    x(i,1) = x1 + (i-1)*dx;
end

%initial guess is a line from (x1,y1) to (x2,y2)
y_guess = ((y2-y1)/(x2-x1))*x - ((y2-y1)/(x2-x1))*x1 + y1;

%calculate y_vector starting with y_guess
```

```

while compare > 0.0000001

    %numerical integration
    for i = 1 : N
        num_int1(i) = y_guess(i,1)*dx;
        num_int2(i) = x(i,1)*y_guess(i,1)*dx;
    end

    A = (1/(x2-x1))*(y2-y1-(1/6)*(x2^3)+(1/2)*(x1^2)*x2-(1/3)*(x1^3)-...
        x2*sum(num_int1)+sum(num_int2));
    B = y1-A*x1;

    %calculate higher order terms
    for i = 1 : N
        y_new(i,1) = A*x(i,1) + B + (1/6)*x(i,1)^3 - (x1^2)*((1/2)*x(i,1)-...
            (1/3)*x1) + x(i,1)*sum(num_int1(1:i)) - sum(num_int2(1:i));
    end

    %compare ynew and yold
    compare = norm(y_new - y_guess);
    disp(compare);

    y_guess = y_guess + relax*(y_new - y_guess);
end

y_final(:,1) = y_guess;

%Solution by traditional methods

%coefficients
A_actual = (1/(cosh(x2)-coth(x1)*sinh(x2)))*...
    (y2+x2-(y1 + x1)*sinh(x2)/sinh(x1));
B_actual = ((y1 + x1)/sinh(x1)) - A_actual*coth(x1);

for i = 1 : N
    y_actual(i,1) = A_actual*cosh(x(i,1))+B_actual*sinh(x(i,1))-x(i,1);
end

plot(x,y_actual,x,y_final);

```

A.2 Flux Gauge Problem, Section 4.1

Source code file: heat_flux_gauge.m

User inputs: system parameters

Source code:

```

clear all;
format('longg');

```

```
%This program calculates the temperature profile in a circular foil heat
%flux gauge
```

```
%Travis J. Moore, Brigham Young University, 2014
```

```
%user inputs
```

```
T0 = 5;
T1 = 1;
L = 1;
A = 0.01;
B = 100;
N = 1000;
relax = 0.1;           %under-relaxation factor
```

```
dr = L/(N-1);         %length of z divisions
compare = 10;
iterations = 0;
```

```
%create z vector
```

```
for i = 1 : N
    r(i,1) = (i-1)*dr;
end
```

```
%intital linear temperature profile guess
```

```
Tguess = T0 + ((T1-T0)/L)*r;
```

```
while compare > 0.0000001
    iterations = iterations + 1;
```

```
    %calculate T(z) from model
```

```
    num_int1(1) = 0;
    num_int2(1) = 0;
```

```
    for i = 2 : N
        num_int1(i) = (r(i,1))*(A*(Tguess(i,1)^4)-A*B)*dr;
        num_int2(i) = (r(i,1))*log(r(i,1))*(A*(Tguess(i,1)^4)-A*B)*dr;
    end
```

```
    T(1,1) = 1 + sum(num_int2);
```

```
    for i = 2 : N
        T(i,1) = 1+sum(num_int2)+log(r(i,1))*sum(num_int1(1:i))-...
            sum(num_int2(1:i));
    end
```

```
    compare = norm(T - Tguess);
    disp(compare);
```

```
    Tguess = Tguess + relax*(T - Tguess);
end
```


A.3 Continuously Moving Fin, Section 4.2

Source code file: moving_fin.m

User inputs: system parameters

Source code:

```
clear all;
format('longg');

%This program calculates the temperature profile in a moving
%convective-radiating fin

%Travis J. Moore, Brigham Young University, 2014

%user inputs
T0 = 1;
Ta = 0.2;
Lstar = 1;
Nc = 4;
Nr = 4;
Pe = 3;
N = 100;
relax = 0.01;      %under-relaxation factor

dX = Lstar/(N-1); %length of z divisions
compare = 10;
iterations = 0;

%create X vector
for i = 1 : N
    X(i,1) = (i-1)*dX;
end

%roots of auxiliary equation
m1 = (Pe+sqrt((Pe^2)+4*Nc))/2;
m2 = (Pe-sqrt((Pe^2)+4*Nc))/2;

%intital linear temperature profile guess
Tguess = T0 + 0*X;

while compare > 0.0000001
    iterations = iterations + 1;

    %numerical integration
    for i = 1 : N
        num_int1(i) = ((Nr*((Tguess(i,1))^4) - (Ta^4)) - Nc*Ta)*...
            exp(m2*X(i,1)) / ((m2-m1)*exp((m1+m2)*X(i,1)))*dX;
        num_int2(i) = ((Nr*((Tguess(i,1))^4) - (Ta^4)) - Nc*Ta)*...
            exp(m1*X(i,1)) / ((m2-m1)*exp((m1+m2)*X(i,1)))*dX;
    end
end
```

```

%calculate constants
c1 = (1/((m2*exp(m2*Lstar))-m1*exp(m1*Lstar)))*...
    ((m2*exp(m2*Lstar))-m1*exp(m1*Lstar))*...
    sum(num_int1)+m2*exp(m2*Lstar)*sum(num_int2));
c2 = 1 - c1;

for i = 1 : N
    T(i,1) = c1*exp(m1*X(i,1))+c2*exp(m2*X(i,1))-exp(m1*X(i,1))*...
        sum(num_int1(1:i))+exp(m2*X(i,1))*sum(num_int2(1:i));
end

compare = norm(T - Tguess);
disp(compare);

Tguess = Tguess + relax*(T - Tguess);
end

```

A.4 Exponential Fin with Variable Thermal Conductivity, Section 4.3

Source code file: exponential_fin.m

User inputs: system parameters

Source code:

```

clear all;
format('longg');

%This program calculates the temperature profile in an exponential
%convective fin with temperature dependent thermal conductivity

%Travis J. Moore, Brigham Young University, 2014

%user inputs
beta = 1;
N = 1;
a = 1;
M = 700;
L = 1;
relax = 0.1;                %under-relaxation factor

dx = L/(M-1);             %length of z divisions
compare = 10;
iterations = 0;

%create x vector
for i = 1 : M
    x(i,1) = (i-1)*dx;
end

%intital linear temperature profile guess

```

```

Tguess = 0.5 + 0*x;

while compare > 0.00001
    iterations = iterations + 1;

    %numerical integration
    %first point uses forward difference approximation of the derivative
    num_int1(1) = (((N*N*Tguess(1,1)-exp(a*x(1,1))*beta*(((Tguess(2,1)-...
        Tguess(1,1))/dx))^2))/(exp(a*x(1,1))*(1+beta*Tguess(1,1)))-...
        a*((Tguess(2,1)-Tguess(1,1))/dx))*dx;
    num_int2(1) = (x(1,1)*(((N*N*Tguess(1,1)-exp(a*x(1,1))*beta*...
        (((Tguess(2,1)-Tguess(1,1))/dx))^2))/(exp(a*x(1,1))*...
        (1+beta*Tguess(1,1)))-a*((Tguess(2,1)-Tguess(1,1))/dx))*dx;

    %middle points use central difference approximation of the derivative
    for i = 2 : M-1
        num_int1(i) = (((N*N*Tguess(i,1)-exp(a*x(i,1))*beta*...
            (((Tguess(i+1,1)-Tguess(i-1,1))/(2*dx))^2))/...
            (exp(a*x(i,1))*(1+beta*Tguess(i,1)))-...
            a*((Tguess(i+1,1)-Tguess(i-1,1))/(2*dx))*dx;
        num_int2(i) = (x(i,1)*(((N*N*Tguess(i,1)-exp(a*x(i,1))*beta*...
            (((Tguess(i+1,1)-Tguess(i-1,1))/(2*dx))^2))/...
            (exp(a*x(i,1))*(1+beta*Tguess(i,1)))-...
            a*((Tguess(i+1,1)-Tguess(i-1,1))/(2*dx))*dx;
    end

    %last point uses backward difference approximation of the derivative
    num_int1(M) = (((N*N*Tguess(M,1)-exp(a*x(M,1))*beta*(((Tguess(M,1)-...
        Tguess(M-1,1))/dx))^2))/(exp(a*x(M,1))*(1+beta*Tguess(M,1)))-...
        a*((Tguess(M,1)-Tguess(M-1,1))/dx))*dx;
    num_int2(M) = (x(M,1)*(((N*N*Tguess(N,1)-exp(a*x(M,1))*beta*...
        (((Tguess(M,1)-Tguess(M-1,1))/dx))^2))/(exp(a*x(M,1))*...
        (1+beta*Tguess(M,1)))-a*((Tguess(M,1)-Tguess(M-1,1))/dx))*dx;

    for i = 1 : M
        T(i,1) = 1-sum(num_int1)+sum(num_int2)+x(i,1)*...
            sum(num_int1(1:i))-sum(num_int2(1:i));
    end

    compare = norm(T - Tguess);
    disp(compare);

    Tguess = Tguess + relax*(T - Tguess);
end

```

A.5 Non-gray Medium Surrounded by Non-Gray Boundaries, Section 6.4

Source code file: radiation_conduction_parallel_plates.m

User inputs: properties of the participating medium and the boundaries

Source code:

```
clear all;
format('longg');
tic;

%This program computes the temperature profile for the combined conduction-
%radiation problem in a plane-parallel, absorbing, emitting, non-gray medium
%surrounded by non-gray boundaries

%Travis J. Moore, Brigham Young University, 2013

%INPUTS
L = 0.1;           %length of medium
k = 1;            %thermal conductivity of medium
n = 1;            %refractive index of medium
T0 = 1000;        %left boundary temperature
TL = 250;         %right boundary temperature
N = 100;          %number z points (including ends)
M = 30;           %number of mu divisions (including ends)
relax = 0.7 ;     %under-relaxation factor

%spectral properties
%the spectrum is divided into three bands with constant properties
lambda1 = 10;     %band A is lambda = 0 to lambda1
                %band B is lambda1 to lambda2
lambda2 = 20;     %band C is lambda2 to lambda = infinity
%left boundary properties
e0A = 0.5;        %emittance in band A
e0B = 0.5;        %emittance in band B
e0C = 0.5;        %emittance in band C
%right boundary properties
eLA = 0.5;        %emittance in band A
eLB = 0.5;        %emittance in band B
eLC = 0.5;        %emittance in band C
%spectral absorption coefficient
kapA = 10;        %absorption coefficient in band A (m-1)
kapB = 10;        %absorption coefficient in band B (m-1)
kapC = 10;        %absorption coefficient in band C (m-1)

%calculate other parameters
dz = L/(N-1);    %length of z divisions in section
dmu = 1/(M-1);  %length of mu divisions
%left boundary
r0A = 1-e0A;     %reflectance in band A
r0B = 1-e0B;     %reflectance in band B
r0C = 1-e0C;     %reflectance in band C
%right boundary
rLA = 1-eLA;     %reflectance in band A
rLB = 1-eLB;     %reflectance in band B
rLC = 1-eLC;     %reflectance in band C
sigma = 5.67E-8; %stefan-boltzmann constant
compare = 10;
```

```

iterations = 0;

%Preallocate arrays
z = zeros(N,1);
mu = zeros(M,1);
RA = zeros(M,1);
RB = zeros(M,1);
RC = zeros(M,1);
int_H6_1_A = zeros(N,M,N);
int_H6_1_B = zeros(N,M,N);
int_H6_1_C = zeros(N,M,N);
int_H6_2_A = zeros(N,N);
int_H6_2_B = zeros(N,N);
int_H6_2_C = zeros(N,N);
int_H12_1_A = zeros(N,M,N);
int_H12_1_B = zeros(N,M,N);
int_H12_1_C = zeros(N,M,N);
int_H12_2_A = zeros(N,N);
int_H12_2_B = zeros(N,N);
int_H12_2_C = zeros(N,N);
int_P_A = zeros(N,M);
int_Q_A = zeros(N,M);
int_P_B = zeros(N,M);
int_Q_B = zeros(N,M);
int_P_C = zeros(N,M);
int_Q_C = zeros(N,M);
int_H1_A = zeros(N,M);
int_H2_A = zeros(N,M);
int_H3_1_A = zeros(N,M);
int_H4_1_A = zeros(N,M);
int_H5_1_A = zeros(M,1);
int_H7_A = zeros(N,M);
int_H8_A = zeros(N,M);
int_H9_1_A = zeros(N,M);
int_H10_1_A = zeros(N,M);
int_H11_1_A = zeros(M,1);
int_H1_B = zeros(N,M);
int_H2_B = zeros(N,M);
int_H3_1_B = zeros(N,M);
int_H4_1_B = zeros(N,M);
int_H5_1_B = zeros(M,1);
int_H7_B = zeros(N,M);
int_H8_B = zeros(N,M);
int_H9_1_B = zeros(N,M);
int_H10_1_B = zeros(N,M);
int_H11_1_B = zeros(M,1);
int_H1_C = zeros(N,M);
int_H2_C = zeros(N,M);
int_H3_1_C = zeros(N,M);
int_H4_1_C = zeros(N,M);
int_H5_1_C = zeros(M,1);
int_H7_C = zeros(N,M);
int_H8_C = zeros(N,M);
int_H9_1_C = zeros(N,M);
int_H10_1_C = zeros(N,M);
int_H11_1_C = zeros(M,1);
int_z1_3_A = zeros(N,M);

```

```

int_z1_3_B = zeros(N,M);
int_z1_3_C = zeros(N,M);
int_z1_5and9_A = zeros(N,M);
int_z1_5and9_B = zeros(N,M);
int_z1_5and9_C = zeros(N,M);
int_z2_A = zeros(N,M);
int_z2_B = zeros(N,M);
int_z2_C = zeros(N,M);
int_H3_2_A = zeros(N,M);
int_H4_2_A = zeros(N,M);
int_H9_2_A = zeros(N,M);
int_H10_2_A = zeros(N,M);
int_H3_2_B = zeros(N,M);
int_H4_2_B = zeros(N,M);
int_H9_2_B = zeros(N,M);
int_H10_2_B = zeros(N,M);
int_H3_2_C = zeros(N,M);
int_H4_2_C = zeros(N,M);
int_H9_2_C = zeros(N,M);
int_H10_2_C = zeros(N,M);
int_H5_2_A = zeros(M,1);
int_H11_2_A = zeros(M,1);
int_H5_2_B = zeros(M,1);
int_H11_2_B = zeros(M,1);
int_H5_2_C = zeros(M,1);
int_H11_2_C = zeros(M,1);
TA = zeros(N,1);
TB = zeros(N,1);
TC = zeros(N,1);
T = zeros(N,1);

%create z vector
for i = 1 : N
    z(i,1) = (i-1)*dz;
end

%create mu vector
for j = 1 : M
    mu(j,1) = (j-1)*dmu;
end

%intital temperature profile guess (linear)
Tguess = T0 + ((TL-T0)/L)*z;

%calculate R for all values of mu
for j = 1 : M
    RA(j,1) = 1/(1-r0A*rLA*exp(-2*kapA*L/mu(j,1)));
    RB(j,1) = 1/(1-r0B*rLB*exp(-2*kapB*L/mu(j,1)));
    RC(j,1) = 1/(1-r0C*rLC*exp(-2*kapC*L/mu(j,1)));
end

%perform integrations that only depend on z and mu (not on T)
for i = 1 : N-1
    for j = 2 : M %start at 2 because the integral will be 0 when mu is 0
        int_P_A(i,j) = RA(j,1)*((z(i,1)/L)*(exp(-kapA*L/mu(j,1))-1)+(1-...
            exp(-kapA*z(i,1)/mu(j,1))))*mu(j,1)*dmu;
    end
end

```

```

int_Q_A(i,j) = RA(j,1)*((z(i,1)/L)*(1-exp(-kapA*L/mu(j,1)))+...
    exp(-kapA*L/mu(j,1))-exp(-kapA*(L-z(i,1))/mu(j,1)))*mu(j,1)*dmu;

int_P_B(i,j) = RB(j,1)*((z(i,1)/L)*(exp(-kapB*L/mu(j,1))-1)+(1-...
    exp(-kapB*z(i,1)/mu(j,1))))*mu(j,1)*dmu;
int_Q_B(i,j) = RB(j,1)*((z(i,1)/L)*(1-exp(-kapB*L/mu(j,1)))+...
    exp(-kapB*L/mu(j,1))-exp(-kapB*(L-z(i,1))/mu(j,1)))*mu(j,1)*dmu;

int_P_C(i,j) = RC(j,1)*((z(i,1)/L)*(exp(-kapC*L/mu(j,1))-1)+(1-...
    exp(-kapC*z(i,1)/mu(j,1))))*mu(j,1)*dmu;
int_Q_C(i,j) = RC(j,1)*((z(i,1)/L)*(1-exp(-kapC*L/mu(j,1)))+...
    exp(-kapC*L/mu(j,1))-exp(-kapC*(L-z(i,1))/mu(j,1)))*mu(j,1)*dmu;
end
end

for j = 2 : M
int_H1_A(:,j) = (e0A/kapA)*mu(j,1)*int_P_A(:,j);
int_H2_A(:,j) = (r0A*eLA/kapA)*exp(-kapA*L/mu(j,1))*mu(j,1)*int_P_A(:,j);
int_H3_1_A(:,j) = (r0A*rLA)*int_P_A(:,j);
int_H4_1_A(:,j) = r0A*int_P_A(:,j);
int_H5_1_A(j,1) = mu(j,1)*dmu;
int_H7_A(:,j) = (eLA/kapA)*mu(j,1)*int_Q_A(:,j);
int_H8_A(:,j) = (rLA*e0A/kapA)*exp(-kapA*L/mu(j,1))*mu(j,1)*int_Q_A(:,j);
int_H9_1_A(:,j) = rLA*int_Q_A(:,j);
int_H10_1_A(:,j) = (rLA*r0A)*exp(-kapA*L/mu(j,1))*int_Q_A(:,j);
int_H11_1_A(j,1) = mu(j,1)*dmu;

int_H1_B(:,j) = (e0B/kapB)*mu(j,1)*int_P_B(:,j);
int_H2_B(:,j) = (r0B*eLB/kapB)*exp(-kapB*L/mu(j,1))*mu(j,1)*int_P_B(:,j);
int_H3_1_B(:,j) = (r0B*rLB)*int_P_B(:,j);
int_H4_1_B(:,j) = r0B*int_P_B(:,j);
int_H5_1_B(j,1) = mu(j,1)*dmu;
int_H7_B(:,j) = (eLB/kapB)*mu(j,1)*int_Q_B(:,j);
int_H8_B(:,j) = (rLB*e0B/kapB)*exp(-kapB*L/mu(j,1))*mu(j,1)*int_Q_B(:,j);
int_H9_1_B(:,j) = rLB*int_Q_B(:,j);
int_H10_1_B(:,j) = (rLB*r0B)*exp(-kapB*L/mu(j,1))*int_Q_B(:,j);
int_H11_1_B(j,1) = mu(j,1)*dmu;

int_H1_C(:,j) = (e0C/kapC)*mu(j,1)*int_P_C(:,j);
int_H2_C(:,j) = (r0C*eLC/kapC)*exp(-kapC*L/mu(j,1))*mu(j,1)*int_P_C(:,j);
int_H3_1_C(:,j) = (r0C*rLC)*int_P_C(:,j);
int_H4_1_C(:,j) = r0C*int_P_C(:,j);
int_H5_1_C(j,1) = mu(j,1)*dmu;
int_H7_C(:,j) = (eLC/kapC)*mu(j,1)*int_Q_C(:,j);
int_H8_C(:,j) = (rLC*e0C/kapC)*exp(-kapC*L/mu(j,1))*mu(j,1)*int_Q_C(:,j);
int_H9_1_C(:,j) = rLC*int_Q_C(:,j);
int_H10_1_C(:,j) = (rLC*r0C)*exp(-kapC*L/mu(j,1))*int_Q_C(:,j);
int_H11_1_C(j,1) = mu(j,1)*dmu;
end

%start while loop
while compare > 1
    iterations = iterations + 1;

    %calculate T(z)

```

```

%first calculate the integrals over z for each value of mu
%creates matrices where rows correspond to discrete z values and
%columns discrete values of mu
for i = 1 : N - 1
    for j = 2 : M %start at 2 because the full integral
                  %will be 0 when mu is 0

%Band A
int_z1_3_A(i,j) = 0.5*n*n*sigma*(((Tguess(i,1))^4)*...
    (F_lambda(lambda1,Tguess(i,1),n))*(exp(-kapA*((2*L)-...
    z(i,1)/mu(j,1)))+(Tguess(i+1,1))^4)*...
    (F_lambda(lambda1,Tguess(i,1),n))*(exp(-kapA*((2*L)-...
    z(i,1)/mu(j,1))))*dz;
int_z1_5and9_A(i,j) = 0.5*n*n*sigma*(((Tguess(i,1))^4)*...
    (F_lambda(lambda1,Tguess(i,1),n))*(exp(-kapA*(L-...
    z(i,1)/mu(j,1)))+(Tguess(i+1,1))^4)*...
    (F_lambda(lambda1,Tguess(i,1),n))*...
    (exp(-kapA*(L-z(i,1)/mu(j,1))))*dz;
int_z2_A(i,j) = 0.5*n*n*sigma*(((Tguess(i,1))^4)*...
    (F_lambda(lambda1,Tguess(i,1),n))*...
    (exp(-kapA*z(i,1)/mu(j,1)))+(Tguess(i+1,1))^4)*...
    (F_lambda(lambda1,Tguess(i,1),n))*...
    (exp(-kapA*z(i+1,1)/mu(j,1))))*dz;

%Band B
int_z1_3_B(i,j) = 0.5*n*n*sigma*(((Tguess(i,1))^4)*...
    (F_lambda(lambda2,Tguess(i,1),n)-...
    F_lambda(lambda1,Tguess(i,1),n))*(exp(-kapB*((2*L)-...
    z(i,1)/mu(j,1)))+(Tguess(i+1,1))^4)*...
    (F_lambda(lambda2,Tguess(i,1),n)-...
    F_lambda(lambda1,Tguess(i,1),n))*(exp(-kapB*((2*L)-...
    z(i,1)/mu(j,1))))*dz;
int_z1_5and9_B(i,j) = 0.5*n*n*sigma*(((Tguess(i,1))^4)*...
    (F_lambda(lambda2,Tguess(i,1),n)-...
    F_lambda(lambda1,Tguess(i,1),n))*...
    (exp(-kapB*(L-z(i,1)/mu(j,1)))+(Tguess(i+1,1))^4)*...
    (F_lambda(lambda2,Tguess(i,1),n)-...
    F_lambda(lambda1,Tguess(i,1),n))*...
    (exp(-kapB*(L-z(i,1)/mu(j,1))))*dz;
int_z2_B(i,j) = 0.5*sigma*(((Tguess(i,1))^4)*...
    (F_lambda(lambda2,Tguess(i,1),n)-...
    F_lambda(lambda1,Tguess(i,1),n))*...
    (exp(-kapB*z(i,1)/mu(j,1)))+(Tguess(i+1,1))^4)*...
    (F_lambda(lambda2,Tguess(i,1),n)-...
    F_lambda(lambda1,Tguess(i,1),n))*...
    (exp(-kapB*z(i+1,1)/mu(j,1))))*dz;

%Band C
int_z1_3_C(i,j) = 0.5*n*n*sigma*(((Tguess(i,1))^4)*...
    (1-F_lambda(lambda2,Tguess(i,1),n))*...
    (exp(-kapC*((2*L)-z(i,1)/mu(j,1)))+...
    ((Tguess(i+1,1))^4)*(1-F_lambda(lambda2,Tguess(i,1),n))*...
    (exp(-kapC*((2*L)-z(i,1)/mu(j,1))))*dz;
int_z1_5and9_C(i,j) = 0.5*n*n*sigma*(((Tguess(i,1))^4)*...
    (1-F_lambda(lambda2,Tguess(i,1),n))*...
    (exp(-kapC*(L-z(i,1)/mu(j,1)))+(Tguess(i+1,1))^4)*...

```



```

        (1-F_lambda(lambda2,Tguess(i,1),n))*...
        (exp(-kapC*(L-z(i,1))/mu(j,1))))*dz;
int_z2_C(i,j) = 0.5*n*n*sigma*((Tguess(i,1))^4)*...
        (1-F_lambda(lambda2,Tguess(i,1),n))*...
        (exp(-kapC*z(i,1)/mu(j,1)))+(Tguess(i+1,1))^4)*...
        (1-F_lambda(lambda2,Tguess(i,1),n))*...
        (exp(-kapC*z(i+1,1)/mu(j,1))))*dz;
    end
end

for h = 1 : N
    for i = 1 : N-1
        for j = 2 : M %start at 2 because first column is always
            %zero because multiplied by mu = 0
            int_H6_1_A(i,j,h) = sigma*n*n*((Tguess(i,1))^4)*...
                (F_lambda(lambda1,Tguess(i,1),n))*...
                mu(j,1)*exp(-kapA*(z(h,1)-z(i,1))/mu(j,1))*dz*dmu;
            int_H6_1_B(i,j,h) = sigma*n*n*((Tguess(i,1))^4)*...
                (F_lambda(lambda2,Tguess(i,1),n)-...
                F_lambda(lambda1,Tguess(i,1),n))*...
                mu(j,1)*exp(-kapB*(z(h,1)-z(i,1))/mu(j,1))*dz*dmu;
            int_H6_1_C(i,j,h) = sigma*n*n*((Tguess(i,1))^4)*...
                (1-F_lambda(lambda2,Tguess(i,1),n))*mu(j,1)*...
                exp(-kapC*(z(h,1)-z(i,1))/mu(j,1))*dz*dmu;
            int_H12_1_A(i,j,h) = sigma*n*n*((Tguess(i,1))^4)*...
                (F_lambda(lambda1,Tguess(i,1),n))*...
                mu(j,1)*exp(-kapA*(z(i,1)-z(h,1))/mu(j,1))*dz*dmu;
            int_H12_1_B(i,j,h) = sigma*n*n*((Tguess(i,1))^4)*...
                (F_lambda(lambda2,Tguess(i,1),n)-...
                F_lambda(lambda1,Tguess(i,1),n))*...
                mu(j,1)*exp(-kapB*(z(i,1)-z(h,1))/mu(j,1))*dz*dmu;
            int_H12_1_C(i,j,h) = sigma*n*n*((Tguess(i,1))^4)*...
                (1-F_lambda(lambda2,Tguess(i,1),n))*...
                mu(j,1)*exp(-kapC*(z(i,1)-z(h,1))/mu(j,1))*dz*dmu;
        end
    end
end

for h = 1 : N
    for i = 1 : N
        int_H6_2_A(i,h) = sum(int_H6_1_A(i,:,h));
        int_H6_2_B(i,h) = sum(int_H6_1_B(i,:,h));
        int_H6_2_C(i,h) = sum(int_H6_1_C(i,:,h));
        int_H12_2_A(i,h) = sum(int_H12_1_A(i,:,h));
        int_H12_2_B(i,h) = sum(int_H12_1_B(i,:,h));
        int_H12_2_C(i,h) = sum(int_H12_1_C(i,:,h));
    end
end

%calcualte integrals over mu

for i = 1 : N
    for j = 2 : M
        int_H3_2_A(i,j) = int_H3_1_A(i,j)*sum(int_z1_3_A(:,j));
        int_H4_2_A(i,j) = int_H4_1_A(i,j)*sum(int_z2_A(:,j));
        int_H9_2_A(i,j) = int_H9_1_A(i,j)*sum(int_z1_5and9_A(:,j));
    end
end

```

```

int_H10_2_A(i,j) = int_H10_1_A(i,j)*sum(int_z2_A(:,j));

int_H3_2_B(i,j) = int_H3_1_B(i,j)*sum(int_z1_3_B(:,j));
int_H4_2_B(i,j) = int_H4_1_B(i,j)*sum(int_z2_B(:,j));
int_H9_2_B(i,j) = int_H9_1_B(i,j)*sum(int_z1_5and9_B(:,j));
int_H10_2_B(i,j) = int_H10_1_B(i,j)*sum(int_z2_B(:,j));

int_H3_2_C(i,j) = int_H3_1_C(i,j)*sum(int_z1_3_C(:,j));
int_H4_2_C(i,j) = int_H4_1_C(i,j)*sum(int_z2_C(:,j));
int_H9_2_C(i,j) = int_H9_1_C(i,j)*sum(int_z1_5and9_C(:,j));
int_H10_2_C(i,j) = int_H10_1_C(i,j)*sum(int_z2_C(:,j));
end
end

for j = 1 : M
int_H5_2_A(j,1) = int_H5_1_A(j,1)*sum(int_z1_5and9_A(:,j));
int_H11_2_A(j,1) = int_H11_1_A(j,1)*sum(int_z2_A(:,j));

int_H5_2_B(j,1) = int_H5_1_B(j,1)*sum(int_z1_5and9_B(:,j));
int_H11_2_B(j,1) = int_H11_1_B(j,1)*sum(int_z2_B(:,j));

int_H5_2_C(j,1) = int_H5_1_C(j,1)*sum(int_z1_5and9_C(:,j));
int_H11_2_C(j,1) = int_H11_1_C(j,1)*sum(int_z2_C(:,j));
end

for i = 1 : N

TA(i,1) = (2/k)*n*n*(sigma*(T0^4)*F_lambda(lambda1,T0,n)*...
sum(int_H1_A(i,:))+sigma*n*n*(TL^4)*F_lambda(lambda1,TL,n)*...
sum(int_H2_A(i,:))+sum(int_H3_2_A(i,:))+sum(int_H4_2_A(i,:))+...
(z(i,1)/L)*sum(int_H5_2_A)-sum(int_H6_2_A(1:i,i))+...
sigma*n*n*(TL^4)*F_lambda(lambda1,TL,n)*sum(int_H7_A(i,:))+...
sigma*n*n*(T0^4)*F_lambda(lambda1,T0,n)*sum(int_H8_A(i,:))+...
sum(int_H9_2_A(i,:))+sum(int_H10_2_A(i,:))+...
(1-(z(i,1)/L))*sum(int_H11_2_A)-sum(int_H12_2_A(i:N,i)));

TB(i,1) = (2/k)*(sigma*n*n*(T0^4)*(F_lambda(lambda2,T0,n)-...
F_lambda(lambda1,T0,n))*sum(int_H1_B(i,:))+sigma*n*n*(TL^4)*...
(F_lambda(lambda2,TL,n)-F_lambda(lambda1,TL,n))*...
sum(int_H2_B(i,:))+sum(int_H3_2_B(i,:))+sum(int_H4_2_B(i,:))+...
(z(i,1)/L)*sum(int_H5_2_B)-sum(int_H6_2_B(1:i,i))+...
sigma*n*n*(TL^4)*(F_lambda(lambda2,TL,n)-...
F_lambda(lambda1,TL,n))*sum(int_H7_B(i,:))+sigma*n*n*(T0^4)*...
(F_lambda(lambda2,T0,n)-F_lambda(lambda1,T0,n))*...
sum(int_H8_B(i,:)) + sum(int_H9_2_B(i,:))+...
sum(int_H10_2_B(i,:))+(1-(z(i,1)/L))*sum(int_H11_2_B)...
-sum(int_H12_2_B(i:N,i)));

TC(i,1) = (2/k)*(sigma*n*n*(T0^4)*(1-F_lambda(lambda2,T0,n))*...
sum(int_H1_C(i,:))+sigma*n*n*(TL^4)*...
(1-F_lambda(lambda2,TL,n))*sum(int_H2_C(i,:))+...
sum(int_H3_2_C(i,:))+sum(int_H4_2_C(i,:))+...
(z(i,1)/L)*sum(int_H5_2_C)-sum(int_H6_2_C(1:i,i))+...
sigma*n*n*(TL^4)*(1-F_lambda(lambda2,TL,n))*...
sum(int_H7_C(i,:))+sigma*n*n*(T0^4)*...

```

```

        (1-F_lambda(lambda2,T0,n))*sum(int_H8_C(i,:))+...
        sum(int_H9_2_C(i,:))+sum(int_H10_2_C(i,:))+...
        (1-(z(i,1)/L))*sum(int_H11_2_C)-sum(int_H12_2_C(i:N,i)));

    T(i,1) = ((TL/L)-(T0/L))*z(i,1)+T0+(TA(i,1)+TB(i,1)+TC(i,1));

end

T(1,1) = T0;
T(N,1) = TL;

compare = norm(T - Tguess);
disp(compare);

Tguess = Tguess + relax*(T - Tguess);
end

time = toc;

```

Source code file: F_lambda.m

User inputs: None. The function is called by
“radiation_conduction_parallel_plates.m.”

Source code:

```

function [F_lambda] = F_lambda(lambda, T, n)

%this function gives the percent of emissive power (in W/m^2 sr)
%of a black body between 0 and the given wavelength at the given
%temperature and refractive index

%Travis J. Moore, Brigham Young University, 2014

%constants
terms = 5; %number of terms in the summation
C2 = 14388;

x = C2/(n*lambda*T);

if x > 2
    for m = 1 : terms
        summation_terms(m) = ((exp(-m*x)/(m^4))*((m*x+3)*m*x+6)*m*x+6);
    end
    F_lambda = (15/(pi^4))*sum(summation_terms);
else
    F_lambda = 1 - (15/(pi^4))*(x^3)*((1/3)-(x/8)+(x^2/60)-...
        (x^4/5040)+(x^6/272160)-(x^8/13305600));
end

```

A.6 Non-gray Thermal Barrier Coating, Section 8.3.2

Source code file: TBC_temp.m

User inputs: system parameters

Source code:

```
clear all;
format('longg');
tic;

%This program computes the temperature profile for the combined conduction-
%radiation problem in a plane-parallel, absorbing, emitting, non-gray medium
%surrounded by non-gray emitting with one reflecting boundary and the other
%reflecting/emitting boundary

%Travis J. Moore, Brigham Young University, 2014

%INPUTS
L = 1;           %length of TBC
k = 0.5;        %thermal conductivity of TBC
T0 = 300;       %substrate temperature
TL = 150;       %interface temperature
N = 200;        %number z points (including ends)
M = 30;         %number of mu divisions (including ends)

%spectral properties
%the spectrum is divided into three bands with constant properties
lambda1 = 0;    %band A is lambda = 0 to lambda1
lambda2 = 4;    %band B is lambda2 to lambda3
lambda3 = 6;    %band C is lambda3 to lambda = infinity
lambda4 = 100;  %assume band C is between lambda3 and lambda4

%use a step approximation of properties in each band
%substrate properties
e0A = 0.4;      %emittance in band A
e0B = 0.9;      %emittance in band B
e0C = 0.7;      %emittance in band C
r0A = 1-e0A;    %reflectance in band A
r0B = 1-e0B;    %reflectance in band B
r0C = 1-e0C;    %reflectance in band C

%interface properties
nA = 2;         %refractive index in band A MUST BE SAME IN ALL BANDS
nB = 2;         %refractive index in band B
nC = 2;         %refractive index in band C

%compute reflectance at TBC/vacuum interface
r1 = 0.5 + (((3*nA+1)*(nA-1))/(6*((nA+1)^2))) + ...
      ((nA*nA*((nA*nA-1)^2)/((nA*nA+1)^3))*log((nA-1)/(nA+1))) - ...
      (2*(nA^3)*(nA*nA+2*nA-1)/((nA*nA+1)*((nA^4)-1))) + ...
      ((8*(nA^4)*((nA^4)+1))/((nA*nA+1)*((nA^4)-1)^2))*log(nA);
rLA = 1-((1-r1)/(nA^2));
```

```

rLB = rLA;
rLC = rLA;

tLA = 1 - rLA; %transmittance in band A
tLB = 1 - rLB; %transmittance in band B
tLC = 1 - rLC; %transmittance in band C

%absorption coefficient
kapA = 5; %absorption coefficient in band A (m-1)
kapB = 20; %absorption coefficient in band B (m-1)
kapC = 15; %absorption coefficient in band C (m-1)

%calculate other parameters
dz = L/(N-1); %length of z divisions
dmu = 1/(M-1); %length of mu divisions
sigma = 5.67E-8; %stefan-boltzmann constant
relax = 0.3 ; %under-relaxation factor
compare = 10;
iterations = 0;

%Preallocate arrays
z = zeros(N,1);
mu = zeros(M,1);
RA = zeros(M,1);
RB = zeros(M,1);
RC = zeros(M,1);
int_P_A = zeros(N,M);
int_Q_A = zeros(N,M);
int_G5_1_A = zeros(N,M);
int_G10_1_A = zeros(N,M);
int_P_B = zeros(N,M);
int_Q_B = zeros(N,M);
int_G5_1_B = zeros(N,M);
int_G10_1_B = zeros(N,M);
int_P_C = zeros(N,M);
int_Q_C = zeros(N,M);
int_G5_1_C = zeros(N,M);
int_G10_1_C = zeros(N,M);
int_G1_A = zeros(N,M);
int_G2_1_A = zeros(N,M);
int_G3_1_A = zeros(N,M);
int_G4_1_A = zeros(M,1);
int_G6_A = zeros(N,M);
int_G7_1_A = zeros(N,M);
int_G8_1_A = zeros(N,M);
int_G9_1_A = zeros(M,1);
int_G1_B = zeros(N,M);
int_G2_1_B = zeros(N,M);
int_G3_1_B = zeros(N,M);
int_G4_1_B = zeros(M,1);
int_G6_B = zeros(N,M);
int_G7_1_B = zeros(N,M);
int_G8_1_B = zeros(N,M);
int_G9_1_B = zeros(M,1);
int_G1_C = zeros(N,M);
int_G2_1_C = zeros(N,M);

```

```

int_G3_1_C = zeros(N,M);
int_G4_1_C = zeros(M,1);
int_G6_C = zeros(N,M);
int_G7_1_C = zeros(N,M);
int_G8_1_C = zeros(N,M);
int_G9_1_C = zeros(M,1);
int_z1_A = zeros(N,M);
int_z2_A = zeros(N,M);
int_z1_B = zeros(N,M);
int_z2_B = zeros(N,M);
int_z1_C = zeros(N,M);
int_z2_C = zeros(N,M);
int_G2_2_A = zeros(N,M);
int_G3_2_A = zeros(N,M);
int_G5_2_A = zeros(N,M);
int_G7_2_A = zeros(N,M);
int_G8_2_A = zeros(N,M);
int_G10_2_A = zeros(N,M);
int_G2_2_B = zeros(N,M);
int_G3_2_B = zeros(N,M);
int_G5_2_B = zeros(N,M);
int_G7_2_B = zeros(N,M);
int_G8_2_B = zeros(N,M);
int_G10_2_B = zeros(N,M);
int_G2_2_C = zeros(N,M);
int_G3_2_C = zeros(N,M);
int_G5_2_C = zeros(N,M);
int_G7_2_C = zeros(N,M);
int_G8_2_C = zeros(N,M);
int_G10_2_C = zeros(N,M);
int_G4_2_A = zeros(M,1);
int_G9_2_A = zeros(M,1);
int_G4_2_B = zeros(M,1);
int_G9_2_B = zeros(M,1);
int_G4_2_C = zeros(M,1);
int_G9_2_C = zeros(M,1);
TA = zeros(N,1);
TB = zeros(N,1);
TC = zeros(N,1);
T = zeros(N,1);
int_H2_A = zeros(N,1);
int_H3_A = zeros(N,1);
int_H2_B = zeros(N,1);
int_H3_B = zeros(N,1);
int_H2_C = zeros(N,1);
int_H3_C = zeros(N,1);

%create z vector
for i = 1 : N
    z(i,1) = (i-1)*dz;
end

%create mu vector
for j = 1 : M
    mu(j,1) = (j-1)*dmu;
end

```

```

%intital temperature profile guess (linear)
Tguess = T0 + ((TL-T0)/L)*z;

%calculate R for all values of mu
for j = 1 : M
    RA(j,1) = 1/(1-r0A*rLA*exp(-2*kapA*L/mu(j,1)));
    RB(j,1) = 1/(1-r0B*rLB*exp(-2*kapB*L/mu(j,1)));
    RC(j,1) = 1/(1-r0C*rLC*exp(-2*kapC*L/mu(j,1)));
end

%perform integrations that only depend on z and mu (not on T)
for i = 1 : N
    for j = 2 : M %start at 2 because the integral will be 0 when mu is 0
        int_P_A(i,j) = RA(j,1)*mu(j,1)*((z(i,1)/L)*...
            (exp(-kapA*L/mu(j,1))-1)+(1-exp(-kapA*z(i,1)/mu(j,1))))*dmu;
        int_Q_A(i,j) = RA(j,1)*mu(j,1)*(exp(-kapA*L/mu(j,1)))*...
            ((z(i,1)/L)*(1-exp(-kapA*L/mu(j,1)))+...
            exp(-kapA*L/mu(j,1))*((1-exp(kapA*z(i,1)/mu(j,1)))))*dmu;
        int_G5_1_A(i,j) = exp(-kapA*z(i,1)/mu(j,1))*mu(j,1)*dmu;
        int_G10_1_A(i,j) = exp(kapA*z(i,1)/mu(j,1))*mu(j,1)*dmu;

        int_P_B(i,j) = RB(j,1)*((z(i,1)/L)*(exp(-kapB*L/mu(j,1))-1)+...
            (1-exp(-kapB*z(i,1)/mu(j,1))))*mu(j,1)*dmu;
        int_Q_B(i,j) = RB(j,1)*mu(j,1)*(exp(-kapB*L/mu(j,1)))*...
            ((z(i,1)/L)*(1-exp(-kapB*L/mu(j,1)))+...
            exp(-kapB*L/mu(j,1))*((1-exp(kapB*z(i,1)/mu(j,1)))))*dmu;
        int_G5_1_B(i,j) = exp(-kapB*z(i,1)/mu(j,1))*mu(j,1)*dmu;
        int_G10_1_B(i,j) = exp(kapB*z(i,1)/mu(j,1))*mu(j,1)*dmu;

        int_P_C(i,j) = RC(j,1)*((z(i,1)/L)*(exp(-kapC*L/mu(j,1))-1)+...
            (1-exp(-kapC*z(i,1)/mu(j,1))))*mu(j,1)*dmu;
        int_Q_C(i,j) = RC(j,1)*mu(j,1)*(exp(-kapC*L/mu(j,1)))*...
            ((z(i,1)/L)*(1-exp(-kapC*L/mu(j,1)))+...
            exp(-kapC*L/mu(j,1))*((1-exp(kapC*z(i,1)/mu(j,1)))))*dmu;
        int_G5_1_C(i,j) = exp(-kapC*z(i,1)/mu(j,1))*mu(j,1)*dmu;
        int_G10_1_C(i,j) = exp(kapC*z(i,1)/mu(j,1))*mu(j,1)*dmu;
    end
end

for j = 2 : M
    int_G1_A(:,j) = (e0A/kapA)*mu(j,1)*int_P_A(:,j);
    int_G2_1_A(:,j) = (r0A*rLA)*exp(-2*kapA*L/mu(j,1))*int_P_A(:,j);
    int_G3_1_A(:,j) = r0A*int_P_A(:,j);
    int_G4_1_A(j,1) = exp(-kapA*L/mu(j,1))*mu(j,1)*dmu;
    int_G6_A(:,j) = (rLA*e0A/kapA)*mu(j,1)*int_Q_A(:,j);
    int_G7_1_A(:,j) = (r0A*rLA)*int_Q_A(:,j);
    int_G8_1_A(:,j) = rLA*int_Q_A(:,j);
    int_G9_1_A(j,1) = mu(j,1)*dmu;

    int_G1_B(:,j) = (e0B/kapB)*mu(j,1)*int_P_B(:,j);
    int_G2_1_B(:,j) = (r0B*rLB)*exp(-2*kapB*L/mu(j,1))*int_P_B(:,j);
    int_G3_1_B(:,j) = r0B*int_P_B(:,j);
    int_G4_1_B(j,1) = exp(-kapB*L/mu(j,1))*mu(j,1)*dmu;
    int_G6_B(:,j) = (rLB*e0B/kapB)*mu(j,1)*int_Q_B(:,j);

```

```

int_G7_1_B(:,j) = (r0B*rLB)*int_Q_B(:,j);
int_G8_1_B(:,j) = rLB*int_Q_B(:,j);
int_G9_1_B(j,1) = mu(j,1)*dmu;

int_G1_C(:,j) = (e0C/kapC)*mu(j,1)*int_P_C(:,j);
int_G2_1_C(:,j) = (r0C*rLC)*exp(-2*kapC*L/mu(j,1))*int_P_C(:,j);
int_G3_1_C(:,j) = r0C*int_P_C(:,j);
int_G4_1_C(j,1) = exp(-kapC*L/mu(j,1))*mu(j,1)*dmu;
int_G6_C(:,j) = (rLC*e0C/kapC)*mu(j,1)*int_Q_C(:,j);
int_G7_1_C(:,j) = (r0C*rLC)*int_Q_C(:,j);
int_G8_1_C(:,j) = rLC*int_Q_C(:,j);
int_G9_1_C(j,1) = mu(j,1)*dmu;
end

%start while loop
while compare > 1
    iterations = iterations + 1;

    %calculate T(z)

    %first calculate the integrals over z for each value of mu
    %creates matrices where rows correspond to discrete z values and
    %columns discrete values ofmu
    for i = 1 : N-1
        for j = 2 : M %start at 2 because the the full integral
                        %will be 0 when mu is 0

            %Band A
            int_z1_A(i,j) = 0.5*(nA*nA)*sigma*(((Tguess(i,1))^4)*...
                (F_lambda(lambda2,Tguess(i,1),nA))*...
                (exp(kapA*z(i,1)/mu(j,1)))+(Tguess(i+1,1))^4)*...
                (F_lambda(lambda2,Tguess(i,1),nA))*...
                (exp(kapA*z(i+1,1)/mu(j,1))))*dz;
            int_z2_A(i,j) = 0.5*(nA*nA)*sigma*(((Tguess(i,1))^4)*...
                (F_lambda(lambda2,Tguess(i,1),nA))*...
                (exp(-kapA*z(i,1)/mu(j,1)))+(Tguess(i+1,1))^4)*...
                (F_lambda(lambda2,Tguess(i,1),nA))*...
                (exp(-kapA*z(i+1,1)/mu(j,1))))*dz;

            %Band B
            int_z1_B(i,j) = 0.5*(nB*nB)*sigma*(((Tguess(i,1))^4)*...
                (F_lambda(lambda3,Tguess(i,1),nB)-...
                F_lambda(lambda2,Tguess(i,1),nB))*...
                (exp(kapB*z(i,1)/mu(j,1)))+(Tguess(i+1,1))^4)*...
                (F_lambda(lambda3,Tguess(i,1),nB)-...
                F_lambda(lambda2,Tguess(i,1),nB))*...
                (exp(kapB*z(i+1,1)/mu(j,1))))*dz;
            int_z2_B(i,j) = 0.5*(nB*nB)*sigma*(((Tguess(i,1))^4)*...
                (F_lambda(lambda3,Tguess(i,1),nB)-...
                F_lambda(lambda2,Tguess(i,1),nB))*...
                (exp(-kapB*z(i,1)/mu(j,1)))+(Tguess(i+1,1))^4)*...
                (F_lambda(lambda3,Tguess(i,1),nB)-...
                F_lambda(lambda2,Tguess(i,1),nB))*...
                (exp(-kapB*z(i+1,1)/mu(j,1))))*dz;

            %Band C
            int_z1_C(i,j) = 0.5*(nC*nC)*sigma*(((Tguess(i,1))^4)*...

```



```

        (1-F_lambda(lambda3,Tguess(i,1),nC))*...
        (exp(kapC*z(i,1)/mu(j,1)))+(Tguess(i+1,1))^4)*...
        (1-F_lambda(lambda3,Tguess(i,1),nC))*...
        (exp(kapC*z(i+1,1)/mu(j,1))) *dz;
    int_z2_C(i,j) = 0.5*(nC*nC)*sigma*((Tguess(i,1))^4)*...
        (1-F_lambda(lambda3,Tguess(i,1),nC))*...
        (exp(-kapC*z(i,1)/mu(j,1)))+(Tguess(i+1,1))^4)*...
        (1-F_lambda(lambda3,Tguess(i,1),nC))*...
        (exp(-kapC*z(i+1,1)/mu(j,1))) *dz;
    end
end

%calcualte integrals over mu
for i = 1 : N
    for j = 2 : M
        int_G2_2_A(i,j) = int_G2_1_A(i,j)*sum(int_z1_A(:,j));
        int_G3_2_A(i,j) = int_G3_1_A(i,j)*sum(int_z2_A(:,j));
        int_G5_2_A(i,j) = int_G5_1_A(i,j)*sum(int_z1_A(1:i,j));
        int_G7_2_A(i,j) = int_G7_1_A(i,j)*sum(int_z2_A(:,j));
        int_G8_2_A(i,j) = int_G8_1_A(i,j)*sum(int_z1_A(:,j));
        int_G10_2_A(i,j) = int_G10_1_A(i,j)*sum(int_z2_A(i:N,j));

        int_G2_2_B(i,j) = int_G2_1_B(i,j)*sum(int_z1_B(:,j));
        int_G3_2_B(i,j) = int_G3_1_B(i,j)*sum(int_z2_B(:,j));
        int_G5_2_B(i,j) = int_G5_1_B(i,j)*sum(int_z1_B(1:i,j));
        int_G7_2_B(i,j) = int_G7_1_B(i,j)*sum(int_z2_B(:,j));
        int_G8_2_B(i,j) = int_G8_1_B(i,j)*sum(int_z1_B(:,j));
        int_G10_2_B(i,j) = int_G10_1_B(i,j)*sum(int_z2_B(i:N,j));

        int_G2_2_C(i,j) = int_G2_1_C(i,j)*sum(int_z1_C(:,j));
        int_G3_2_C(i,j) = int_G3_1_C(i,j)*sum(int_z2_C(:,j));
        int_G5_2_C(i,j) = int_G5_1_C(i,j)*sum(int_z1_C(1:i,j));
        int_G7_2_C(i,j) = int_G7_1_C(i,j)*sum(int_z2_C(:,j));
        int_G8_2_C(i,j) = int_G8_1_C(i,j)*sum(int_z1_C(:,j));
        int_G10_2_C(i,j) = int_G10_1_C(i,j)*sum(int_z2_C(i:N,j));
    end
end

for j = 1 : M
    int_G4_2_A(j,1) = int_G4_1_A(j,1)*sum(int_z1_A(:,j));
    int_G9_2_A(j,1) = int_G9_1_A(j,1)*sum(int_z2_A(:,j));

    int_G4_2_B(j,1) = int_G4_1_B(j,1)*sum(int_z1_B(:,j));
    int_G9_2_B(j,1) = int_G9_1_B(j,1)*sum(int_z2_B(:,j));

    int_G4_2_C(j,1) = int_G4_1_C(j,1)*sum(int_z1_C(:,j));
    int_G9_2_C(j,1) = int_G9_1_C(j,1)*sum(int_z2_C(:,j));
end

for i = 1 : N

    TA(i,1) = (2/k)*((nA*nA)*sigma*(T0^4)*F_lambda(lambda2,T0,nA)*...
        sum(int_G1_A(i,:))+sum(int_G2_2_A(i,:))+sum(int_G3_2_A(i,:))+...
        (z(i,1)/L)*sum(int_G4_2_A)-sum(int_G5_2_A(i,:))+...

```

```

(nA*nA)*sigma*(T0^4)*F_lambda(lambda2,T0,nA)*sum(int_G6_A(i,:))+...
    sum(int_G7_2_A(i,:))+sum(int_G8_2_A(i,:))+...
    (1-(z(i,1)/L))*sum(int_G9_2_A)-sum(int_G10_2_A(i,:));

    TB(i,1) = (2/k)*((nB*nB)*sigma*(T0^4)*(F_lambda(lambda3,T0,nB)-...
F_lambda(lambda2,T0,nB))*sum(int_G1_B(i,:))+sum(int_G2_2_B(i,:))+...
    sum(int_G3_2_B(i,:))+(z(i,1)/L)*sum(int_G4_2_B)-...
    sum(int_G5_2_B(i,:))+(nB*nB)*sigma*(T0^4)*...
    (F_lambda(lambda3,T0,nB)-F_lambda(lambda2,T0,nB))*...
    sum(int_G6_B(i,:))+sum(int_G7_2_B(i,:))+ sum(int_G8_2_B(i,:))+...
    (1-(z(i,1)/L))*sum(int_G9_2_B)-sum(int_G10_2_B(i,:));

    TC(i,1) = (2/k)*((nC*nC)*sigma*(T0^4)*(1-F_lambda(lambda3,T0,nC))*...
    sum(int_G1_C(i,:))+sum(int_G2_2_C(i,:))+sum(int_G3_2_C(i,:))+...
    (z(i,1)/L)*sum(int_G4_2_C)-sum(int_G5_2_C(i,:))+...
    (nC*nC)*sigma*(T0^4)*(1-F_lambda(lambda3,T0,nC))*...
    sum(int_G6_C(i,:))+sum(int_G7_2_C(i,:))+sum(int_G8_2_C(i,:))+...
    (1-(z(i,1)/L))*sum(int_G9_2_C)-sum(int_G10_2_C(i,:));

    T(i,1) = ((TL/L)-(T0/L))*z(i,1) + T0 + (TA(i,1) + TB(i,1) + TC(i,1));

end

T(1,1) = T0;
T(N,1) = TL;

compare = norm(T - Tguess);
disp(compare);

Tguess = Tguess + relax*(T - Tguess);
end

```

A.7 Genetic Algorithm for TBC, Section 8.8

Source code file: genetic_algorithm_TBC.m

User inputs: System parameters and genetic algorithm parameters

Source code:

```

clear all;
format('longg');
tic;

%This program find the optimum parameters of a thermal barrier coating
%system using a genetic algorithm based on measured data

%Travis J. Moore, Brigham Young University, 2014

```

```

%user inputs
M = 5;           %number of unknown properties to be determined:
                 %T0, TL, kappa, e0, n, k
N = 100;        %number of points in temperature profile
P = M;          %total number of genes in each individual
Q = 4;          %number of frequencies in band
                 %(IT WILL ACTUALLY BE ONE MORE THAN THIS)
L = 0.00015;    %thickness of TBC (meters)
lambda1 = 2;    %lower wavelength of measurement band
lambda2 = 2.4;  %upper wavelength of measurement band
string = 10;    %number of bits in each binary string
lower_T0 = 1700; %lower bound of substrate temp for binary string
upper_T0 = 2000; %upper bound of substrate temp for binary string
lower_TL = 1500; %lower bound of surface temp for binary string
upper_TL = 1900; %upper bound of surface temp for binary string
lower_e0 = 0.1; %lower bound of emittance for binary string
upper_e0 = 1;   %upper bound of emittance for binary string
lower_n = 1.6;  %lower bound for refractive index for binary string
upper_n = 2.2;  %upper bound for refractive index for binary string
lower_kap = 0.1; %lower bound of absorption coefficient for binary string
upper_kap = 150; %upper bound of absorption coefficient for binary string
pop_size = 201; %number of individuals in each generation
                 %MUST BE ODD NUMBER
tourn_size = 10; %percent of population size used in tournament selection
mut_rate = 70;   %percent chance of mutation for each chromosome
cross_times = 3; %number of times crossover is performed
prec = 0.001;   %parameter precision
meas_error = 0; %percent measurement error added to measured signals

%constants and initialization
sigma = 5.67E-8; %stefan-boltzmann constant
dz = L/(N-1);   %length of z divisions
iteration = 0;
min_f = 10;

%Preallocate arrays
z = zeros(N,1);
frequencies = zeros(Q+1,1);
wavelengths = zeros(Q+1,1);
calculated_signals = zeros(N+Q+1,pop_size);
minimum_fitness = zeros(11,1);
T0 = zeros(1,pop_size);
TL = zeros(1,pop_size);
e0 = zeros(1,pop_size);
n = zeros(1,pop_size);
kappa = zeros(1,pop_size);
k = zeros(1,pop_size);
total_error = zeros(pop_size,1);
fitness = zeros(pop_size,1);

%instrument response function: 2 - 2.4 new IRF
IRF = [29480000000; 26970000000; 24910000000; 22730000000; 20540000000];

%simulated measurements
%N = 100, kap = 100, T0=1500, TL=1300,e=0.8, n =2.1 L = 0.0002 2 - 2.4???

```

```

measured_signals = [6.22E-11; 6.49E-11; 6.71E-11; 6.88E-11; 7.00E-11];
measured_signals = measured_signals.*IRF;

%add measurement error
measured_signals = (meas_error/100)*(measured_signals)+measured_signals;

%create z vector
for i = 1 : N
    z(i,1) = (i-1)*dz;
end

%create wavelength vector
for i = 1 : Q + 1
    wavelengths(i,1) = lambda1 + ((lambda2 - lambda1)/Q)*(i-1);
end

%create frequency vector
for i = 1 : Q + 1
    frequencies(i,1) = wavelength_to_freq(wavelengths(i,1),1);
end

%create initial population

%create random array of zeros and ones and convert it to string
current_gen_bin_array = num2str(randi([0 1],pop_size,string*P));
%remove spaces from string
for i = 1 : pop_size
    current_gen_bin(i,:) = strrep(current_gen_bin_array(i,:), ' ', '');
end

%start genetic algorithm
for count = 1 : 1000
    iteration = iteration + 1;

    %forward problem
    for i = 1 : pop_size
        %convert the binary string to real TL
        TL(i) = round(bin2real(current_gen_bin(i,1:string), lower_TL,...
            upper_TL, string)/prec)*prec;
        %convert the binary string to real e0
        e0(i) = round(bin2real(current_gen_bin(i,1*string+1:2*string),...
            lower_e0, upper_e0, string)/prec)*prec;
        %convert the binary string to real T0
        T0(i) = round(bin2real(current_gen_bin(i,2*string+1:3*string),...
            lower_T0, upper_T0, string)/prec)*prec;
        %convert the binary string to real kappa
        kappa(i) = round(bin2real(current_gen_bin(i,3*string+1:4*string),...
            lower_kap, upper_kap, string)/prec)*prec;
        %convert the binary string to real n
        n(i) = round(bin2real(current_gen_bin(i,4*string+1:5*string),...
            lower_n, upper_n, string)/prec)*prec;

        %if T0 < TL, switch them around
        if T0(i) < TL(i)
            T0_temp = T0(i);

```

```

    T0(i) = TL(i);
    TL(i) = T0_temp;
    T0_string_temp = current_gen_bin(i,2*string+1:3*string);
    current_gen_bin(i,2*string+1:3*string)=...
        current_gen_bin(i,1:string);
    current_gen_bin(i,1:string) = T0_string_temp;
end

%call forward problem function to calculate the signal and
%temperature profile for each individual
calculated_signals(:,i) = forward_problem_TBC(T0(i),TL(i),...
    kappa(i),e0(i),n(i),L,N,Q,lambda1,lambda2);
end

%the fitness of each individual is the Euclidean norm of the error
%between the calculated and measured error
for i = 1 : pop_size
    fitness(i,1)=norm(measured_signals-...
        calculated_signals(N+1:N+Q+1,i).*IRF);
end

%find the best fit individual
[min_f, min_f_index] = min(fitness);
disp(min_f);
minimum_fitness(count+11,1) = min_f;

%break the loop if the best fit does not change after 11 generations
if minimum_fitness(count+11,1) == minimum_fitness(count,1)
    break;
end

%elitism: put the best fit in the new generation
new_gen_bin(1,:) = current_gen_bin(min_f_index,:);

%use tournament selection for the rest of the new generation
for i = 2 : (pop_size+1)/2
    for j = 1 : cross_times
        %tournament selection
        %create pool of mothers and fathers
        mother_pool = randi(pop_size, round((tourn_size/100)*pop_size), 1);
        father_pool = randi(pop_size, round((tourn_size/100)*pop_size), 1);

        %pick the most fit mother
        [mother_fit, mother_index] = min(fitness(mother_pool));
        mother_index = mother_pool(mother_index);

        %pick the best fit father
        [father_fit, father_index] = min(fitness(father_pool));
        father_index = father_pool(father_index);

        for j = 1 : cross_times
            %crossover at gene corresponding to a parameter
            chromosome_crossover_point = randi(P-1)*string;
            new_gen_bin(i,1:chromosome_crossover_point)=...

```

```

        current_gen_bin(mother_index,1:...
        chromosome_crossover_point);
new_gen_bin(i,chromosome_crossover_point+1:string*P)=...
    current_gen_bin(father_index,...
    chromosome_crossover_point+1:string*P);
new_gen_bin(((pop_size+1)/2)-1+i,1:...
    chromosome_crossover_point)=current_gen_bin(...
    father_index,1:chromosome_crossover_point);
new_gen_bin(((pop_size+1)/2)-1+i,...
    chromosome_crossover_point+1:string*P)=...
    current_gen_bin(mother_index,...
    chromosome_crossover_point+1:string*P);
    end
end
end

%mutation - one in each parameter
for i = 2 : pop_size
    for j = 1 : P
        if rand(1) < mut_rate/100
            rand_point = randi(string);
            if new_gen_bin(i,(j-1)*string + rand_point) == '0'
                new_gen_bin(i,(j-1)*string + rand_point) = '1';
            else
                new_gen_bin(i,(j-1)*string + rand_point) = '0';
            end
        end
    end
end
end

%replace old generation with new
current_gen_bin = new_gen_bin;
end

%optimum parameter set
[final_min_fit, final_min_fit_index] = min(fitness);
TL_final = bin2real(current_gen_bin(final_min_fit_index,1:string),...
    lower_TL,upper_TL,string);
e0_final = bin2real(current_gen_bin(final_min_fit_index,...
    1*string+1:2*string), lower_e0, upper_e0, string);
T0_final = bin2real(current_gen_bin(final_min_fit_index,...
    2*string+1:3*string),lower_T0, upper_T0, string);
kappa_final = bin2real(current_gen_bin(final_min_fit_index,3*string+1:...
    4*string), lower_kap, upper_kap, string);
n_final = bin2real(current_gen_bin(final_min_fit_index,...
    4*string+1:5*string),lower_n, upper_n, string);

final_chromosome = forward_problem_TBC(T0_final,TL_final,...
    kappa_final,e0_final,n_final,L,N,Q,lambda1,lambda2);
final_parameters = [T0_final; TL_final; e0_final; n_final; kappa_final];
final_signals = final_chromosome(N+1:N+Q+1).*IRF;

time = toc;

```

Source code file: forward_problem_TBC.m

User inputs: None. The function is called by “genetic_algorithm_TBC.m.”

Source code:

```
function [forward_problem_TBC] = forward_problem_TBC(T0,TL,kappa,e0,n,L,...
                                                    N,num_waves,lambda1,lambda2)

%this function computes the irradiation on a detector from a TBC system

%Travis J. Moore, Brigham Young University, 2014

%define all of the constants
dz = L/(N-1); %length of z divisions
thetaA = 15; %acceptance angle of detector in degrees
thetaArad = thetaA*(pi/180); %acceptance angle of detector in radians
sigma = 5.67E-8; %stefan-boltzmann constant

%Preallocate arrays
z = zeros(N,1);
int_1 = zeros(N,1);
int_2 = zeros(N,1);
wavelengths = zeros(num_waves,1);
frequencies = zeros(num_waves,1);
detector = zeros(num_waves,1);

%create z vector
for i = 1 : N
    z(i,1) = (i-1)*dz;
end

%substrate interface
r0 = 1-e0; %reflectance

%TBC surface
rb = 0.5+((3*n+1)*(n-1)/(6*((n+1)^2)))+...
    ((n*n*((n*n-1)^2)/((n*n+1)^3))*log((n-1)/(n+1)))-...
    (2*(n^3)*(n*n+2*n-1)/((n*n+1)*((n^4)-1)))+...
    ((8*(n^4)*((n^4)+1))/((n*n+1)*((n^4)-1)^2))*log(n);
rL = 1-(1-rb)/(n^2); %reflectance
tL = 1 - rL; %transmittance

%assume a linear temperature profile
T = T0 + ((TL-T0)/L)*z;

%once the temperature profile is calculated, the signal to the detector can
%be calculated over the spectrum

%discretize the spectrum over which measurements will be made
for i = 1 : num_waves + 1
    wavelengths(i,1) = lambda1 + ((lambda2 - lambda1)/num_waves)*(i-1);
```

```

end

for i = 1 : num_waves + 1
    frequencies(i,1) = wavelength_to_freq(wavelengths(i,1),1);
end

%calculate detector signals

%calculate R terms with mu = 1
Rlam = 1/(1-r0*rL*exp(-2*kappa*L));

%perform numerical integrals over z at and compute irradiation at discrete
%frequencies
for j = 1 : num_waves + 1
    for i = 1 : N
        int_1(i,1) = planck_freq(frequencies(j,1),T(i,1),n)*...
            exp(-kappa*(L+z(i,1)))*dz;
        int_2(i,1) = planck_freq(frequencies(j,1),T(i,1),n)*...
            exp(-kappa*(L-z(i,1)))*dz;
    end
    detector(j,1) = tL*Rlam*(e0*planck_freq(frequencies(j,1),T0,n)*...
        exp(-kappa*L)+r0*kappa*sum(int_1)+...
        kappa*sum(int_2))*(1-cos(thetaArad));
end

%put the temp profile and signals in a vector
forward_problem_TBC = cat(1,T,detector);

```

Source code file: `planck_freq.m`

User inputs: None. The function is called by the “forward_problem_TBC.m”
function which is called by “genetic_algorithm_TBC.m.”

Source code:

```

function [planck_freq] = planck_freq(freq, T, n)

%this function gives the spectral emissive power of a black body based
%on the Planck Function
%units: W/(m^2 Hz)

%Travis J. Moore, Brigham Young University, 2014

%constants
c0 = 2.998E8;
h = 6.626E-34;
k = 1.3807E-23;

planck_freq = (2*pi*h*(freq^3)*n*n)/((c0*c0)*(exp((h*freq)/(k*T))-1));

```


A.8 Instrument Response Function for OFT, Section 10.9

Source code file: IRF_OFT.m

User inputs: Properties and parameters of optical fiber thermometer system.

Source code:

```
clear all;

%This program finds the instrument response function using the FTIR signals
%collected from a blackbody radiator at different temperatures

%Travis J. Moore, Brigham Young University, 2014

%user inputs
L = 2.23;           %length of fiber
D = 0.0004;        %fiber diameter
Tinf = 300;        %ambient temperature
Tsur = 300;        %surroundings temperature
e = 0.5;           %coating emittance
k = 2;             %thermal conductivity of fiber
h = 2;             %average convection coefficient along fiber
n = 1.5;           %refractive index of fiber
kappa = 0.15;      %spectral absorption coefficient
N = 100;           %points along fiber
num_temps = 6;     %number of temperatures in calibration
num_freqs = 6;     %number of frequency

%constants
C1 = 0.59552137E-16; %Wm^2/sr
C2 = 0.014387752;   %mK
c0 = 299792458;     %speed of light, m/s

dz = L/(N-1);      %length of z divisions in fiber
%create z vector
for i = 1 : N
    z(i,1) = (i-1)*dz;
end

%black body temperatures (K)
TC(1) = 628;
TC(2) = 704;
TC(3) = 847;
TC(4) = 923;
TC(5) = 992;
TC(6) = 1122;

%import CSV files
load BB_628.csv;
load BB_704.csv;
load BB_847.csv;
load BB_923.csv;
load BB_992.csv;
```

```

load BB_1122.csv;

%create a single matrix of the wavenumbers
wavenumbers = BB_628(:,1); %inverse centimeters

%convert to wavelength
wavelengths = (1./wavenumbers).*10000; %micrometers

%convert to frequency
frequency = (c0./(wavelengths./1000000)); %Hertz
frequency_TH = (c0./(wavelengths./1000000)).*1E-12; %Tera-Hertz

freq(1) = frequency(247);
freq(2) = frequency(254);
freq(3) = frequency(260);
freq(4) = frequency(268);
freq(5) = frequency(275);
freq(6) = frequency(283);

%concatenation of signal files into a single matrix
signals = [BB_628(247,2) BB_704(247,2) BB_847(247,2) BB_923(247,2)...
  BB_992(247,2) BB_1122(247,2);
  BB_628(254,2) BB_704(254,2) BB_847(254,2) BB_923(254,2) BB_992(254,2)...
  BB_1122(254,2);
  BB_628(260,2) BB_704(260,2) BB_847(260,2) BB_923(260,2) BB_992(260,2)...
  BB_1122(260,2);
  BB_628(268,2) BB_704(268,2) BB_847(268,2) BB_923(268,2) BB_992(268,2)...
  BB_1122(268,2);
  BB_628(275,2) BB_704(275,2) BB_847(275,2) BB_923(275,2) BB_992(275,2)...
  BB_1122(275,2);
  BB_628(283,2) BB_704(283,2) BB_847(283,2) BB_923(283,2) BB_992(283,2)...
  BB_1122(283,2)];

%calculate temperature profile
for i = 1 : num_temps
  T(:,i) = temp_profile(TC(i)+273.15,Tinf,Tsur,e,k,h,L,D,N);
end

%numerical integration terms
for i = 1 : N
  for j = 1 : num_temps
    for l = 1 : num_freqs
      num_int(i,j,l) = (planck_freq(freq(l),T(i,j),n)*...
        exp(-kappa*(L-z(i,l))))*dz;
    end
  end
end

%calculate G term
for i = 1 : num_temps
  for j = 1 : num_freqs
    G(i,j) = (planck_freq(freq(j),TC(i)+273.15,n))*exp(-kappa*L)...
      +kappa*sum(num_int(:,i,j));
  end
end
end

```

```

%compute first order curve fit to data pairs
for i = 1 : num_freqs
    p(i,:) = polyfit(signals(:,i),G(i,:) ',2);
end

%IRF for each frequency
A = p(:,1);
B = p(:,2);
C = p(:,3);

```

Source code file: temp_profile.m

User inputs: None. The function is called by the “IRF_OFT.m”

Source code:

```

function [temp_profile] = temp_profile(TC,Tinf,Tsur,e,k,h,L,D,N)

%This function uses the parameters of an OFT system and outputs the
%temperature profile along the fiber

%Travis J. Moore, Brigham Young University, 2014

dz = L/(N-1);                    %length of z divisions in fiber
sigma = 5.67E-8;                %stefan-boltzmann constant

%create z vector
for i = 1 : N
    z(i,1) = (i-1)*dz;
end

%select which temps will be used to linearize the T^4 terms
Tlin = Tsur;

%particular solution
Tp = ((h*Tinf)+(e*sigma*(Tsur^4)))/(h+(e*sigma*(Tlin^3)));

%roots of auxliary equation
p = ((4/(k*D))*(h+(e*sigma*(Tlin^3))))^(1/2);

%constants
c1 = TC-Tp-((Tinf-Tp+(Tp-TC)*exp(p*L))/(exp(-p*L)-exp(p*L)));
c2 = (Tinf-Tp+(Tp-TC)*exp(p*L))/(exp(-p*L)-exp(p*L));

for i = 1 : N
    T(i,1) = (c1*exp(p*z(i,1)))+(c2*exp(-p*z(i,1))) + Tp;
    if T(i,1) < Tinf
        T(i,1) = Tinf;
    end
end
end

```

```
for i = 2 : N
    if T(i,1) > T(i-1,1)
        T(i,1) = Tinf;
    end
end

temp_profile = T;
```